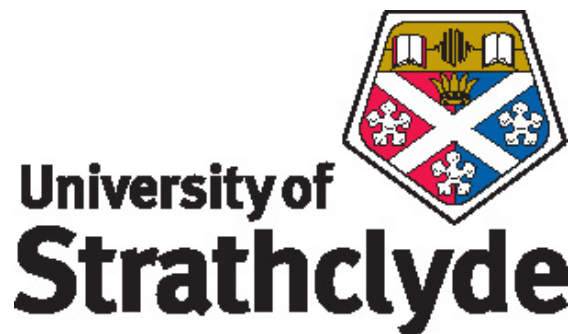**University of Strathclyde**

Institute of Photonics

Hybrid GaN/organic device fabrication by inkjet printing

by

Min Wu

A thesis presented in fulfilment of the requirements for the

**degree of Doctor of Philosophy to the University of Strathclyde,**

Department of Physics

·2009·

This thesis is the result of the author's original research. It has been composed by the author and has not been previously submitted for examination which has led to the award of a degree. The copyright of this thesis belongs to the author under the terms of the United Kingdom Copyright Acts as qualified by University of Strathclyde Regulation 3.51. Due acknowledgement must always be made of the use of any material contained in, or derived from, this thesis.
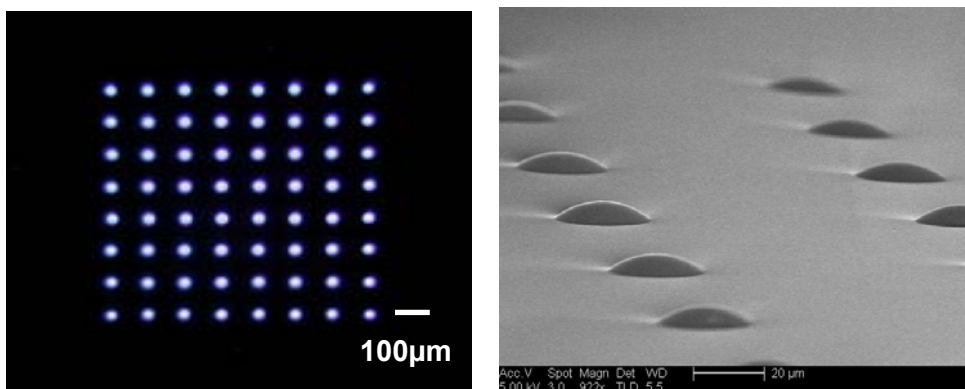
Inkjet printed micro-dots array of truxene oligofluorene T3/CHDV blends
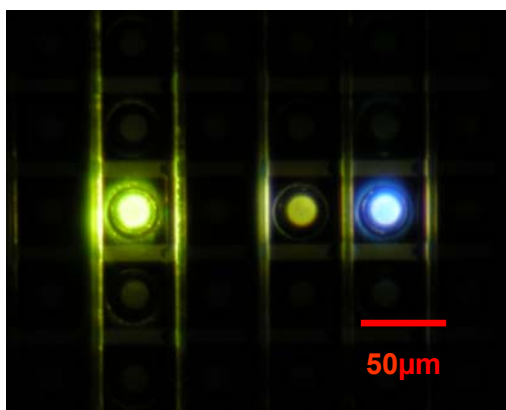
Representative optical image of the "turned on" pixels of a hybrid GaN/organic device with inkjet printed colour-converters: crosslinked F6BT/CHDV blends (left) and truxene oligofluorene T3/CHDV blend (right)

To my parents

Acknowledgements

My deepest thanks go to my supervisors Prof. Martin Dawson and Dr. Erdan Gu for their guidance, inspiration, patience and support, particularly helping me overcome all the difficulties during my PhD studies. They taught me how to be a good researcher with their knowledge and manners of scientific thinking. I am honoured to be their student.

Many thanks must be given to Dr. Benoit Guilhabert for teaching me patiently on 'clean room' processes at the beginning of my PhD work and providing invaluable advice and discussions during my studies. I also want to thank Dr. Allan Mackintosh and Dr. Alex Kuehne for their great help in the organic materials work. I appreciate Prof. Peter Skabara and Dr. Alexander Kanibolotsky for supplying the organic light emitting materials and Prof. Duncan Graham's group for collaborations on the bio-arrays work. I acknowledge Dr. Haoxiang Zhang, Dr. Zheng Gong and Dr. David Massoubre for their advice on the integration work of the micro-LEDs.

I also would like to thank David Elfstrom, Alicja Zarowna, Yujie Chen, Yanfeng Zhang, Jonathan McKendry, Dr. Handong Sun, Dr. Paul Edwards, Dr. Olaf Rolinski, David Millar, Mark McGrady, and Gordon McPhee for their help in my experiments. I am grateful to everyone who has ever helped me during my work.

I sincerely thank my parents for their unconditional love, support and encouragement all the time. Special thanks go to my dear friend Yun for helping me throughout all the problems.

Abstract

This thesis presents the application of the inkjet printing technique to hybrid inorganic/organic devices combining the advantages of both materials. Organic light emitting blend materials have been integrated onto the surface of AlInGaN micro-structured light emitting diodes (micro-LEDs) as the colour-converters using inkjet printing. Silver nanoparticles ink has also been printed to make electrical interconnections to the micro-LEDs.

Organic polymers have attractive properties which can be designed for various applications. In this thesis, we focus on the organic guest-host materials system where novel deep UV transparent polymers are the host and novel organic light emitting materials including truxene oligofluorenes and crosslinkable polyfluorenes are the respective guests. These blend materials protect the light emitting materials from oxidation and are highly transparent in the LED emitting region (UV-blue), and so are suitable for colour conversion. Two novel lithography-free techniques, electrohydrodynamic patterning and "bottom up" curing, have also been demonstrated to fabricate functional polymeric structures from the deep UV transparent polymers.

The inkjet printing technique is the main method used here to produce microstructures from organic blend materials. The surface morphology, profile and fluorescence properties of the printed micro-dots have been studied in detail. Then these micro-dots are integrated as colour-converters onto the individual pixels of the micro-LEDs with excellent alignment by inkjet printing. The electrical and spectral properties of such hybrid inorganic/organic device have been studied and the corresponding colour conversion efficiency has also been calculated.

Besides the organic materials, inorganic silver nanoparticle ink has been inkjet printed to form conductive tracks for the interconnection of the micro-LEDs. The electrical performance of the printed silver tracks is characterised to be comparable to the standard sputtered Ti/Au track, which indicates the feasibility of replacing the Ti/Au track with the printed silver track to simplify the fabrication process and decrease the materials consumption.

Content

Chapter 1 General introduction

Light emitting diodes (LEDs) have been realized for many applications, from the backlighting of mobile phones to full-size outdoor colour displays, and from traffic lights to car headlamps. They offer advantages such as higher luminescence efficiency, longer lifetime and less heat production over other illumination sources such as the incandescent bulb. The primary materials for LED production include gallium nitride (GaN)-based inorganic semiconductor which are dominant in the ultraviolet (UV)-blue-green spectral range and have potential for amber to red and even into the near infra-red (IR). In this work, we introduce novel micro-structured LEDs based on GaN which have many individual emitters of size 5-75 microns on a single chip. These devices possess attractive features for application in many areas of science and technology, including mask-free lithography, optical lab-on-chip and novel forms of microscopy.

In the parallel, the rapid development of organic electronic materials shows great potential for display applications as they possess advantageous mechanical, electrical and luminescent properties especially in polymeric form. The specific materials properties of the polymers facilitates the fabrication of the polymeric structures and devices by various scalable patterning techniques in different shapes and sizes, providing economic advantages over the more elaborate fabrication required by inorganics.

The complementary properties of the GaN and organic electronic materials offer the attractive prospect of a new form of hybrid organic/inorganic optoelectronics, combing the advantageous features of both. Devices envisaged include microdisplays

and white light programmable sources, where the organics serve the function of colour conversion, and integrated organics semiconductor lasers and optical amplifiers, where the nitride provide a monolithic pump source interfaced to electronics.

In this thesis, the main focus is exploring various patterning techniques to aid in this such as the electrohydrodynamic patterning, bottom-up curing and especially drop-on-demand inkjet printing, to fabricate functional polymeric microstructures from novel ultra-violet transparent polymers and light-emitting materials blends. These functional light-emitting material blend microstructures have been integrated onto the emitters of the micro-LEDs to form hybrid inorganic/organic device through the inkjet printing technique. Furthermore, the drop-on-demand inkjet printing technique has also been utilized in simplifying the fabrication process of the micro-LEDs themselves by fabricating printed electrodes from silver nanoparticles.

This first chapter aims to introduce the background on the micro-LEDs, concepts associated with the polymeric materials and processing techniques for the polymers.

1.1 Introduction of light emitting diodes

Gallium nitride is the common Ⅲ-Ⅴ semiconductor material used in the LEDs. It can form a ternary and quaternary alloy system with aluminium nitride (AlN) and indium nitride (InN). As the bandgap energy is 6.2eV for AlN, 0.7eV for InN and ~3.4eV for GaN respectively, this Ⅲ-Ⅴ alloy system covers the visible spectrum from blue to red [1]. Figure 1.1 shows the plotting of the bandgap energies of these nitride materials versus their lattice constant at room temperature.
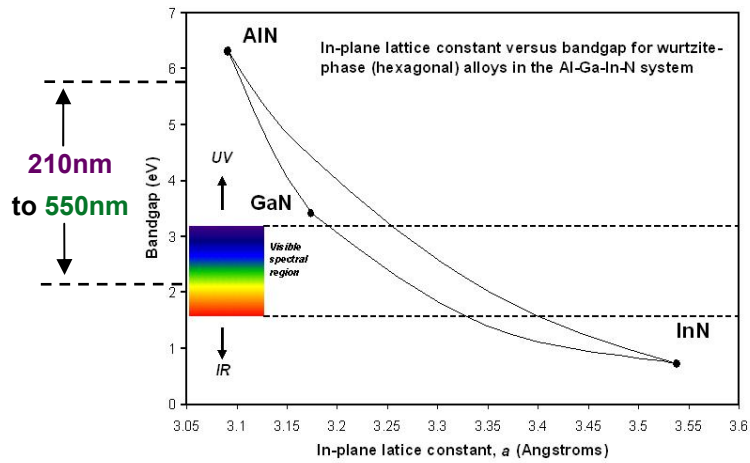
Figure 1.1 Plotting of bandgap energies of III-nitride materials versus their lattice constant. After [1].

1.1.1 Basic principles on light emitting diodes

The light emitting diode (LED), which is familiar to most people, is a semiconductor chip encapsulated by a polymer dome (Figure 1.2). The typical LED chip is usually measured to be about 0.35mm x 0.35mm and is bonded to the lead frame via thin gold wires. The frame provides two leads, one for the positive anode contact and another for the negative cathode contact. The epoxy resin is deposited on the chip in liquid phase and cured in a thermal process. This polymer encapsulation is mechanically able to protect the LED chip and is shaped as a lens for direction of the output light beam. Its refractive index (~1.5) aids light to escape from the chip.
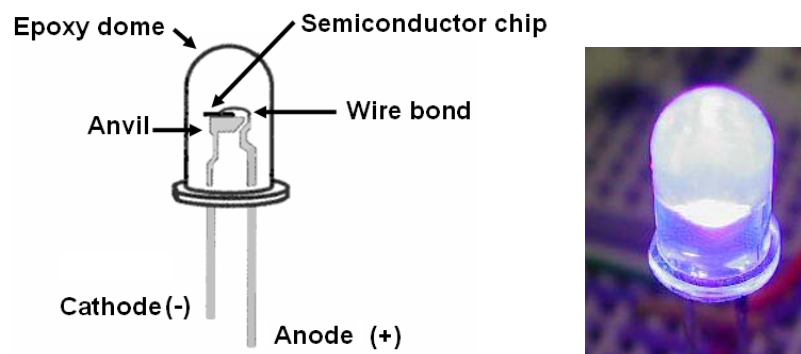
Figure 1.2 Schematic of a light emitting diode and photograph of an operational blue LED.

The basic structure of the LED is a p-n junction, which decides the interfacing of two semiconductors with n- or p- type conductivity. In the n-type semiconductor, electrons are the majority charge carriers; whilst in p-type semiconductors, the holes (with the positive charge due to the absence of electrons) are the majority. The periodic atomic arrangement in a semiconductor crystal results in an energy band structure and the manifold energy levels of electrons create the conduction bands and valence bands (Figure 1.3). The band gap corresponds to the forbidden energy region between the valence and conduction bands. Its value, E_g, determines the wavelength of the light emitted from the LED and is given by [2]:

$$E_g = E_c - E_v \qquad (1.1)$$

where E_c is called the conduction band minimum and E_v is called the valence band maximum and E_g is normally given in electron-volts. In the energy band, the electrons are energetically located close to the minimum of the conduction band while the holes thermalize to the maximum of the valence band. There are usually two categories of semiconductors, direct-gap and indirect-gap. Figure 1.3 shows the schematic simplified band structure of direct-gap and indirect-gap semiconductors. The horizontal axis in the diagram is the crystal momentum, which depends on the crystal orientation in the band structure and is directly proportional to the wavenumber k [2].
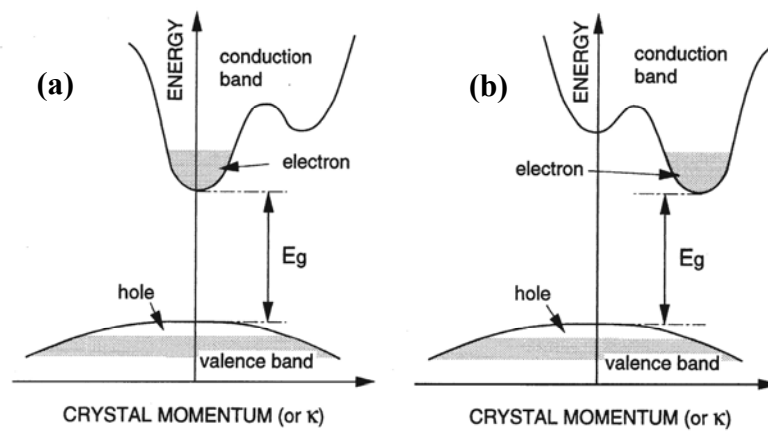
Figure 1.3 Simplified band structures of (a) direct-gap and (b) indirect-gap semiconductors. After [2].

In direct-gap semiconductors, the bottom of the conduction band coincides the top of the valence band in *k*-space (Figure 1.3-a) whereas in indirect band-gap semiconductors, the bands do not coincide (Figure 1.3-b). A band-to-band transition results in photon emission via electron-hole recombination. In direct band-gap semiconductors, the electron transition occurs with the crystal momentum constant. However, due to the difference in *k*-space between the conduction band minimum and valence band maximum in indirect band-gap semiconductors, the transition occurs with a change in the momentum and requires assistance of a phonon (quantum of lattice vibration). Hence, the probability of an indirect transition is much smaller than that of the direct transition and efficiency is reduced in comparison to the direct semiconductors. Consequently, light-emitting devices usually use direct band-gap semiconductors. Figure 1.4 shows the band-to-band recombination processes in these two types of semiconductors in detail [2].
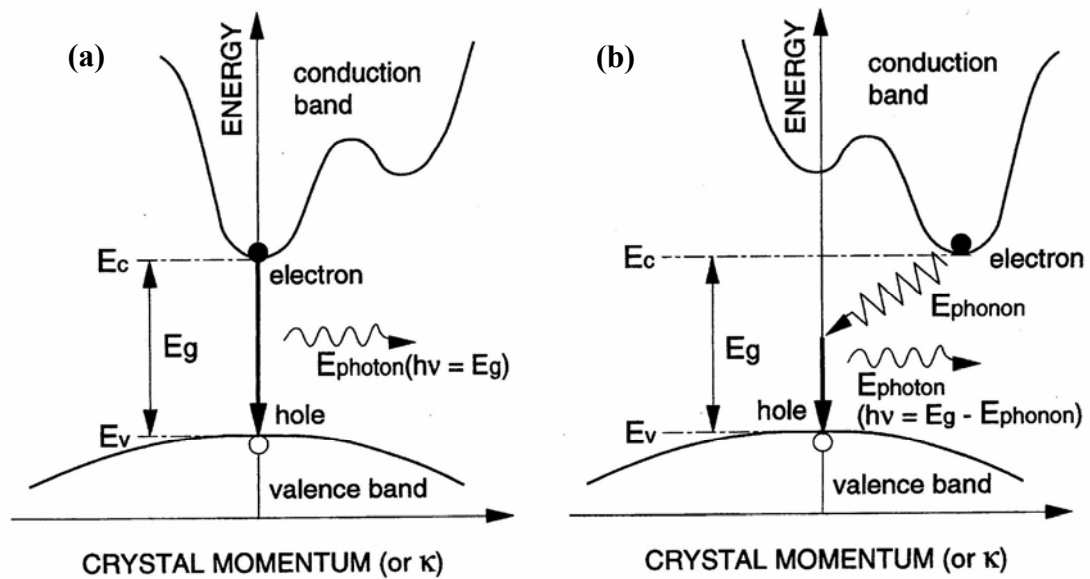
Figure 1.4 Band-to-band recombination processes in (a) direct and (b) indirect bandgap semiconductors. After [2].

When light of photon energy $> E_v$ shines on a semiconductor, energy from the photons is imparted to electrons in the valence band and promotes them to the

5

conduction band. This process is called optical absorption. The reverse process is electron-hole pair recombination releasing the excess energy. The recombination may be radiative or non-radiative. In nonradiative processes, the excess energy is imparted to phonons and dissipated in the form of heat. In the radiative process, photons dissipate the excess energy, which is usually approximately equal to the bandgap, and this process is called luminescence. The recombination process determines the lifetime in both n-type and p-type materials as τ_n and τ_p. The value of τ_n is given by the combination of the radiative τ_r and nonradiative τ_{nr} lifetime [3]:

$$\frac{1}{\tau_n} = \frac{1}{\tau_r} + \frac{1}{\tau_{nr}} \qquad (1.2)$$

The fundamental basis of an LED is a p-n junction. If the structure is formed by two semiconductors of same material (or within a single crystal), the term 'homojunction' is used; if the structure is formed by two semiconductors with related structure but different bandgap, the term 'heterojunction' is used. When the junction is under zero bias, it is in a thermal equilibrium state and the conduction and valence bands have to bend to accommodate the Fermi energy (E_F) through the junction. In n-type materials, the Fermi energy level is close to the conduction band edge and in p-type materials it is near the valence band edge. Figure 1.5 shows the charge carrier distribution in a p-n homojunction and heterojunction, respectively, under zero and forward bias [4]. Under forward bias, the minority electrons and holes tend to drift/diffuse to the opposite side and recombine through the junction. The diffusion length, on average, is L_n and L_p. The space-charge region formed by the diffusion is called the depletion region and its width is W_D (W_{DH} for the double heterostructure, see Figure 1.5).

(a)
Homojunction
under zero bias

(b)
Homojunction
under forward
bias

(c)
Double
Heterojunction
under forward
bias
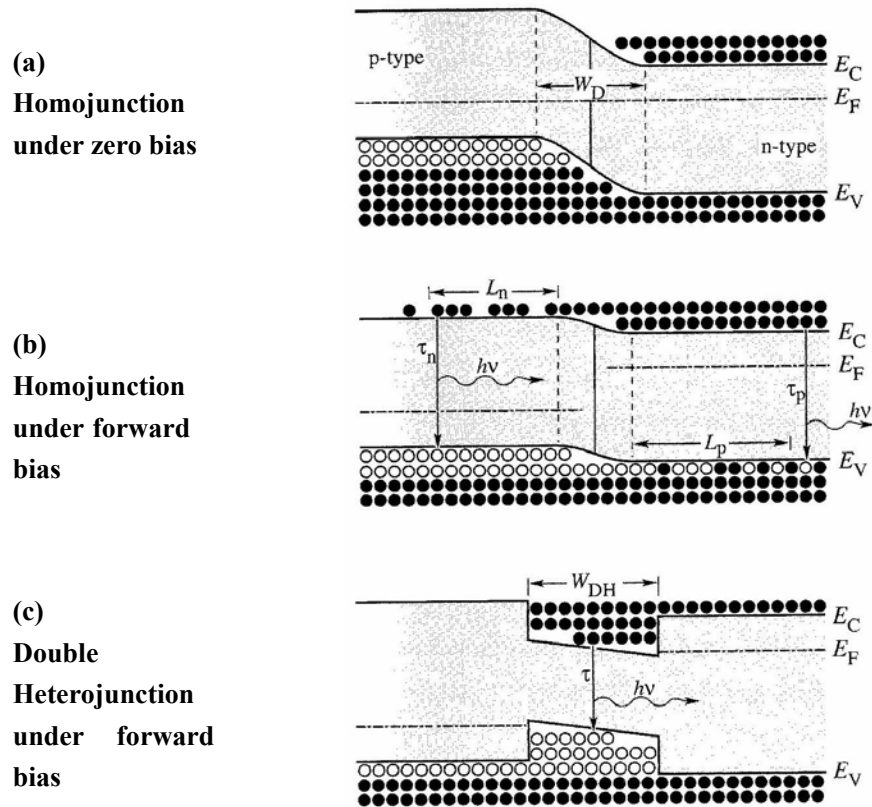
Figure 1.5 P-n homojunction under (a) zero and (b) forward bias, p-n heterojunction (c) under forward bias. In homojunctions, charge carriers diffuse over the diffusion lengths L_n and L_p before recombination. In heterojunctions, charge carriers are confined by the potential barriers. After [4].

It is clear to see that under forward bias, the excess minority carriers are distributed over a long distance in the homojunction (Figure 1.5-b), which results in reduced concentration of the minority carriers during the diffusion and an increase in the recombination lifetime. Hence recombination in the homojunction design is not efficient. However, in the double heterostructure (two back-to-back heterojunctions), the active region is confined by the barriers to a thin layer (~0.1μm), which is much smaller than the typical diffusion length (for example, the diffusion length of electrons in p-type GaAs is given by $L = (D\tau)^{1/2} = $ (220 cm^2/s×10^{-8} s)$^{1/2} \approx 15$μm, where D is the diffusion constant and τ is the electron minority carrier lifetime.) (Figure 1.5-c). Thus the carrier concentration is increased and the recombination lifetime is decreased. In consequence, light emitting devices usually employ a double heterostructure or quantum wells (which are effectively ultrathin to double

heterostructures) for higher efficiency. A quantum well (QW) structure consists of a wide bandgap layer (barrier) / a narrow bandgap layer (well) / a wide bandgap layer (barrier) with the well thickness comparable to the de Broglie wavelength of the electron in the material (~5-10nm typically). In the well layer, the injected electrons and holes are quantized in the direction perpendicular to the layer, and the kinetic energy is quantized into discrete energy levels which are called "energy subbands" in the valence and conduction bands. But carriers are not restricted in the direction parallel to the well layer and the continuum states are formed. In the quantum well structure, light emission still results from the electrons transitions between the valence and conduction band, which is same as in the bulk materials. Quantum size effects becomes apparent in this case with a two-dimensional 'step like' density of states and an energy gap increased compared to that in the bulk materials. This energy effect results in shorter wavelength emission due to the increased bandgap in the quantum well than the corresponding wavelength in bulk materials of the same composition.

GaN-based LEDs usually use multi quantum well structures typically of InGaN with GaN barriers. Figure 1.6 shows the typical structure of a blue-emitting InGaN/GaN quantum well LED. This is formed by processing a multi-layer thin-film epitaxial layer structure on a typically sapphire substrate. Both n and p contacts are on the top surface as the sapphire substrate is electrically non-conducting. The p-metal contact (see section 1.1.2 for further detail) utilizes a transparent metal layer to help the spreading of the injected current and provides hole injection while the n-metal contact injects electrons. When a forward bias is applied, electrons and holes are injected from the n-type and p-type GaN layers and recombine in the InGaN quantum well region (2~3nm thick for each quantum well) for photon generation. In order to minimize the current requirement and heating effects, a current blocking layer, usually made by an insulator such as SiO_2, is deposited to keep the light emission area small (down to ~16μm).
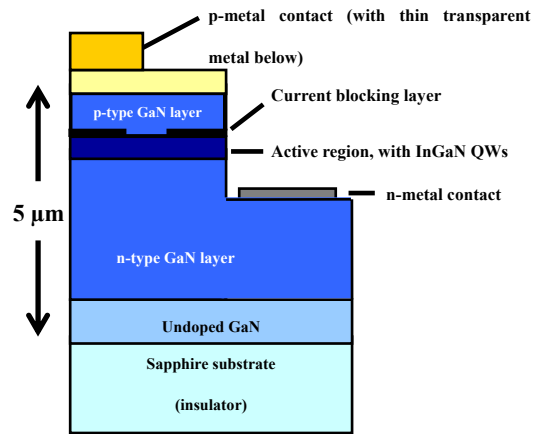
Figure 1.6 Typical InGaN/GaN quantum well LED structure.

1.1.2 Introduction to GaN micro-structured light emitting diodes (micro-LEDs)

Micro-structured light emitting diodes, which form the focus of work described in this thesis, are defined by shaping the surface of the conventional LED epitaxial layer into emitter pixels of a few tens of microns each in diameter via an optical lithography process. The individual emitting elements on the single chip are referred as 'micro-LED array' and may assume any configuration permitted by contacting and lithography including such as disks, stripes and rings (see Figure 1.7).
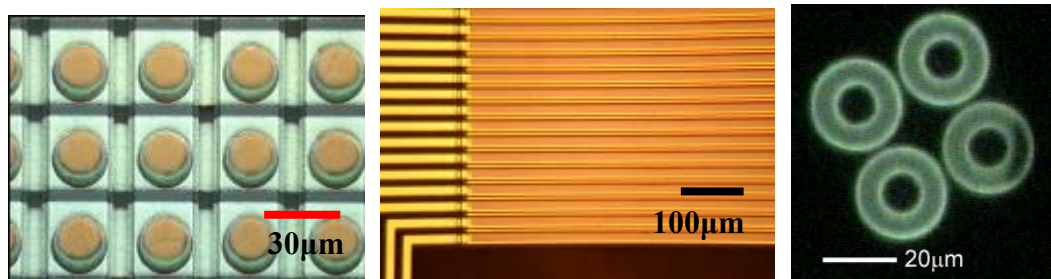
Figure 1.7 Various configurations of micro-LEDs, disks (left), stripes (middle) and rings (right).

Taking the disk-shaped micro-LEDs as an example, the typical diameter of each emitter is in the range 1~75μm. The consequences of fabricating such small LED pixels on the single chip include increase of light-extraction efficiency by the

9

scattering light from the side-walls of the micro-LEDs; improvement of the current injection uniformity; independent pixel controllability via several addressing schemes; ability to directly project and image the patterns thus formed. Due to these advantages, several research groups including our own are interested in this area devoted effort to the development of micro-LEDs since their inception in 2001 [5-10]. The micro-LEDs have been applied in various areas including the micro-displays [5], micro-optics [6] and microfluidic systems [11].

The fabrication method for micro-LEDs in GaN is conventional photolithography combined with the Inductively Coupled Plasma (ICP) dry etching which is the key process. ICP dry etching has been the most regularly dry process used in the GaN-based device fabrication dating back to the 1990's [12]. In ICP, plasma (a gas with atoms in an ionized state) is generated by the power supplies and accelerated toward the substrate to be etched in a high vacuum (10^{-3} *Torr*) chamber (Figure 1.8). Energy is also coupled into the plasma inductively by the coil around the chamber. The advantage of this system is that the ion energy and plasma density are independent and controllable, which facilitates the process optimisation. Using ICP with the following typical gases and conditions, which are 30 sccm Cl_2 and 10 sccm Ar at 5m*Torr* pressure and 30℃ temperature, results in controlled etching of GaN with etch rate up to ~27μmhr^{-1}. Typical fabrication details of the micro-LEDs used in this work are described in section 1.1.2.1.
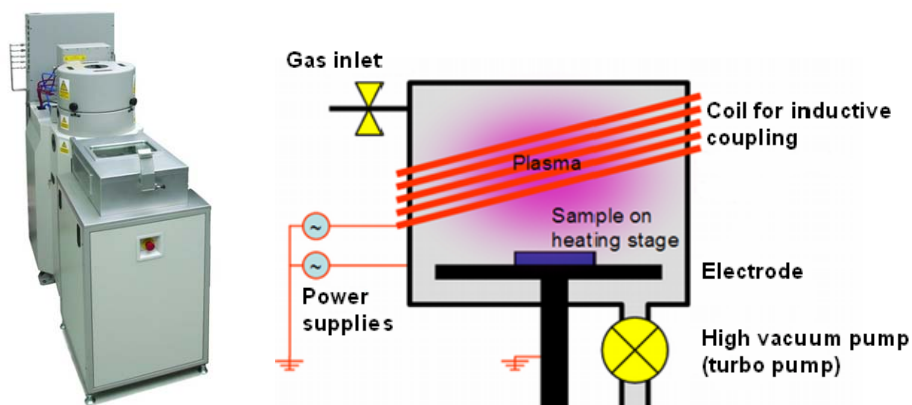
Figure 1.8 Image of the ICP tool (left) and schematic of the ICP dry etching chamber (right).

The micro-LEDs fabricated in our group cover the emission range from UV to green. Figure 1.9 shows the representative normalized spectral data of UV (~370nm), blue (~450nm) and green (~500nm) micro-LEDs. In this work, the performance of the micro-LEDs is normally characterised by measuring the current-voltage (I-V) curve and the optical output power vs. current. The current-voltage curve describes the resistance and turn-on voltage of the device, indicating the electrical properties of the LED. In what follows, the I-V curve is measured by an HP4155B parametric analyzer. Figure 1.10 is a typical current-voltage curve taken from our GaN-based devices in forward bias. A linear approximation tangent (red line in Figure 1.10) to the curve intersecting with the voltage axis defines the 'turn-on' voltage point of the device. As the diode I-V characteristic becomes linear when $V > V_{turn-on}$, the series resistance of the diode can be calculated from the equation below [13]:

$$R_s \approx \frac{dV}{dI} \tag{1.3}$$

where I is the injected current, V is the driving voltage, and R_s is the series resistance of the diode. It is noted that this calculation is not practical to evaluate diode resistance at high voltage due to device heating effects. It is reported that the turn-on voltage and series resistance of the diode increases as the diode is cooled [4].
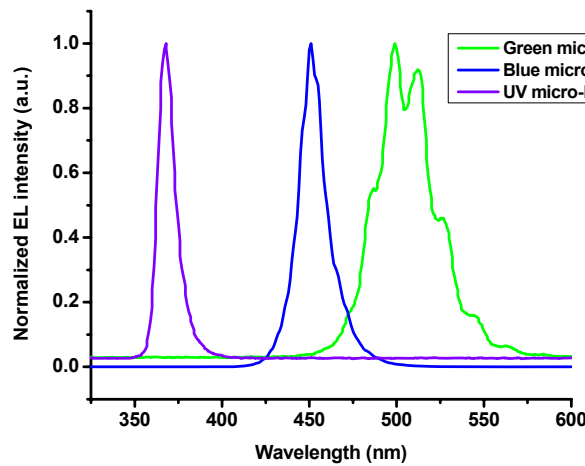
Figure 1.9 Normalized spectra of UV, blue and green micro-LEDs.
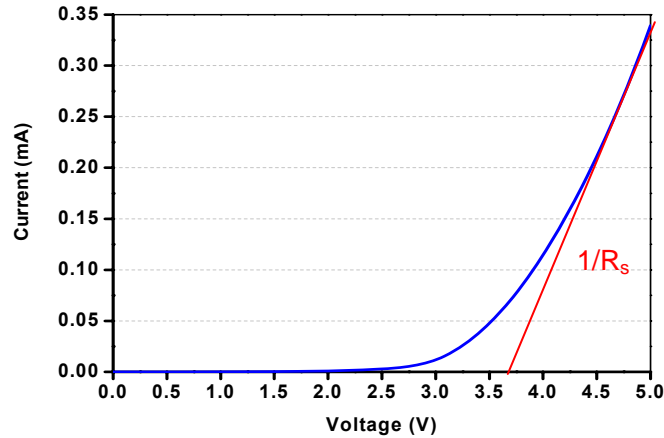
Figure 1.10 Typical current-voltage curve of the LED from our GaN-based device.

The optical output power curve shows how much light is emitted from the device as a function of driving current. During these measurements, a calibrated Si photo-detector (of active area 78.5mm^2) is typically placed ~2mm from the LED emitter to collect the emitted photons. The power data plotted versus the injected currents is known as an 'L-I' curve. This curve also includes the information about the thermal rolling over and breakdown of the LED device.

There are two ways for the LED to extract the light from GaN-on-sapphire micro-LEDs, which are from the p-side (top-emitting) and from the n-side (flip-chip), respectively. Figure 1.11 shows schematics of these two light extraction configurations.
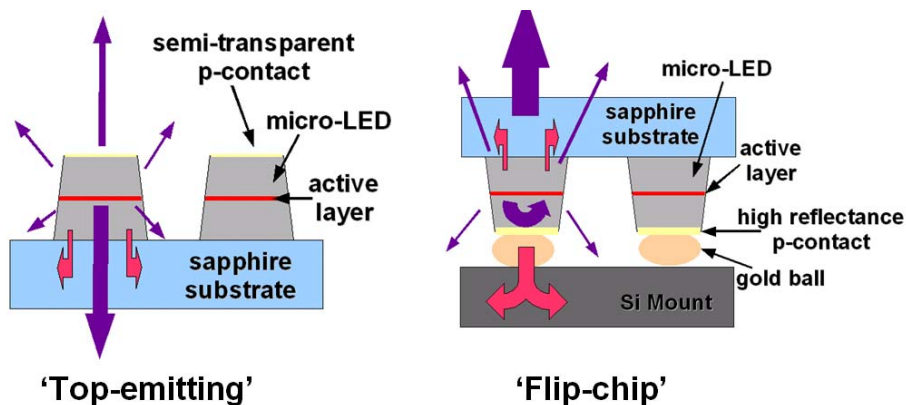
Figure 1.11 Schematics of "top-emitting" and "flip-chip" configurations for GaN micro-LEDs. The purple arrows represent the extracted light and the red arrows represent the heat.

The major difference between these two configurations is the thickness of the metal (Ni/Au) layer on the p-doped GaN. In the top-emitting format, as the light is extracted from the p-side, the thickness of the metal layer needs to be as small as possible to prevent light absorption by the metal while maintaining an ohmic contact. However, in the flip-chip format, the metal layer may be made thick enough to also act as a mirror reflector on the p-side. The light travelling towards the p-side is reflected by the thick metal layer and emits through the n-side. As a consequence, more light is extracted. The flip-chip devices, in consequence, usually permit higher power operation, but -for certain configuration- can be more limited in pixel size range and array scaling. The gold balls in the flip-chip devices are used for bonding and packaging and the ball shape is formed by melting a gold wire, which is similar as the soldering process.

1.1.2.1 Top-emitting matrix-addressable micro-LEDs

The first type of device used in this work is that of the 64×64 array top-emitting matrix-addressable LEDs. Here, the pixel diameter is ~16μm (effective emission area) on a 50μm centre-to-centre pitch. The fabrication process of these devices starts with formation of a rectangular mesa and micro-pillar structure where the mesas are in the form of ridges etched down to the substrate (sapphire) with each row of emitters lying along the ridge and sharing the same n electrode. The matrix-addressing is completed by p-metal lines running down each column at right angles to the row and forming contacts for each micro-pillar element. The mesa structure is defined by conventional photolithography and ICP etching with a Cl_2 and Ar gas mixture. A 200nm thick SiO_2 layer is deposited by Plasma Enhanced Chemical Vapour Deposition (PECVD), patterned by photolithography and wet-etched by Buffered Oxide Etchant (BOE) to act as "hard mask" for later ICP etching. Afterwards, the sample is etched by ICP with the plasma consisting of 30 sccm Cl_2 and 10 sccm Ar at

5m*Torr* pressure and 30℃ temperature in the chamber. Hence the mesa structure is formed and the micro-pillar structure is realised by the same process. Then the ohmic contact of Ni/Au (3nm/9nm) is evaporated and patterned by a lift-off process to form the current spreading layer. The following step is the deposition of the Ti/Au (20nm/120nm) n-contact metal tracks running along each row as well as the ring-shaped contact on the spreading layer by means of magnetron sputtering. A 200nm thick SiO_2 layer is deposited by PECVD onto the surface to act as an isolation layer and is then etched using a photolithography-defined mask to expose the n electrode and the ring-shaped contact by Reactive Ion Etching (RIE). The final step is accomplished by defining the interconnection of each pixel by the p-metal Ti/Au (20nm/120nm) via sputtering and a lift-off process. Figure 1.12 is the cross-sectional schematic and corresponding plan-view optical images of these top-emitting matrix-addressable micro-LEDs [14].
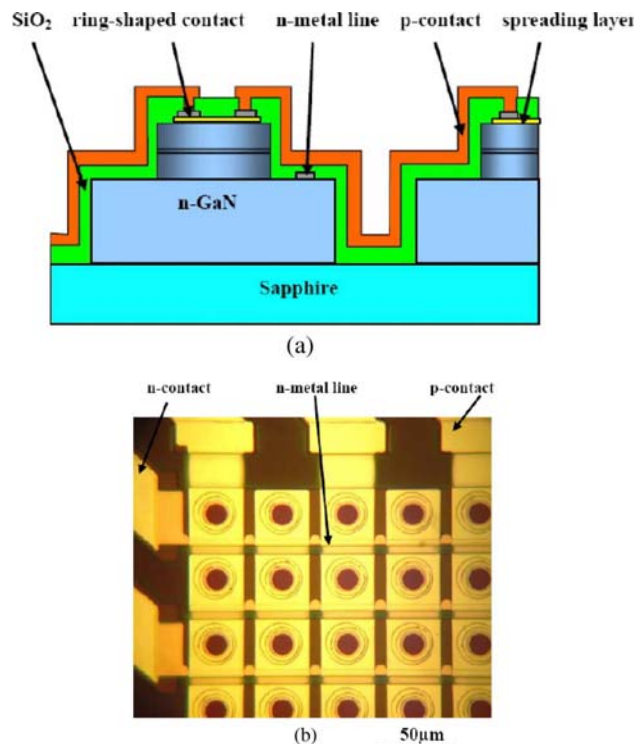
Figure 1.12 (a) Cross-sectional schematic and (b) plan-view optical image of the top-emitting matrix-addressable micro-LEDs.

These top-emitting matrix-addressable micro-LEDs show uniform emission along the n-GaN mesa, which is due to the n-metal line introduced for suppressing the resistance variation along the n-GaN mesa [14]. Figure 1.13 is a microscope image of two rows in this device turned on pixels under 4V dc operation [14].
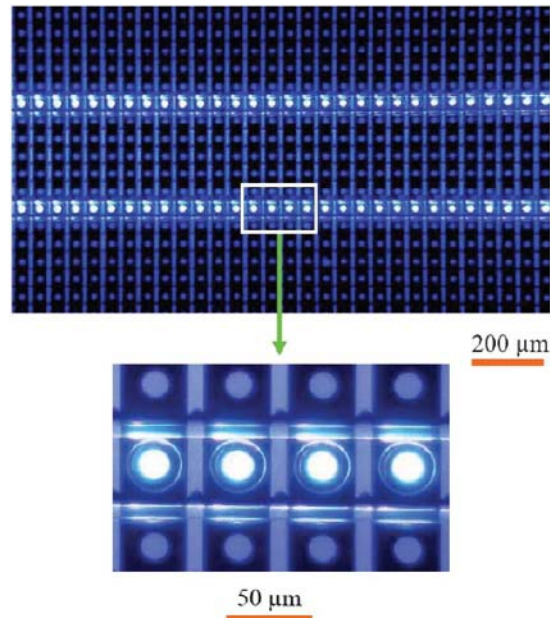
Figure 1.13 Microscope images of turned on pixels in the top-emitting matrix-addressed micro-LED array (operating at ~450nm in this case).

The current-voltage curve and light output power (or power density) are the primary characteristics for the device utilised in this work. In Figure 1.14-a is shown the typical I-V curve of the 64×64 top-emitting matrix-addressable micro-LEDs with 370nm emission indicating that the turn-on voltage is ~4.4V. The output power of this device at 7mA is 6μW (2.98W/cm^2 optical power density at a driving current density of 870.8A/cm^2). Figure 1.14-b is the typical output power characteristic of this device where the power and the injected currents are normalized by the area (200.96μm^2 emission area for power measurement and 803.84μm^2 pixel area for current injection in this case as the ring-shaped contact results in smaller effective emission area (~16μm) than the pixel area (~32μm)). The power efficiency of this device is calculated to be ~0.7% and this low efficiency may be due to the

insufficient light collection during the power measurement.
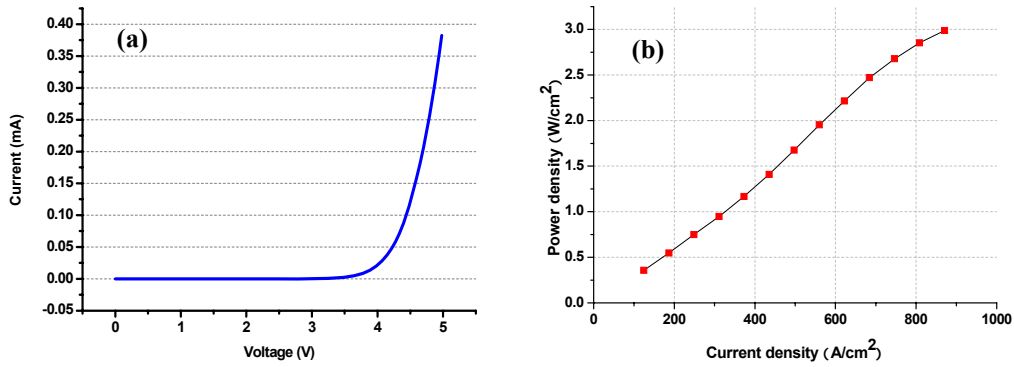
Figure 1.14 Typical (a) I-V curve (b) output power characteristic of the top-emitting matrix-addressable micro-LEDs (operating at ~370nm in this case).

1.1.2.2 Flip-chip matrix-addressable micro-LEDs

The second type of device used in this work is the flip-chip matrix-addressable micro-LEDs. The top-emitting matrix-addressable micro-LED fabrication sequence can be modified into the flip-chip configuration where the structure is inverted on the sapphire substrate acts as an upper window for light emission. Instead of a thin Ni/Au spreading layer, a thick Ni/Au/Ti/Au multilayer with respective thickness of 3nm, 7nm, 50nm and 200nm is employed as a reflective p-contact in this case [15]. As one-step evaporation cannot ensure the low contact resistance and high reflectivity, the fabrication of this multilayer is accomplished via two evaporation steps. In addition, the ring-shaped contact is no longer necessary in this case. Apart from this, the rest of the procedures are the same as the top-emitting format. Figure 1.15 shows the cross-sectional schematic and plan-view optical images of the flip-chip matrix-addressable micro-LEDs. After device fabrication, the backside of the device (sapphire) is polished and thinned down to ~80μm by Chemical Mechanical Polishing (CMP) from an initial thickness of ~300μm in order to let the light through.
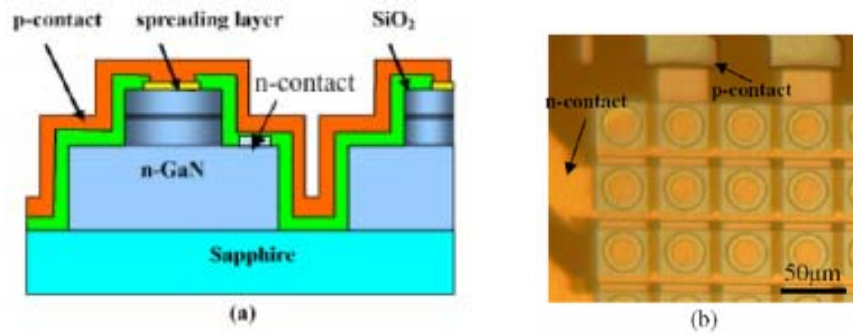
Figure 1.15 (a) Cross-sectional schematic and (b) plan-view optical images of the flip-chip matrix-addressable micro-LEDs (compare with Figure 1.9).

To show the emission uniformity of this type of LED array, all the pixels in the same row/column were connected in parallel and the representative emission pattern is shown in Figure 1.16. It is obvious that the overall uniformity of the device both pixel-to-pixel and line-to-line is very good and no apparent emission intensity difference is observed.
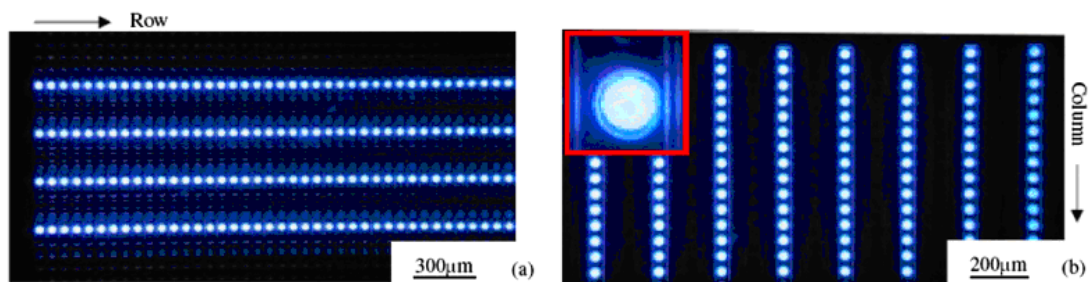
Figure 1.16 Uniformly test patterns in (a) rows and (b) columns of the flip-chip matrix addressable LED array.

Figure 1.17 shows typical I-V curves of the 64×64 flip-chip matrix-addressable micro-LEDs emitting at blue (470nm) and UV (370nm) wavelengths comparing to the top-emitting device format. The blue device usually has lower turn-on voltage than the UV device no matter what the configuration of the device is, primarily due to the lower bandgap. At the same emission wavelength the flip-chip device is marginally better than the top-emitting device in I-V characteristics, due to the fact that the flip-chip device has larger p-contact area (20μm) than that of the

top-emitting device (16μm) which reduces the series resistance of the micro-LEDs [14, 15]. In addition, the thicker spreading layer in flip-chip device gives more uniform current injection and reduces the spreading resistance [15]. For the light output power characteristics, the measured power and injected currents are normalised by the emission area to make an accurate comparison (Figure 1.18). It is clear that the output power density from the flip-chip device is significantly higher than that from the top-emitting device. This is attributed to the factors above and that more light is extracted when the light emits through the sapphire rather than the semi-transparent (and thus partially absorbing) spreading layer. It is also aided by the mirror functionality of the p contact.
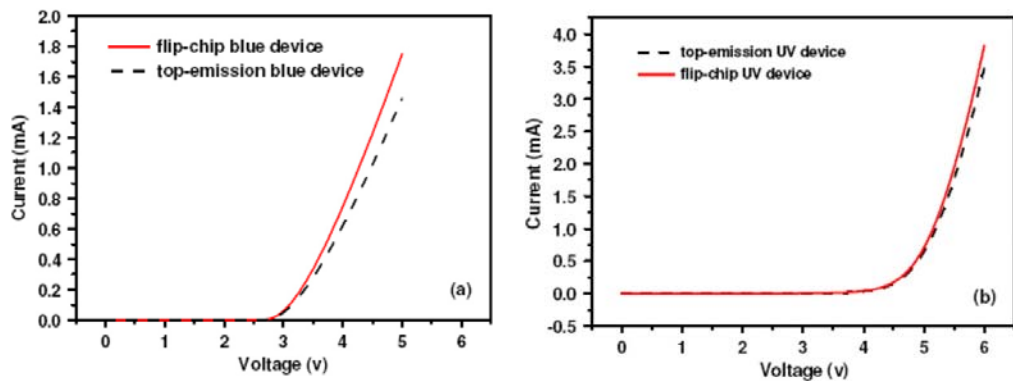
Figure 1.17 I-V curves of (a) blue and (b) UV flip-chip matrix-addressable micro-LEDs compared with the corresponding top-emission device.
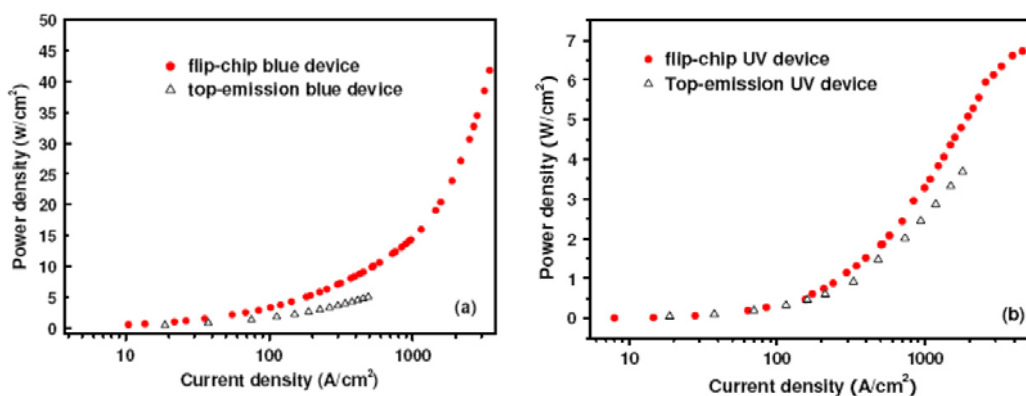
Figure 1.18 Output power characteristics of (a) blue and (b) UV flip-chip matrix-addressable micro-LEDs compared with the corresponding top-emission device.

1.1.2.3 Planar micro-LEDs

The structure of the third type of device used in this work is quite different to the previous two types. The major difference is its mesa-free structure compared with the mesa-etched devices. The fabrication process of this device has been simplified without degrading the electrical and optical performance. The key step of the process flow here is the selective electrical passivation by a plasma treatment of the p-type GaN (p-GaN) layer above the LED active region, which avoids mesa etching for pixel definition and dielectric deposition for electrical isolation [14, 15]. We call this fabrication route "planar process" and the device with micro-scale pixels fabricated from this route the "planar micro-LEDs".

Before depositing the metal contact layers, the GaN surface is treated with 18% aqueous hydrochloric acid (HCl) to remove the native oxides. The designed patterns are the defined by a standard lift-off process on the semitransparent current spreading layer of Ni/Au (8nm/16nm) deposited by electron beam evaporation. Then the samples underwent rapid thermal annealing at 500°C for 120s in oxygen-nitrogen ambient to form an ohmic contact on the p-GaN. The n-GaN layer was subsequently exposed in a defined area by Inductively Coupled Plasma (ICP) dry etching. Next, a single photoresist mask was formed to define the n-pads, p-pads and tracks. Subsequently the samples with the photoresist mask on were treated by Reactive Ion Etching (RIE) with gas flows comprising Ar and CHF_3 (10sccm/ 5sccm). The chamber pressure was 30m*Torr* and the plasma power was 200W for 60s total treatment. A 40nm/150nm Ti/Au layer was deposited finally by sputtering to form the pads and tracks by lift-off, which means only the areas of Ti/Au were previously plasma treated for electrical passivation.

The plasma treatment increases the resistance of p-GaN surface and prevents the current leakage from p-GaN-metal interface, which is similar to mesa-isolation in conventional process [14, 15]. Figure 1.19 shows the resulting DC I-V characteristics

with different pre-metallization plasma treatments. It is observed that all the treatments result in significant reduction in current compared to the non-treated structure and the CHF$_3$ treatment has much higher electrical resistivity than either of the H$_2$ and the CF$_4$ treatments. Figure 1.20-a shows the schematic cross-sectional structure of one pixel in such a planar device and Figure 1.20-b is the plan-view optical microscopy image of the particular planar device used in this work, where the pixel diameter is 100μm, 70μm, 50μm, 30μm, 20μm and 10μm.
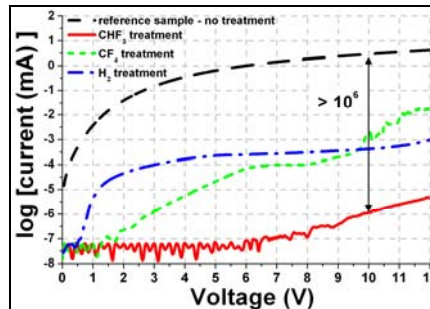
Figure 1.19 I-V characteristics of co-planar Ti/Au electrode structures deposited onto p-GaN given different pre-metallization plasma treatments.
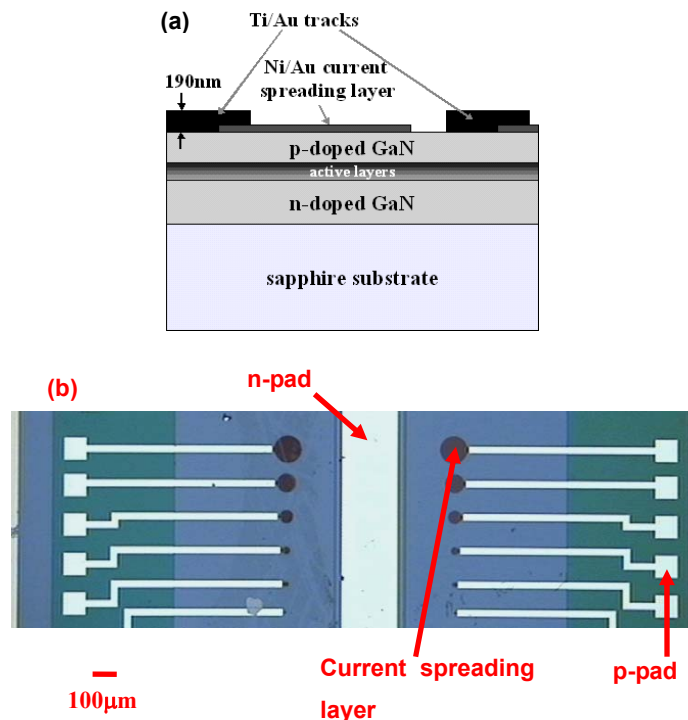
Figure 1.20 (a) Schematic cross-section structure and (b) plan-view optical microscopy image of the planar device. Compare the structure in (a) to Figure 1.12-a and Figure 1.15-a, respectively. The pixel diameter is 100μm, 70μm, 50μm, 30μm, 20μm and 10μm.

Electrical and optical power characteristics of the planar devices were measured. Figure 1.21 is a typical I-V curve of the planar device with an emission area ~70μm in diameter at 450nm wavelength, indicating the turn-on voltage is ~4.8V. Figure 1.22 shows the typical output power characteristic of this device where the power and the injected currents are normalised by the area (3846.5μm² for power measurement and current injection). The typical power of this planar device is 207.5μW under 3mA injection current (5394.5W/cm² optical light output power density under injected current density of 77.9A/cm²).
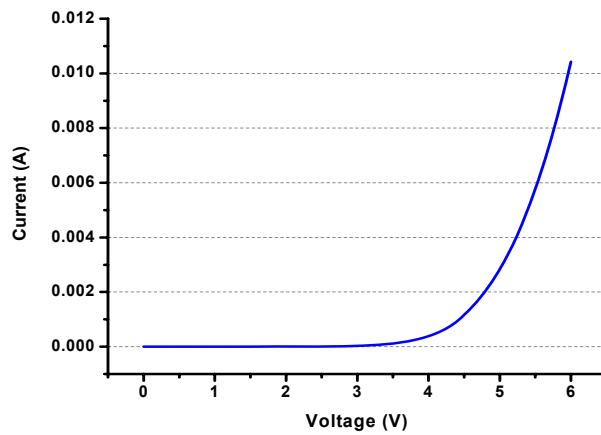
Figure 1.21 Typical I-V curve of planar device pixel with ~70μm emission diameter.
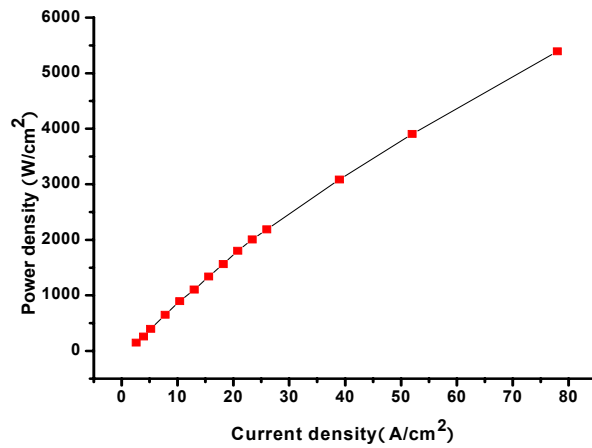
Figure 1.22 Typical area normalised power-current curve of the planar device.

1.2 Polymeric materials

As mentioned in the General Introduction, we are interested in exploring hybrid inorganic/organic devices fabricated by microstructuring polymeric and organic electronic materials onto our gallium nitride devices. Here we overview the basic concepts of the organic materials and their processing techniques.

1.2.1 Basic concepts of polymer materials

The word *polymer* is derived from the classical Greek *poly* meaning "many" and *meres* meaning "parts". Therefore, a polymer refers to a large molecule converted the monomers by combining with other molecules of the same or different type. The resulting structure of the monomer combinations usually enclosed in square brackets (e.g. –[A]–, A represents the monomer combinations) is usually called the repeating unit. Polymers are either homopolymers if there is only one repeating unit in the polymer molecules or copolymers if there is more than one repeating unit. The repeating units in the copolymers may be arranged in various conformations such as random, alternating, block and graft (see Figure 1.23, with the repeating units A and B as an example) [16].

Figure 1.23 Schematic structures of various types of copolymers: (a) random; (b) alternating; (c) block; (d) graft. "A" and "B" are the repeating units of the copolymers. After [16].

The simplest linkage of monomers is along a single main chain. However, in

some cases, the side growth of each polymer chain may be terminated before the chain links up with another chain, which results in branched polymers (see Figure 1.24-a). In other cases, growing polymer chains become chemically linked to each other, which results in the crosslinked polymers or polymer network (see Figure 1.24-b) [17].
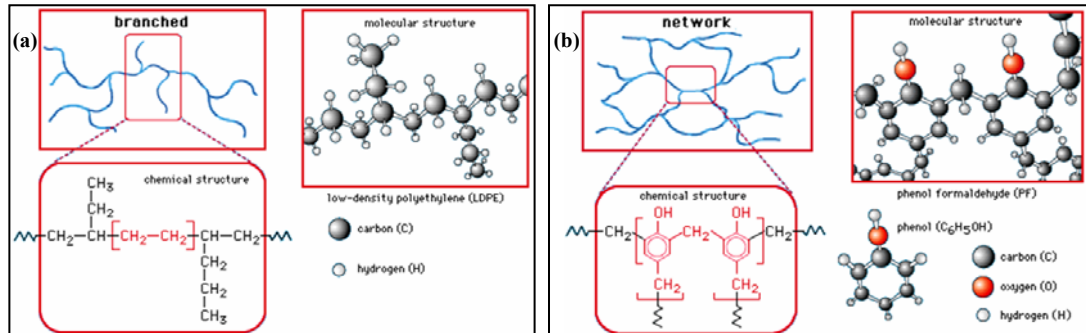
Figure 1.24 (a) Branched polymers and (b) crosslinked polymers or polymer network. After [17].

Polymer chain-structures determine the final characteristics of the bulk polymer such as the tensile strength, the Young's modulus of elasticity and the glass transition temperature [18, 19]. Regarding the tensile strength, a simple linear polymer with long chain length usually has higher tensile strength than the crosslinked polymers which have a shorter chain length. The glass transition temperature T_g is a specific temperature point when a crystalline or semicrystalline polymer changes phase between a hard, brittle, glassy solid and a soft, rubbery, amorphous material. There is a large-scale cooperative movement of chain segments, hence any structure features or external condition which affects chain mobility will influence the glass transition temperature. For instance, the intermolecular connection formation in crosslinked polymers reduces the chain mobility and thus increases the T_g, while branching increases the chains separation and therefore decrease the T_g. Another advantage of polymers is the ability to blend before the polymerisation. Two polymers can be mixed together and maintain their chains coexisting and interacting without being chemically bonded or phase separated. Consequently, the blend materials inherit the properties of both components.

1.2.2 Representative categories of polymer materials

Transparent polymers are one category of the polymer family, which are widely applied for the commercial LED encapsulation purposes (see e.g. Figure 1.2). In addition, they are also used in waveguides [20, 21], microfluidics [22, 23] and even inorganic lasers such as vertical cavity surface emitting lasers (VCSELs) [24, 25]. Here, we introduce the most popular application of transparent polymers that of encapsulation and the epoxy-based polymers are the major materials for this application. They are crosslink polymerized to a high degree and are very stable with temperature. They also possess excellent chemical, mechanical and insulating properties. The polymerisation of epoxies is by thermosetting with a catalyst agent. Figure 1.25-a shows the chemical structure of a representative epoxy polymer and Figure 1.25-b is the transmission spectrum of a 20μm thick film of a commercial epoxy, Norland NOA63 as measured in-house. One shortcoming of the commercial epoxy is the transmission decreases quickly in the ultraviolet wavelength region e.g. from ~68% at 300nm to ~28% at 270nm for the film in Figure 1.25-b, which is one challenge we address later.
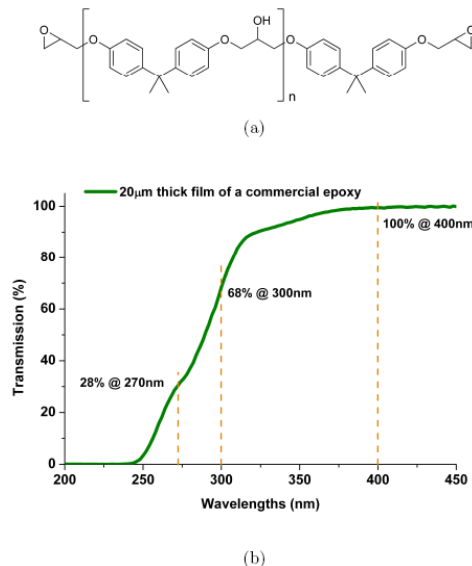
Figure 1.25 (a) Chemical structure of a representative epoxy polymer (n is the number of the repeating units); (b) the transmission spectrum of a 20μm thick commercial epoxy polymer film (Norland NOA63). Note that this film loses transparency below ~400nm.

The transparent polymers used in this thesis are photosensitive epoxy-based and vinyl-based polymers which polymerise under UV light. The polymers exhibit high transparency down to deep UV wavelengths (<300nm) after the curing process (polymerisation and crosslinking). In addition, these materials show very good processability and also miscibility for blending, which will be introduced later in Chapter 2.

Another representative category of polymers is the light emitting copolymers, which were demonstrated first in the early 1990s [26]. These polymers have been applied in organic displays [27] and are under development for organic laser [28]. When light emitting polymers absorb energy, this can excite electrons in the molecules from the ground state to higher electronic states. When the electrons relax from these excited states, the polymers emit photons and luminescence is observed. The energy for electron excitation can be generated either optically or electrically. In this work, we focus on photopumped light emitting polymers. Luminescence generation through molecular excitation by ultraviolet or visible light photons is called photoluminescence, which includes fluorescence and phosphorescence. Fluorescence is a property of some certain molecules which can absorb light at a particular wavelength and emit light at a longer wavelength after a short interval. The phosphorescence process has a similar manner to fluorescence but with a much longer excited state lifetime. The different mechanisms occurring when the molecules absorb energy from photons are presented by the Jablonski energy diagram (see Figure 1.26) [29]. Table 1.1 gives the timescale of each mechanism.

The typical fluorescence process starts when a suitable molecule is excited from the ground singlet electronic state (S_0) to excited singlet electronic states (S_n, n=1, 2, 3...) by an incoming photon in $\sim 10^{-15}$s. Each electronic state is further subdivided into a number of vibrational and rotational energy levels according to the atomic nuclei and bonding orbitals (rotational energy states are ignored in Figure 1.26). In most organic molecules, all electrons are spin-paired (have opposite spins) in the

ground state. As very few molecules have enough internal energy to exist in any state other than the lowest vibrational level of the ground state at room temperature, the excited electrons firstly tend to relax to the lowest excited energy level in $\sim 10^{-12}$s. Then these electrons return to the ground state with accompaniment of emitting photons at longer wavelength in $\sim 10^{-9}$s (i.e. fluorescence).
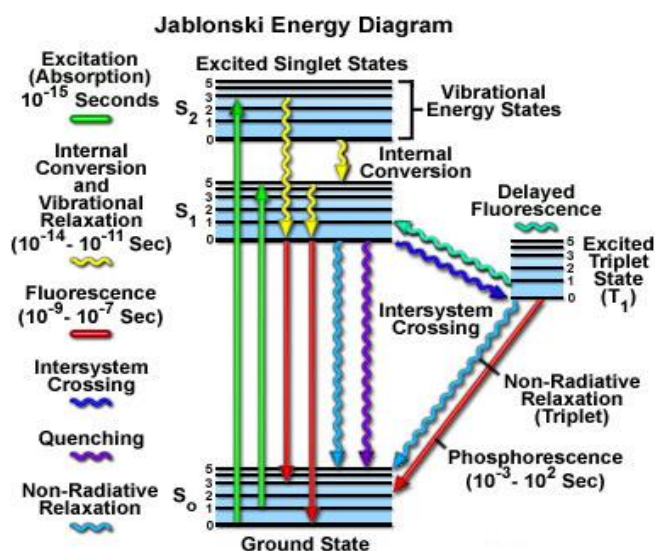
Figure 1.26 Jablonski energy diagram illustrating different mechanisms occurring in light emitting polymers. After [29].

Table 1.1 Timescales of different mechanisms of photoluminescence

Transition	Process	Timescale (seconds)
$S_0 \rightarrow S_1$ or S_n	Absorption	10^{-15}
$S_n \rightarrow S_1$	Internal conversion	$10^{-14} \sim 10^{-10}$
$S_1 \rightarrow S_1$	Vibrational relaxation	$10^{-12} \sim 10^{-10}$
$S_1 \rightarrow S_0$	Fluorescence	$10^{-9} \sim 10^{-7}$
$S_1 \rightarrow T_1$	Intersystem crossing	$10^{-10} \sim 10^{-8}$
$S_1 \rightarrow S_0$	Non-radiative relaxation	$10^{-7} \sim 10^{-5}$
$T_1 \rightarrow S_0$	Phosphorescence	$10^{-3} \sim 100$
$T_1 \rightarrow S_0$	Non-radiative relaxation	$10^{-3} \sim 100$

Apart from the fluorescence process, there are other relaxation pathways. The excited state energy could be released non-radiatively as heat (light blue wavy arrow in Figure 1.26), or through a second type of non-radiative process such as quenching by collision of the excited fluorophore with another molecule (purple wavy arrow in

Figure 1.26), or by intersystem crossing to the lowest excited triplet state (dark blue wavy arrow in Figure 1.26). The energy crossing to the triplet state will result either in phosphorescence emission or a transition back to the excited singlet state yielding delayed fluorescence. Molecules undergo the spin conversion process to produce unpaired electrons for intersystem crossing and this leads to the low probability of this energy crossing. It is observed that molecules in a triplet state usually have high chemical reactivity, which could result in photobleaching. Dissolved oxygen in light emitting polymers is an effective quenching agent as the ground state of oxygen molecules is normally a triplet and can be excited to reactive singlet state, leading to the bleaching reaction with the fluorophore [30]. Therefore, some applications of light emitting polymers are carried out in nitrogen to avoid the photobleaching effect from dissolved oxygen.

As the coupling between the closely spaced vibrational energy levels of the ground state and thermal motion creates a wide range of photon energy during the fluorescence process, the fluorescence spectrum usually covers a band of wavelengths instead of several sharp lines. A Stokes shift is normally observed in the spectrum of light emitting polymers, in which the emitted photons have less energy compared to the absorbed photons and are shifted to longer wavelength. Figure 1.27 gives a representation example (here of truxene oligofluorene T3) showing the various effects of these processes.
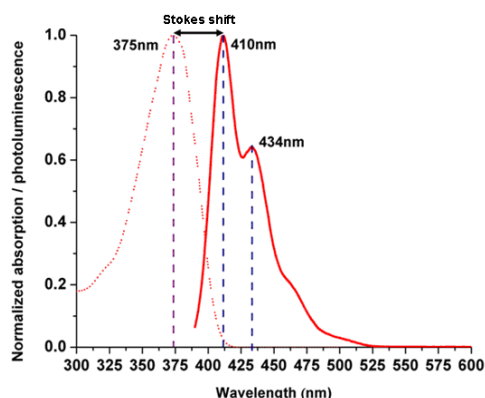
Figure 1.27 Typical absorption/emission spectra of a light emitting polymer in liquid state used in this work. The Stokes shift is wider, as is substructure within the fluorescence due to the respective singlet states.

1.3 Overview of polymers patterning technique

The diversity of existing synthetic and biological polymers and the ability to design new types of polymers give the rising interests in patterning functional polymers. These functional polymer structures at different length scales play an important role in various areas like light emitting display [31], cell and tissue engineering [32, 33], and optical component production such as gratings and photonic crystals [34, 35]. In this section, we will overview some patterning techniques of polymers divided into two categories: conventional photolithography and mask-free printing techniques including nanoimprinting, microcontact printing and dip-pen nanolithography (DPN). The respective patterning methods and their applications will be described briefly. Other patterning techniques such as instability-induced patterning, bottom-up curing and inkjet printing used in this work will be introduced separately in later chapters.

1.3.1 Conventional photolithography technique

The photolithography technique has been recognised as one of the main methods used for patterning not only inorganic semiconductor materials as described in earlier sections of this Chapter, but also organic polymers. The standard process flow of photolithography is shown in Figure 1.28 [36]. First, a photoresist is spun on to entirely cover the bare or coated substrate. Then the photoresist is exposed under photoirradiation after proper alignment through the master mask with the required pattern. Depending on the chemistry of the photoresist, either a positive or a negative replica of the master pattern is produced by dissolving the selected area of the photoresist in an appropriate solvent at the development stage. Thereafter, the photoresist pattern can be transferred to the underlying substrate or coating layer by (wet or dry) etching. In some cases of polymer patterning, the pattern is directly formed by photoirradiating the photosensitive monomer-, oligomer- (small number

of monomer repeats) or polymer-coated surface through the mask and developing without the further etching process for pattern transfer. Thus the photolithographically-defined patterns are used either in their own right or as templates for subsequent pattern transfer to other functional materials. The irradiation triggers the photopolymerisation, photocrosslinking, functionalisation and decomposition reaction of the polymer materials.
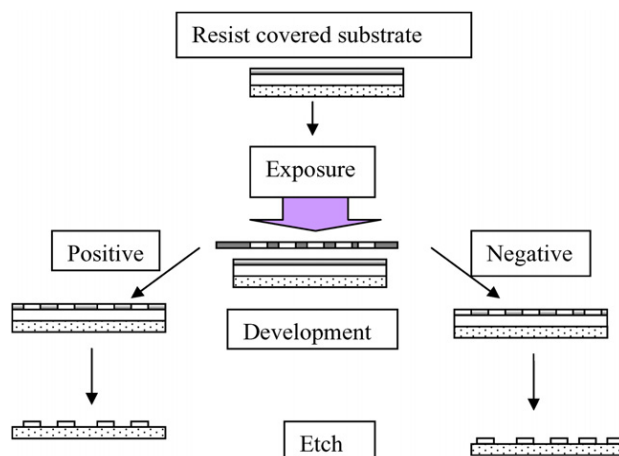
Figure 1.28 Illustrations on various stages of the photolithography technique. After [36].

Photolithography is known as a cost-effective, high-yield technique which is suitable for large-area production with accurate alignment and controlled topography. This technique is of course a standard, versatile and mature technology applied in micro-device fabrication. The resolution of the patterns is ~0.5μm if the photoirradiation is UV light (usually an i-line process at ~370nm) and it can be increased to sub-100nm by using electron beam lithography. In addition to the applications in the traditional semiconductor industry, photolithography also features in functional polymer micro- and nano- structures applied in organic LED production [37], polymer-dispersed liquid-crystal displays [38], optical components [39], data storage device [40], cells and proteins microarrays [41-43]. Figure 1.29 shows some examples of thus patterned polymers in display and biological applications. Figure 1.29-a shows a full-colour display device fabricated from three

oxetane-functionalized electroluminescent spirobifluorene-*co*-fluorene polymers emitting red, green and blue light respectively [37]. The pattern was achieved by photocrosslinking soluble polymers into an insoluble polymer network without destroying their electrical and optical properties. The efficiency of this device is even comparable to the state-of-art organic LEDs. The biological patterns generated from photolithography enable the manipulation and localization of the cells, and also control the cell-cell and cell-substrate interaction. The advantage of photolithography patterning is that it provides geometric confinement of cells and lateral compositional patterns for cell adhesion, which suppresses time-dependent deterioration of the cell array. Figure 1.29-b is a planar array of 3T3 fibroblasts confined within poly(ethylene glycol) (PEG) hydrogel microwells [41]. The cell occupancy reached 96.7% and the cells remained viable for 24 hours. Figure 1.29-c is an array of two distinct types of dye-labelled cells encapsulated in poly(ethylene glycol) diacrylate (PEGDA) by multistep photoirradiation of polymer photocrosslinking [43].
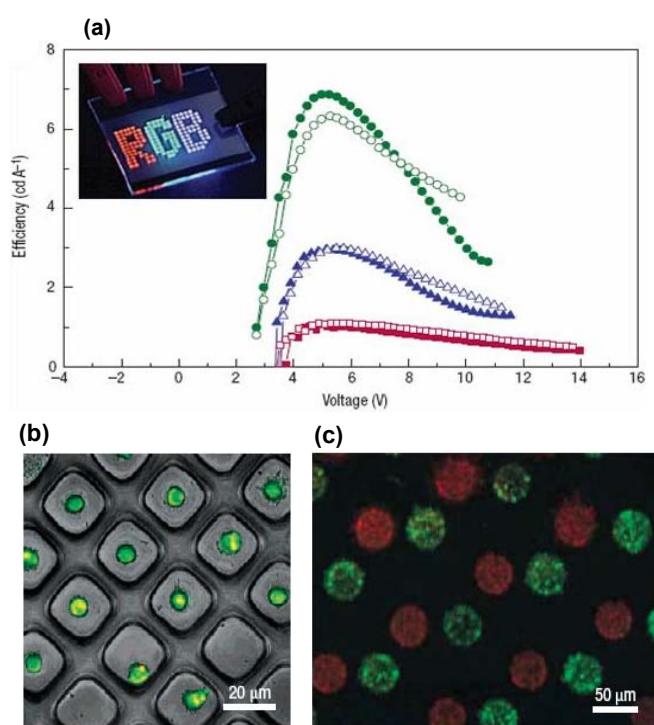
Figure 1.29 Photolithography patterned polymer applications: (a) organic LEDs emitting red, green and blue light; (b) Confocal microscopy image of 3t3 fibroblasts confined in PEG microwells; (c) Fluorescence microscopy image of two types of cells in PEGDA encapsulation. After [37, 41, 43].

1.3.2 Mask-free printing techniques

There are two major challenges for the photolithography technique in polymer work. One is how to maintain the feature of low-cost and high-resolution and the other is how to pattern the functional polymers without compromise in properties. Using a mask is the key process of pattern formation and transfer in photolithography and each design of the production calls for a separate mask, which impedes the adaptation of changing technologies, demands and business needs. Besides, direct photoirradiation can result in polymer degradation and the deterioration of its electronic and optical properties due to the weak bonds in some conjugated polymers or high photosensitivity in bioactive species. For these reasons, mask-free and cost-effective printing techniques have become alternative methods for patterning polymers. Here we generally introduce three such printing techniques: nanoimprinting, microcontact printing and dip-pen nanolithography.

The first printing technique is nanoimprinting lithography (NIL), which is also known as soft lithography technique. This process is realized by pressing a mould against a soft thermoplastic polymer or a liquid polymer precursor [44] (Figure 1.30-a). The solid state pattern is formed by either cooling (thermal NIL) or UV-photocuring the precursor (UV-NIL) [45]. Both thermal and UV NIL can reach ~5nm horizontal resolution [46, 47]. There are a wide range of conducting polymers [48], block copolymers [49] and thermosetting polymers [50] that have been used for thermal NIL at temperatures above the polymer glass transition temperature. The difficulty in thermal NIL is patterning the highly viscous polymers. Compared with the thermal NIL, UV-NIL has higher curing rates and intermediate viscosities. However, the high resolution patterns in UV-NIL are usually affected by oxygen sensitivity and polymer shrinkage [51] in the photosetting. Therefore, ongoing developments on UV-NIL focus on new designs of photochemically sensitive polymers with oxygen inhibition, shrinkage suppression and easy mould release. Figure 1.30-b and Figure 1.30-c give an example indicating the potential superiority

of the NIL technique in contrast with photolithography [52]. The multilevel imprint pattern (Figure 1.30-c) of photocurable polyhedral silsesquioxane derivative is formed by one single step of NIL using the corresponding multi-tier template (Figure 1.30-b), which would require multiple photoresist layers and exposure steps if photolithography was used.
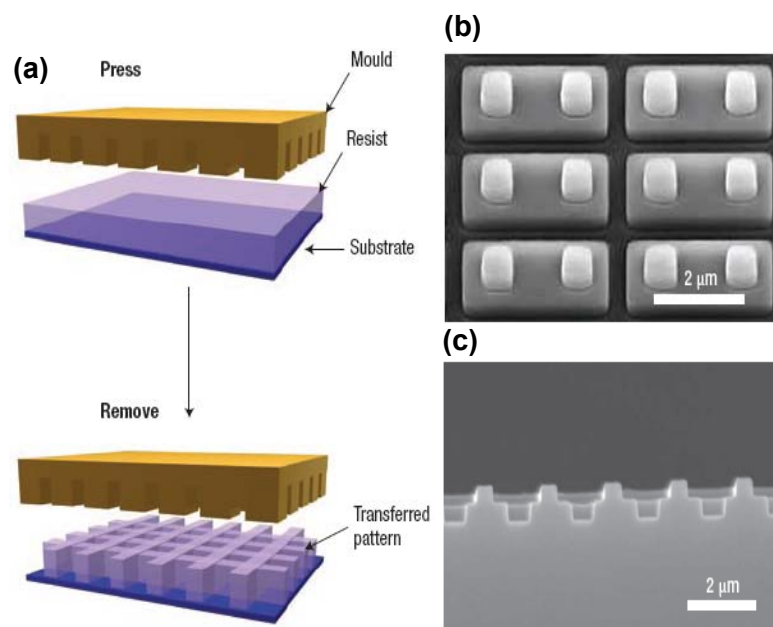
Figure 1.30 (a) Schematic of nanoimprinting lithography; Scanning Electron Microscopy (SEM) image of (b) multi-tier template and (c) cross-sectional image of corresponding pattern. After [44, 52].

The second printing technique is micro-contact printing, which is efficient in large-area fabrication with submicrometre spatial resolution [53]. Micro-contact printing is also suitable for reel-to-reel or sheet-to-sheet production and avoids expensive optical instrumentation. In micro-contact printing, an "ink" material is transferred to the substrate by close conformal contact with a rigid or elastic stamp with bas-relief features (Figure 1.31-a) [44]. The control of contamination, deformation of the stamp and lateral diffusion of ink are main aspects influencing the quality of the micro-contact printing pattern [54-56]. Micro-contact printing can be classified into two types: direct and indirect. In direct micro-contact printing, the polymer solution is directly transferred from the stamp carrier to the substrate; while

in indirect micro-contact printing, a polymer or a monomer is selectively deposited on a pre-patterned surface, following with surface-initiated polymerization, site-specific electropolymerisation and polymer multilayer deposition [57-59]. Strong interaction between the polymer "ink" and the surface will result in high-resolution patterning. For instance, patterns with resolution of ~80nm can be achieved by electrostatic interaction between cationic poly(acrylic acid) and a cationic poly(allylamine hydrochloride)-coated surface (Figure 1.31-b) [60]. Figure 1.31-c is an example of indirect micro-contact printing with surface-initiated polymerisation on a pre-patterned surface [61]. Micro-contact printing has made great contributions to applications in plastic electronics, optics, biology and surface science and will continue to play an important role in polymer patterning combined with other patterning techniques as it still has drawbacks on multilayer and multicomponent production.
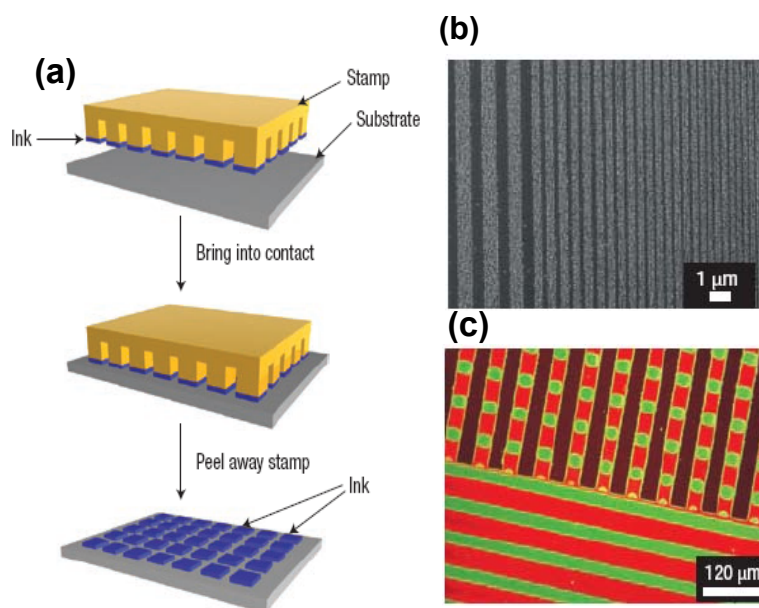
Figure 1.31 (a) Schematic of micro-contact printing; (b) Image of 96-nm polystyrene beads deposited on the lines of patterned polyelectrolyte complexes; (c) Fluorescence image of patterned tertiary brush of acridine-stained poly(methacrylic acid) (dark area) /poly(methacryloylethylphosphate) (bright red area) / poly(N-isopropylacrylamide) (green area). After [44, 60, 61].

The third printing technique is dip-pen nanolithography (DPN). This utilises an "ink"-coated tip of an Atomic Force Microscope (AFM) to deposit the ink molecules

to the underlying surface due to a liquid meniscus formation between the tip and the substrate and the physical or chemical adsorption of the ink to the surface [62] (Figure 1.32-a). The scanning speed, the volume of meniscus, the surface chemistry, the ambient humidity and temperature will affect the resolution of the pattern formed by DPN [62-65]. Similar to the micro-contact printing, there are two ways of depositing the "ink". One is by direct deposition of substrate polymer molecules from their solution or melts [66]; the other is delivering the surface-reactive precursors to the pre-patterned surface and triggering the subsequent polymerisation reaction [67]. DPN patterning is widely used in producing micro- and nano- arrays of proteins and DNA for studies on biological recognition and throughput diagnostics. Figure 1.32-b shows various sizes of protein A/G dots generated under different contact time between the AFM tip and gold substrate [68]. Protein A/G is a recombinant fusion protein that combines both Protein A and Protein G which are immunoglobulin-binding bacterial proteins. It is observed that the shorter the contact time is, the smaller the protein dot size is. And Figure 1.32-c is the AFM image of human IgG protein immobilized onto a thus formed protein A/G template [68].
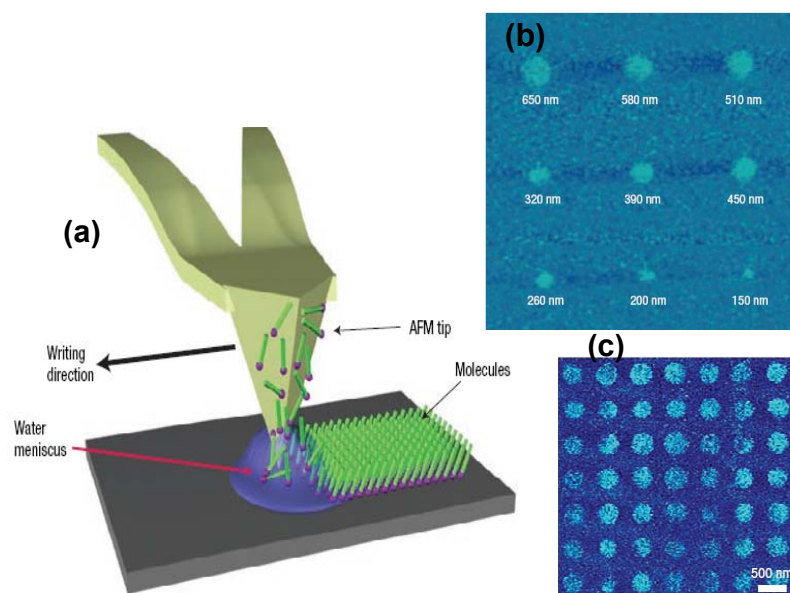
Figure 1.32 (a) Schematic of DPN technique; (b) Phase-tapping-mode AFM images of protein A/G dots generated under different contact time (650nm: 8s, 580nm: 7s, 510nm: 6s, 450nm: 5s, 390nm: 4s, 320nm: 3s, 260nm: 2s, 200nm: 1s, 150nm: 0.5s); (c) Topographical tapping mode AFM image of the fluorescence-labelled human IgG nanoarray immobilized onto protein A/G templates. After [62, 68].

1.4 Summary

In this chapter, we first introduced the basic principles of light emitting diodes. The photon generation in LEDs is due to the electron and hole recombination within the p-n heterostructure or quantum well. Rather than detailed discussion on the broad-area conventional LEDs, we focused on micro-structured LEDs (micro-LEDs) which have advantages in light extraction efficiency and increase in current injection uniformity, independent control of pixels and flexible pixel shape and size. The performance of the micro-LEDs is defined by the current-voltage curve and output power-injection current curve. The current-voltage curve indicates the electrical performance of the LED with information on the turn-on voltage and the dynamic resistance of the diode. The output power-injection current curve suggests the breakdown of the device and the saturation point of the radiative recombination of the electron-hole pairs. Thereafter, three types of configurations of micro-LEDs used in this work were described respectively including the fabrication details, typical electrical performance and light output power characterization.

Polymer materials were introduced in the second part of this chapter. The basic concepts of polymer materials were explained first to give a general picture. Then two categories of polymer materials were listed. Transparent polymers such as epoxies are usually used in the LED encapsulation due to their great mechanical robustness and chemical resistance. The poor transparency of those materials in the deep UV wavelength motivates the design of new transparent polymers, which have high transparency for wavelength below ~300nm and will be introduced in Chapter 2. Another category of polymer, the light emitting polymer, was discussed as well. In the light emitting polymers, the electrons are delocalised and change their energy state when energy (i.e. optical) is absorbed. Photons are produced in tens of nanoseconds with internal rotational and vibrational relaxation. These light emitting polymers play an important role in display applications.

The work in this thesis aims to employ different patterning techniques to

fabricate functional polymer structures suitable for compatibility with the GaN micro-LEDs. Thus the final part in this chapter focuses on an overview of polymer patterning techniques. The conventional photolithography technique was first reviewed with its process flow and applications in displays and biology. There are two major challenges in the photolithography technique for such applications which are how to make improvements without cost increase and resolution loss and how to pattern functional polymers without compromising their properties. Hence, mask-free printing is becoming a rapid established alternative. Three printing techniques, respectively nanoimprinting, micro-contact printing and dip-pen nanolithography were introduced with respect to patterning method and applications. There are also other techniques applied in polymer patterning such as instability-induced patterning and inkjet printing, which are used in this work and will be discussed in detail in later chapters.

References

1. H. Morkoc, *Nitride semiconductors and devices* (Springer, Berlin, 1999).

2. M. Fukada, *Optical Semiconductor Devices* (John Wiley & sons, New York, 1999).

3. J. Singh, *Semiconductor Optoelectronics: Physics and Technology* (McGraw-Hill, Singapore, 1995).

4. E. F. Schubert, *Light Emitting Diodes* (Cambridge University Press, Cambridge, 2003).

5. H.X. Jiang *et al.*, "III-nitride blue microdisplays," *Appl. Phys. Lett.* **78**, 1303 (2001).

6. I. Ozden *et al.*, "A matrix addressable 1024 element blue light-emitting InGaN QW diode array," *Phys. Stat. Sol.* **188**, 139 (2001).

7. C.W. Jeon *et al.*, "Fabrication of two-dimensional InGaN-based micro-led arrays," *Phys. Stat. Sol.* **192**, 325–328 (2002).

8. S. Wu *et al.*, "Micro-pixel design milliwatt power 254nm emission light emitting diodes," *Jpn. J. Appl. Phys.* **43**, L1035 (2004).

9. M.E. Gaevski *et al.*, "280nm emission deep UV LEDs with integrated fresnel microlenses," *MRS Proceedings* (2006).

10. M. Khizar *et al.*, "Nitride deep-ultraviolet light-emitting diodes with microlens array. *Appl. Phys. Lett.* **86**, 173504 (2005).

11. J.A. Chediak, *et al.*, "Heterogeneous integration of CdS filters with GaN LEDs for fluorescence detection microsystems," *Sens. Act. A.* **111**, 1-7 (2004).

12. J. Lee *et al.*, "Dry Etching of GaN and Related Materials: Comparison of Techniques," *IEEE J. Sel. Top. Quant.* **4**, 557 (1998).

13. S.M. Sze, *Modern semiconductor device physics*. Wiley Interscience, ISBN 0-471-15237-4.

14. Z. Gong *et al.*, "Matrix-addressable micropixellated InGaN light-emitting diodes with uniform emission and increased light output," *IEEE Trans. Electron Devices*

54, 2650 (2007).

15. Z. Gong *et al.*, "Efficient flip-chip InGaN micro-pixellated light-emitting diode arrays: promising candidates for micro-displays and colour conversion," *J. Phys. D: Appl. Phys.*, **41**, 094002 (2008).

16. R.O. Ebewele, *Polymer science and technology* (CRC Press LLC, Florida, 2000).

17. A.D. Jenkins *et al.*, "Glossary of basic terms in polymer science," IUPAC *Pure Appl. Chem.* **68**, 2287 (1996).

18. D.R. Paul, L.H. Sperling, *Multicomponent polymer materials* (American Chemical Society, Washington, DC, 1986).

19. A.D .Jenkins, *Polymer science: a material science handbook* (Northholland, New York, 1972).

20. N. Pelletier *et al.*, "Integrated mach-zehnder interferometer on SU-8 polymer for versatile pressure sensor," *IEEE sensors* **4**, 640 (2005).

21. N. Pelletier *et al.*, "Single-mode rib optical waveguides on SOG/SU-8 polymer and integrated mach-zehnder for designing thermal sensors," *IEEE sensors* **6**, 565 (2006).

22. L. Jiang *et al.*, "Integrated waveguide with a microfluidic channel in spiral geometry for spectroscopic applications," *Appl. Phys. Lett.* **90**, 111108 (2007).

23. C. Monat *et al.*, "Integrated optofluidics: a new river of light," *Nature Photonics* **1**, 106 (2007).

24. K.S. Kim *et al.*, "Single mode operation of a curved-mirror-vertical-emitting laser with an active distributed bragg reflector," *Jpn. J. Appl. Phys.* **41**, L827 (2002).

25. R.I. Aldaz *et al.*, "Monolithically-integrated long vertical cavity surface-emitting laser incorporating a concave micromirror on a glass substrate," *Opt. Exp.* **12**, 3967 (2004).

26. J.H. Burroughes *et al.*, "Light-emitting diodes based on conjugated polymers," *Letters to Nature* **347**, 539 (1990).

27. K. Mullen, U. Scherf, *Organic light-emitting devices: synthesis, properties and applications* Wiley-VCH ISBN 3-527-31218-8.

28. I.D.W. Samuel *et al*., "Organic semiconductors lasers," *Chem. Rev.* **10**, 1272 (2006).

29. B. Herman *et al*., Fluorescence microscopy, basic concepts in fluorescence. http://micro.magnet.fsu.edu.

30. N. Grassie *et al*., *Polymer degradation and stabilization* (Cambridge University Press, Cambridge, 1985)

31. T. Shimoda *et al*., "Inkjet printing of light-emitting polymer displays," *Mater. Res. Soc. Bull.* **28**, 821 (2003).

32. M. Thery *et al.*, "The extracellular matrix guides the orientation of the cell division axis," *Nature Cell Biol.* **7**, 947 (2005).

33. S.J. Hollister, "Porous scaffold design for tissue engineering," *Nature Mater.* **4**, 518 (2005).

34. S. Valkama *et al.*, "Self-assembled polymeric solid films with temperature-induced large and reversible photonic-bandgap switching," *Nature Mater.* **3**, 872 (2004).

35. M. Campbell *et al*., "Fabrication of photonic crystals for the visible spectrum by holographic lithography," *Nature* **404**, 53 (2000).

36. S. Roy, "Fabrication of micro- and nano-structured materials using mask-less processes," *J. Phys. D: Appl. Phys.* **40**, R413 (2007).

37. C.D. Muller *et al*., "Multi-colour organic light-emitting displays by solution processing," *Nature* **421**, 829 (2003).

38. R. Penterman *et al*., "Single-substrate liquid-crystal displays by photo-enforced stratification," *Nature* **417**, 55 (2002).

39. H.K. Wu *et al*., "Reduction photolithography using microlens arrays: Applications in grey scale photolithography," *Anal. Chem.* **74**, 3267 (2002).

40. M.B. Lee *et al.*, "Silicon planar-apertured probe array for high-density near-field

optical storage," *Appl. Opt.* **38**, 3566 (1999).

41. A. Revzin *et al.*, "Surface engineering with poly(ethylene glycol) photolithography to create high-density cell arrays on glass," *Langmuir* **19**, 9855 (2003).

42. W.G. Koh *et al.*, "Poly(ethylene glycol) hydrogel microstructures encapsulating living cells," *Langmuir* **18**, 2459 (2002).

43. D.R. Albrecht *et al.*, "Photo- and electropatterning of hydrogel encapsulated living cell arrays," *Lab Chip* **5**, 111 (2005).

44. Z.H. Nie *et al.*, "Patterning surface with functional polymers," *Nat. Mater.* **7**, 277 (2008).

45. L.J. Guo, "Nanoimprint lithography: Methods and material requirements," *Adv. Mater.* **19**, 495 (2007).

46. S.Y. Chou et al., "Sub-10 nm imprint lithography and applications," *J. Vac. Sci. Technol. B* **15**, 2897 (1997).

47. F. Hua *et al.*, "Polymer imprint lithography with molecular-scale resolution," *Nano Lett.* **4**, 2467 (2004).

48. M. Behl *et al.*, "Towards plastic electronics: Patterning semiconducting polymers by nanoimprint lithography," *Adv. Mater.* **14**, 588 (2002).

49. H.W. Li *et al.*, "Ordered block-copolymer assembly using nanoimprint lithography," *Nano Lett.* **4**, 1633 (2004).

50. H. Schulz *et al.*, "New polymer materials for nanoimprinting," *J. Vac. Sci. Technol. B* **18**, 1861 (2000).

51. M. Colburn *et al.*, "Characterization and modelling of volumetric and mechanical properties for step and flash imprint lithography photopolymers," *J. Vac. Sci. Technol. B* **19**, 2685 (2001)

52. G.M. Schmid *et al.*, "Implementation of an imprint damascene process for interconnect fabrication," *J. Vac. Sci. Technol. B* **24**, 1283 (2006).

53. A. Kumar *et al.*, "Features of gold having micrometer to centimetre dimensions

can be formed through a combination of stamping with an elastomeric stamp and an alkanethiol ink followed by chemical etching," *Appl. Phys. Lett.* **63**, 2002 (1993).

54. C.Y. Hui *et al.*, "Constraints on microcontact printing imposed by stamp deformation," *Langmuir* **18**, 1394 (2002).

55. R.B.A. Sharpe *et al.*, "Ink dependence of poly(dimethylsiloxane) contamination in microcontact printing," *Langmuir* **22**, 5945 (2006).

56. R.K. Workman *et al.*, "Molecular transfer and transport in noncovalent microcontact printing," *Langmuir* **20**, 805 (2004).

57. R.R. Shah *et al.*, "Using atom transfer radical polymerization to amplify monolayers of initiators patterned by microcontact printing into polymer brushes for pattern transfer," *Macromolecules* **33**, 597 (2000).

58. F. Zhou *et al.*, "Fabrication of positively patterned conducting polymer microstructures via one-step electrodeposition," *Adv. Mater.* **15**, 1367 (2003).

59. X.P. Jiang *et al.*, "Side-by-side directed multilayer patterning using surface templates," *Adv. Mater.* **13**, 1669 (2001).

60. J. Park *et al.*, "Chemically nanopatterned surfaces using polyelectrolytes and ultraviolet-cured hard molds," *Nano Lett.* **5**, 1347 (2005).

61. F. Zhou *et al.*, "Multicomponent polymer brushes," *J. Am. Chem. Soc.* **128**, 16253 (2006).

62. R.D. Piner *et al.*, "'Dip-pen' nanolithography," *Science* **283**, 661 (1999).

63. S.H. Hong *et al.*, "Multiple ink nanolithography: Toward a multiple-pen nano-plotter," *Science* **286**, 523 (1999).

64. S.H. Hong *et al.*, "A nanoplotter with both parallel and serial writing capabilities," *Science* **288**, 1808 (2000).

65. K.B. Lee *et al.*, "Protein nanoarrays generated by dip-pen nanolithography," *Science* **295**, 1702 (2002).

66. M. Yang *et al.*, "Direct writing of a conducting polymer with molecular-level

control of physical dimensions and orientation," *J. Am. Chem. Soc.* **128**, 6774 (2006).

67. P. Xu *et al*., "Peroxides-catalyzed in situ polymerization of surface orientated caffeic acid," *J. Am. Chem. Soc.* **127**, 11745 (2005).

68. S.W. Lee *et al.*, "Biologically active protein nanoarrays generated using parallel dip-pen nanolithography," *Adv. Mater.* **18**, 1133 (2006).

Chapter 2 Organic materials guest-host system and processing

This chapter describes an organic guest-host material system with organic light emitting materials embedded in a novel ultra-violet (UV) transparent host polymer. We first introduce UV transparent host polymers designed by the Pure and Applied Chemistry Department of the University of Strathclyde. The organic light emitting guest materials used are then introduced and the characteristics of the guest-host system are presented. The UV transparent polymers possess high UV transparency in film phase and convenient processability by not only standard photolithographic procedures but also other novel patterning methods such as electrohydrodynamic patterning and a method named "bottom-up curing through an aperture". The theoretical background of electrohydrodynamic patterning is explained and the microstructure fabrication from these polymers by this technique is described. The aperture used in "bottom up curing" method is fabricated through photolithography and details on the pattern fabrication are presented.

2.1 Deep ultra-violet transparent polymers: the 'host'

Traditional encapsulation materials, for LEDs are epoxy-based polymers. However, as LED devices have recently been extended in emission into the UV and deep UV

wavelength region, now covering the range of 240-370nm, the conventional polymers are no longer suitable for fully transparent encapsulation. Hard materials like sapphire and diamond could satisfy these transparency requirements but the processing is expensive and difficult. Hence, alternative new designs of polymers for high transparent optical element fabrication are necessary. As described below, novel deep UV transparent polymers have been designed in collaboration with the Pure and Applied Chemistry Department of the University of Strathclyde. These polymers are designed to be suitable for standard photolithographic procedures and dry etching without losing the transparency down to the deep UV wavelength region. Furthermore, they show attractive properties as hosts for light emitting materials.

The issue of achieving high UV transparency is to eliminate the UV-absorbing components as much as possible in the polymer film after curing. It is known that aromatic units present high absorption in UV-blue wavelength and that an aliphatic monomer is able to be photo-processed. In the work described below, epoxy- and vinyl ether bifunctional 1,4-cyclohexanedimethanol derivatives as shown to give low UV absorption and good mechanical properties after polymerization depending on the particular photoacid generator (PAG) used [1]. The PAGs absorb electromagnetic radiation of certain wavelengths and form an acid to initiate the crosslinking via a cationic polymerisation. The monomers for crosslinking used here are 1,4-cyclohaxanedimethanol diglycidyl ether (CHDG), trimethylolpropane triglycidyl ether (TMTG) and 1,4-cyclohexanedimethanol divinyl ether (CHDV). All these monomers have low viscosities as they are small molecules and lack the intermolecular forces to induce high viscosity. Therefore, the CHDG materials have been prepolymerised to obtain good spin-coating properties and the TMTG is added to CHDG to improve the thermal stability and control the crosslink density. The specific PAGs used for the CHDG are p-(phenylthiol)triphenylsulfonium hexafluorophosphate (TAS-PF6) and p-(phenylthiol)triphenylsulfonium hexafluoroantimonate (TAS-SbF6). For the CHDV, the PAGs is

p-(Octyloxy)diphenyliodonium hexafluoroantimonate (DAI-SbF6). Figure 2.1 shows the chemical structures of the monomers and the prepolymerised CHDG. Figure 2.2 shows the PAGs used in this work.
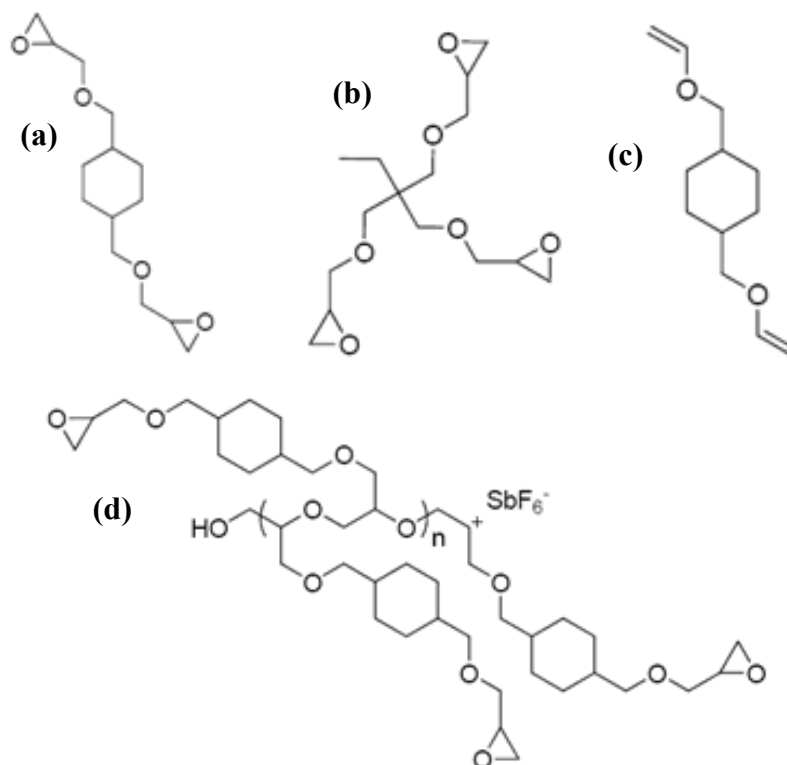
Figure 2.1 Chemical structure of the monomers: (a) CHDG; (b) TMTG; (c) CHDV; (d) prepolymerised CHDG.
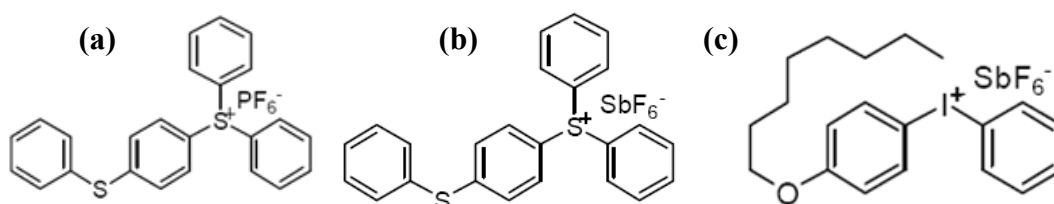
Figure 2.2 Chemical structures of the PAGs: (a) TAS-PF6; (b) TAS-SbF6; (c) DAI-SbF6.

The UV-blue optical transmission spectra of the prepolymerised CHDG polymers and CHDV with 0.5 wt% PAG (DAI-SbF6) were measured by a Varian Cary 300 UV-visible spectrometer. The polymer film was spin-coated on a clean

quartz or sapphire wafer which is fully transparent in the UV-blue wavelength region. Then the film was cured by a UV lamp emitting at 368nm with the exposure dose of 20.16J/cm^2 for the transmission spectra measurement. The thickness of the polymer film was approximately 20μm in each case. Figure 2.3 shows the transmission spectra of the prepolymerised CHDG polymers and CHDV polymers compared to the commercial Norland NOA63 polymer of the same thickness. The wavelength of 80% transparency for NOA63 is at ~310nm, while for the prepolymerised CHDG polymers with post-baking it is at ~225nm and for the CHDV polymers it is at ~225nm. We note that NOA63 show absorption up to ~380nm for a film ~20μm thick. A post-baking step helps in removing the residue of the acid from the PAG decomposition and improves the transmission.
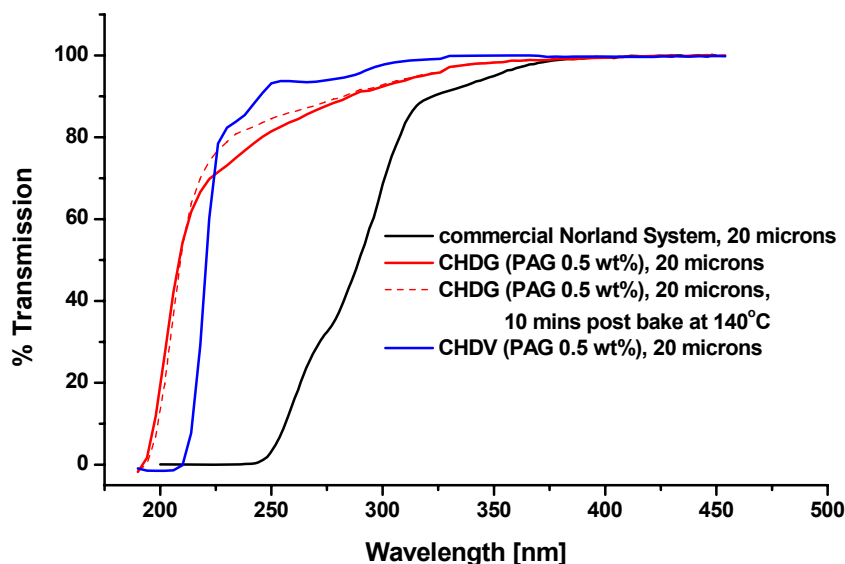
Figure 2.3 Transmission spectra of the prepolymerised CHDG and CHDV polymers compared to the commercial Norland NOA63.

The prepolymerised CHDG/TMTG blend polymers have excellent properties of UV-blue transparency and are suitable for standard photolithographic procedures. Our previous work has shown spherical and cylindrical micro-lenses fabricated from these polymers by standard photolithography and dry etching, suitable for

micro-optical elements integrated on the GaN-based micro-LEDs [2]. Moreover, these polymeric micro-lenses have also formed intracavity lasers in the single-mode fibre-VCSEL (Vertical Cavity Surface Emitting Laser) [3]. The prepolymerised CHDG/TMTG blend polymers are also suitable for other novel patterning methods such as the electrohydrodynamic technique and the "bottom up" curing which are described in the following sections of this chapter. The CHDV monomers react with the PAGs differently to the CHDG monomers, and CHDV cannot be prepolymerised for photolithographic procedures due to its limited miscibility with the PAGs. However, the CHDV monomers have good miscibility with the light emitting polymers and their low viscosity is suitable for the inkjet printing work described in Chapter 3.

2.2 Organic light emitting materials: the guest-host system

Organic light emitting materials used in this work are fluorene-based conjugated oligomers and polymers which consist of monomer units covalently bonded with alternating single and double bonds. This bond arrangement form an electron cloud overlap around the molecules, which results in electron delocalisation and semiconducting behaviour [4]. Figure 2.4 shows a generic structure of polyfluorene, which R1 represents alkyl or alkoxyl group.

The light emitting molecules carry fluorene units in the backbone. The fluorene-based conjugated polymers used in this work include star-shaped oligofluorenes, crosslinkable polyfluorenes, PFO (poly(9,9-dioctyfluorene)), F8BT (poly(9,9-dioctyfluorene-*co*-2,1,3-benzo-thiadiazole)) and PolyDPP (homo-polymer of 1,4-diketo-2,5-di-2-ethylhexyl-3,6-pyrrolo-[3,4-*c*]pyrrole (DPP)). The structure of blue-emitting PFO and green-emitting F8BT are well-known and the fluorescence

properties of these polymers are well studied. PolyDPP is a red-emitting polymer synthesised by Prof. B. Tieke's group in University of Cologne. DPP is functionalized with alkyl chains and polymerised resulting in red fluorescing PolyDPP. The chemical structures of PFO, F8BT and PolyDPP are shown in Figure 2.5. The Star-shaped oligofluorenes and crosslinkable polyfluorenes are the main focus in this work and will be introduced in following sections.
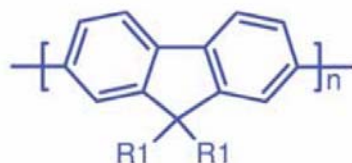
Figure 2.4 Generic structure of polyfluorene conjugated polymers. R1 represents alkyl or alkoxyl group. After [4].
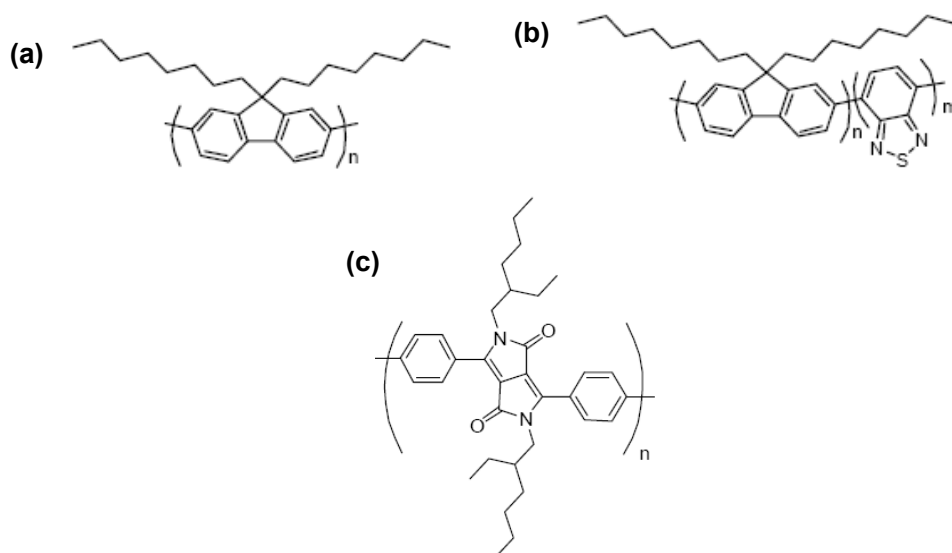
Figure 2.5 Chemical structures of (a) PFO, (b) F8BT and (c) PolyDPP.

2.2.1 Star-shaped oligofluorenes

Organic luminescent materials have been widely used and applied in organic LEDs for displays, solid state lighting and lasers. In this section, the organic light emitting materials used in this thesis work are introduced, which are (i) the star-shaped

oligofluorenes and the crosslinkable polyfluorenes. This first sub-section deals with the oligofluorenes.

Fluorene-based conjugated organics are one of the key families of materials used in organic electronics, and form a wide range of organic semiconductors. The first category of fluorenes we consider is oligofluorenes, consisting of up to 4 repeats of the basic fluorene monomer unit. They are formed into star-shaped molecules by forming three oligofluorene arms of equal length attached to a central truxene core, giving so-called truxene oligofluorenes. In our studies, each of the three arms consists of 1-4 fluorene repeats, giving star-shaped nanosized molecules designated T1-T4, respectively. These materials were developed by Prof. P.J. Skabara of the Department of Pure and Applied Chemistry at the University of Strathclyde, and are custom-synthesised for our work. Figure 2.6-a shows the chemical structures of the T1-T4 materials and Figure 2.6-b gives a three dimensional representation of a T3 molecule as a specific example.
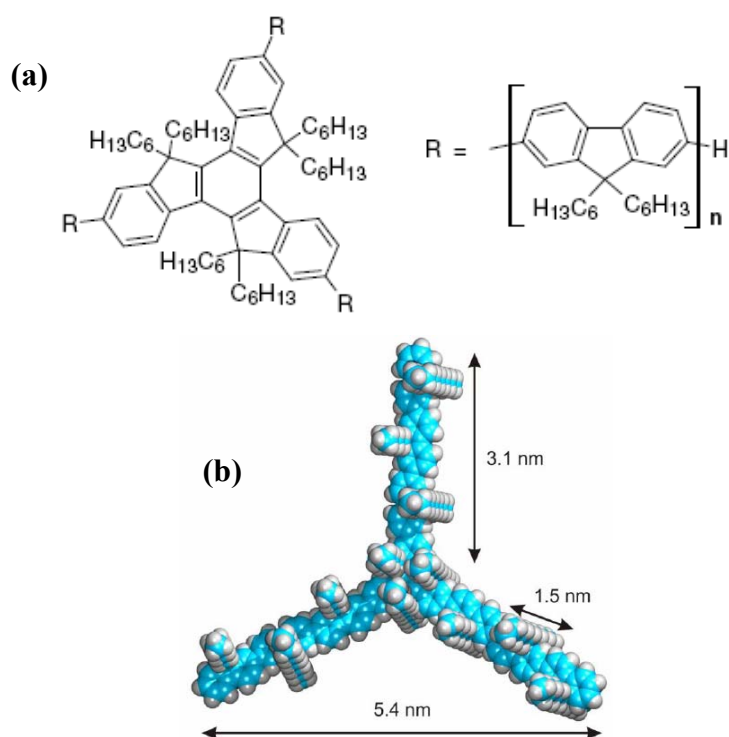
Figure 2.6 (a) Chemical structures of the T1-T4 materials (n = 1, 2, 3, 4); (b) three dimensional structure of the T3 molecule.

The oligofluorenes are characterised by uniform molecular structure and high chemical purity. The synthesis of these oligofluorenes is described as directly attaching the fluorene arms of the appropriate length to the central truxene core, which differs from the repetitive divergent method of adding arms by Suzuki coupling [5]. The absorption, emission, thermal and electrochemical properties of these materials have been presented previously [6]. The absorption spectra for compounds T1-T4 show strong π-π^* electron absorption bands red-shifting peaks from 343nm to 374nm when the chain length is increased both the solution and the solid state. The oligomers (T1-T4) show efficient fluorescence both in solution and solid state with photoluminescence (PL) quantum yield close to the linear polyfluorenes (for poly(9,9-dioctylfluorene), 0.78 in solution and 0.4 in film) [6, 7]. Figure 2.7 shows the PL spectra of respective T1-T4 films spin-coated from toluene solution excited at 370nm. It can be seen that the PL peaks in the blue region of the spectrum, and that vibronic substructure is visible in the spectral shape as described in Chapter 1. Figure 2.8 gives the absorption spectra of T1-T4 materials in toluene solution and film state and Table 2.1 summarizes the absorption and photoluminescence peaks of T1-T4 materials in solution and film state. The absorption spectra data were obtained from the Department of Pure and Applied Chemistry, University of Strathclyde.
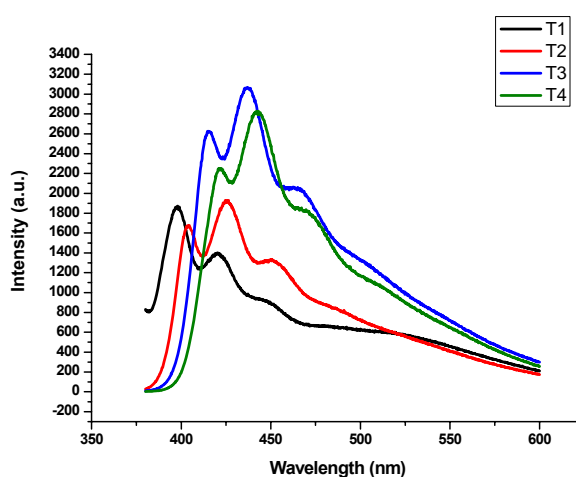
Figure 2.7 Measured PL spectra of T1-T4 films spin-coated from the toluene solution.
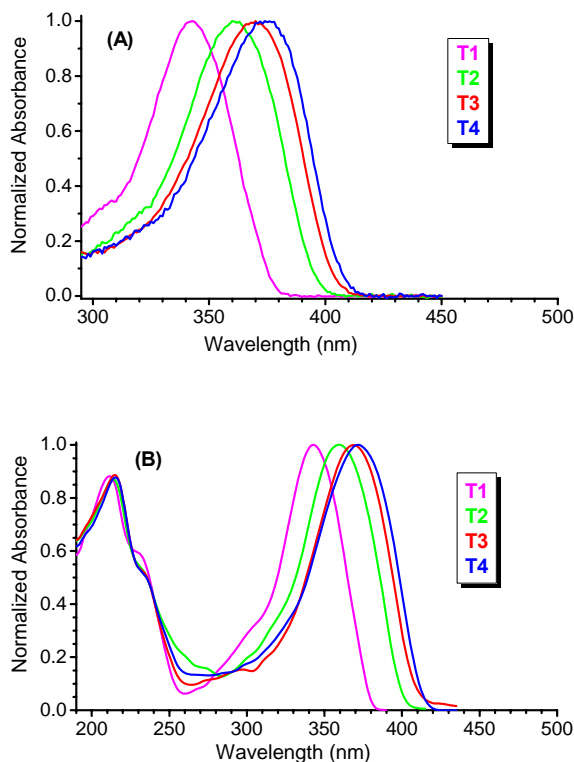
Figure 2.8 Absorption spectra of T1-T4 materials in (a) toluene solution and (b) film.

Table 2.1 Absorption and photoluminescence peaks of the T1-T4 materials

Compound	Absorption peak (solution)	Absorption peak (film)	Photoluminescence peak (solution)	Photoluminescence peak (film)
T1	~343	~343	~377, ~398, ~416	~397, ~420, ~446
T2	~362	~359	~400, ~424, ~452	~403, ~425, ~451
T3	~372	~369	~410, ~434, ~457	~415, ~436, ~465
T4	~377	~372	~414, ~438, ~467	~421, ~442, ~472

The truxene oligomers were mixed with the CHDV polymers to improve the processability to be suitable for the inkjet printing method described in Chapter 3. The photoluminescence spectra indicate that the advantageous fluorescence properties of the truxene materials have been maintained in this Truxene/CHDV guest-host blend system. Figure 2.9 shows the PL spectrum of the T3/CHDV blend polymers. The fluorescence vibronic peaks are at ~409nm, ~428nm and ~458nm,

which are similar to T3 in solution.
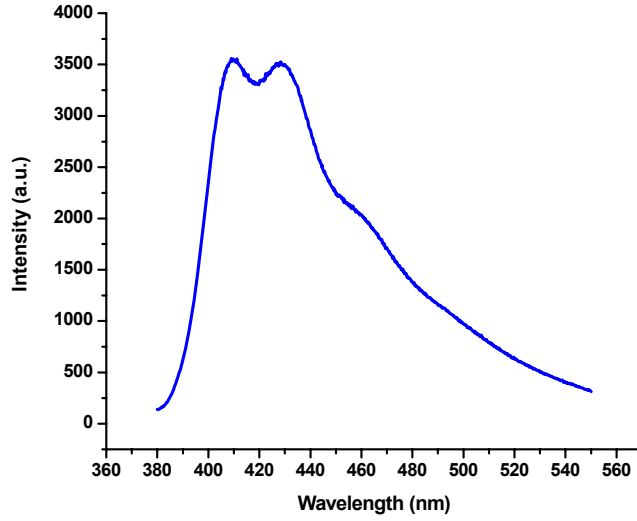
Figure 2.9 PL spectrum of the T3/CHDV blend (T3:CHDV = 1:10 in volume)

For optoelectronic applications such as organic lasers, the fluorescence lifetime of the materials is an important parameter to be considered, and this has yet to be explored for these truxene oligofluorenes. We therefore measured these characteristics using time-correlated single photon counting (TCSPC). The sample was excited by a laser diode emitting at 374nm with 200ps pulse width and 1.0MHz maximum repetition rate [8]. The fluorescence was collected by an objective lens. A time-to-amplitude converter (TAC) generated voltage pulses proportional to time delays between START and STOP signals [9]. These pulses were then collected and accumulated in a multi-channel analyzer (MCA) to create the intensity vs. time decay curve. The time decay of fluorescence intensity can be represented by a model of the form:

$$I(t) = \sum_i \alpha_i e^{-t/\tau_i} \qquad (2.1)$$

where α_i and τ_i are the amplitude and decay time of the ith component respectively. [19] In this work, the fluorescence signal was collected at 450nm, being close to the main wavelength peak of the truxene blend. The values of α_i and τ_i

were determined from the experimental data by a non-linear least-squares fitting procedure. This fitting process was repeated until the value of the reduced chi-squared (χ^2) passed through a minimum. The corresponding fluorescence lifetime parameters were then found [10]. Figures 2.10, 2.11, 2.12 and 2.13 are TCSPC data of the T3 in toluene solution (1.5mg/ml), T3 in a film state (from toluene solution), T3/CHDV blend solution (0.5wt%) and T3/CHDV cured blend polymers, respectively. In these figures, the blue dot curve is the reference (prompt) function characterising the impulse response of the excitation source and detection system, the red dot curve is the fluorescence decay, while the green dot curve is the fitted function. All the fitted lifetime errors show 3 deviations. The fitting results are summarized in Table 2.2. The TCSPC data revealed that the fluorescence decay of the T3 in toluene solution was fitted to be a single exponential decay with a lifetime of 0.78 ± 0.01 ns ($\chi^2 = 1.22$). As the single exponential decay fitting for T3/CHDV blend solution resulted in high chi-square, double exponential decay was better fitted with a dominant decay time (τ_1) of 0.67 ± 0.01ns ($\chi^2 = 1.06$). It is noted that the weak decay time (τ_2) in this double exponential decay fitting is comparable to the time calibration (~15ps), which is considered to result from the scattered excitation light. The decay curve of T3/CHDV polymerized truxene blend was better fitted to the double exponential decay ($\chi^2 = 1.00$) with a strong short lifetime component (τ_1) and a weaker long lifetime component (τ_2) compared to the high chi-squared fitting result ($\chi^2 = 2.74$) from the single exponential decay fitting. It is found that in the spun film of T3, the fluorescence lifetime fitting is more complicated. Comparatively low chi-squared fitting result ($\chi^2 = 1.25$) was obtained from the three exponential decay fitting. The dominant short decay of the fluorescence lifetime (τ_1) is comparable to the corresponding solution state. The shortest lifetime component (τ_3) is considered as the excitation light scattering. And the weak long lifetime component (τ_2) is postulated to result from some minor aggregate formation of truxene oligomers in the cured polymer matrix. In the truxene blend, the concentration is higher (~5 times)

than that in toluene and the truxene chain conformation may be restricted due to the interaction with the polymer matrix. The truxene molecules may have a low degree of aggregation and be trapped in the matrix after the polymerization. The longer radiative lifetime may be due to either the significant absorption of the aggregates under main exciton absorption band or directly excited excitons can efficiently migrate to the sites of aggregation [11]. Further detailed study is required to understand the full effects of the blending process, but the time-resolved measurements provide further evidence that the optical properties are at least not strongly altered whatever the host is.

Table 2.2 Summary of the TCSPC fitting results on T3

		Truxene (T3) in toluene	Truxene (T3) spun film	Truxene (T3)/CHDV blend solution	Truxene (T3)/CHDV polymerized blend polymers
Fitting result 1	τ_1	0.78 ± 0.01 ns	0.46 ± 0.01 ns	0.64 ± 0.01 ns	0.77 ± 0.01 ns
	χ^2	1.22	5.53	1.83	2.74
Fitting result 2	τ_1		0.51 ± 0.01 ns (63.99%)	0.67 ± 0.01 ns (90%)	0.68 ± 0.01 ns (82.5%)
	τ_2		0.02 ± 0.01 ns (36.11%)	0.05 ± 0.03 ns (10%)	1.23 ± 0.12 ns (17.5%)
	χ^2		1.77	1.06	1.00
Fitting result 3	τ_1		0.48 ± 0.01 ns (58.64%)		
	τ_2		2.07 ± 0.6 ns (1.69%)		
	τ_3		0.01 ± 0.01 ns (39.67%)		
	χ^2		1.25		

Figure 2.10 TCSPC curves of the T3 in toluene solution (fitting result 1).
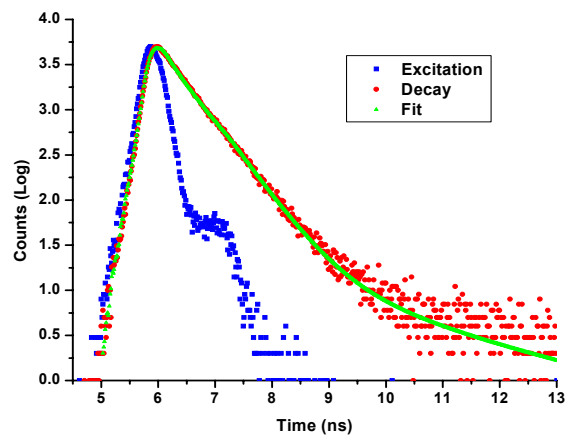
Figure 2.11 TCSPC curves of the T3 in film state (fitting result 3).
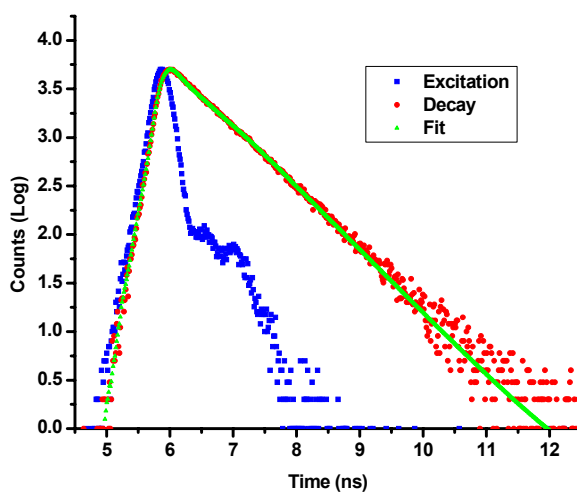
Figure 2.12 TCSPC curves of the T3/CHDV blend in solution (fitting result 2).
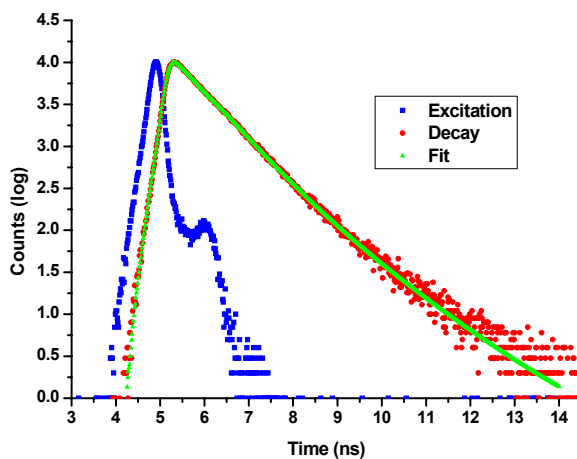
Figure 2.13 TCSPC curves of T3/CHDV polymerized blend polymers (fitting result 2).

2.2.2 Crosslinkable polyfluorenes

In this section we introduce the polymeric fluorene materials we have studied.

There is a novel class of crosslinkable vinyl ether functionalised fluorene polymers is also adopted in this work. The fluorene-based polymer backbone has been integrated with green, orange and red emitters, which allows tunable emission colours whilst retaining the fluorene backbone absorption at ~368 nm [12]. These materials are beneficial for application in photonic multicolour arrays with just one excitation wavelength, as described later. These materials were synthesised by our collaborators in the group of Prof. K. Meerholz at the University of Cologne.

The homo-polyfluorenes are known for their broad absorption with maximum at ~368nm and emission at blue wavelengths. Therefore, only green and red emitters need to be incorporated through Suzuki coupling in order to achieve RGB capability. The vinyl ether group in the resulting light emitting polymers helps incorporation into the CHDV matrix and leads to a denser crosslinking network. Instead of dissolving in the matrix like the truxene oligofluorenes, these new light emitting polymers become a part of the crosslinking network, which restricts the diffusion of the oxygen, moisture and solvent, resulting improved protection of these light emitting polymers. Figure 2.14 shows the chemical structures of the polymers with blue, green, orange and red emission.
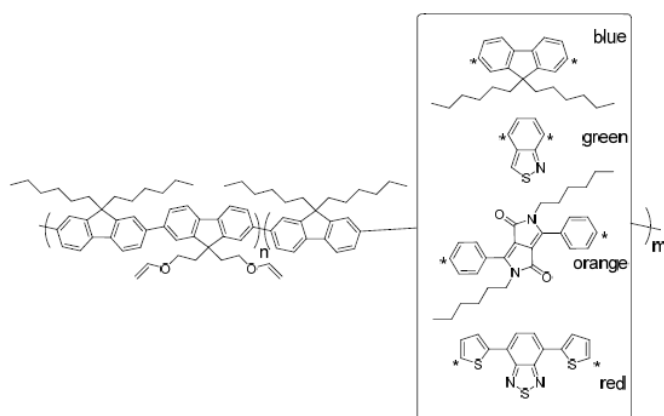
Figure 2.14 Chemical structures of the crosslinkable polyfluorene light emitting polymers (m, n were chosen to be 1).

Our work has focused on the green light emitting polymers, which is crosslinkable F6BT (poly(4,7-dibromo-2,1,3-benzothiadiazole)). The absorption and emission spectra of this crosslinkable F6BT in chloroform solution are shown in Figure 2.15. The absorption maximum and a second maximum are at ~365nm and ~437nm, respectively, while the emission peak is at ~545nm with a small peak at ~423nm. The PL spectrum of the crosslinkable F6BT/CHDV blend polymer solution (2wt%) is presented in Figure 2.16. The emission peak is at ~535nm which is blue-shifted compared to that in the chloroform solution and this may due to the different solvent (toluene) in the blend solution. The small peak at blue wavelength disappearance may be due to the interaction between the CHDV matrix and the crosslinkable F6BT, which requires further analysis.
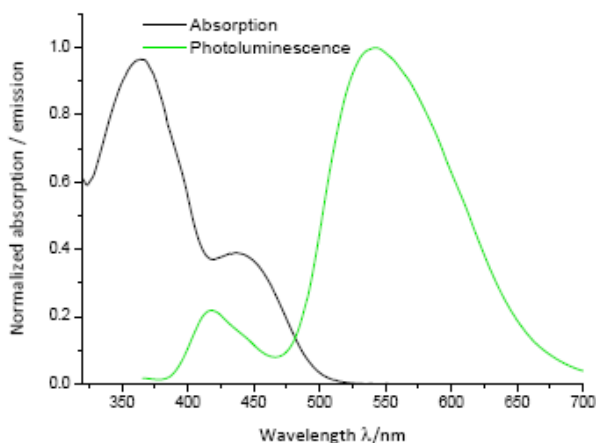
Figure 2.15 Normalized absorption and PL spectra of crosslinkable F6BT in chloroform solution.
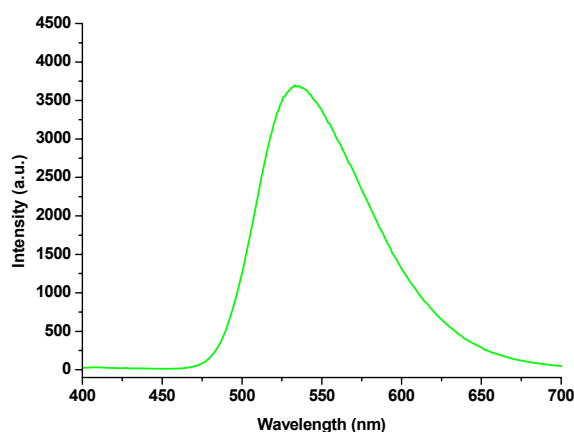
Figure 2.16 PL spectrum of the crosslinkable F6BT/CHDV blend polymers solution.

2.3 Novel pattern fabrication in ultra-violet transparent polymers

Direct patterning of microstructures without using photoresist, exposure, development and etching steps has become attractive recently as it has many advantages, such as simplifying the fabrication process, increasing yield and reducing cost. It is also applied regularly in polymeric device fabrication since it prevents the polymer materials from being damaged by resist, UV exposure, chemical development and etching [13]. Electrohydrodynamic patterning is a novel method to form microstructures without requiring lithography. Polymeric pillar arrays have been formed by this technique as reported in the literature [14-16]. In this work, we use the deep UV transparent CHDG polymers to fabricate microstructures by electrohydrodynamic patterning. In addition, the CHDG polymers have also been patterned for bio-analysis by another novel method of "bottom up" curing through an aperture.

2.3.1 Electrohydrodynamic patterning

As the pixels on micro-LEDs produce divergent light, it is necessary to fabricate microlenses or waveguides on top of LED array to collimate the light for applications such as a micro-projection light source in mask-free lithography. The electrohydrodynamic patterning allows direct fabrication of waveguides on the micro-LED pixels. By applying a voltage between the electrode on the micro-LED surface and a UV transparent polymer film, the polymer film rises, aligns to the micro-LED array structure and can be photo-cured by switching on the LED pixels. Here we simply use the electrodes fabricated by photolithography to form polymeric microstructures as a preliminary study.

2.3.1.1 Theoretical background and application

Dielectric media experience a force in an electric field gradient. Strong fields can produce forces which overcome the surface tension in thin liquid films, inducing an instability that results in pillars of the material parallel to the field force in two flat electrodes. If the upper electrode is patterned, the pattern is replicated in the thin film. Schäffer *et al.*, for example, used polystyrene above its glass transition temperature T_g for such pattern formation and then cooled the polymer below its T_g to fix the structures [14].

This experiment uses two capacitor plates to form a strong electric field. As there are some polar molecules possessing negative charge in the polymer, those will feel the electric field force towards the upper $(+V_e)$ electrode. This destabilising force will overcome the stabilizing effect of surface tension acting at the film-air interface to make the thin polymer film replicate a pattern on the top plate. When the space between the capacitor plates is empty, the electric field strength is only dependent on the voltage U and the distance between two plates d [17], which is:

$$E = U / d \tag{2.2}$$

The destabilising pressure p scales with the square of the electric field strength in the polymer film, E_p [18]:

$$p = \varepsilon_0 \varepsilon_p \left(\varepsilon_p - 1 \right) E_p^2 \tag{2.3}$$

where ε_0 and ε_p is the dielectric permittivity of the vacuum and the polymer respectively. When the polymer is placed in the capacitor, the electric field strength will depend on the thickness of the polymer film h and the dielectric constant ε_p, together with the voltage U applied between the two plates and the electrode spacing d : [15]

$$E_p = \frac{U}{\left(\varepsilon_p d - \left(\varepsilon_p - 1\right)h\right)} \tag{2.4}$$

There is a local perturbation in the film thickness h, which results in a pressure gradient driving a flow of the dielectric liquid film. And the dominant perturbation wavelength λ is given by the force balance between the destabilizing pressure gradient p, the film thickness h and the surface tension γ (see Figure 2.17):

$$\lambda = 2\pi \sqrt{\frac{2\gamma}{\partial p / \partial h}} \tag{2.5}$$

For instance, if we consider two separate polymer film thickness: $h_1 = 1/2d$, $h_1 = 1/3d$, from the equation (2.4), it can be found that:

$$E_{p1} = \frac{U}{\frac{1}{2}\varepsilon_p d + \frac{1}{2}d} \qquad , \qquad E_{p2} = \frac{U}{\frac{2}{3}\varepsilon_p d + \frac{1}{3}d}$$

and $E_{p1} < E_{p2}$ as the $\varepsilon_p > 1$ in most materials. According to equation (2.3), it is known that $p_1 < p_2$. This means that the polymer has potential to increase its height in order to decrease the energy and reach a stable state. That is the key reason why the polymer will "jump" to the top electrode and it occurs in the negative-charged molecules prior to other molecules.

The discussion applies to the situation of an un-patterned upper electrode. When the electrode is patterned, the distance between the two plates will vary (shown in Figure 2.17).
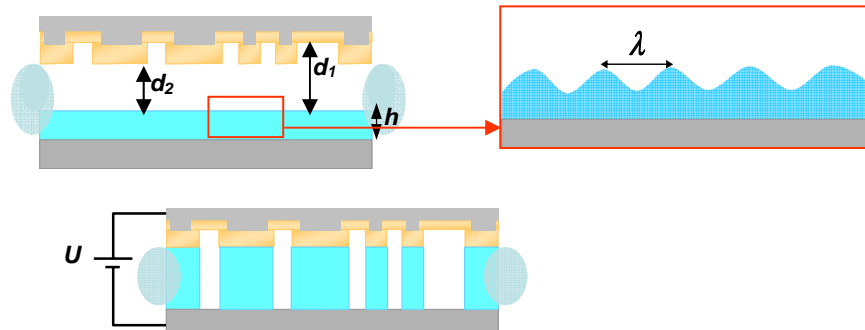
Figure 2.17 Schematic representation of the patterned upper electrode. The symbols are defined in the text above, and the respective features labelled in Figure 2.19.

If we consider two different distance between the two plates: d_1, $d_2 = 2/3d_1$, from the equation (2.4), it can be found that:

$$E_{p1} = \frac{U}{\varepsilon_p d_1 - (\varepsilon_p - 1)h} \quad , \quad E_{p2} = \frac{U}{\frac{2}{3}\varepsilon_p d_1 - (\varepsilon_p - 1)h}$$

It is obvious that $E_{p1} < E_{p2}$, so $p_1 < p_2$ according to the equation (2.3). This means the polymer in the area which is closer to the upper plate will "jump" prior to the polymer in the other areas.

The detailed formation of the polymer shaping induced by the electric field is quite complicated, as the surface of the polymer layer is not as flat as the ideal instance and the electric field distribution will change. The interaction of the electric field with different media had been theoretically explained [19] and the dynamics of the electric field induced shaping has been modelled as well using three-dimensional non-linear simulations [20] and linear stability analysis [20-23]. Linear stability analysis can even predict an exponential growth rate, with the time scale of the structure formation, which has been practically proved in the early stage of the growth [24]. Those theoretical studies were extremely helpful during the further optimization work of this experiment.

2.3.1.2 Experiment set-up and electrode fabrication

Electrode fabrication is a crucial step in the experiment. It requires a clean and clear surface to ensure the uniformity of the electric field between two parallel plates. Thus, all the fabrication work was carried out in the clean room. As a highly-doped silicon wafer is conductive and often used for the bottom electrode, the electrode fabrication mainly concerns the upper one. The process is shown in the Figure 2.18.

```
                    ┌─────────────────────────┐
                    │   Clean the quartz glass │
                    └────────────┬────────────┘
                                 │
                    ┌────────────▼────────────┐
                    │  Deposit two silicon dioxide │
                    │    spacers by PECVD      │
                    └────────────┬────────────┘
              ┌──────────────────┴──────────────────┐
              │                                      │
    ┌─────────▼─────────┐              ┌─────────────▼─────────────┐
    │ Un-patterned      │              │  Patterned electrode:     │
    │ electrode:        │              │                           │
    └─────────┬─────────┘              └─────────────┬─────────────┘
              │                                      │
    ┌─────────▼─────────┐              ┌─────────────▼─────────────┐
    │ Deposit a 10nm-thick layer of │  │ Spin a layer of photoresist │
    │ gold between the two spacers  │  │ between the two spacers     │
    └───────────────────┘           └─────────────┬─────────────┘
                                                   │
                                    ┌──────────────▼──────────────┐
                                    │ Pattern the layer with lithography │
                                    └──────────────┬──────────────┘
                                                   │
                                    ┌──────────────▼──────────────┐
                                    │ Deposit a 10nm-thick layer of gold │
                                    │ on the patterned photoresist │
                                    └─────────────────────────────┘
```
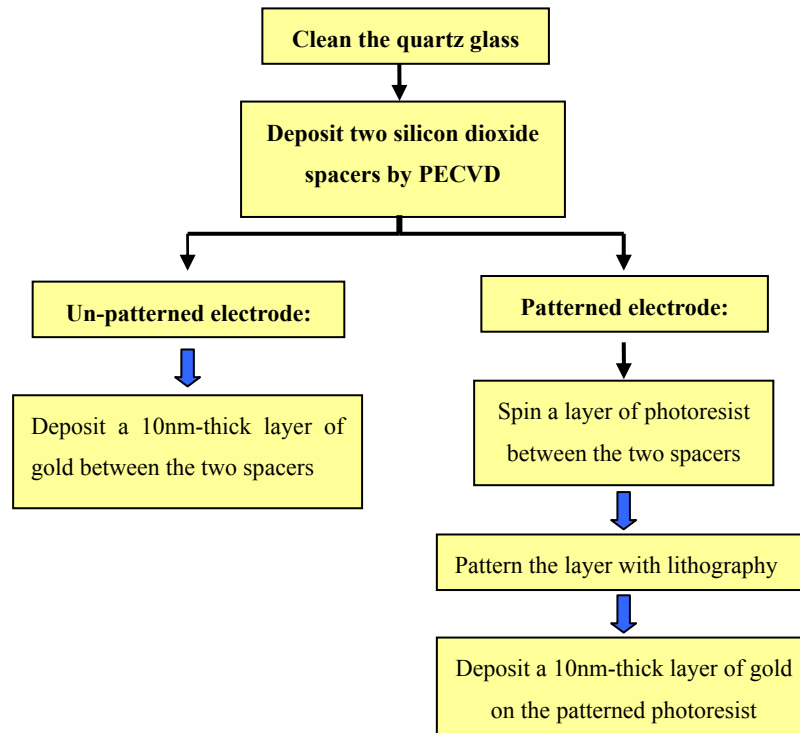
Figure 2.18 The process flow of the electrodes fabrication.

In order to get a clean electrode, a Piranha strong acid solution (H_2SO_4: H_2O_2 = 4:1) was chosen to wash the quartz glass in the initial step, instead of normal solvent. Two silicon dioxide spacers were designed to fix and make parallel the gap between the two electrodes and those were prepared by Plasma Enhanced Chemical Vapour Deposition (PECVD). The gap can be tuned by using different heights of the silicon dioxide spacers using different deposition time. The unpatterned upper electrode was covered with 10nm thick gold layer to be conductive. The patterned upper electrode after fabrication by lithography procedures is schematically shown in Figure 2.19 and a layer of 10nm thick gold was deposited as a conductive medium. Figure 2.20 is the stylus (Dektak) profile data of the test silicon dioxide spacers (height = 2μm for demonstration) and Figure 2.21 shows the Dektak profile data of the upper electrode with a spiral (test) pattern. It is found that the thickness of the pattern is ~450nm and the top of the pattern is quite flat. However, there is some residue of undeveloped photoresist remaining in between the patterns.
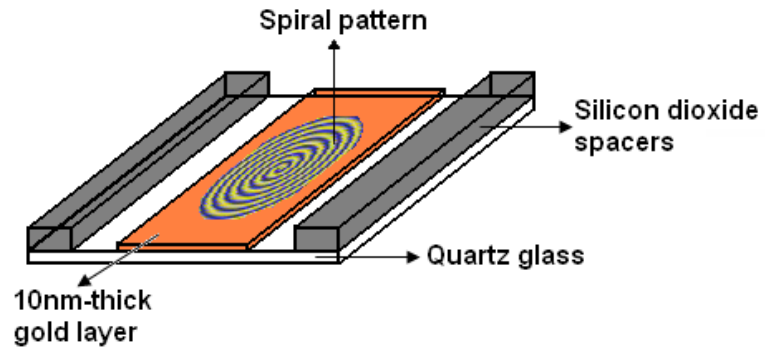
Figure 2.19 Schematic image of the patterned upper electrode. The special pattern was chosen arbitrarily in order to illustrate the technique.
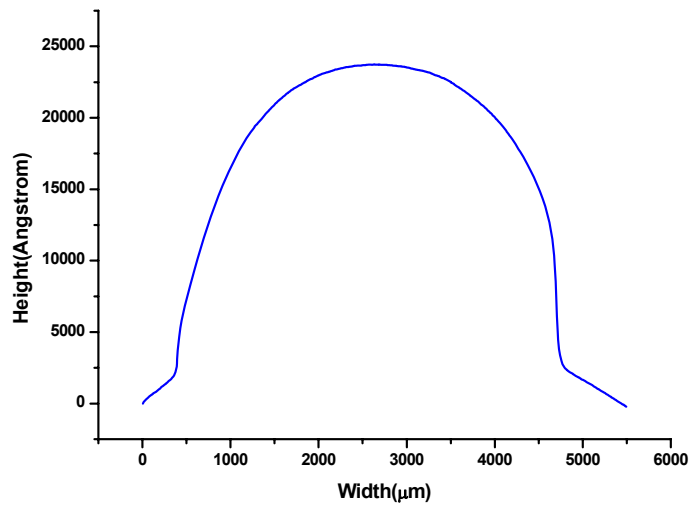

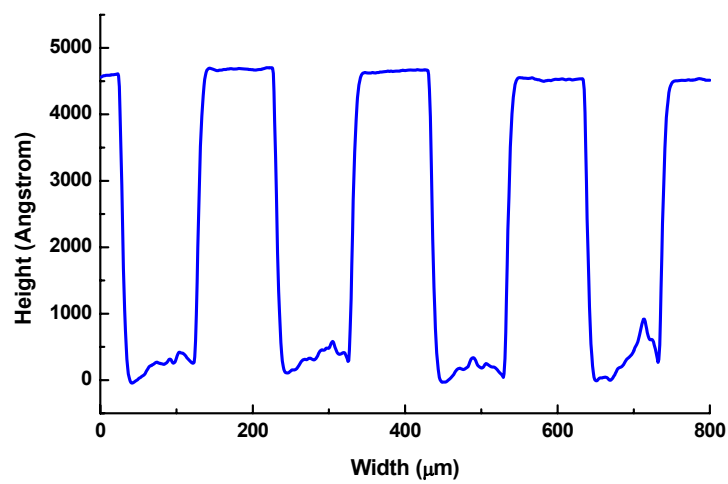Figure 2.20 Stylus profilometer (Dektak) data of the test silicon dioxide spacers.

Figure 2.21 Stylus profilometer (Dektak) data of the upper electrode with the test spiral pattern.

2.3.1.3 Pattern fabrication and characterisation

The photolithographic prepolymerised CHDG system is designed for a spin coating process and hence thick to very thin films can be spun. For the method to produce submicron structures via electrically induced formation, polymer films of a few hundred nm thickness are required. The material was spread onto a silicon wafer used as the bottom electrode and the film was spun at 5000-7000rpm for 60s depending on the desired thickness. Besides the spinning speed, the weight ratio between the polymer and toluene solution will also affect the thickness of the polymer. Table 2.3 shows the thickness with different spinning speed and the weight ratio. It is observed that more toluene and higher spinning speed can result in a much thinner polymer layer (around 200nm-thick), which can meet the various thickness requirements of the experiment.

Table 2.3 Polymer thickness with the spinning speed and the weight ratio

Thickness (nm) / Speed (rpm)	Weight ratio (polymer: toluene)						
	1:1	1:2	1:3	1:4	1:5	1:6	1:8
5000	2092	1043	693.6	492.2	414.7	338.9	242.5
6200	1854	984.4	636.5	455.3	396.8	319.6	225.3
7000	—	—	—	—	364.4	302.6	206.7

The set-up of this experiment is quite simple and is shown in Figure 2.22. Initially, a thin polymer film was spin-coated from toluene solution onto a silicon wafer serving as a bottom electrode. Some areas of the polymer were wiped away by acetone, leaving a rectangular area of polymer layer of width the same as the distance between the two SiO_2 spacers (height = 1μm). Then wires were attached by taping them onto the gold layer and the silicon bottom electrode. A voltage of 80V ($E_p \sim 10^7$ V/m) was applied and the structure formation was monitored by using a microscope.

When structures had formed, a UV lamp was placed over the electrodes cured the polymer for around 15min. And the upper electrode is lifted off from the structures. The maximum output of the lamp is at 368nm with a power of 6mW/cm^2. Using this polymer cured by photo-induced polymerization, it is not necessary to apply high temperature to perform a thermally cure or go above the glass transition temperature T_g. Forming and fixing structures at ambient temperature is beneficial to a wide range of applications which are sensitive to the temperature. We aimed for the first in-situ photo-cured electrohydrodynamic patterning. However, a paper reporting the similar idea [25] appeared during our work was under way.
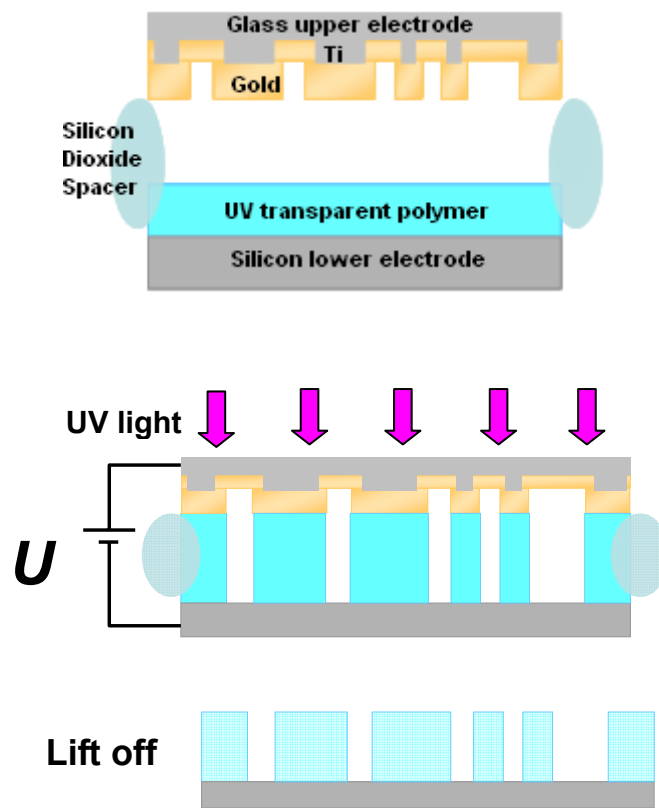

Figure 2.22 Schematic set-up of the electrohydrodynamic experiment.

Some initial results have been obtained with both the un-patterned electrodes and the patterned ones. Figure 2.23 shows some microstructures formed by the un-patterned and patterned electrodes. Figure 2.23-a is the structures formed in 400nm thick polymer film from unpatterned upper electrode and the minimum

dimension of the structure is 10μm in diameter and 1μm in thickness. In the Figure 2.23-a, the top of the pattern becomes flat which indicates the "jumping" of the polymer is completed and that a pillar structure has been formed.

Figure 2.23-b shows the picture of the experiment with the patterned electrode (the spiral lines). It can be seen clearly that the spiral structure has been formed. And the Figure 2.24 gives the stylus profilometry data of the red area in Figure 2.23-b. Though there are some features in-between the patterns induced by the undeveloped photoresist structures on the upper electrode, the major pattern appears similar to the Dektak profile of the spiral patterned upper electrode, which proves that the pattern on the upper electrode has been replicated to the polymer by the electric field force. The shape of the structure needs further work, but the basic principle has been demonstrated satisfactorily here.
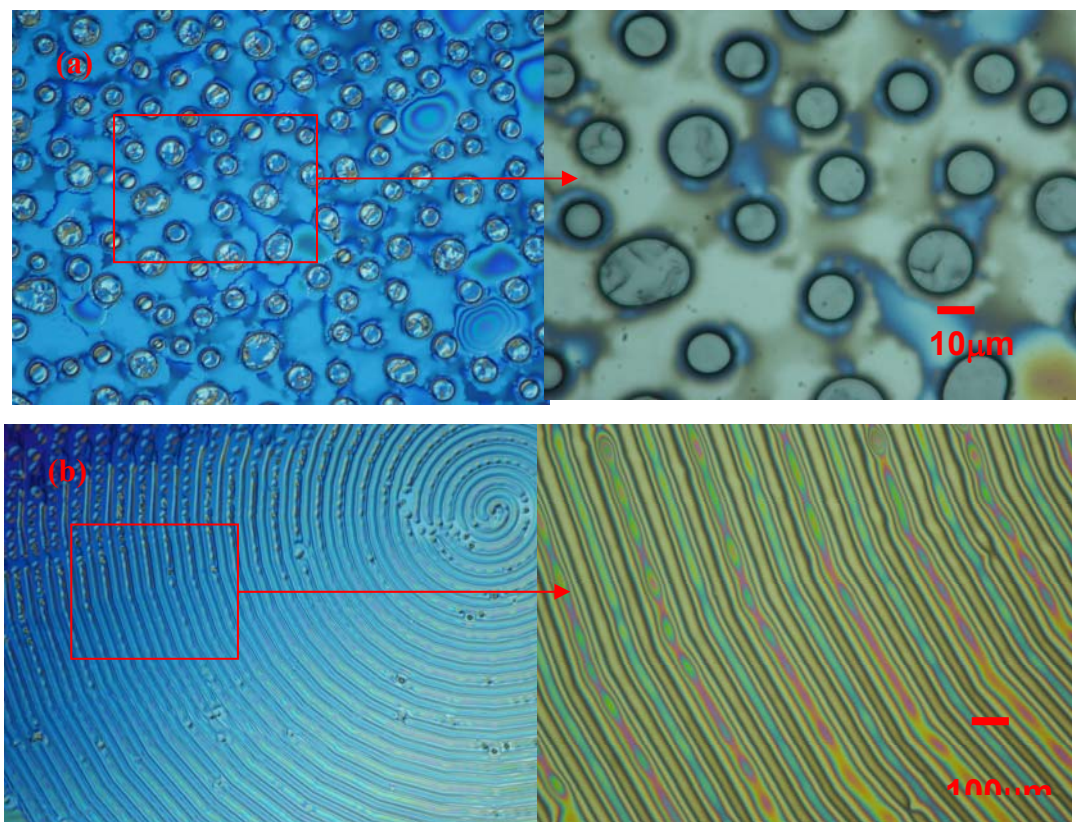
Figure 2.23 Optical micrographs of microstructures formed from (a) the unpatterned and (b) the patterned upper electrode.
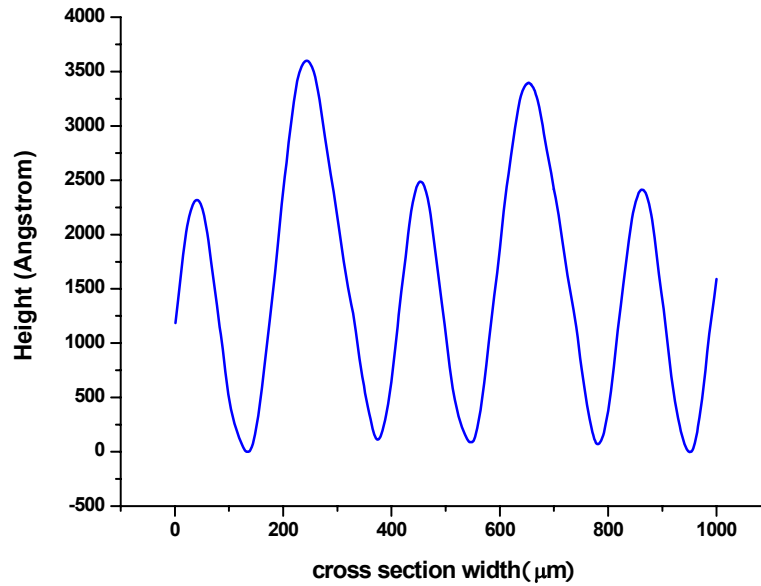
Figure 2.24 Stylus profilometry (Dektak) of the microstructures formed by the patterned upper electrode.

2.3.2 Bottom-up curing through an aperture

Another novel method of patterning photo-curable polymer is directly using an aperture mask. This was undertaken partly with the idea of lab-on-chip bio- and chemical sensing applications of the GaN micro-LEDs, with each LED pixel aligned to a polymer microstructure. The prepolymerised CHDG/TMTG blend polymers could thus be applied, for example, to attach bio-molecules on their surface for analytical utilisation. To achieve this high surface functionality, the prepolymerised CHDG/TMTG blend polymers can be cured to form structures from the bottom through apertures under UV illumination. The bottom of the polymer layer would then be fully cured but that part doses to the surface would not. The subsequent washing-off step removes the uncured excess materials, thus leaving a gelled but still highly functional surface.

Figure 2.25 shows the layout of the experiment. The process is as follows: the polymer film is laid down on top of a quartz or a UV transparent glass substrate

which is then placed on top of the aperture mask. The aperture mask is made by a piece of quartz cover-slip with a patterned titanium layer which blocks the UV light in un-patterned areas. A polymer covered quartz substrate is placed on the titanium face of the mask and then UV light is shone from the other side of the aperture mask. Hence, the photo-curable polymer in the patterned area will be fully cured by the UV light through the aperture. After this exposure step, the substrate is washed by acetonitrile and then dried in a stream of air. The cured polymer with a pattern from the aperture mask stays on the substrate while the uncured material is washed off.
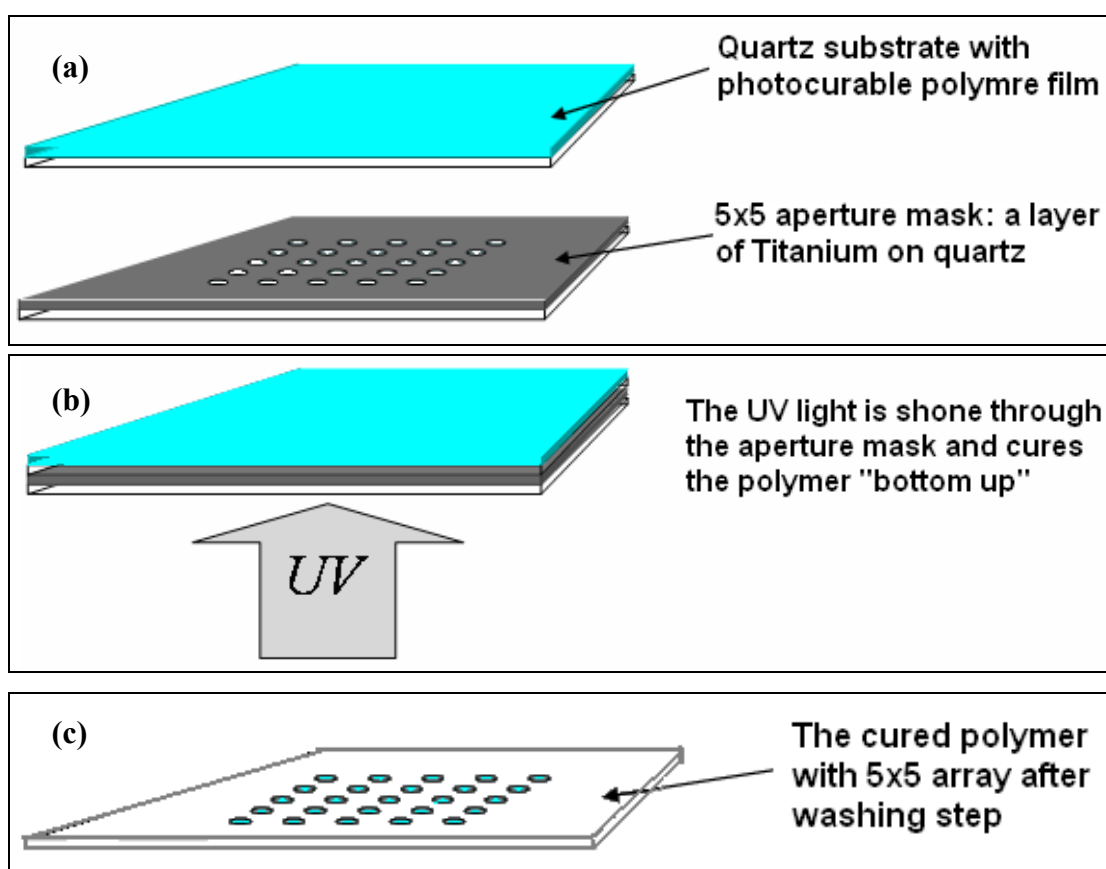

Figure 2.25 The layout of the "bottom up" UV curing technique: (a) quartz substrate with polymer film and aperture mask were prepared first; (b) the quartz substrate was placed on top of the aperture mask and the UV light was shone through the aperture; (c) the aperture mask was removed and the uncured polymer was washed away, leaving a 5×5 array of cured polymer dots on quartz substrate.

2.3.2.1 Aperture mask fabrication

The fabrication process of the aperture mask is quite significant to the "bottom up" curing experiment as it determines whether the polymer pattern is good or not. The etching step is the key to the final shaping. A short description of the process is as below:

- Clean the quartz substrate

- Sputter a layer of Titanium

- Spin a layer of photoresist

- Pattern the layer with photolithography into an aperture array

- Wet-etch the Titanium layer while the photoresist is used as a mask

- Strip the photoresist

The quartz substrate was first cleaned by Piranha solution (H_2SO_4:H_2O_2 = 4:1), and afterwards by acetone, methanol and deionised water. The titanium layer is 200nm thick and was etched by the solvent Buffered Oxide Etchant (BOE). It is found that the wet-etching is suitable for the patterns on a large scale (above 100μm). Actually it still works during the small scale etching, but the final diameter after etching is not equal to that of the mask, and is usually larger than it, which is due to the increasing etching time with decreasing pattern diameter. Stripping the photoresist is a necessary step to reveal the final shape of the pattern on the titanium layer, and acetone is used for stripping. Figure 2.26 shows aperture masks with different diameters after striping the photoresist.

Figure 2.26 Aperture masks with different diameters after striping the photoresist: (a) 8μm; (b) 14μm; (c) 18μm.

2.3.2.2 Applications of polymer shaping by aperture masks

The "bottom up" UV curing through an aperture mask can achieve a high surface functionality of the prepolymerised CHDG/TMTG system. The materials sitting nearest to the substrate is fully cured, while that further away from the substrate and UV light source is not fully cured up to the surface which means there are still unreacted epoxy groups left on the surface. Meanwhile, the bottom of the structures adheres well to the substrate. The UV exposure time for curing the polymers is kept less than 7min when 1wt% TAS-SbF6 PAGs is used. The residual epoxy group could react with the amine functionalized oligonucleotides (supplied by Prof. Duncan Graham group at the University of Strathclyde). These oligonucleotides are single-stranded DNA base sequences used in DNA microarrays. The fluorescent labels used to verify the attachment of such oligonucleotides are spotted to the polymeric structures from an aqueous solution. Figure 2.27 shows the polymer spots array formed by the "bottom up" UV curing from the 50μm aperture mask of a 5×5 array. The images were taken from the same spots array under different colour of the background. Figure 2.28 is a schematic view of the oligonucleotide attachment.
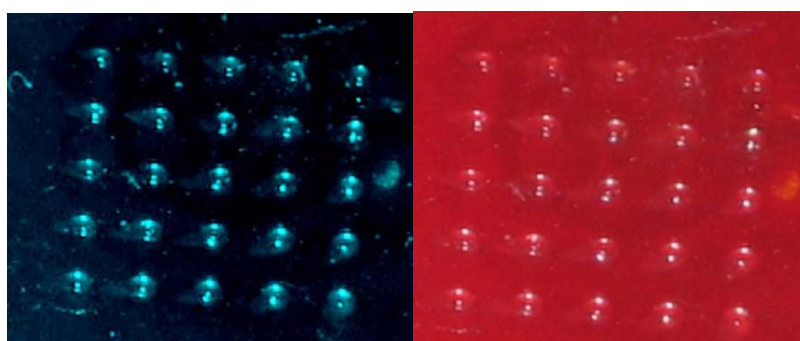
Figure 2.27 The polymer spots array formed by the "bottom up" UV curing.

After the unreacted oligonucleotides are washed off by deionised water, the sample is dried and inspected under a confocal fluorescence microscope. The images (Figure 2.29) show the green-blue fluorescence from the label only appears at the

surface of the structure, which proves the amine functionalized oligonucleotides are attached only on the surface without diffusion into the structure. Figure 2.29 presents the fluorescence images taken with the in-focus plane slices through the polymeric structure from bottom to top.
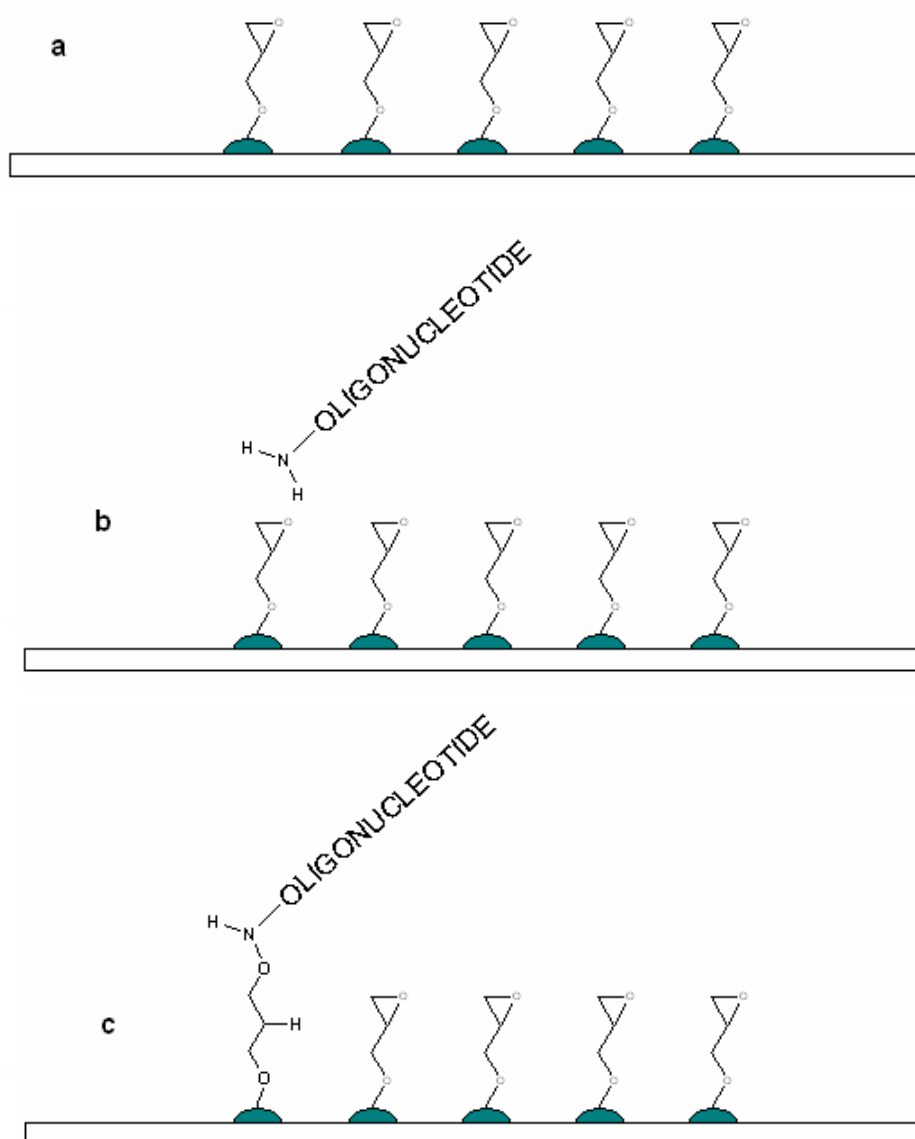
Figure 2.28 Schematic view of the oligonucleotide attachment to the structures shown above: (a) side view of 5×5 structure with epoxy functionality on surface; (b) amine modified oligonucleotide attached to the surface; (c) surface bound oligonucleotide.
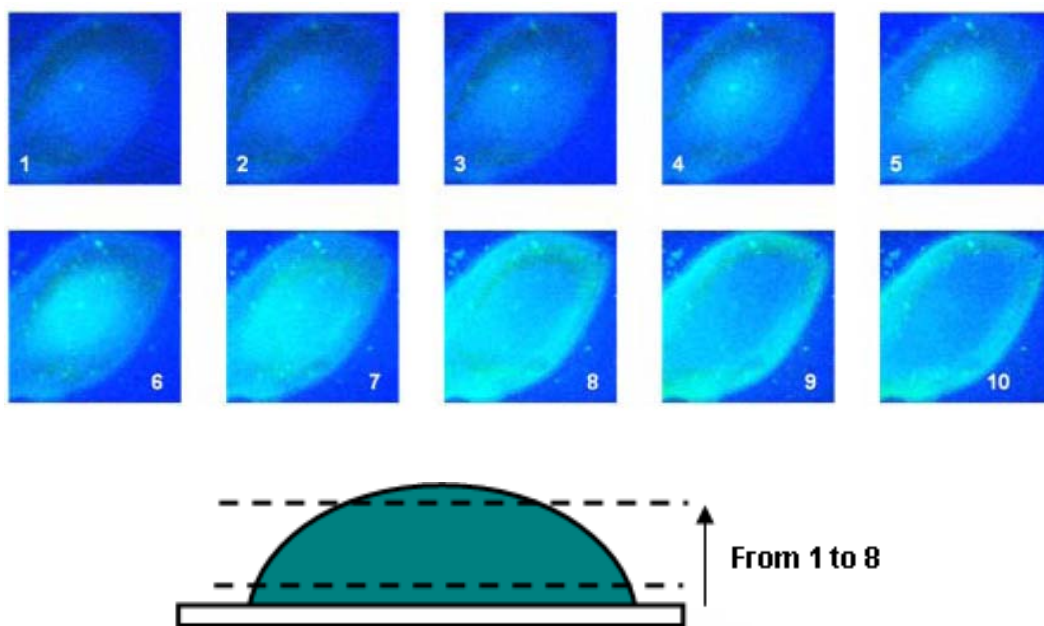
Figure 2.29 Confocal fluorescence images of a polymeric structure with the oligonucleotides attached. Images 1-8 show successive in-focus plane slices through the domed polymeric structure.

By blending the organic light-emitting polymer with the CHDV system, photo-luminescent structures can also be produced using patterned UV exposure techniques (e.g. standard photolithography or UV direct writing).

Shaping this blend polymer by "bottom up" UV curing through the aperture mask is almost the same process as described before: laying down a droplet of the blend polymer onto a cover-slip, putting it on the mask, switching on the UV lamp till the formation of the pattern in the droplet becomes visible, and then washing off finally.

PFO, F8BT and PolyDPP have been adopted as the guest material for blue, green and red emission in the CHDV hosted blend system respectively. Figure 2.30 shows the pictures of blue, green and red light emitting polymers blended with the CHDV matrix patterning by "bottom up" UV curing through the 100μm aperture mask under UV (368nm) illumination.
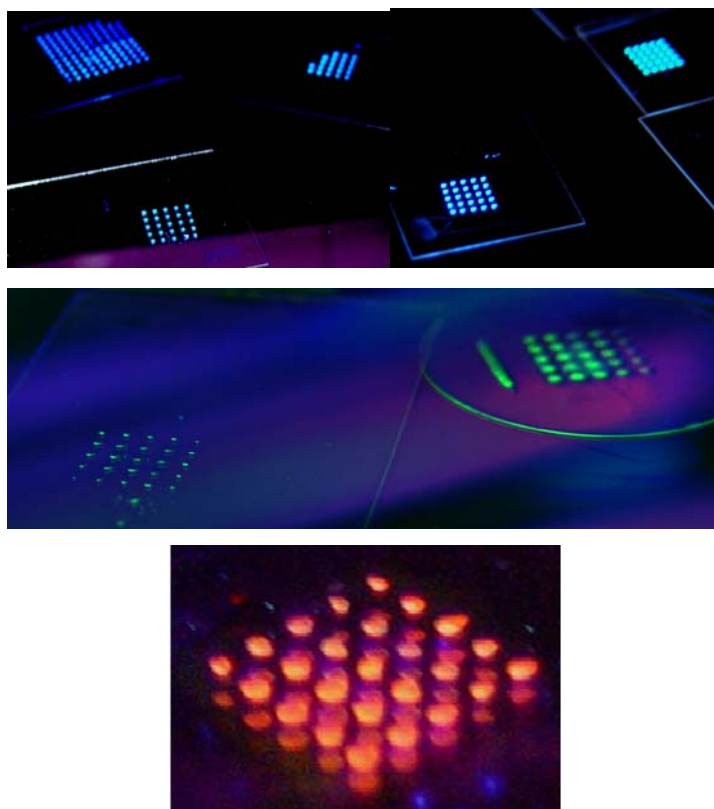
Figure 2.30 Images of organic luminescent blend polymers (PFO (top), F8BT (middle) and PolyDPP (bottom)) patterned by "bottom up" UV curing. The concentration is 0.1 wt% light emitting polymers in CHDV matrix.

2.5 Summary

In this chapter, the organic guest-host system of blending novel organic light emitting materials with novel deep UV transparent polymers was introduced. The novel deep UV transparent polymers which perform as the host materials were developed from the CHDG, TMTG and CHDV monomers with different PAGs to initiate the polymerisation. The transmission spectra of these polymers show ~80% transparency at deep UV wavelength range down to 225nm while ~80% transparency cuts off at 310nm for the commercial NOA63 polymers. These host polymers present good processability for not only standard photolithography procedures but also some novel patterning methods. The guest materials in the blend system are the novel truxene

oligofluorenes and crosslinkable polyfluorenes. Truxene oligofluorenes are blue-emitting and exhibit high fluorescence quantum yield and chemical stability. The emission spectrum shows the truxene oligofluorenes/CHDV blend has similar fluorescence properties to the neat materials, which the fluorescence lifetime measurements further show. The crosslinkable polyfluorenes are vinyl ether functionalized fluorene polymers emitting in the wavelength range from blue to red, and they all have similar absorption maxima at ~368nm. It is found from the PL spectrum that the fluorescence property of these neat materials is not altered after blending with the CHDV monomers. These deep UV transparent host polymers can maintain the photoluminescence of the neat light emitting organics and protect them from the diffusion of oxygen and moisture. The processability of the light emitting guest-host system is also improved.

The prepolymerised CHDG polymers have been patterned by electrohydrodynamic method. Polymeric pillars and spirals have been formed by overcoming the surface tension in the electric field. The theoretical background of the experiments has been introduced and experimental details have been described. In addition, a dot array of the CHDG polymers has been fabricated by the "bottom up" curing method for bio-analysis. An organic light emitting polymer/CHDV blend dot array has also been formed by the same method.

References

1. A.J.C. Kuehne, "UV transparent and light emitting photo-polymers for optoelectronic applications," PhD thesis (2008).

2. B. Guilhabert *et al*., "Patterning and integration of polyfluorene polymers on micropixellated UV AlInGaN light-emitting diodes," *J. Phys. D* **41**, 094008 (2007).

3. N. Laurand *et al*., "Tunable single-mode fibre-VCSEL using an intracavity polymer microlenses," *Opt. Lett.* **32**, 2831 (2007).

4. I. D. W. Samuel and G. A. Turnbull, "Polymer Lasers: Recent Advances," *Materials Today*, 28-35 (September, 2005).

5. X.H. Zhou *et al.*, "Synthesis and relationships between the structures and properties of monodisperse star-Shaped oligofluorenes," *Org. Lett.* **5**, 3542 (2003).

6. A.L. Kanibolotsky *et al*., "Synthesis and properties of monodisperse oligofluorene-functionalized truxenes: highly fluorescent star-shaped architectures," *J. Am. Chem. Soc*. **126**, 13695 (2004).

7. C. Xia *et al*., "Decreased aggregation phenomena in polyfluorenes by introducing carbazole copolymer units," *Macromolecules* **34**, 5854 (2001).

8. C.D. McGuiness *et al.*, "Selective excitation of tryptophan fluorescence decay in proteins using a subnanosecond 295 nm light-emitting diode and time-correlated single-photon counting," *Appl. Phys. Lett.* **86**, 261911 (2005).

9. D.J.S. Birch, R.E. Imhof: Topics in Fluorescence Spectroscopy vol 1: Techniques, (New York: Plenum 1991) **Ch. 1**.

10. R.F. Steiner: Topics in Fluorescence Spectroscopy vol 2: Principles, (New York: Plenum 1992) **Ch. 1**.

11. T. Nguyen *et al*., "Conjugated polymer aggregates in solution: control of interchain interactions," *J. Chem. Phys*. **110**, 4068 (1999)

12. A.J.C. Kuehne *et al.*, "Novel vinyl ether functionalized fluorene polymers for

active incorporation into common photoresist matrices," *Tetrahedron Lett*. **49**, 4722 (2008).

13. S.Y. Chou *et al.*, "Lithographically induced self-construction of polymer microstructures for resistless patterning," *Appl. Phys. Lett.* **75**, 1004 (1999).

14. E. Schaffer *et al.*, "Electrically induced structure formation and pattern transfer," *Nature* **403**, 874 (2000).

15. E. Schaffer *et al.*, "Electrohydrodynamic instabilities in polymer films," *Europhys. Lett.* **53**, 518 (2001).

16. Z. Lin *et al.*, "Electric field induced instabilities at liquid/liquid interface," *J. Chem. Phys.* **114**, 2377 (2001).

17. F.W. Sears. *University physics seventh editions* (Addison-wesley publication company, Canada, 1987).

18. N.E. Voicu *et al.*, "Electric-field-induced pattern morphologies in thin liquid films," *Adv. Funct. Mater.* **16**, 926 (2006).

19. L.D. Landau. *Electrodynamics of continuous media* (Pergamon, Oxford, 1984).

20. R. Verma *et al.*, "Electric field induced instability and pattern formation in thin films," *Langmuir* **21**, 3710 (2005).

21. L.F. Pease *et al.*, "Limitations on length scales for electrostatically induced submicrometre pillars and holes," *Langmuir* **20**, 795 (2004).

22. Z. Lin *et al.*, "Structure formation at the interface of liquid/liquid bilayer in electric field," *Macromolecules* **35**, 3971 (2002).

23. S. Herminghaus *et al.*, "Dynamical instability of thin liquid films between conducting media," *Phys. Rev. Lett*. **83**, 2359 (1999).

24. K.A. Leach *et al.*, "Early stage in the growth of electric field-induced surface fluctuations," *Macromolecules* **38**, 4868 (2005).

25. M.D. Dickey *et al.*, "Photocurable pillar arrays formed via electrohydrodynamic instabilities," *Chem. Mater.* **18**, 2043 (2006).

Chapter 3 Inkjet printing technology for hybrid integration

Inkjet printing is a very attractive technology for many applications involving functional polymers. In this chapter, we first give a general overview to describe the advantages of the inkjet printing technique. As the inkjet printer used in this work is a piezo-based drop-on-demand (DoD) printer, the working principle of this kind of system is then described. We also study the droplet formation, influenced by adjusting the printer parameters such as driving voltage on the nozzle, firing frequency and pulse length of the jetting waveform. Functional microstructures of different materials such as organic light emitting materials blends and metallic nanoparticles etc. have been fabricated by this inkjet printing technique and the properties of these structures have also been studied.

3.1 Introduction

The past decade has witnessed the emergence of broad applications for inkjet printing technology including in light emitting displays, organic electronics, tissue engineering and nanotechnology. Inkjet printing is a patterning method which breaks up a solution into droplets and delivers picolitre volumes of these materials onto a substrate. The inkjet printing system is usually composed of ink-dispensers and a PC-controlled translation stage and monitoring system, which are readily prepared for complex pattern fabrication. Generally speaking, the key process of the

conventional photolithographic technique is "etch-down" by a plasma or chemical solution. However, during the inkjet printing, "add-on" and "direct-write" are the main methods for pattern formation. These latter methods avoid the need of masks, which results in low-cost, efficient use of materials and elimination of contamination.

Combinatorial polymer research offers new application opportunities for inkjet printing, as a bottleneck is presented in the preparation of polymer micro-patterns due to the rapid progress on synthesising large numbers of chemically different polymers. A variety of functional polymers have been patterned successfully by inkjet printing, such as polythiophenes [1], polyfluorenes [2], polyphenylenevinylenes derivatives [3] and metal-containing polymers [4]. Moreover, patterns of quantum dots [5], metallic nanoparticles [6], carbon nanotubes [7], DNA [8] and proteins [9] have also been fabricated by inkjet printing. Furthermore, a process named reactive inkjet printing [10] permits increased versatility by reaction of chemical agents on surfaces.

A few highlights of patterning functional materials by the inkjet printing technique are given below. Firstly, we consider fabrication of organic electronic device such as film effect transistors (FETs), a crucial part of which involves inkjet printing. In most cases, a water based ink of poly(3,4-ethylenedioxythiophene): poly(styrenesulfonate) (PEDOT:PSS) is inkjet deposited as the gate, source and drain electrodes of polymer FETs. The feature size of the electrodes is usually critical to the device performance, as smaller distance between source and drain electrodes results in higher current output and faster transistor switching speed. Moreover, comparatively high drop accuracy is required as, for instance, there are approximately a million transistors in an active matrix polymer display and a single error would cause an electrically-short and ruin the whole device. Therefore, lithographic methods are used to assist inkjet printing in meeting the challenges of spatial resolution and drop accuracy. Both photolithography and soft lithography have been explored in this combined method. Sirringhaus et al. have used the optical

lithography method to predefine the substrate with different surface-energy patterns which controls the flow and spreading width of the inkjet printed droplet [11]. A 5 μm or less channel length between source and drain electrodes has been achieved by this technique, and channel length as narrow as 250nm could be obtained if the surface energy pattern was defined by electron beam lithography. Wang et al. showed a similar approach with nanoimprint lithography [12]. Trenches of the hydrophobic insulating polymer polymethylmethancrylate (PMMA) were fabricated by silicon stamping, oxygen plasma treatment and subsequent heating process. These trenches were afterwards filled with PEDOT:PSS solution by inkjet printing to form source and drain electrodes. The channel length was around 250~300nm in this case.
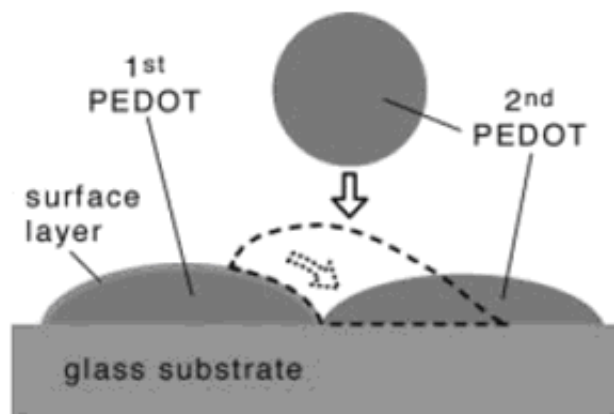
Figure 3.1 Schematic representation of the self-aligned printing process developed by Sirringhaus et al. A second printed droplet of PEDOT:PSS dewets from the hydrophobic surface of the first printed droplet. After [11]

To achieve even lower cost of fabrication, sole use of inkjet printing as the patterning tool must be accomplished. Sirringhaus et al. have shown the capability of defining sub-100nm channel length by a lithography-free inkjet printing technique [13]. By selective modification on the surface of the first conductive pattern, a partially overlapped second printed pattern is repelled and dries to the edge of the first pattern due to the lower surface energy (see Figure 3.1). The surface

modification was carried out by either adding surfactant in the ink or by post plasma treatment. It was observed that the "ON" current and switching speed were increased by over two orders of magnitude because of the resulting narrower channel length [13].

The first demonstration of electrical greyscale imaging capability by inkjet printing was presented by Jabbour *et al.* (see Figure 3.2) [14]. They dispensed a hydrogen peroxide based ink to alter the conductivity of a PEDOT:PSS anode by varying the oxidation state of PEDOT:PSS, which reduced the processing steps compared to the conventional technique.
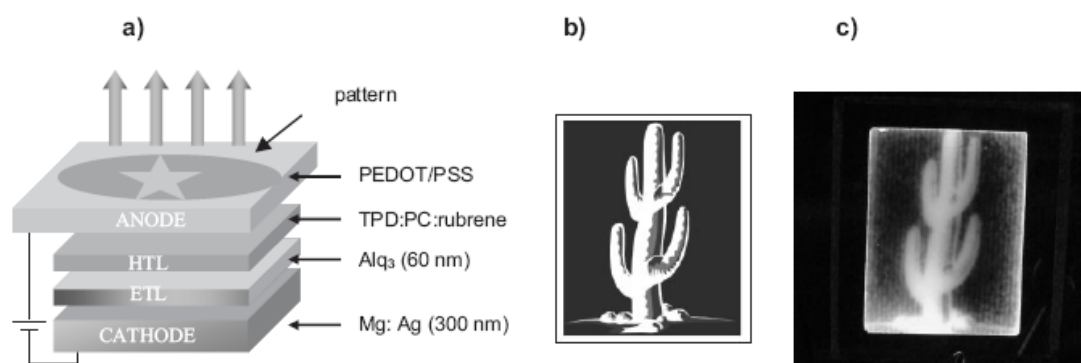

Figure 3.2 a) Architecture of an OLED where the PEDOT:PSS is patterned by inkjet printing. b) Cactus logo designed using the software package and c) corresponding OLED image. Device dimensions: 1.3 in. (length) × 1.5 in. (width). TPD: N′,N′-bis(3-methylphenyl)-N′,N′-diphenyl benzidine; PC: polycarbonate; Alq3: tris(8-hydroxyquinoline)aluminium. After [14]

Applications in biotechnology represents another wide area for inkjet printing, such as generating DNA arrays [8] and protein bio chips [9]. In biotechnology, the printing conditions need optimisation for each individual system as heat or shear stress can potentially damage the materials. Three dimension printing (3DP) has been utilised in a wide variety of biomaterials and can reduce the number of the post-processing steps and control the spatial distribution of the materials composition and microstructures by modifying the printing parameters [15]. The 3DP refers to an additive technology creating a three dimensional object by successive layers. Direct 3DP was used to fabricate tissue scaffolds, which however restricted the range of the

pore size and shape to some degree [16, 17]. In order to overcome this limitation from direct 3DP, Wu et al. introduced an indirect 3DP technique which demonstrated the scaffolds with features of diameter of 500μm and a height of 1mm [15]. The miniaturisation of bioanalytical processes enables tool development for application to clinical diagnosis. Biochips fabricated by inkjet printing can consist of thousands of different bio-molecules used to detect specific analytes from complex biological samples such as blood and urine, enabling highly parallel analysis. Figure 3.3 shows a typical protein bio-chip process. The existing inkjet printing technology can dispense droplets from 10nl to 10μl dynamically or even femtolitre volume, and transfer 1200 solutions simultaneously [9].
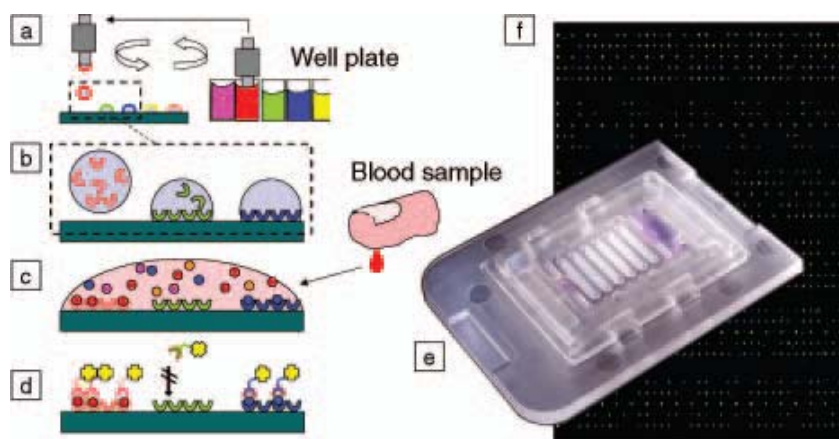

Figure 3.3 Biochip basics: (a) arraying of capture probes onto the biochip surface by, for example, drop-on-demand (DOD) print heads or pin arrays; (b) immobilization of the capture probes onto the chip; (c) incubation of a biological sample on the finished biochip and binding of analytes to the specific capture probes; (d) fluorescent detection probes quantify bound analytes. (e) Photograph of a Zyomyx protein biochip inside a fluidic cassette; chip dimensions are 15 mm×25 mm. (f) after laser scanning, fluorescent spots indicate specific analyte binding events on the biochip. After [9].

Inkjet printing can form microstructures not only from a single material but also deposition for reactants [10] or etching agents [18]. For instance, Kilbey's group used inkjet printing to anchor the polymerization initiator onto a gold-coated substrate and then grow polymer brushes through atom-transfer radical polymerization (ATRP) [10].

Inkjet printing has also been used as a tool for etching coated substrate to create polymer microstructures e.g. by Schubert et al. [18]. Solvent droplets deposited on the spin-coated surface dissolved the polymer underneath to gradually form holes during the solvent evaporation. Figure 3.4 shows how the hole-structure could be varied from simple holes to honeycomb-like and grid-like structures by changing the solvent, the deposition pattern and the underlying polymer layer [18].
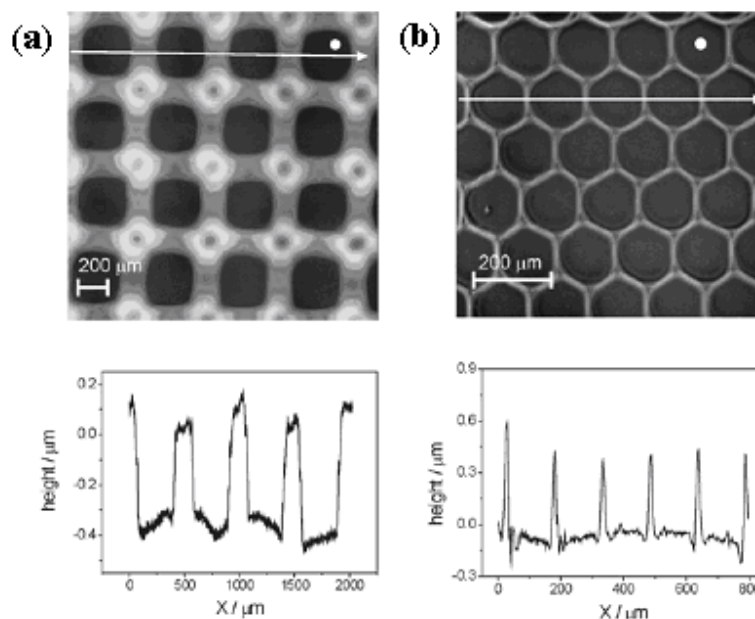
Figure 3.4 a) Rectangular holes etched in polystyrene by printing a rectangular array of 70μm acetophenone droplets (shown to scale as the white circle in the upper right). From top to bottom: height map and profile. b) Hexagonal holes etched by a printing hexagonal array of 30μm isopropyl acetate droplets. After [18].

3.1.1 Instrumentation

Generally speaking, the inkjet printing technique may be divided into two categories: continuous inkjet and drop-on-demand inkjet, as described below.

The principal mechanism of the continuous inkjet printing process was developed in the early 1960s. In such a system, a fluid reservoir is highly pressurised through the small orifice of the drop generator. A stream of ink is continuously broken up into uniform droplet with similar size to the ejection aperture. These drops

are formed by a mechanical oscillation within the nozzle cavity and the stream of droplets then passes through an electrostatic field with two high voltage deflection plates. When the electric charge deflects the droplet individually from the stream into a gutter or directly to the substrate, it is called a binary-deflection inkjet; when multiple droplets are deflected to the desired location on the substrate, it is called a multiple deflection inkjet (Figure 3.5) [19].
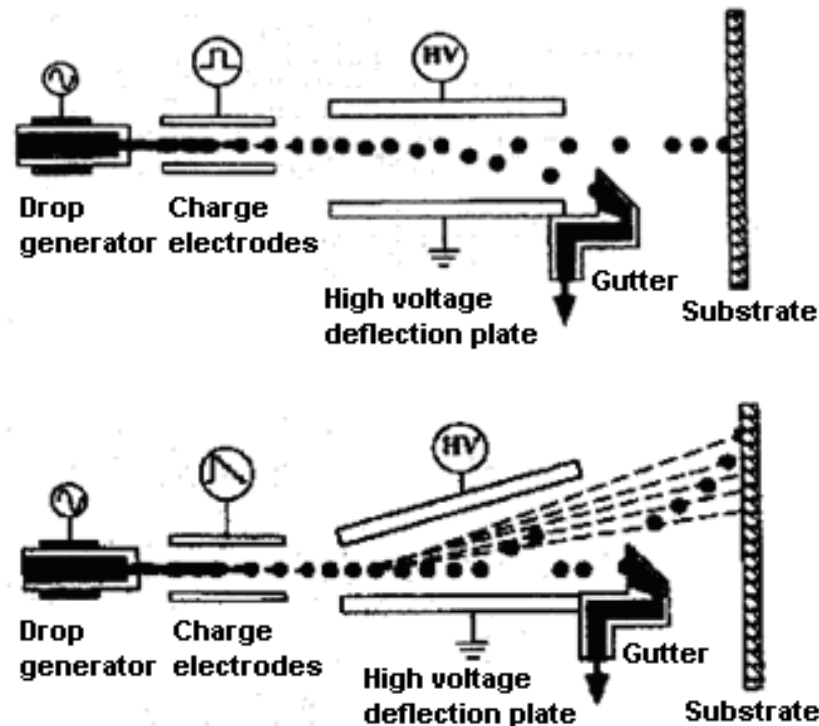
Figure 3.5 Schematic images of the continuous inkjet system: binary-deflection (top) and multiple-deflection (bottom). After [19].

Continuous inkjet printing is mainly applied in industrial applications including product labelling, coding and marking due to its fast printing speed. However, the drop-on-demand inkjet is superior in the majority of printing work today because of its smaller droplet dispensing, having fewer limitations on the properties of ink and higher printing accuracy and resolution [20]. The drop-on-demand inkjet is composed by a nozzle dispensing fluid and an actuator giving impulses to the fluid. The driving methods of the impulse are either thermal or piezo-electrical. In the

piezo-electrically driven inkjet, droplets are generated by a pressure wave from the piezocrystal deformation after applying a voltage. In the thermal inkjet, a small bubble is formed by heat transfer from a heated plate, acting like a pressure generator, which then forces the ink out of the nozzle. The bubble collapses until the heat is fully dispensed and the chamber is refilled by capillary action. Figure 3.6 shows the drop formation mechanism during the thermal inkjet process [21].
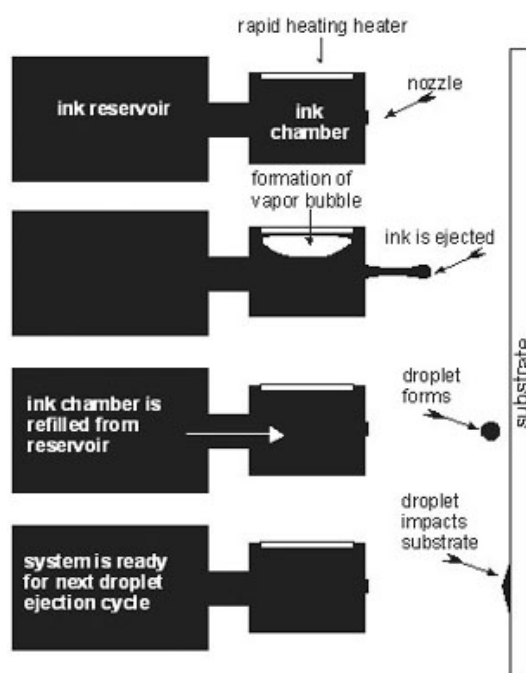
Figure 3.6 The mechanism of drop formation in thermal inkjet system. After [21].

Though desktop inkjet printers are affordable, there are a number of disadvantages such as restrictions on organic solvents from using plastic cartridges and printheads, difficulties on monitoring droplet formation and deposition, and limitations on substrates for polymer microarrays [20]. Selected inkjet printers for producing functional polymer microstructures are shown in Table 3.1, and drop placement accuracy, frequency (droplet number jetted per nozzle per second), number of nozzles and drop volume are respectively compared [22].

Table 3.1 Overview of selected inkjet printers for functional printing

Apparatus	Workspace (mm × mm ×mm)	Drop placement accuracy (µm)	Drop volume (pL)	Number of parallel nozzles	Frequency (kHz)	Heating (°C)
MicroDrop Autodrop	200 × 200 × 80	10 ± 2	30-500	1-8	2	160
Microfab Jetlab-II	150 × 150 × 25	10 ± 5	20-1000	1-16	20	220
Litrex 70	200 × 200 × 1.2	± 20	30	128	40	70
Litrex 142	370 × 470 × 1.2	<15	10	128	10	70
GeSiM Nanoplotter	260 × 270 × 43	25 ± 5	100-2000	1-8	1	-
Perkin-Elmer BioChip	1450 × 980 × 890	20 ± 2	325	4	0.5	-
Dimatix DMP-2800	200 × 300 × 50	± 25	1-10	16	20	60

The work described in this thesis uses the FUJIFILM Dimatix Materials Printer (DMP). The DMP-2800 (Figure 3.7) is a cost-effective, easy-to-use precision materials deposition system, which allows the deposition of fluidic materials on an 8×11 inch or A4 substrate of any pattern at a 5 - 254µm dot pitch (100 - 5080 dpi), utilising a disposable piezo ink jet cartridge. The printer can handle either rigid or flexible substrates up to 25mm thick with the adjustable height control. The vacuum platen which secures the substrate in place could be heated up to 60°C while the nozzles in the cartridge may reach up to 70°C. The DMP also offers a variety of fully editable pattern templates including dots, lines, hatch etc. and accepts optional Gerber file imports. The convenient PC-controlled operation facilitates the user to edit the pattern, the piezo drive waveform, the cleaning cycle, the cartridge setting and the substrate setting to optimise process parameters for the user's applications. The built-in drop-watch camera allows direct observation of the actual jetting of the fluid and changes in jetting characteristics after modifying the drive waveform

through the cartridge setting editor at the mean time. Additionally, a further built-in camera in the system, the fiducial camera, allows positioning of the print origin to match substrate placement, matching the drop placement to a previously patterned substrate and providing substrate rotation alignment using reference marks. It permits measurement of features and locations, inspection and image capture of printed patterns or drops, and cartridge alignment when using multiple cartridges.
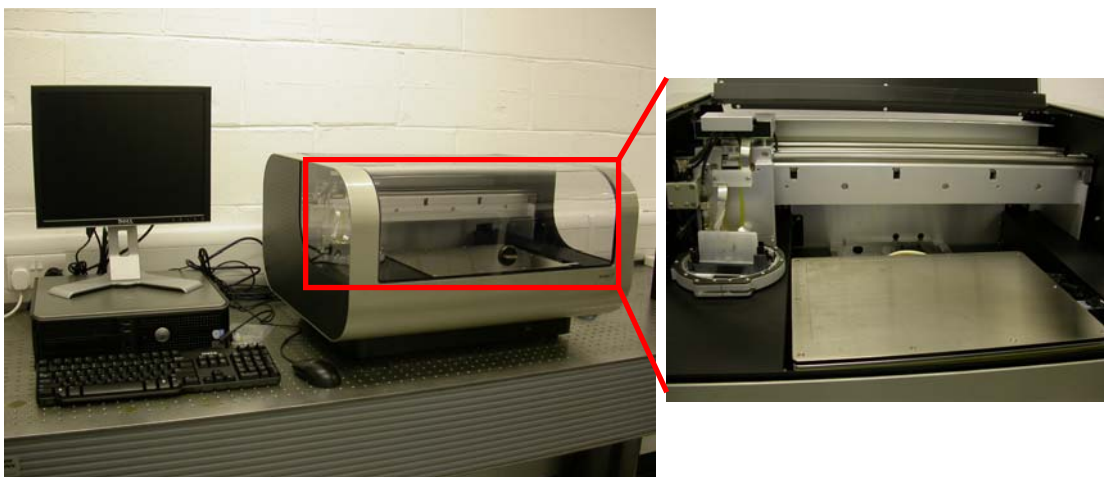

Figure 3.7 Image of the DMP-2800 printer in our lab

The FUJIFILM Dimatix has a MEMS-based cartridge-style printhead that allows users to fill their own fluids and print immediately. The snap-in cartridge has a reservoir of 1.5ml which reduces fluid waste and it is compatible with a wide variety of fluids including aqueous and solvent-based fluids, solutions and particle suspensions (Figure 3.8). According to the manufacturer's specifications, the jettable fluid for the system should have a viscosity between 2~30cP and a surface tension between 0.028 - 0.033N/m at the operating temperature. Each user-fillable cartridge has 16 silicon nozzles linearly spaced by 254 microns with typical drop sizes of 1 and 10 picolitres, while manufacturer's specifications indicate that the drop size repeatability is within 3.5% untuned and about 0.5% tuned. The typical size of the nozzle delivering 1 and 10 picolitre drop is 9μm and 21.5μm respectively. Cartridges

can be refilled with the same fluid and replaced to facilitate printing of a series of fluids.

Figure 3.8 Image of the cartridge for DMP-2800 printer

3.1.2 Physical aspects of inkjet printing

For all the applications of inkjet printing, it is essential to study how the fluid properties and printing parameters affect the deposition performance. The detailed working principle of the piezo-electrically driven printer used in this study (DMP-2800) is presented below, showing each segment of the driven waveform [23].

At the standby position of the piezo, the fluid chamber is slightly depressed (Figure 3.9 (a)). When the firing pulse decreases the voltage to zero, it brings the piezo back to a neutral straight (or relaxed) position with the chamber at its maximum volume. In this phase the fluid is drawn into the chamber through the inlet and it also pulls on the meniscus at the nozzle, as shown in Figure 3.9 (b). The next phase of the pulse is the main drop ejection phase where the chamber is compressed and pressure generated to eject a drop (Figure 3.9 (c)). The final phase is the

recovery phase where the piezo voltage is brought back down (phase 3) and the chamber decompresses partially refilling in preparation for the next pulse (phase 4). There is also a pull back on the ejected drop and the nozzle meniscus at this point (Figure 3.9 (d)).
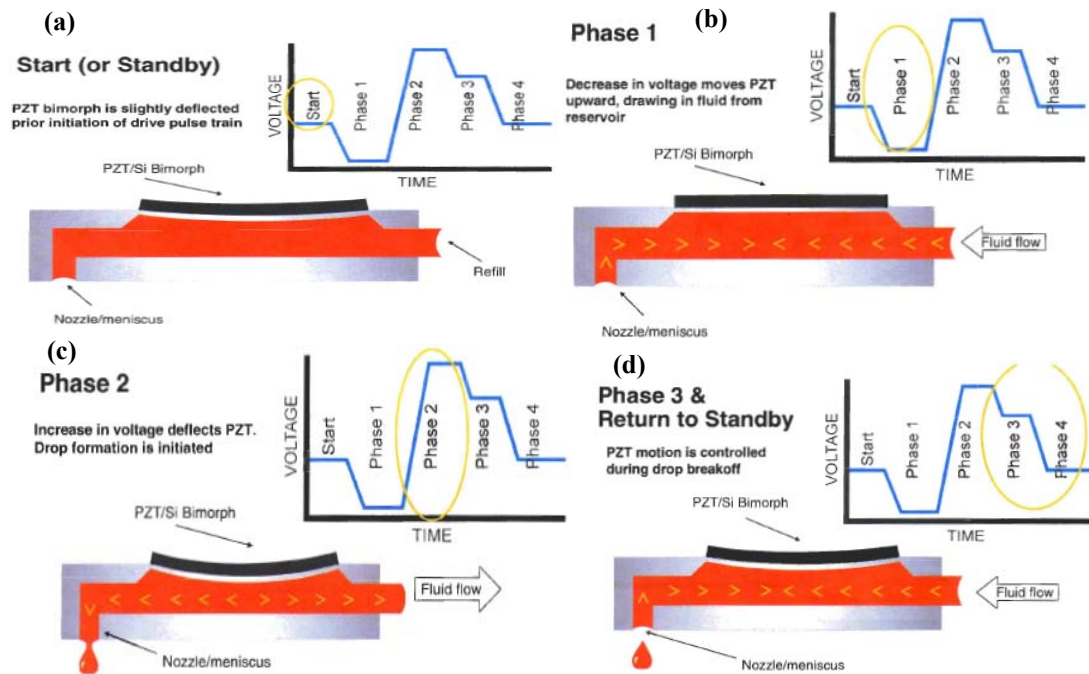

Figure 3.9 The mechanism and corresponding waveform segment of the piezo-driven Dimatix Materials Printer. After [23].

3.1.2.1 Influence on droplet formation

The typical drop formation in this printer (DMP-2800) is shown in the series of representative images from our system shown in Figure 3.10. The evolution of the drop formation (c.f. also Figure 3.9) may be described as follows. First, a pressure wave is applied on the liquid in the nozzle resulting in the ejection of the liquid. Initially, the meniscus extends quickly outward until a liquid column with a round leading edge is formed (images 1-5 in Figure 3.10). After a short time, the liquid column begins to stretch due to the velocity difference between the column head and the liquid at the nozzle exit. The speed of the liquid at the nozzle exit falls until no

more fluid flows into the column and the decrease of the voltage in phase 3 of the waveform in the DMP printer even results in sucking some liquid back. During the stretching, the liquid at the nozzle exit forms a neck and the radius of the liquid thread keeps thinning until it pinches off at the nozzle with a tail (images 6-13 in Figure 3.10). A second neck also begins to appear toward the head of the column. Because of the small radius of curvature, the pressure is high in the tail tip at the pinch-off point. The surface of liquid contracts to reduce the surface energy and the second neck continues to evolve until the liquid thread breaks up to a primary drop and a secondary unsymmetrical thread. The secondary thread continues contraction and form a satellite drop (images 19-22 in Figure 3.10). Recombination of the primary drop and satellite may occur depending on the size and velocity (images 23-27 in Figure 3.10). The accuracy of the materials deposition would be affected if the satellite drop and the primary drop do not merge. Therefore, it is very important to eliminate the satellites in fabricating functional structures.
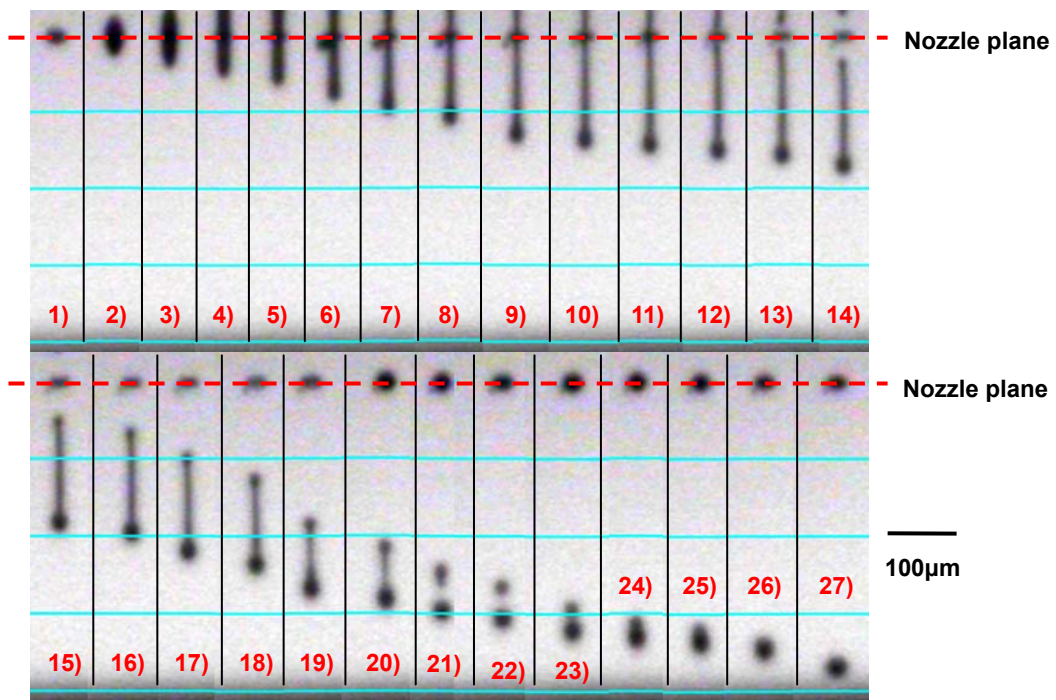

Figure 3.10 Sequence of images of drop formation for the single-pulse waveform of the DMP printer at 16V, 5kHz frequency and 11.520μs pulse length.

The waveform of this printer is single-peaked. The respective performance of the single-peak and the double-peak waveform has been described previously [24, 25]. In the single-peak waveform, the fall time of the pulse is longer through two steps (phase 3 and 4 - see Figure 3.9). The voltage falling with a certain time duration in the phase 3 produces suction within the nozzle, promoting the stretching and necking of the liquid thread. However, the pinch-off of liquid is more influenced by the nozzle plate and becomes less uniform in the single-peak waveform. The key challenge is that it is difficult for the satellite drop to merge with the primary drop in the single-peak case. Regardless of the fluid properties, previous experiments by Dong *et al.* show that the pulse length will affect the velocity of the fluid and recombination of the primary drop and satellite [25]. Therefore, optimisation of the drop formation is crucial for this printer.

For the cartridge delivering ~10pl droplets, the printer presents best performance according to the manual when the drop velocity reaches ~8m/s. Hence, we adjust the applied voltage to get a stable ejection of the drop as the starting point of optimisation and then adjust the pulse length to obtain the maximum velocity. Once the peak velocity is obtained, the fluid is matched to the acoustics of the pumping chamber. Then optimization on drop formation can be carried out if necessary by adjusting the waveform segment.

CHDV polymers with 0.2 wt% PAG were used as the model material for the optimization. This material will serve as the matrix for the light emitting materials in later study and this optimisation provides reference parameters in the subsequent patterning work afterwards. The cartridge ejecting ~10pl droplets was used in the optimization study. It was observed that the ejection of the CHDV droplet was stable around 16V voltage. The adjustment in frequency shows the drop velocity is not much altered by the frequency (Figure 3.11) when the voltage and total pulse length is kept constant at 16.5V and 11.520μs respectively. The pulse length was then adjusted when the voltage and frequency were 16.5V and 5 kHz respectively. The

velocity of the droplet versus the pulse length is plotted in Figure 3.12. The peak velocity appears when the pulse length is ~14.080μs. Figure 3.13 shows the plot of applied voltage versus the drop velocity when the pulse length and frequency are 14.080μs and 5 kHz, respectively. It is obvious that the higher the voltage applied, the faster the droplet flies. However, it is observed that the tail after the head of the liquid thread becomes longer under higher applied voltage and it is then much more difficult for the satellite to recombine with the primary drop. Hence, the optimum parameters for printing performance are achieved from the coordination between the droplet velocity and the formation. The maximum voltage the printer can reach is 40V with an increasing step of 0.1V. The frequency can be adjusted from 1kHz to 5kHz. The pulse length is controlled by a duration scaler to go up and down (1.1-0.9). From the above, the optimized parameters for the CHDV polymers are ~17.8V for the applied voltage, 5 kHz for the frequency and 14.080μs for the pulse length.
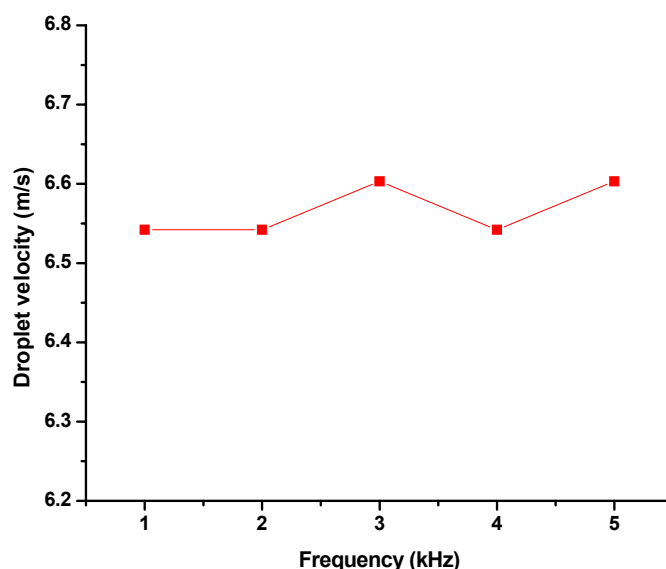

Figure 3.11 Plotting of the frequency versus the CHDV droplet velocity. Voltage and pulse length were held constant at 16.5V and 11.520μs.
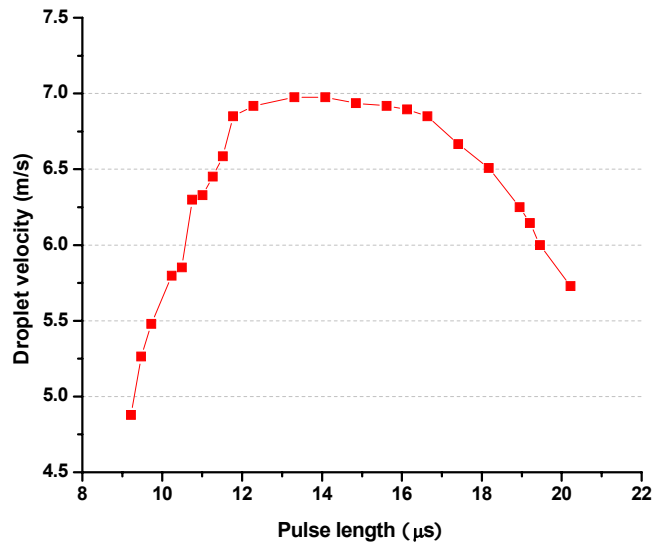
Figure 3.12 Plotting of the pulse length versus the CHDV droplet velocity. Voltage and frequency were 16.5V and 5kHz, respectively.
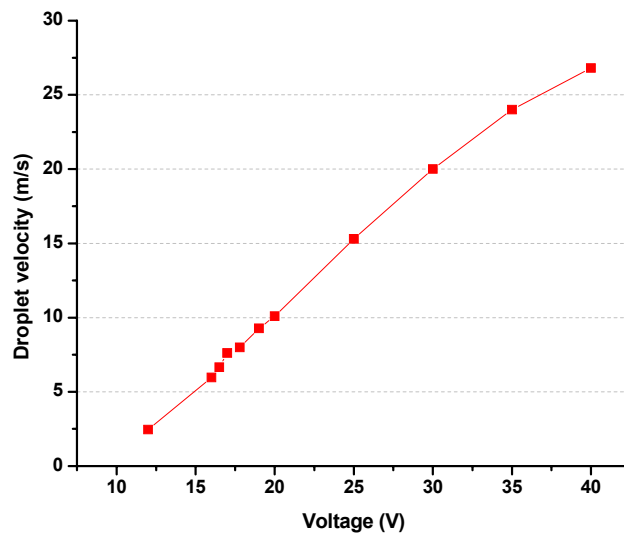
Figure 3.13 Plotting of the applied voltage versus the CHDV droplet velocity. Pulse length and frequency were 14.080μs and 5kHz, respectively.

Fluid properties including the viscosity, surface tension, density and volatility are also the major element affecting the droplet formation. High volatility will cause the polymer crust formation and ultimately clog the nozzle. Therefore, a boiling point higher than 100℃ is preferred for this printer. Numerical simulations [26-28] have

been carried out to predict the pinch-off process of the liquid thread, based on the fluid properties and thread diameter. For this specific printer, the optimum fluid properties are ~10-12cP for viscosity and ~28-33mN/m for surface tension. Density greater than 1g/cm^3 is also beneficial. Combinatorial adjustments on printing parameters and fluid properties would promote the optimisation of the droplet formation.

3.1.2.2 Challenges for printing polymer solutions

There are some major challenges in printing polymer solutions other than the printing parameters, such as the solvents in the solution and the droplet behaviour on the substrate. Polymer solutions usually contain solvents and appropriate combinations of the solvents and substrates are crucial to obtain homogeneous inkjet printed films. There is a well-known phenomenon observed in the inkjet printed features, which is called the "coffee-ring" effect as the residue of dried (liquid) coffee has a ring-like shape with dark perimeter. This ring-like stain is general to many solvents. After the evaporation of the printed solvent droplet, the solution is deposited with a ring marking the original contact line. Explanations for the cause of this phenomenon have been debated. Deegan *et al.* [29, 30] give a theory that when the contact line is pinned an outward flow is created in a drying droplet as the increased evaporation from the edge of the drop needs to be compensated by a flow from the interior. Sommer *et al.* [31] suggest the ring shape formation is independent of the pinned contact line, Hu *et al.* [32] point out that the pinned contact line is not the only requirement for the ring effect phenomenon and the suppression of the Marangoni flow (mass transfer along the interface due to the surface tension gradient) resulting from the latent heat of evaporation is also needed. Although the debate continues, this ring effect has been prevented by mixing a low and a high boiling point solvent in a certain ratio [5, 33]. In this work, the polymer solutions are

prepared either without any solvent or by vacuuming the solvent out to prevent the subsequent features from the ring effect.

The interaction between the fluid droplets with a substrate is also important when determining the dimension of the deposits. Some researchers have studied the physical behaviour of spreading and drying of the droplets on the substrates and created models to predict the final dimension of the deposits [34, 35]. The final dimension depends most on the contact angle of the droplet on the substrate as it is obvious that a high contact angle localizes the droplet. Hence the surface treatment of the substrate is an important method to alter the profile of the ink-jet deposition. The primary materials used in this work are silicon-based materials such as glass, silicon and silicon dioxide. Therefore, silane coupling chemistry is adopted to create a self-assembled monolayer on the substrate for modifying the surface. Some silane coupling agents have been studied previously on silicon-based materials [36-38]. The 1H,1H,2H,2H-perfluorooctyldimethylchlorosilane (PFODCS) (ABCR, Karlsruhe, Germany) was chosen to be the coupling agent in this work. The chlorine atom in the chemical structure of PFODCS reacts with the siloxyl groups of the oxide on the substrate to form covalent bonds between the monolayer and the substrate. The grafting reaction on the surface of silicon-based materials is shown in Figure 3.14. Different substrates are first washed by Piranha solution (H_2SO_4:H_2O_2 = 1:4) and then ultrasonically cleaned by acetone and methanol. PFODCS is afterwards vapour deposited on the substrates at room temperature and atmospheric pressure. The truxene T3/CHDV blends were adopted as the model fluid and the contact angle results for this on different substrates treated with PFODCS are summarised in Table 3.2. It is obvious that contact angle increases significantly after the treatment. Figure 3.15 shows the optical images of T3/CHDV droplet contact angle being measured on the glass substrate before and after the PFODCS treatment.
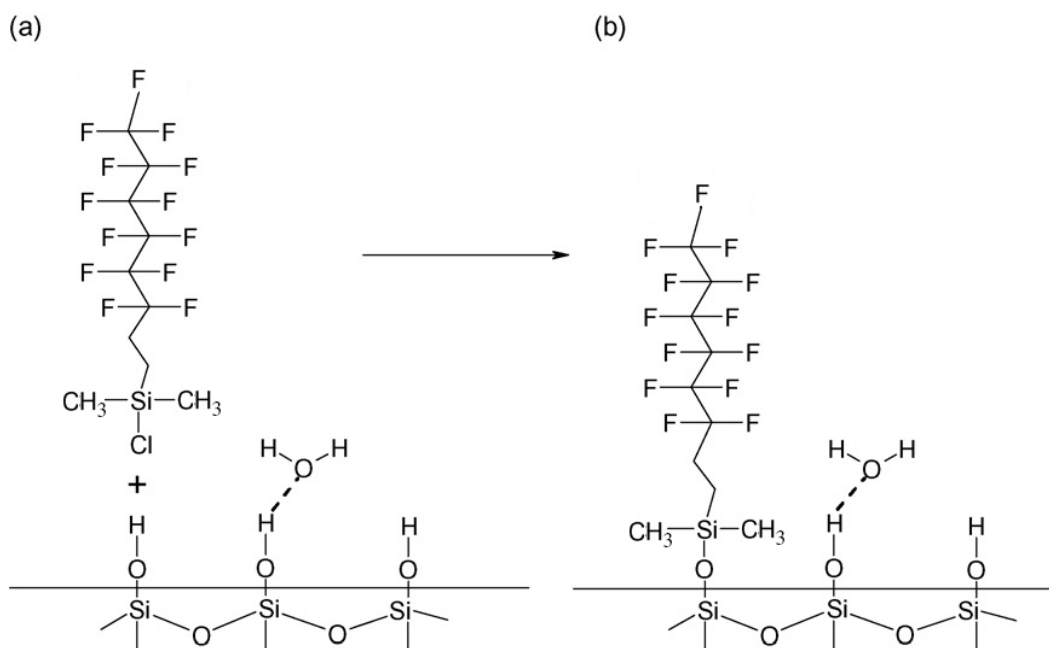
Figure 3.14 Schematic representation of PFODCS grafting reaction.

Table 3.2 Summary of contact angle results of truxene T3/CHDV blends on different substrates

Effect of PFODCS vapour deposition	Contact angle (^{o})	
	Before the treatment	After the treatment
Silicon	4.21	51.4
Silicon Dioxide	2.41	39.05
Glass	5.43	51.11

Figure 3.15 Optical images of T3/CHDV droplet contact angle being measured on the glass substrate (a) before and (b) after PFODCS treatment.

3.2 Applications

Inkjet printing techniques have been applied in many areas, as presented in the introductory part of this chapter. In our work, various materials have been printed to form functional patterns by the DMP-2800 inkjet printer, including truxene oligofluorene T3/CHDV blends, crosslinkable polyfluorene F6BT/CHDV blends, and silver nanoparticles dispersed in water solution.

3.2.1 Organic light emitting materials blends

The first materials used in the printing work are the truxene oligofluorene T3/CHDV blends. Highly n-doped Si (100) substrates were used for printing. They were first washed by Piranha solution (H_2SO_4:H_2O_2 = 1:4), and then ultrasonicated for 3 minutes each in both acetone and methanol. After drying with a N_2 flow, the substrates were treated with PFODCS through vapour deposition to change the surface energy and thus the contact angle of the drops. The vapour deposition was carried out by using a Petri dish at room temperature and atmospheric pressure. The effect of this treatment on different kinds of substrates and materials was summarised in previous section of this chapter. For T3/CHDV blends, the contact angle could be altered to 51°. The T3 materials are in solid state and mixed with CHDV monomer and PAGs to form a phase-uniform solution by ultrasonication. The concentration of T3 in the CHDV matrix is 0.5 wt% with 0.5 wt% PAGs for demonstration. When the voltage in the silicon MEMS inkjet printhead is increased, the zirconate titanate piezoelectric (PZT)/Si bimorph in the printhead deforms, compressing the chamber of the print-head to generate the pressure to eject a drop [39].

Truxene oligofluorene T3/CHDV blends have been firstly used to demonstrate the excellent capabilities of this printer. The drop pitch could be easily altered and during the multilayer printing, the spots in the first layer could be accurately covered

by the subsequent layers. Figure 3.16 shows optical images of printed T3/CHDV blends array in different drop pitch and layers under UV illumination. The images also demonstrate the large area printing ability of the printer.
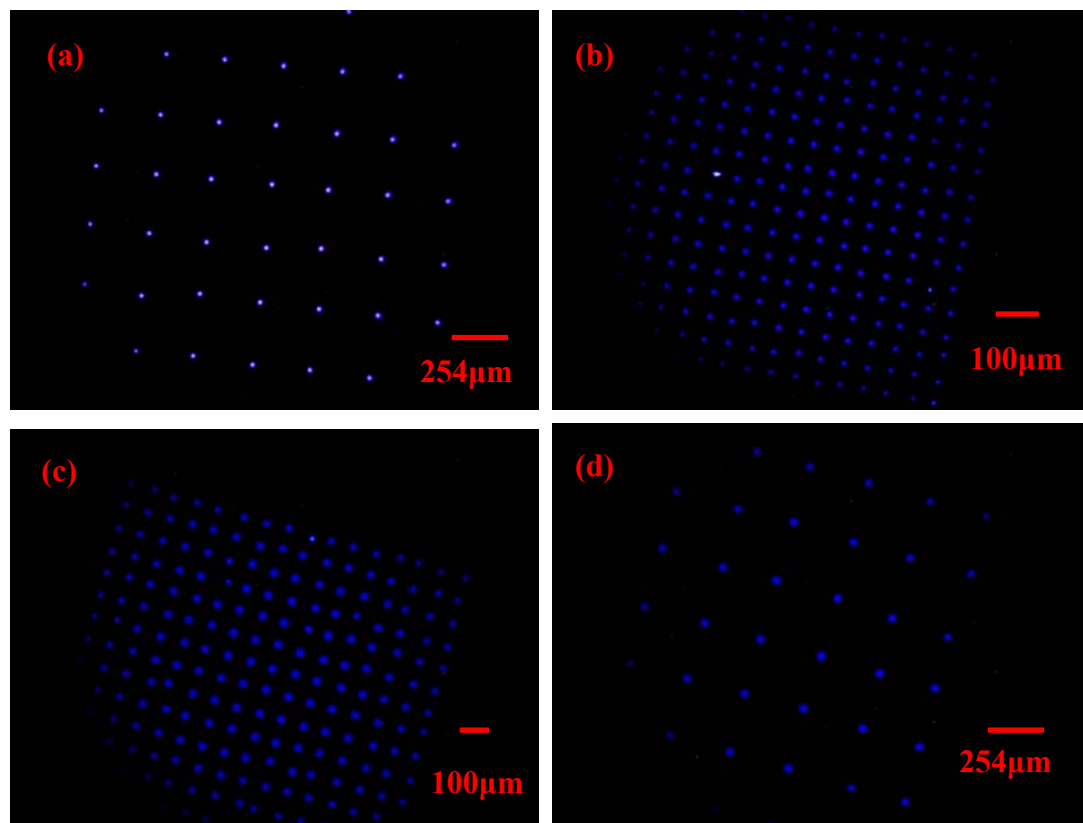

Figure 3.16 Optical images of a printed T3/CHDV blends array under UV illumination: (a) 1 layer in 254μm drop pitch; (b) 1 layer in 100μm drop pitch; (c) 2 layers in 100μm drop pitch; (d) 4 layers in 254μm drop pitch.

Uniform ~10pl truxene blend droplets were formed from the nozzles at 14.5V, allowing printing of a 'test' 8×8 array pattern with 100μm centre-to-centre pitch on the pre-treated Si substrate. After the array was printed, the sample was put under an ultraviolet (370 nm in wavelength) lamp at an energy density of 15mWcm^{-2} for 15 minutes in order to polymerise the monomer. A well-defined 'microdot' array was thus fabricated.

Scanning Electron Microscopy (SEM) characterized the shape and uniformity of the micro-patterned arrays and the image is shown in Figure 3.17. The image was

taken using an accelerating voltage of 10kV with 200X and 1500X (inset) magnification, respectively.
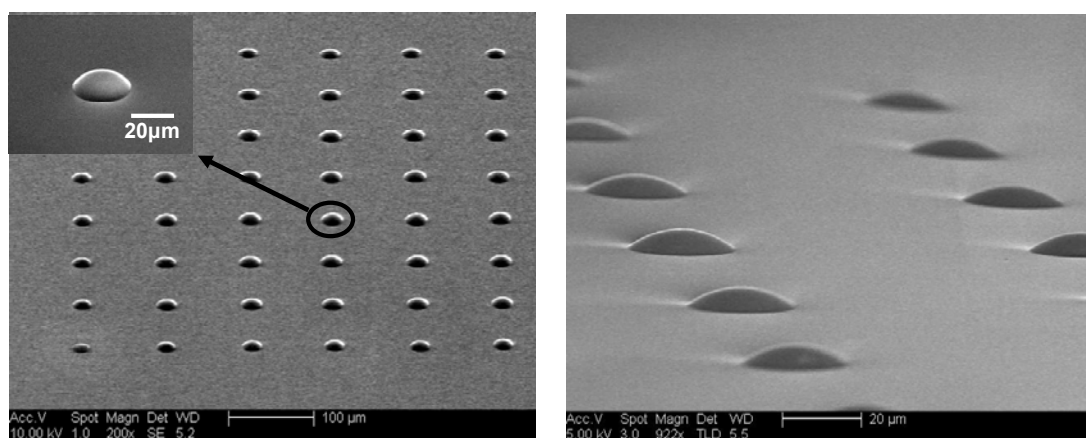

Figure 3.17 Oblique SEM images of the dot array and of a representative single microdot.

From these images, it is evident that the micro-dot structures in the array are quite uniform and that the base diameter and height of each dot are around 24μm and 2.6μm, respectively. The surface topography of the microdot formed by a 10 pl droplet was studied by Atomic Force Microscopy (AFM). The measured curve is fitted to the equation below:

$$(x - x_0)^2 + (y - y_0)^2 = R^2 \tag{3.1}$$

where x_0 and y_0 are deviation amplitudes of the coordinates on the measured curve from the curvature centre and the R is the radius of the curvature. Figure 3.18 shows that the profile curve of the dot fits the calculated curve very well with a radius of curvature of 30μm, which means the microdot has a spherical shape. These lens-shape structures are largely transparent to the ultraviolet light due to the polymer matrix and offer potential as surface-emitting organic laser structures, for example, if printed on laser mirrors [40]. A volume reduction up to ~20% of the uncured material was observed during the process, but it was confirmed that there is no mass reduction due to volatilisation of the printed blend. It is possible that this volume reduction is

caused by the wetting and absorption of the blend material into the treated substrate or the density increase by cationic polymerisation of the CHDV molecule which leads to volume shrinkage [41]. Nevertheless, this in no way detracts from the reproducibility of the printed arrays.
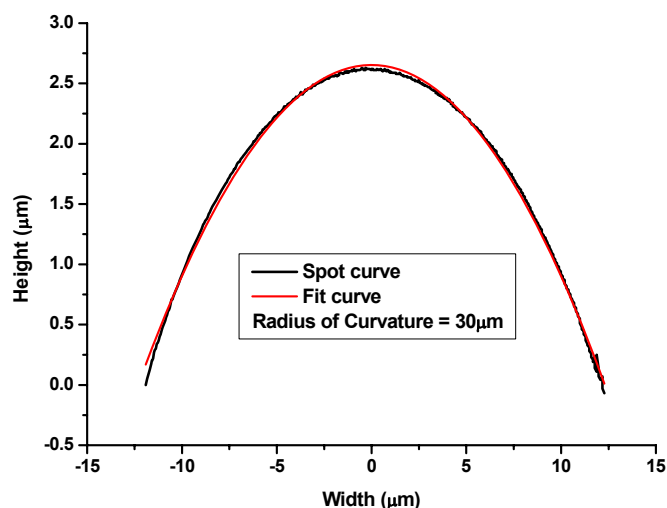

Figure 3.18 AFM profile curve (black) of a representative microdot, together with fitting (red).

Since the fluorescent nano-materials (the T3 molecules) are embedded in the UV transparent polymer matrix, we took a wide field optical microscope image of the whole microdot array under UV lamp illumination. Inset (a) in Figure 3.19 shows this micrograph with an image capture time of 8s. All the dots emitted bright and uniform photoluminescence, indicating that blending the truxene oligofluorenes into the polymer matrix had not significantly affected their fluorescence properties (c.f. Chapter 2). This assumption was further tested by measuring the PL of a single micro-dot in the array. A laser beam at 325nm wavelength was used as the excitation source for the measurement and focused to a spot 10μm in diameter by an objective lens. The power density of the focused laser beam was estimated to be 3Wcm^{-2} (the measurement set-up used here is in Prof. R.W. Martin's labs in the department of Physics). Inset (b) in Figure 3.19 shows the image taken under such excitation

conditions and the main part of the figure shows the single microdot PL spectrum. Luminescence peaks were found for blue emission at 412, 438 and 470nm, which is a little red-shift from those obtained from the neat truxene material described in Chapter 2. The red-shift in the spectrum may due to some aggregates of the oligofluorene truxene in the matrix during ultrasonicating the blend solution, as the linear/branched oligofluorene structure has potential to aggregate caused by inter/intra molecular interactions arising from solid state sample formation [42]. However, these results further indicate that both the blending and ink-jet printing processes have not had noticeable detrimental effects on the truxene oligofluorenes.

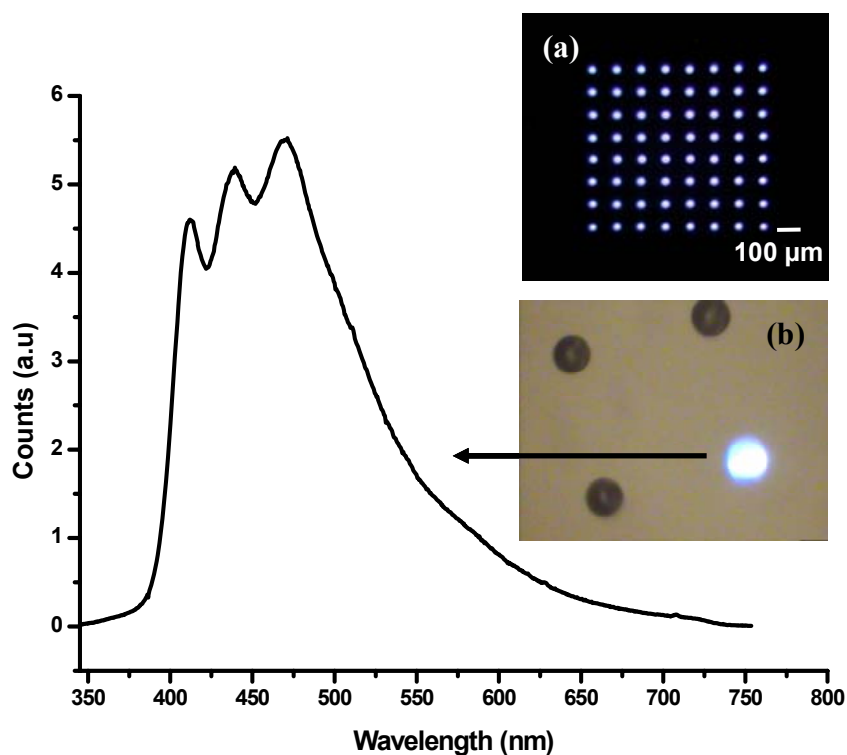Figure 3.19 Photoluminescence spectrum of a single (UV) photoexcited micro-dot, together with (inset) optical micrographs of the full photoexcited array under UV lamp illumination (a) and a single-photoexcited microdot under UV lamp illumination (b).

We also fabricated, following the same procedure, truxene blend micro-arrays in same concentration under 16.5V nozzle voltage using a newly developed cartridge

delivering ~1pl drops. The optical images under normal and UV illumination are shown in Figure 3.20. Figure 3.21 is the spot curve measured by AFM and the fitting curve. The shape of these microdots was measured by AFM to be 12µm in diameter and 1µm in height. The radius of the curvature is fitted to be 17µm. The spot curve fits to the equation very well, suggesting the structure has an excellent spherical shape. We note that these structures are among the smallest yet produced directly by inkjet printing.
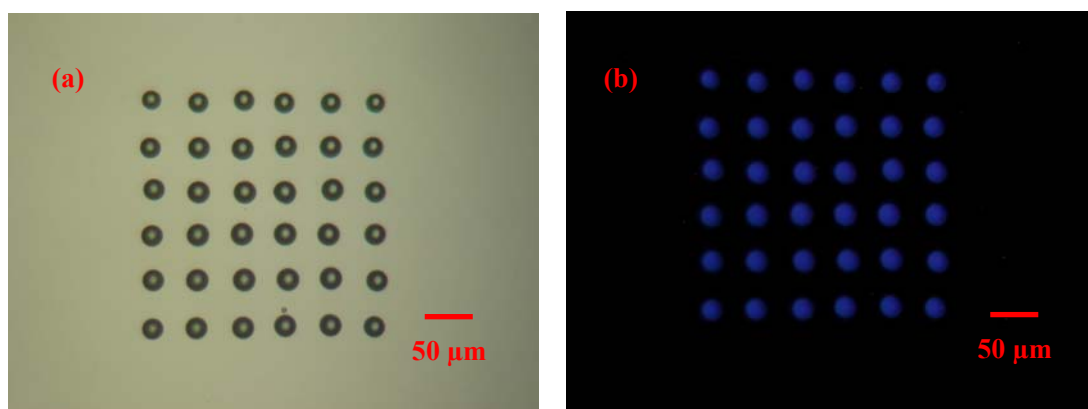

Figure 3.20 Optical images of T3/CHDV blends printed by ~1pl droplet under (a) normal and (b) UV illumination.
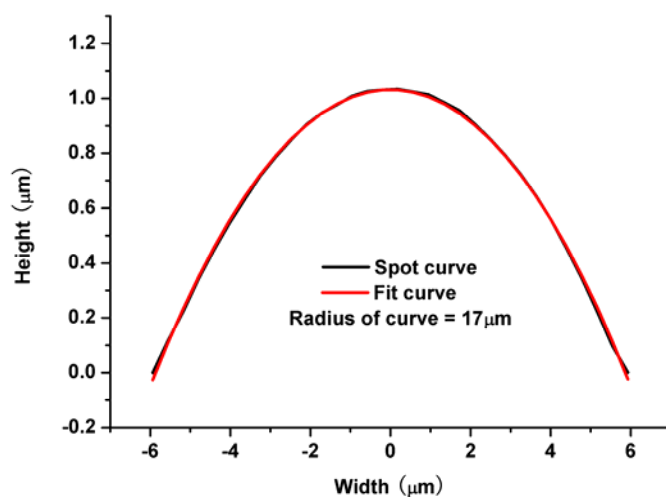

Figure 3.21 AFM profile curve (black) of a representative microdot, together with fitting (red).

In order to conveniently investigate the fluorescence properties of the microstructures, we built our own PL measurement set-up for micro-scale fluorescing structures (micro-PL). Figure 3.22 is the schematic of the set-up mainly comprising a diode laser emitting at 375nm (Power Technology, Alexander, AR. USA) for optically pumping the structures (red arrow with solid line), an 60× objective lens (Nikon, Japan) for focusing the laser beam on one single spot of the sample (red arrow with solid line), CCD camera for monitoring and aligning the focused laser beam (red arrow with dash dot line), another objective lenses for guiding the fluorescence into the spectrometer (Model: DPM-HV, JOBIN YVON, Edison, N.J. USA) which collects fluorescence signals and generates the spectrum (red arrow with dash line).
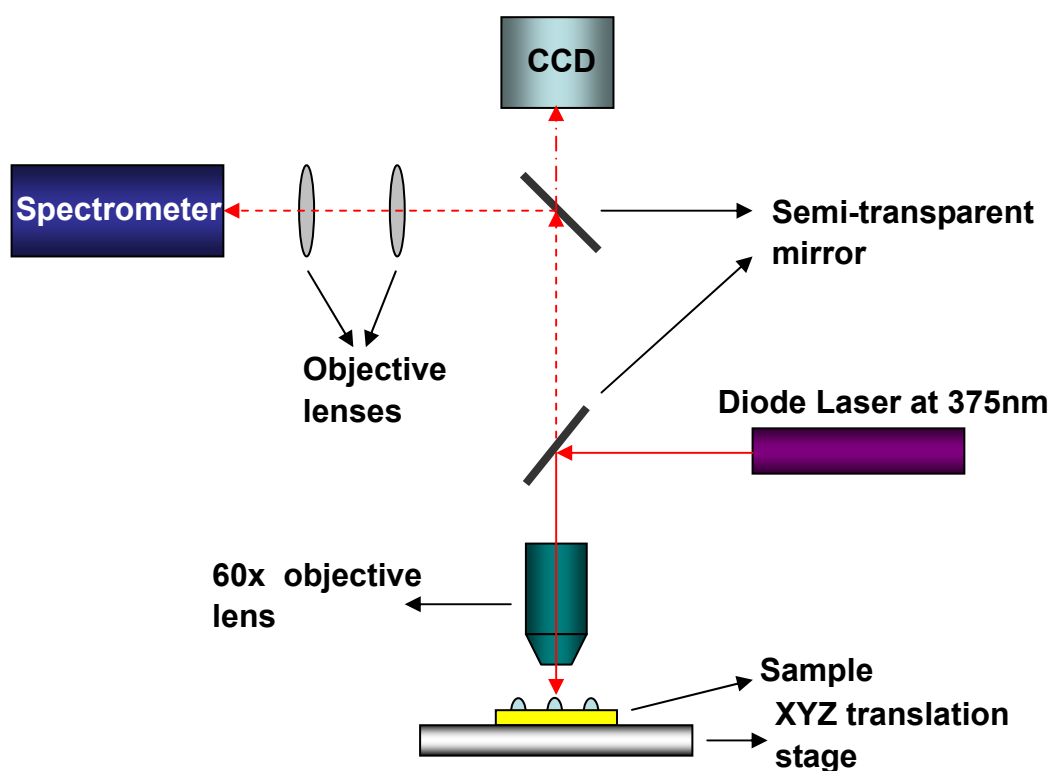

Figure 3.22 Schematics of the micro-PL set-up. Red arrows indicate the beam path.

Figure 3.23 is a series of images captured from the CCD camera in the micro-PL set-up during the measurement. Figure 3.23-a is a corner of the T3/CHDV

blends array printed by ~1pl droplet without any laser beam on. Firstly it is observed that the laser beam, focused into a ~5μm spot, is not aligned on the spot of the array (Figure 3.23-b). Then the laser beam is moved to one single spot of the array (Figure 3.23-c). The micro-spot is optically pumped by the focused laser beam and shows fluorescence as further proved by putting a long-pass coloured glass filter with a cut-off wavelength at 420nm in front of the CCD camera to filter the scattered light from the laser (Figure 3.23-d).
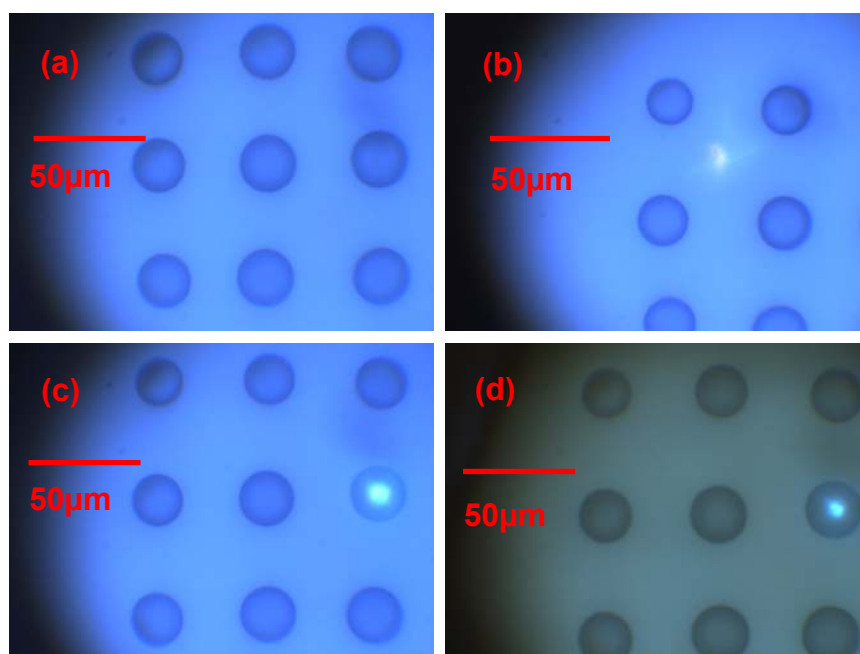
Figure 3.23 Series of images obtained from the CCD camera in the micro-PL set-up: (a) a corner of the printed spot array; (b) laser beam focused to a spot between array spots; (c) laser spot aligned on the single printed truxene blends spot; (d) laser aligned on the single printed truxene blends spot after filtering the UV light from the laser.

The PL spectrum generated from Figure 3.23-c is shown in Figure 3.24. The fluorescence peaks are measured to be ~409nm, ~428nm and ~460nm. The peaks are much closer to the neat truxene than the results from T3/CHDV blends printed by the ~10pl cartridge. This indicates the ultrasonication for this blend solution preparation is better to suppress the aggregation of T3 molecules. The fluorescence properties of the truxene oligofluorenes are well maintained.
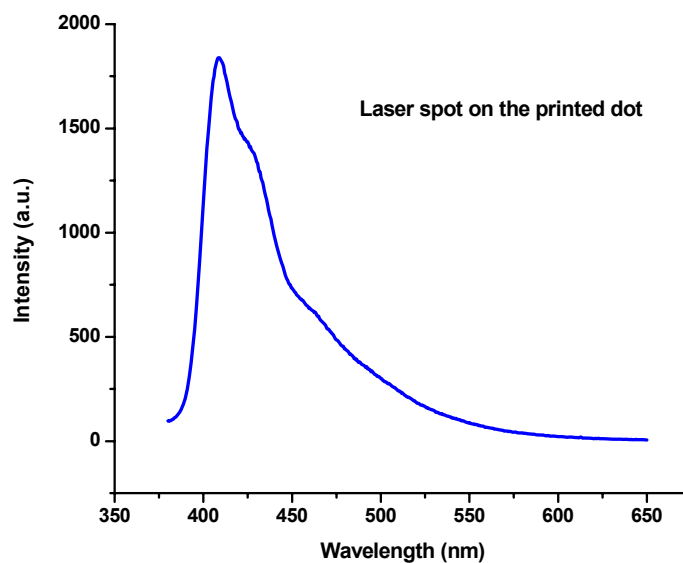
Figure 3.24 PL spectrum of the single T3/CHDV blends spot printed by ~1pl droplet.

In addition to the T3/CHDV blends, printability and pattern formation have also been demonstrated from crosslinkable polyfluorene F6BT/CHDV blends by the DMP inkjet printer. The concentration of F6BT in the CHDV matrix is 10mg/ml with 0.2 wt% PAG. Figure 3.25 shows the optical images of the printed structures under normal and UV illumination and the diameter of the spot is ~23µm. In addition, Figure 3.26 shows the PL spectrum of a single F6BT/CHDV blend spot in the array. The fluorescence peak of the spectrum is at ~530nm which is very similar to that of the neat materials (~533nm) described in Chapter 2.
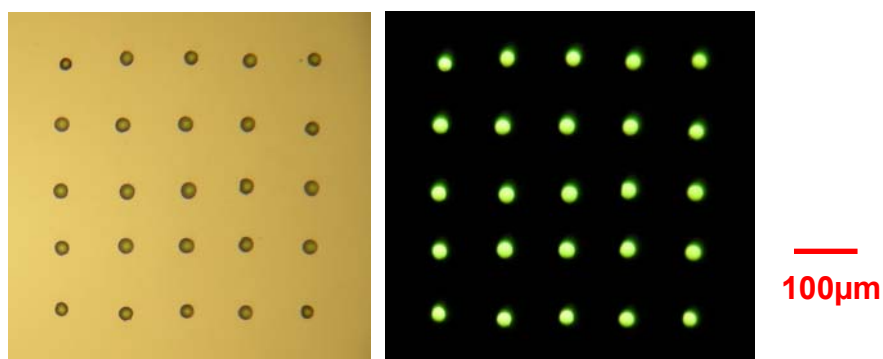
Figure 3.25 Optical images of printed F6BT/CHDV blends under (a) normal and (b) UV illumination.
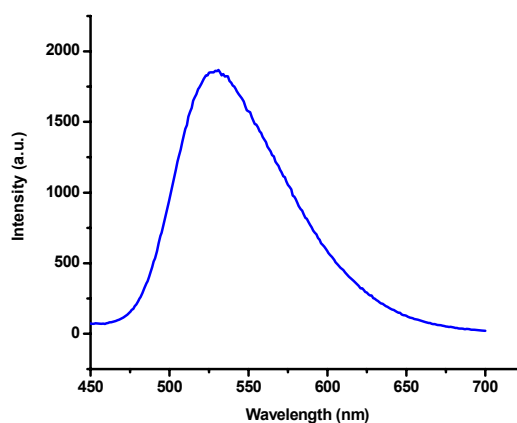
Figure 3.26 PL spectrum of the single F6BT/CHDV blend spot.

3.2.2 Other applications

Polymer solutions are not the only materials that may be deposited by the DMP-2800 inkjet printer. Solutions containing metallic nanoparticles were printed for electrical applications and enhancement of Surface-Enhanced Raman Resonance Scattering (SERRS). The electrical applications of the printed metallic nanoparticles will be studied in Chapter 5 and here we present the role of the printed features in the SERRS analysis.

Raman spectroscopy is a powerful tool to investigate the chemical state of the bonds in carbon materials. SERRS is a process that enhances the Raman signals from the molecules adsorbed on metal surfaces and particles. The enhancement factors of Raman scattering from single dye molecules adsorbed on aggregated Ag nanoparticles have been observed to be up to $\sim 10^{14}$ [43] . The SERRS enhancement has been attributed to two mechanisms. The primary contribution is the local electromagnetic field enlargement due to the special optical properties of the metals which support surface plasmon resonances at visible wavelengths [44]. Another factor is the chemical enhancement mechanism, which results from the adsorbed induced charge transfer transition between the molecule and metal or interaction of

chemisorbed molecules with ballistic electrons generated from plasmon excitation [44]. SERRS is widely applied in bioanalysis such as selective detection of labelled DNA sequences for instance. However, the DNA itself is inactive to SERRS and adsorbs poorly to the metal surface and there is also an issue of controlling the assembly of the nanoparticles to turn on the enhancement in a controlled and reproducible manner. Therefore, our co-workers in Prof. Graham's group (Department of Pure and Applied Chemistry) introduced a method to show selective turning on of the SERRS effect on dye-assembled and DNA functionalized silver nanoparticles [45]. In this preliminary work shown here, we simply prepared the printed silver nanoparticles features and assembled the features with azo dye which is active to SERRS analysis. These dye-coded silver nanoparticles features are now basically ready for further DNA functionalisation and sequence detection.

Figure 3.27 is the optical image of the 6×6 array of silver nanoparticle spots printed on a substrate of silicon oxide on silicon. The silver nanoparticles are ~30nm in diameter and dispersed in water. After the water dries, the nanoparticles aggregate which is shown in the SEM images (Figure 3.28) and the aggregation is beneficial for maximising the SERRS signals. Figure 3.29 shows the SERRS spectra of one feature of the azo dye-assembled silver nanoparticles. The Raman spectrum only arises when the nanoparticles are excited (Figure 3.29-b) with the characteristic peak of the azo dye at 1406 cm^{-1}. These initial results are satisfying and further optimisation on aggregation controlling is required.
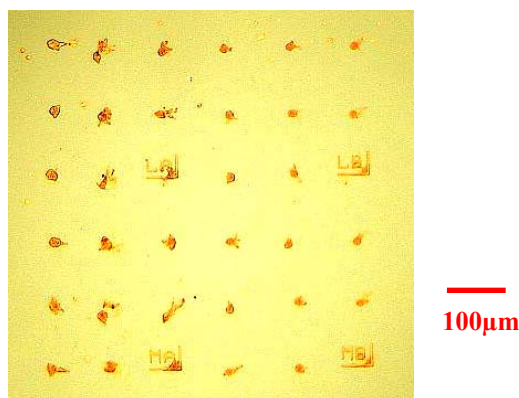

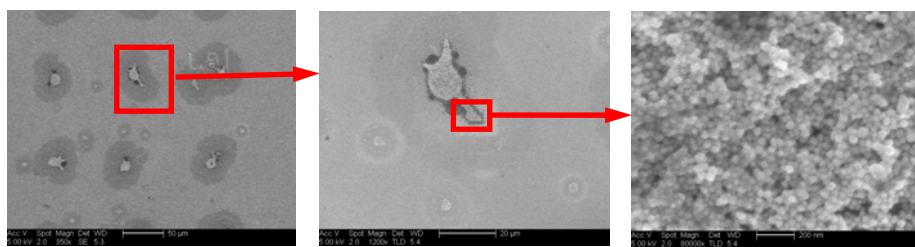Figure 3.27 Optical image of 6×6 silver nanoparticles array.

Figure 3.28 SEM images of the dried silver nanoparticles in the printed array.
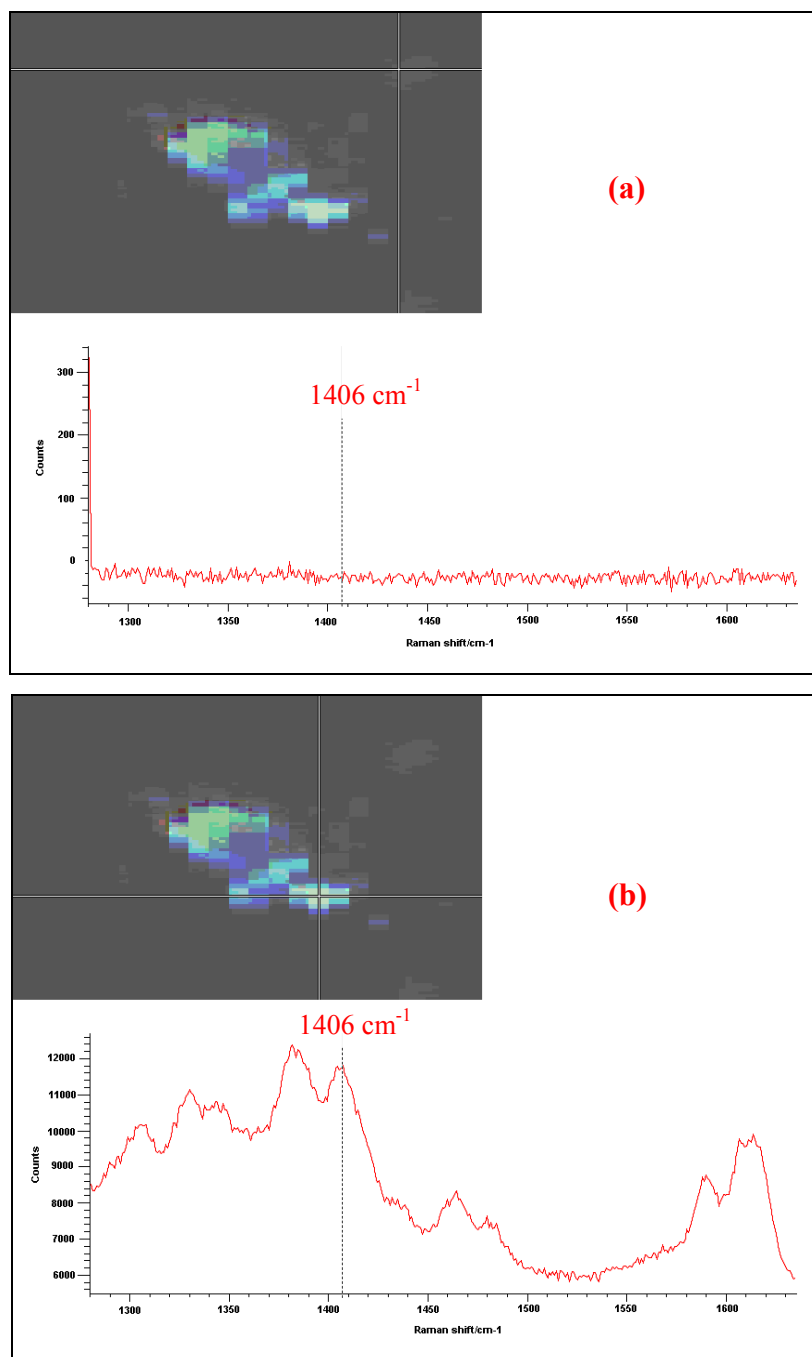

Figure 3.29 SERRS spectra of non-excited (a) and excited (b) azo dye-assembled Ag nanoparticles. The cross cursor in the inset image shows where was excited and the spectrum was taken.

3.3 Summary

In this chapter, the diverse applications of the inkjet printing technique have first been reviewed. Secondly, two categories of inkjet printing technique have been introduced which are continuous inkjet and drop-on-demand inkjet. Then the feature properties of some selected inkjet printers for functional structures fabrication have been summarised. The main focus of this chapter is the DMP-2800 inkjet printer and its applications. The superior properties of this inkjet printer have been described in detail.

The controllability and reproducibility of the droplets are crucial to fabricate functional structures. Hence we explained the working principle of the DMP printer and studied the factors influencing the drop formation of the printer including the frequency, driving voltage and pulse length. The CHDV polymers were adopted as a model material to present the optimized parameters of the printer. Besides the printing parameters, the fluid properties and the droplet behaviour on the substrate also affect the profile of the final printed structure. One silane coupling agent is used in this work for the treatment to modify the hydrophilicity of the surface.

In this work, we have fabricated various microstructures using the DMP printer. Truxene T3/CHDV blends have been printed from the cartridges delivering ~10pl and ~1pl droplets. The dimensions of the T3/CHDV printed microstructures are 24μm wide and 2.6μm high for the ~10pl droplet, and 12μm wide and 1μm high for the ~1pl droplet. The PL spectra of the single excited spot in the printed array were obtained from the home-built micro-PL set-up and are similar to those of the neat truxene oligofluorene. The crosslinkable F6BT/CHDV was also printed by this printer. The diameter of the printed features is ~23μm and the micro-PL spectrum shows similar emission peak as the neat F6BT polymers. In addition to the organic materials, the metallic nanoparticle solution could also be deposited by the printer. A water-based silver nanoparticle solution was printed and assembled with azo dyes. These dye-coded nanoparticles are ready for detecting DNA sequences by SERRS.

References

1. M.F. Mabrook *et al.*, "An inkjet-printed chemical fuse," *Appl. Phys. Lett.* **86**, 013507 (2005).

2. Y. Xia *et al.*, "Polymer bilayer structure via inkjet printing," *Appl. Phys. Lett.* **88**, 163508 (2006).

3. Y. Liu *et al.*, "Polymer-based rectifying diodes on a glass substrate fabricated by ink-jet printing," *Macromol. Rapid Commun.* **26**, 289 (2005).

4. A.L. Dearden *et al.*, "A Low curing temperature silver ink for use in ink-jet printing and subsequent production of conductive tracks," *Macromol. Rapid Commun.* **26**, 315 (2005).

5. E. Tekin *et al.*, "Inkjet Printing of Luminescent CdTe Nanocrystal-Polymer Composites," *Adv. Funct. Mater.* **17**, 23 (2007).

6. J. Perelaer *et al.*, "Ink-jet printing and microwave sintering of conductive silver tracks," *Adv. Mater.* **18**, 2101 (2006).

7. K. Kordas *et al.*, "Inkjet printing of electrically conductive patterns of carbon nanotubes," *Small* **2**, 1021 (2006).

8. A. Bietsch *et al.*, "Inkjet deposition of alkanethiolate monolayers and DNA oligonucleotides on gold: evaluation of spot uniformity by wet etching," *Langmuir* **20**, 5119 (2004).

9. F.G. Zaug *et al.*, "Drop-on-demand printing of protein biochip arrays," *MRS Bulletin* **28**, 837 (2003).

10. A.Y. Sankhe *et al.*, "Inkjet-printed monolayers as platforms for tethered polymers," *Langmuir* **21**, 5332 (2005).

11. S.E. Burns *et al.*, "Inkjet printing of polymer thin-film transistor circuits," *MRS Bulletin* **28**, 829 (2003).

12. J.Z. Wang *et al.*, "Low-cost fabrication of submicron all polymer field effect transistors," *Appl. Phys. Lett.* **88**, 133502 (2006).

13. C.W. Sele *et al.*, "Lithography-free, self-aligned inkjet printing with

sub-hundred-nanometre resolution," *Adv. Mater.* **17**, 997 (2005).

14. Y. Yoshioka *et al.*, "Inkjet printing of oxidants for patterning of nanometre-thick conducting polymer electrodes," *Adv. Mater.* **18**, 1307 (2006).

15. M. Lee *et al.*, "Scaffold fabrication by indirect three-dimensional printing," *Biomaterials* **26**, 4281 (2005).

16. B.M. Wu *et al.*, "Effects of solvent-particle interaction kinetics on microstructure formation during three-dimensional printing," *Polym. Eng. Sci.* **39**, 249 (1999).

17. S.S. Kim *et al.*, "Survival and function of hepatocytes on a novel three-dimensional synthetic biodegradable polymer scaffold with an intrinsic network of channels," *Ann. Surg.* **228**, 8 (1998).

18. B.-J. de Gans *et al.*, "Polymer-relief microstructures by inkjet etching," *Adv. Mater.* **18**, 910 (2006).

19. H.P. Le, "Progress and trends in ink-jet printing technology," *J. Imag. Sci. Tech.* **42**, 49 (1998).

20. B.-J. de Gans *et al.*, "Inkjet printing of polymer micro-arrays and libraries: instrumentation, requirements, and perspectives," *Macromol. Rapid Commun*, **24**, 659 (2003).

21. Technical articles: principle of digital printing, http://www.pdsconsulting.co.uk (2007).

22. E. Tekin, "Thin film libraries of functional polymers and materials prepared by inkjet printing," PhD thesis (2007).

23. Dimatix Materials Printer DMP-2800 series user manual, Dimatix FUJIFILM Inc. USA.

24. H. Dong *et al.*, "An experimental study of drop-on-demand drop formation," *Phys. Fluids* **18**, 072102 (2006).

25. H. Dong *et al.*, "Visualization of drop-on-demand inkjet: Drop formation and deposition," *Rev. Sci. Instrum.* **77**, 085101 (2006).

26. R.M.S.M. Schulks, "The contraction of liquid filaments," *J. Fluid Mech.* **309**,

277 (1996).

27. P.K. Notz *et al.*, "Dynamics and breakup of a contracting liquid filament," *J. Fluid Mech.* **512**, 223 (2004).

28. D. Henderson *et al.*, "The motion of a falling liquid filament," *Phys. Fluids* **12**, 550 (2000).

29. R.D. Deegan *et al.*, "Travelling waves and defect-initiated turbulence in electroconverting nematics," *Phys. Rev.E* **62**, 756 (2002).

30. R.D. Deegan, "Pattern formation in drying drops," *Phys. Rev. E* **61**, 475 (2000).

31. A.P. Sommer *et al.*, "Formation of crystalline ring patterns on extremely hydrophobic supersmooth substrates: extension of ring formation paradigms," *Crystal Growth Des.* **5**, 551 (2005).

32. H. Hu *et al.*, "Marangoni effect reverses coffee-ring depositions," *J. Phys. Chem. B* **110**, 7090 (2006).

33. B.-J. de Gans *et al.*, "Inkjet printing of well-defined polymer dots and arrays," *Langmuir* **20**, 7789 (2004).

34. M. Ikegawa *et al.*, "Droplet behaviours on substrates in thin-film formation using ink-jet printing," *JSME Int J. Ser. B* **47**, 3 (2004).

35. J.E. Stringer *et al.*, "Droplet behaviour in inkjet printing," *Mater. Res. Soc. Symp. Proc.* **860E**, LL2.6.1 (2005).

36. D.L. Angst *et al.*, "Moisture absorption characteristics of organosiloxane self-assembled monolayers," *Langmuir* **7**, 2236 (1991).

37. A. Fuchs *et al.*, "Wetting and surface properties of (modified) fluoro-silanised glass," *Colloids Surf. A* **307**, 7 (2007).

38. B. Bhushan *et al.*, "Surface modification of silicon and polydimethylsiloxane surface with vapour-phase-deposited ultrathin fluorosilane films for biomedical nanodevices," *J. Vac. Sci. Technol. A* **24**, 1197 (2006).

39. J. Sumerel *et al.*, "Piezoelectric ink jet processing of materials for medical and biological applications," *Biotechnol. J.* **1**, 976 (2006).

40. N. Laurand *et al.*, "Tunable single-mode fibre-VCSEL using an intracavity polymer microlens," *Optics Lett.* **32**, 2831 (2007).

41. T.H. Chiang *et al.*, "A study of monomer's effect on adhesion strength of UV-curable resins," *Int. J. Adhes. Adhes.* **26**, 520 (2006).

42. W.Y. Lai *et al.*, "Enhanced solid-state luminescence and low-threshold lasing from starburst macromolecular materials," *Adv. Mater.* **21**, 355 (2009).

43. J. Kneipp *et al.*, "SERS- a single-molecule and nanoscale tool for bioanalysis," *Chem. Soc. Rev.* **37**, 1052 (2008).

44. A. Campion *et al.*, "Surface-enhanced raman scattering," *Chem. Soc. Rev.* **27**, 241 (1998).

45. D. Graham *et al.*, "Control of enhanced raman scattering using a DNA-based assembly process of dye-coded nanoparticles," *Nat. Nanotechnol.* **3**, 548 (2008).

Chapter 4 Hybrid inorganic/organic light emitting device fabrication via inkjet printing

Recently, there has been considerable interest in developing 'hybrid' light-emitting technologies based upon gallium nitride optoelectronics. Electrically injected gallium nitride hetero-structures offer customized direct band-gaps in the ultraviolet to visible spectral range and can selectively and efficiently transfer excitation either non-radiatively (Förster Resonant Energy Transfer or FRET) [1,2] or radiatively [3] to an overlayer based on alternative light-emitting materials. This approach has important implications for areas including; colour conversion and white-light generation for solid-state lighting [4], microdisplays [5], bioscience [6], instrumentation [7] and photo-pumped organic semiconductor lasers [8]. It has to date been embodied primarily using conventional inorganic phosphors [9], inorganic semiconductor nanocrystals (mainly CdSe/ZnS colloidal quantum dots) [1] and, to a lesser degree, organic polymers [3]. Here, we report development of such devices based mainly on printed *organic* structures as a technologically and scientifically interesting alternative. Colour conversion is the main application of such devices. Truxene oligofluorene/CHDV blends and crosslinkable F6BT/CHDV blends have been adopted as the colour converter materials and the hybrid organic/GaN-based devices were fabricated from these materials. The morphology, photoluminescence (PL) properties and colour conversion efficiency of these devices is reported in this chapter.

4.1 Background on hybrid device fabrication

In chapter 1, we described the advantages of the light emitting diodes (LEDs) made by inorganic semiconductor AlInGaN materials and introduced the novel micro-structured light emitting diodes. The micro-LED array used to pilot hybrid device fabrication was described in Chapter 1 and contains 64×64 micro-disc elements in a few square millimetres device active area, emitting light at UV or visible wavelengths. This presents as an excellent pattern-programmed micro-projection source for various display and instrumentation applications. However, each micro-LED only emits at one single wavelength defined by the particular nitride epitaxial structure used. Therefore, when there is an increasing demand on small-scale programmable light sources for use in micro-displays, imaging systems and integrated lab-on-chip devices, it is anticipated that the hybrid inorganic/organic device would combine the attractive electrical properties of GaN-based materials and high photoluminescence yields of organic molecules to open a new route of developing low-cost and highly efficient light sources. Exploration such hybrid device technology has been realised under both radiative (colour down conversion) and non-radiative (Föster resonance energy transfer (FRET)) energy transfer conditions [10]. Figure 4.1-a shows the schematic hybrid device structure for radiative energy transfer and Figure 4.1-b shows the hybrid quantum well structure in the FRET study. For completeness, we review the early work in these areas in the following two sections, before going on to describe the new developments based on inkjet printing.
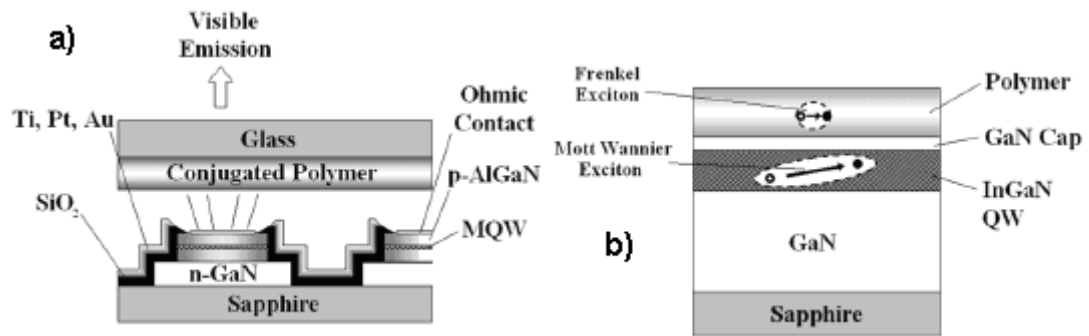
Figure 4.1 (a) Hybrid device fabricated by polymer layer radiatively excited by the micro-LED; (b) Schematic structure of hybrid device under FRET condition. After [10]

4.1.1 Radiative method (colour down conversion)

For display and lighting applications when full-colour (blue-, green- red-) and white-light emission are required, the most common way to achieve this from the AlInGaN LEDs is through the spectral wavelength down conversion. Traditionally, one or more visible phosphors absorbed short wavelength light at UV/blue from the LEDs and emitted secondary longer wavelength light. Phosphors are usually rare-earth doped metal oxide materials with grain size around tens of micrometers, therefore the size of the emitting elements needs to be much larger than the typical grain size of the phosphors when the phosphors are used as the colour converter [9].

Rapid development in organic optoelectronic materials opens another choice on the colour down converter such as conjugated light emitting polymers and oligomers (organic semiconductors). The organic materials are low-cost and easily processed from solution. The emission wavelength can be tailored by molecular engineering [11], which makes these materials suitable for AlInGaN LED down conversion. Another benefit of the hybrid inorganic/organic devices is that they take full advantage of the advantageous complementary optical and electronic properties of GaN-based and organic materials. The only requirement for developing hybrid device through the radiative method is that there is photon absorption in the polymer from the AlInGaN LEDs and the polymer can efficiently convert the energy to longer

wavelength. There are different techniques to fabricate hybrid devices under the radiative condition. Here we present two techniques studied previously, film and self-alignment to fabricate hybrid device using dyes and polyfluorenes.

A film of luminescent materials is commonly used in fabricating hybrid devices and such device fabrication has been undertaken on commercially available GaN-based LEDs. Guha et al. demonstrated that layer of 4-diyanomethylene-2-methyl-6-(*p*-dimethylaminostyryl)-4*H*-pyran (DCM) dispersed in PMMA and either evaporated or spin-coated to a sodalime glass, which then was put in proximity contact to a commercial Nichia GaN LED to form a hybrid device [12]. Ermako et al. prepared a hybrid device by placing the 4-dimethylaminochalcone (DMAC) and Nile Red dyes dissolved in epoxy in the reflector of the commercial LED chip and achieved green and red light from a UV-blue GaN-based LED [13]. Hide et al. reported white light generated from an InGaN/conjugated polymer hybrid LED by combining red-emitting poly(2-methoxy-5-(2'8-ethyl-hexyloxy)-1,4-phenylene vinylene) (MEH-PPV) and green-emitting poly(2-butyl-5-(2'8-ethyl-hexyl)-1,4-phenylene vinylene) (BuEH-PPV) with a blue-emission GaN-based LED [14]. Figure 4.2 shows the structure of the hybrid device using a commercial GaN-based LED as repoted in [13].
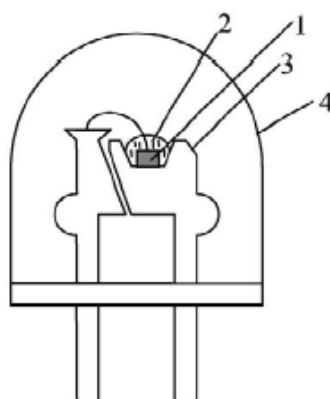

Figure 4.2 Hybrid device fabricated by commercial LED: 1. semiconductor emitting element; 2. organic luminescent substance; 3. reflector; 4. epoxy lens. After [13].

In addition to the commercially available GaN-based LEDs, the

micro-pixellated UV (370nm) AlInGaN LEDs have also been explored for the hybrid device fabrication. In Chapter 1, the fabrication of the micro-array LEDs in our research group was introduced. The individual pixels in the array are 20μm in diameter and 30μm in centre-to-centre spacing and they emit up to about 1μW power in top emission format. Organic light emitting materials poly(9,9-dioctylfluorene-*co*-9,9-di(4-methoxy)phenylfluorene) (F8DP), poly(9,9-dio-ctyfluorene-*co*-2,1,3-benzo-thiadiazole) (F8BT), and Dow Red F were used as the colour converters by us and our collaborators at Imperial College, London., as their absorption spectra overlap the emission spectrum of the UV micro-LEDs (see Figure 4.3) [3].
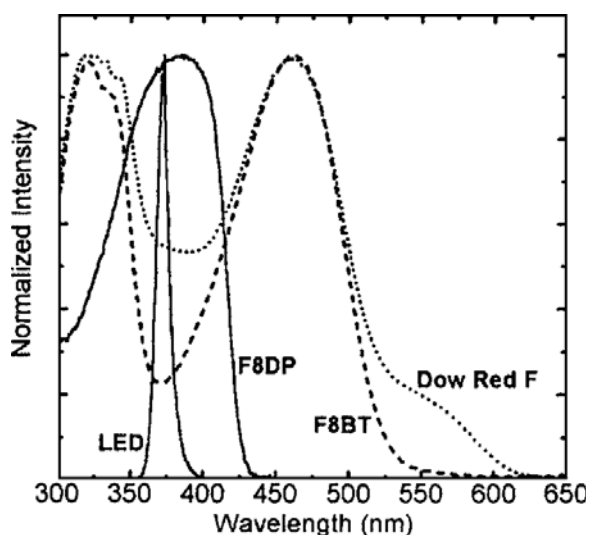
Figure 4.3 Normalized absorption of F8DP (solid line), F8BT (dashed line) and Dow Red F (dotted line) and emission spectrum of AlInGaN micro-LEDs (indicated). After [3].

Around 200nm thick films of these materials were spin-coated from a toluene solution with the concentration of 20mg/ml. Quartz was used as the film substrate and, after deposition, the polymer side was placed into close contact with the UV micro-LED structure. The longer wavelength emission from the polymer films was generated from optically excited photons by the UV emission of micro-LEDs and detected by a fibre-coupled spectrometer with a charge coupled device (CCD)

detector. Figure 4.4 shows the blue, green, red conversion achieved respectively from the F8DP, F8BT and Dow Red F hybrid devices. The photoluminescence spectra of F8DP-based hybrid device shows peaks at 425, 450 and 480nm corresponding to F8DP vibronic structure and the blue emission has Commision International de L'Eclairage (CIE 1931) (x, y) coordinates (0.16, 0.03). The emission from F8BT-based hybrid device has CIE (1931) coordinates (0.42, 0.56) at peak wavelength 545nm. Meanwhile, the red emission from the Dow Red F-based hybrid LED has a broad spectrum with the peak at 660nm and CIE (1931) coordinates (0.67, 0.32). Both the images and spectra in Figure 4.4 show obvious spectral conversion from the hybrid device. Four pixels were turned on in each case for these demonstrations.
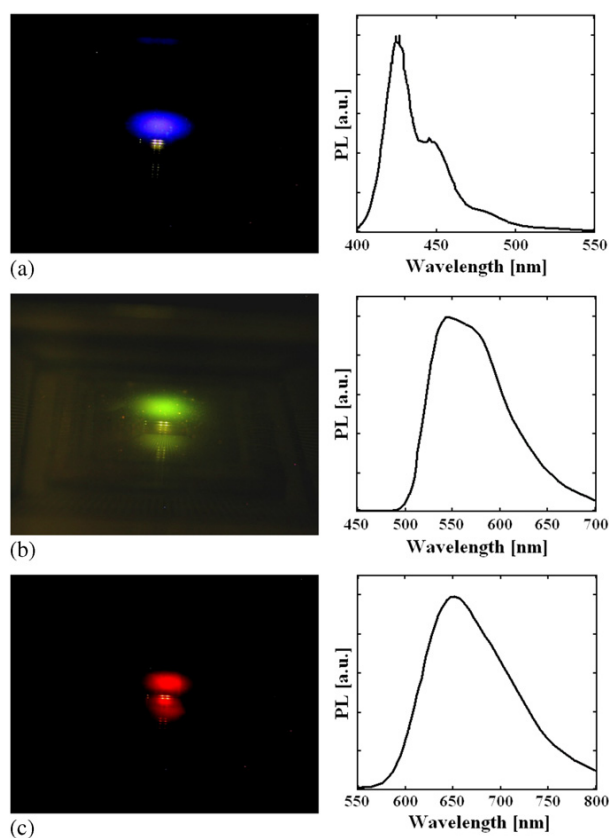

Figure 4.4 Oblique view of 4 UV pixels pumping the a) F8DP, b) F8BT and c) Dow Red F films, together with the corresponding measured PL spectra.

White hybrid devices were also fabricated from these polymers as there was a

suitable match of the absorption and emission characteristics. Using either the conventional multilayer structure in sequence or blending three polymers in specific concentration ratio, the white light hybrid device could be produced on AlInGaN micro-LEDs [3]. Figure 4.5 is the schematic picture of multilayer structure and blending structure.
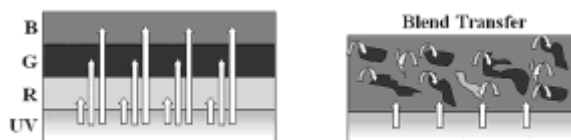

Figure 4.5 Schematic picture of multilayer (left) and blending (right) white light structure. After [10].

In the multilayer structure, the sequential RGB polymers were pumped directly by the UV micro-LEDs underneath and in the blended structure, the blue polymer was pumped first and then an internal energy transfer excited the green and red emitters. The blending structure reduces the complexity and time of the fabrication and also supports the incomplete non-radiative energy transfer between all the three colour polymers. In the blending structure system, the F8DP is the host, and the F8BT and Dow Red F are the guest emitters to which the internal energy transfers. Different concentration ratios of F8DP, F8BT and Dow Red F have been studied. Figure 4.6-a shows the CIE (1931) coordinates of several hybrid device A-D under different concentration ratios of the three coloured polymers and Figure 4.6-b shows the overall emission spectra the hybrid device A-D [3].
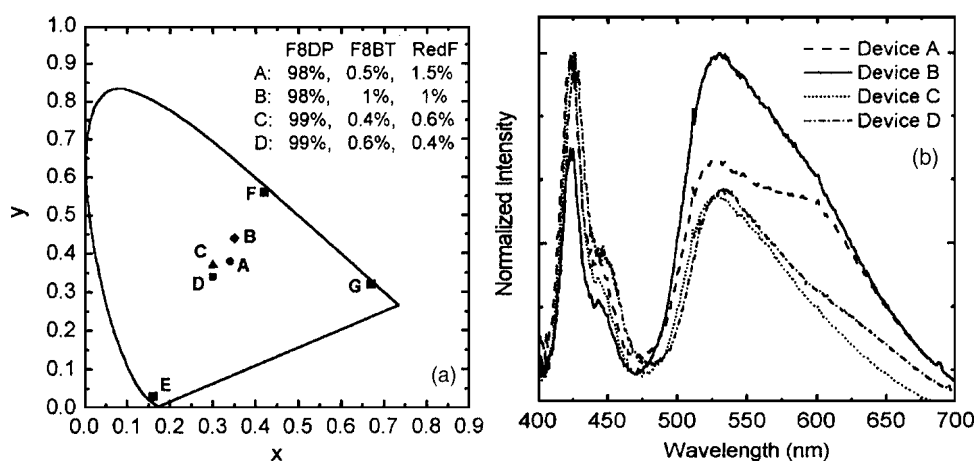

Figure 4.6 (a) CIE (1931) coordinates of the hybrid devices A-D under different concentration ratios of the three colour polymers; (b) emission spectra of the hybrid devices A-D. After [3].

Another way to fabricate the hybrid LEDs is via the "self-alignment" technique. In our group, we fabricated hybrid micro-strip LEDs using the blue light emitting polymer poly(9, 9-dioctylfluorene) (PFO) [15]. The fabrication of the micro-stripe LEDs has been described in Chapter 1. In the hybrid device, PFO (0.3 wt% including solvent) was blended with a divinyl functionalised monomer and a photoacid generator (0.05 wt% to the monomer) and spin-coated onto the surface of the full packaged UV micro-stripe device. The thickness of the PFO blend was ~20μm. Polymeric structures were formed through local curing by the UV beam generated from the micro-stripes underneath. A current of 5.0mA was injected to each single micro-stripe to produce an optical power of 18μW. The PFO blend film was cured for 0.5s with the exposure dose of 15.7mJ/cm^2. Then the unexposed area of the blend layer was washed off in toluene and a single stripe of PFO blend integrated on the LED was formed. Figure 4.7-a shows a comparison between a turned-on bare UV LED stripe (lower) and a turned-on stripe with the integrated PFO blend (upper). The image indicates the LED stripe has been fully covered by the PFO blend and the capability of direct writing the organic light emitting materials on the micro-LED was demonstrated. Figure 4.7-b compares the emission spectra of the bare UV LED stripe and the hybrid stripe. From the spectra, it is observed that the spectrum in the visible region is similar to that of pure PFO, which means the emission wavelength of the LED has been successfully converted. The peak at 370nm is residual pump light through the hybrid device due to the low concentration of the PFO in the blend in this first demonstration.
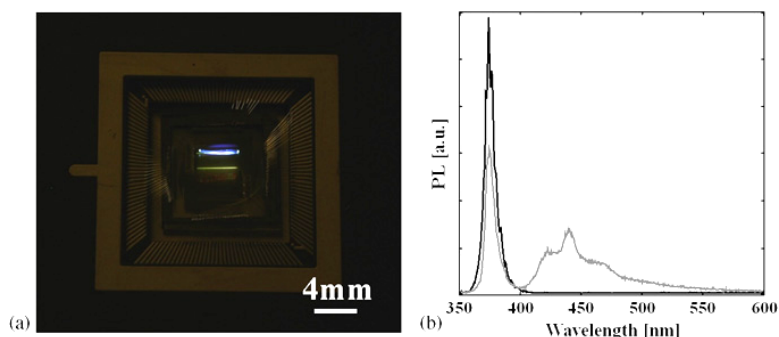

Figure 4.7 (a) Optical image of the turned-on bare micro-LED stripe (bottom) and hybrid LED stripe (top); (b) Emission spectrum of the bare UV stripe (black line) and the hybrid stripe (grey line).

4.1.2 Non-radiative method (Föster resonance energy transfer)

Apart from the radiative hybrid method, other hybrids utilising Föster resonance energy transfer (FRET) [16] have also raised much interest. This work was formally outside of the scope of the current thesis, but we include a discussion of the key results here for completeness. The energy transfer here in FRET occurs via dipole-dipole coupling between excitons in inorganic InGaN-based quantum wells to excitons in the conjugated polymers. These types of inorganic/organic semiconductor structures require not only significant overlap between the InGaN donor emission spectra and the polymer acceptor absorption spectra, but also very small (few nm) dipole separation distance as the FRET is mediated by dipole-dipole interactions [17, 18]. Figure 4.8 shows the scheme and the energy-level diagram illustrating the energetic alignment to maximise the resonant coupling between the inorganic and organic materials [2]. The geometry of this hybrid device of the organic energy acceptor materials placed in sufficiently close proximity around a few nm on top of the inorganic quantum well with a thin spacer, providing an ideal system of non-radiative interactions between inorganic Mott-Wannier (M-W) excitons and organic Frenkel excitons. This first demonstration uses photopumping of the InGaN quantum wells to initiate the process.
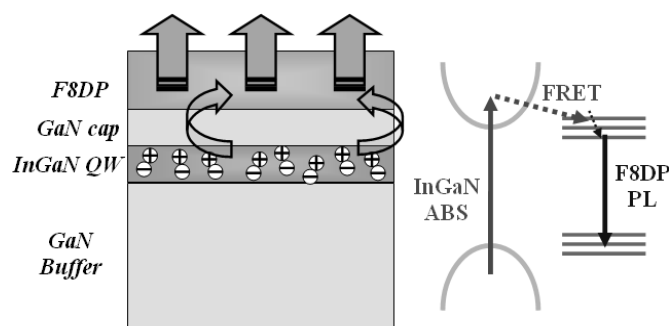

Figure 4.8 Schematic image of hybrid inorganic/organic heterostructures and an energy-level diagram of non-radiative energy transfer: excitations generated from the absorption (ABS) of the InGaN quantum well may resonantly transfer the energy to the singlet excited state of the F8DP polymer layer. After [2].

As the requirement for the FRET structures are rather strict, the structure of the quantum well and polymer layers are both important to demonstrate the resonant coupling. It has been reported that the emission from InGaN can be tuned to provide more spectral overlap to F8DP [19]. The hybrid device is fabricated by depositing a thin layer of F8DP (approximately thickness 5-10nm) on top of specifically prepared InGaN/GaN single quantum well samples with thin GaN caps (of controlled thickness 2.5-15nm). The GaN cap thickness defines the separation distance between the quantum well and polymer, and altering this thickness can control the FRET process resulting in enhancement of the F8DP emission (relative to that of simple radiative transfer) for small separation distance. Figure 4.9 shows the time-integrated photoluminescence spectra obtained at temperature of 15K from three hybrid GaN/F8DP devices A, B, C with different GaN cap layer thickness of 11.8 ± 0.8nm, 3.2 ± 0.5nm and 1.9 ± 0.5nm, respectively. The spectra show the emission peaks from the InGaN quantum well at 387nm, 397nm and 388nm for hybrid devices A, B and C, respectively and vibronic peaks from the polymer at 425nm and 455nm. The difference of the well composition and thickness result in the variation of the emission peaks from the quantum wells and it did not significantly affect the hybrid device study as due to the comparable spectral overlap of the quantum well emission and polymer absorption. The integrated intensity of all three quantum wells was measured to be similar despite the difference in the cap thickness. From the spectra, the quenching of the quantum well emission accompanied by enhancement of the polymer emission proves the non-radiative energy transfer between the quantum well and polymer as the radiative energy transfer is not affected by cap-thickness. However, this process of transferring electrons from InGaN/GaN quantum well to the polymer layer is inhibited by large energy offset from the barrier created at the interface of GaN/F8DP in the order of 1.5eV [20, 21]. Therefore, appropriate control experiments with ~500nm emission from the quantum well were adopted to eliminate any enhancement of the polymer emission from the effects at the
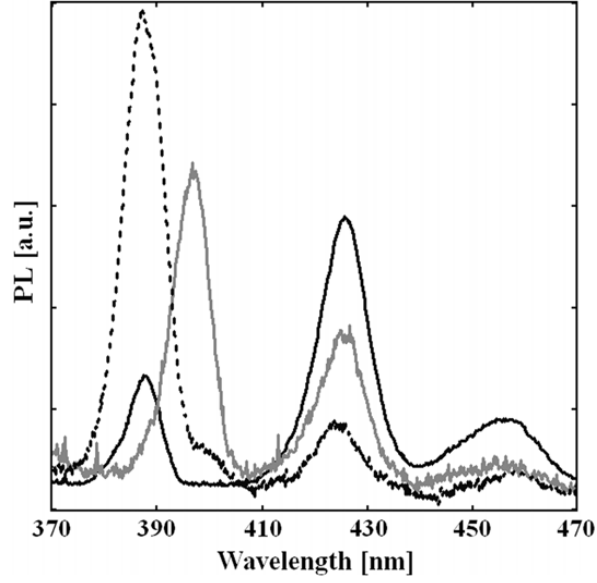
GaN/F8DP interface [2].

Figure 4.9 Time integrated photoluminescence spectra of hybrid device A (black dashed line), B (grey line) and C (black line) at 15K. After [10].

In addition to the cap thickness dependence, the temperature dependence of the GaN quantum well PL data and the dynamics of the FRET process have also been studied. Figure 4.10 is the PL decay curve of the quantum well at 15K fitted to a bi-exponential decay [22]. The shorter decay component is expected from the spectral overlap of the laser pulse and GaN quantum well emission and the longer component represents the recombination decay of the quantum well. Then, the model of the dynamics can be described as $e^{-k_1 t} + e^{-k_{qw} t}$, where k_1 is representative of the laser excitation and k_{qw} is the quantum well recombination decay rate. The fitting to this model obtained the value for $k_1 = 40$ ns^{-1} with corresponding laser pulse duration of 25ps (the resolution of the streak camera). The recombination rate of a QW, in the absence of a polymer over-layer, can be written as

$$k_{qw} = k_r + k_{nr} \tag{4.1}$$

while in the case of a hybrid QW the recombination rate is written as

$$k_{qw}^{h} = k_{r} + k_{nr} + k_{F} \qquad (4.2)$$

where the radiative and non-radiative decay rates are k_{r} and k_{nr}, respectively, while k_{F} is the characteristic Föster transfer rate from the quantum well to the polymer layer. Table 4.1 is the summary data of the radiative decay rate (k_{qw}) before the polymer layer deposition, the recombination rate (k_{qw}^{h}) and estimated Föster transfer decay rate (k_{F}) after polymer layer deposition of hybrid device A, B and C, respectively, from the fitting procedure. The corresponding decay lifetimes to the radiative decay rates of the quantum well with absence of the polymer layer were calculated between 0.72 and 0.92ns. It is noted that singe quantum well devices were used here. Previously reports [23, 24] showed good agreement with the results presented here for the decay lifetime in the 0.5~0.8ns range for similar InGaN/GaN quantum wells at low temperature.
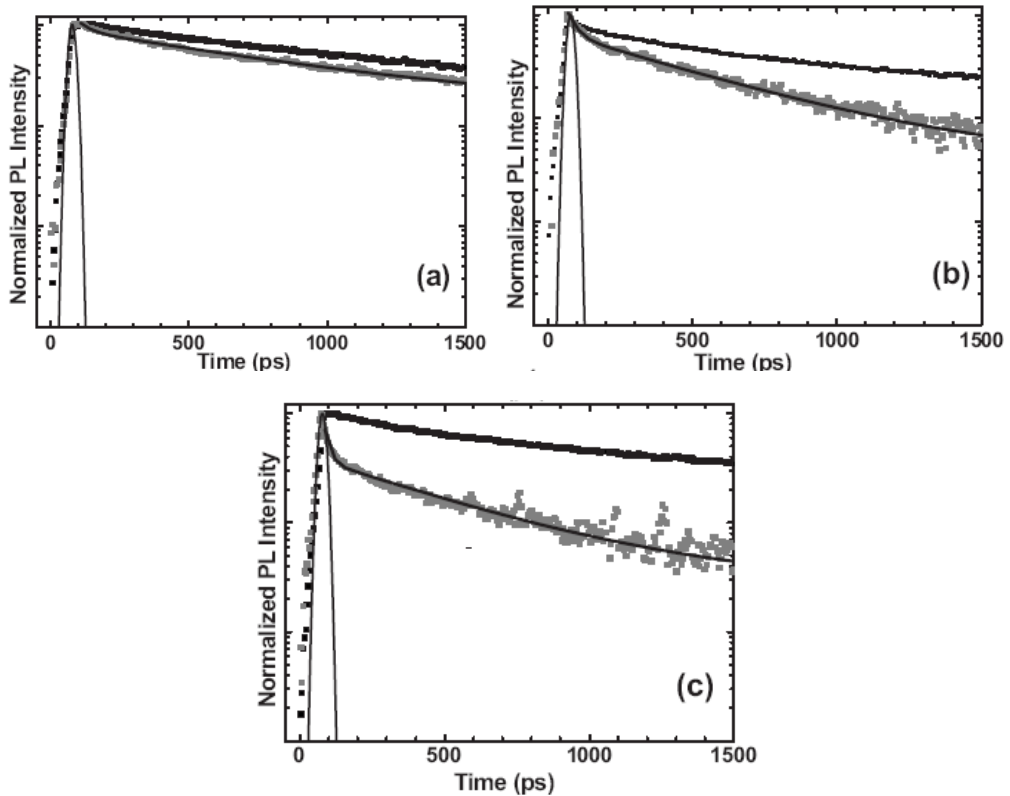

Figure 4.10 PL decay curves of hybrid device A, B and C without (black point) and with (grey point) the F8DP layer, and the bi-exponential fitting curve (black solid line). After [22].

Table 4.1 The radiative decay rate (k_{qw}) before the polymer layer deposition, the recombination rate (k_{qw}^{h}) and estimated Föster transfer decay rate (k_{F}) after polymer layer deposition of hybrid device A, B and C respectively (After [10])

Hybrid	k_{qw} (ns^{-1})	k_{qw}^{h} (ns^{-1})	k_{F} (ns^{-1})
A	1.10	1.27	0.17
B	1.39	2.17	0.78
C	1.30	2.27	0.97

It is evident that the recombination rate of the hybrid device after the polymer layer deposition is greater than for the quantum well without the polymer layer. From the equations (4.1) and (4.2), the FRET rate can be calculated from the hybrid decay rate and the original quantum well radiative rate (see Table 4.1):

$$k_{F} = k_{qw}^{h} - k_{qw} \qquad (4.3)$$

It is obvious that the estimated FRET rate increases significantly as the GaN cap thickness decreases, indicating the separation distance dependence from the polymer.

Regarding the temperature dependence of the hybrid device through FRET, previous detailed reports showed strong temperature dependence for InGaN quantum well with the PL intensity dropping as the temperature increases [25]. Figure 4.11–a shows the PL emission of an InGaN quantum well with 2.5nm GaN cap layer over a temperature range (77-275K) [2].   In contrast, the F8DP polymer is almost entirely temperature independent due to the strongly localized (tightly bound) excited states in organic semiconductors. Figure 4.11–b is the PL spectra of 5nm F8DP film on a quartz substrate in the same temperature range, indicating the temperature independence of F8DP. Data from the hybrid structure shown in Figure 4.11–c are significantly different from that in Figure 4.11–b. The PL intensity of F8DP layer becomes more intense and the temperature dependence appears suggesting the energy transfer from the quantum well emission to the polymer. Any unanticipated

polymer/GaN interface effect according to the temperature dependence has also been ruled out by studying the integrated PL intensity of F8DP in a hybrid structure with a green-emission GaN quantum well [2]. It is observed that the overall PL intensity decreases in the hybrid device when the temperature increases due to the temperature dependence from the quantum well. However, previous study shows the FRET rate reduces slower with the temperature than the radiative recombination rate thus the enhancement due to FRET is more significant at higher temperature [10].
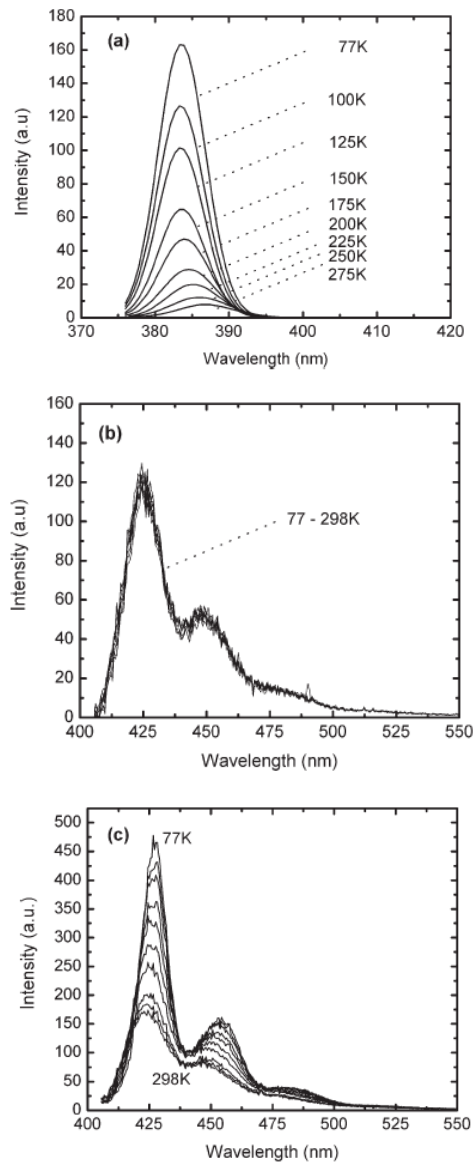

Figure 4.11 (a) Temperature-dependent PL spectra of InGaN quantum well; (b) PL spectra of an F8DP layer at temperature of 77, 100, 150, 175, 200, 225, 250 and 275K with no temperature dependence appearing; (c) temperature-dependent PL spectra of hybrid F8DP/InGaN heterostructure. After [2].

The evolution of the dominant type of excitation with temperature in the InGaN quantum wells has been generally agreed in previous reports [26-28]. Excitons may be localised by impurities and well width variations at low temperature. As temperature rises, the excitons escape and become delocalized as so-called "free excitons" while the specific temperature depends on the quantum well structure parameters [27]. Free carriers become dominant at sufficiently high temperature and excitation rate. It is reported that radiative recombination rate reduces faster than the Föster resonance energy transfer rate with temperature [26] and the FRET rate is higher at room temperature than at 7K for a conjugated polymer guest-host system [29]. When the temperature increases, the excitons and free carriers in the quantum well become more sensitive to the non-radiative recombination and thus the total PL emission intensity will be reduced Hence, the motivation of adopting FRET method in a hybrid structure is to harvest those excitations from the quantum well which would normally non-radiatively decay, as the FRET rate is much faster than the radiative decay in quantum well and any other non-radiative decay at higher temperatures. Delocalized excitons will appear more at higher temperature and also import the difficulties in modelling the process in the hybrid structure though this will further enhance the FRET process over the non-radiative decay from quantum well excitations.

4.2 Inkjet printing light emitting materials as the colour converter on micro-LEDs

In this study, we explored further the radiative approach to fabricating hybrid devices with the micro-LEDs. As it is very difficult to control and define polymeric microstructures from the spin-coating and self-align techniques, we took advantage of the drop-on-demand inkjet printing technique to deposit well-defined

microstructures on the micro-LED elements and obtain the colour conversion. The novel truxene-core oligofluorene materials (T3) and crosslinkable F6BT were used as the organic colour converter materials in the fabrication of the hybrid micro-LEDs, as their absorption spectra have excellent overlap with the emission spectrum of the UV micro-LEDs. The characteristics of these materials have been described in Chapter 2.

There are two major challenges for integrating the organic materials onto the device by inkjet printing. One is how to process the materials and the other is how to deposit the materials onto such small device elements. The main technical challenge of processing organic light-emitting materials is the incompatibility with conventional photolithography materials [30]. Our work on the incorporation of the nanosized oligofluorene truxene with the novel UV-transparent organic photoresist materials opens up an alternative approach to process and micro-pattern of the organic fluorescent nanocomposites [31]. The polymerisation of oligofluorene truxene blends is photo-induced and leads to a cross-linked network, which allows the creation of optical structures. The UV-transparent negative photoresist matrix used is 1,4-cyclohexanedimethanol divinyl ether (CHDV)(Sigma-Aldrich) with the photoacid generator (PAG): p-(octyloxyphenyl) phenyliodonium hexafluoroantimonate (ABCR, Karlsruhe, Germany). Our study suggested the reduction of oxygen diffusion and photo-oxidation after encapsulating the fluorescent molecules with this polymer matrix [31]. The characteristics of the blend materials have been described, and the photopolymerisation mechanism has also been explained, in Chapter 2.

In order to address another challenge of the integration experiment, we explored the advanced inkjet printing technique to create polymeric microstructures and integrate these microstructures on the top of micro-LEDs pixels to achieve color down conversion. The inkjet printing system we used was Dimatix DMP-2800 described in Chapter 3.

Precise alignment and controllable flow are required for this experiment. Thanks to the intelligent function of the instrument, we could successfully achieve the accurate alignment during the deposition, which meets one requirement of this integration experiment. The controllable flow allows the organic droplet to stay stably on top of the pixel before photopolymerisation without any excess flowing into the channel between pixels, and suitable surface treatment further helps to achieve this controllability.

The micro-LEDs used in this hybrid device fabrication are the matrix-addressable top-emission format UV micro-LEDs. As described in the device fabrication details of Chapter 1, there was a SiO_2 insulation layer with in the ring-shaped contact (see Figure 4.12) which offers an opportunity of surface property alteration for the organic materials. The 1H,1H,2H,2H-perfluorooctyldimethylchloro-silane (ABCR, Karlsruhe, Germany) can form a monolayer on the SiO_2 layer to change the surface energy and thus the contact angle of the organic droplet generated from the nozzle of the inkjet printing system (see Figure 4.12) [32]. For instance, by using this treatment, the measured contact angle of truxene blends on a SiO_2 surface was altered from ~2° to ~39° which would effectively prevent the oligofluorene truxene drop from overflowing. Such treatment has been described in Chapter 3 in detail.
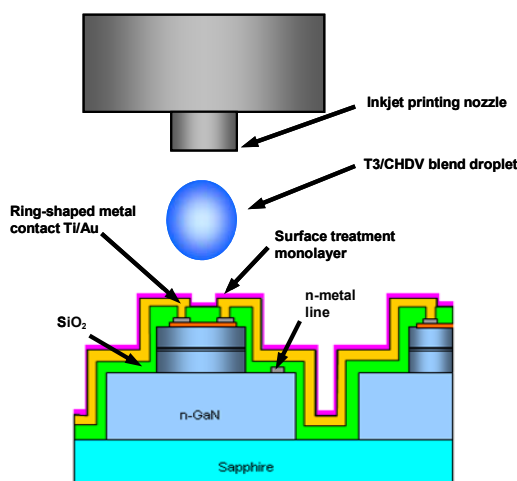

Figure 4.12 Schematic picture of inkjet printing one organic light emitting molecules/CHDV blend droplet on one pixel of the matrix addressable micro-LEDs.

In Chapter 3, we discussed the limitations in printing polymer solutions. Printing the polymer from solvent would result in the "coffee-stain" effect and produce uneven microstructures. Due to the excellent miscibility between the organic light emitting molecules and the CHDV matrix, however, it is not necessary to add any solvent into the blend to obtain a phase-uniform solution. This solventless blend facilitated the fabrication of uniform microstructures by preventing the ring-like stain formation due to the solvent evaporation [33].

Since the two major challenges have been overcome, the integration experiment was ready to be carried out as follows. The organic/CHDV blend was first prepared ready for inkjet printing. Also the surface treatment monolayer was formed on the device surface through vapour deposition. After the inkjet printing system deposited the blend droplet on the top of micro-LED pixel, the whole packaged device was exposed under an ultraviolet (370nm in wavelength) lamp at an energy density of ~15mW/cm^2 for 15min in order to fully polymerize the monomers of CHDV. We have fabricated hybrid micro-LEDs using the truxene-core oligofluorene blends with different blending concentrations and the crosslinkable F6BT. The detailed characteristics of these hybrid devices are shown below.

4.2.1 Truxene oligofluorene as the colour converter

In Chapter 2 it was shown that the absorption spectrum of the truxene-core oligofluorene T3 has an overlap with the emission spectrum of the GaN-based micro-LEDs and thus it is possible to use the T3/CHDV blend as the colour converter for the hybrid device fabrication. The T3/CHDV blend with 1wt%, 5wt% and 10wt% T3 concentration and 0.5wt% PAG to initiate the photopolymerisation was prepared for the fabrication of hybrid inorganic/organic LED devices. It is estimated that, at the concentration of 10wt%, there are around 10^{13} T3 molecules in 1pl of blend. Figure 4.13-a gives plane-view optical images under white light illumination, which

shows that the microstructures of 1wt%, 5wt% and 10wt% T3 (from left to right) in CHDV matrix have been successfully inkjet printed on the treated micro-LED pixel surface. The corresponding oblique-view close-up images of the microstructures taken by SEM (Figure 4.13-b) show the printed polymer microstructure has a smooth surface and well defined edges, demonstrating the effect of the surface treatment and excellent alignment. Three different concentrations of the blends have been successfully printed on respective micro-LEDs pixels, which shows that the processability of the blend materials is not strongly concentration-dependent. This property would give opportunity to engineer higher concentration if it is required in further applications.
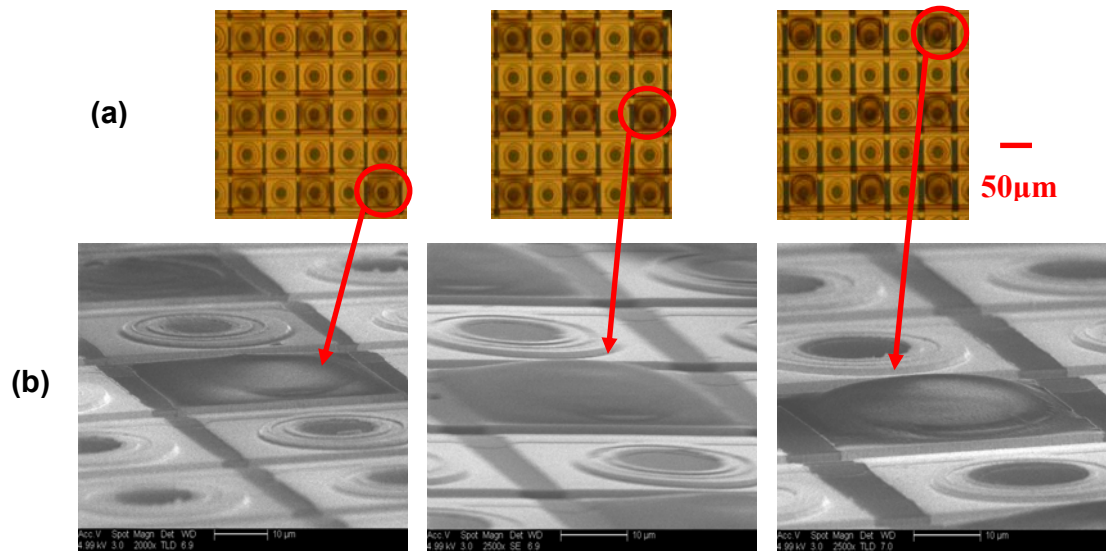

Figure 4.13 (a) Optical microscope image of 1wt%, 5wt% and 10wt% (from left to right) T3 in CHDV matrix integrated on the micro-LEDs pixels; (b) Oblique SEM images of the inkjet printed T3/CHDV blend microstructure of corresponding concentration on single micro-LED pixels.

In order to have a close look at an integrated pixel, we took detailed Atomic Force Microscopy (AFM) images of both a bare micro-LED pixel (left) and a hybrid pixel (right) with 1wt% T3 blend (see Figure 4.14). This further proved that the polymer was smoothly deposited on the pixel with a clean edge. The green curve in Figure 4.15 is the profile curve of the bare micro-LED pixel extracted from the AFM image and the red curve is the hybrid pixel profile indicating the approximate

thickness of the polymer blend layer above. The thickness of the polymer layer is ~1.4µm for 1wt% T3, ~2.4µm for 5wt% T3 and ~2.9µm for 10wt% T3 respectively.
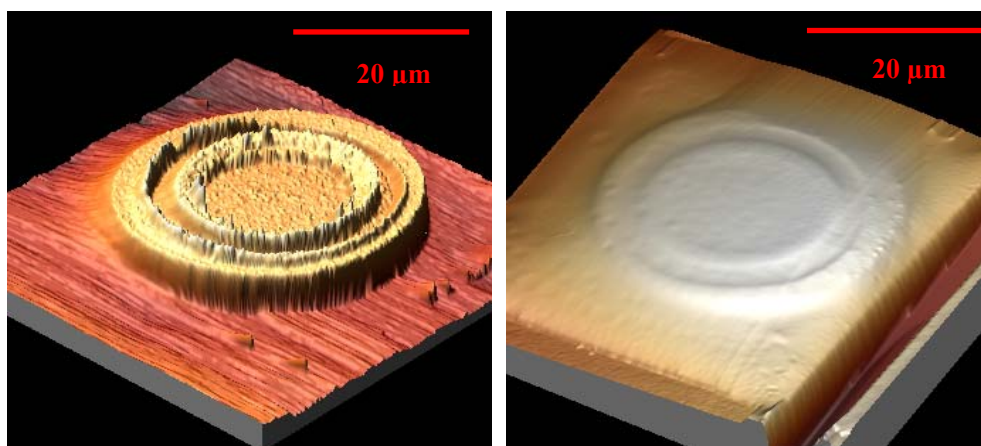

Figure 4.14 AFM images of the bare pixel (left) and the hybrid pixel (right).
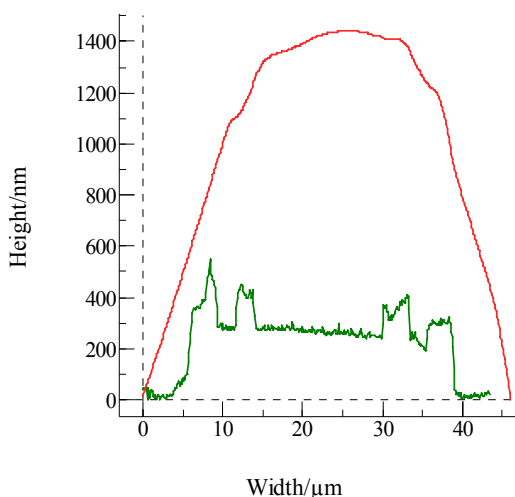
Figure 4.15 AFM profile curves of the bare pixel (green) and the hybrid pixel (red).

Figure 4.16-a shows the comparison images (for 5wt% T3 concentration) between one turned-on bare pixel (top) in the array of micro-LEDs and one turned-on T3/CHDV integrated pixel (bottom). The integrated pixel emitted blue light which originating from the oligofluorene truxene molecules, showing the visible colour conversion phenomenon after integration. Figure 4.16-b and Figure 4.16-c are the optical images of three turned-on adjacent and spaced pixels respectively, which are

integrated with T3/CHDV blends. These images further prove not only the excellent alignment but also the high controllability of the inkjet printing technique used in this work.
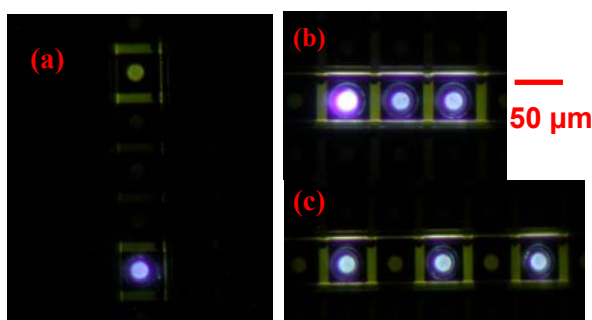

Figure 4.16 Optical microscope images of turned-on pixels (a) two pixels: bare micro-LED pixel (top) and T3/CHDV blend integrated on the pixel (bottom); (b) three adjacent pixels with T3/CHDV blend; (c) three alternating pixels with T3/CHDV blend.

Ideally, the electrical properties of the inorganic light emitter should not be influenced by the integration of the organic fluorescent microstructure. We therefore first characterized the current-voltage (I-V) performance of the LED pixels before and after the integration of T3/CHDV blend microstructures. Our measurements show that the turn-on voltage (3.6V) and I-V characteristics of the representative micro-LED pixels did not change after T3/CHDV integration (see Figure 4.17), demonstrating that the integration achieved by inkjet printing does not degrade the electrical performance of the inorganic micro-LEDs in the hybrid device.
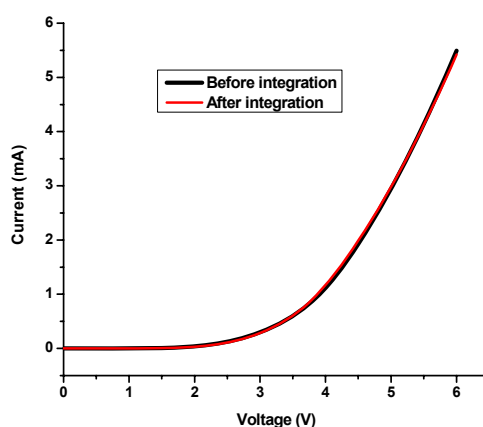

Figure 4.17 I-V curves before and after 1wt% T3 blend droplets integrated on the pixel.

133

As the aim of the integration is to down convert the UV light emitted from the inorganic LED to visible wavelength via optical pumping the organic light emitting molecules, we have carried out spectral measurements to investigate the colour conversion of the integrated device. Figure 4.18 is the normalized photoluminescence spectrum of printed T3/CHDV blend microstructure pumped by the AlInGaN micro-LEDs underneath with an injection current of 7mA. This spectrum was measured by using a home-built micro-PL system, which was specially designed for measuring PL spectra from micro-scale emitters (described in Chapter 4). It was observed that there were two parts of emission in the spectrum, one was the oligofluorene truxene molecule emission at 408nm, 428nm and 458nm respectively, another one was the transmitted UV emission at 368nm from the micro-LED pixel. The photons emitted from the micro-LED pixel at short wavelength are radiatively transferred to the truxene molecules in the polymer matrix, generating longer wavelength emission. As the CHDV matrix is UV-transparent, the unconverted UV light transmits through the matrix, forming the predominant peak in the spectrum. This observation clearly demonstrates the optical pumping of organic light emitting molecules by the UV micro-LED pixel to achieve UV to blue colour conversion.
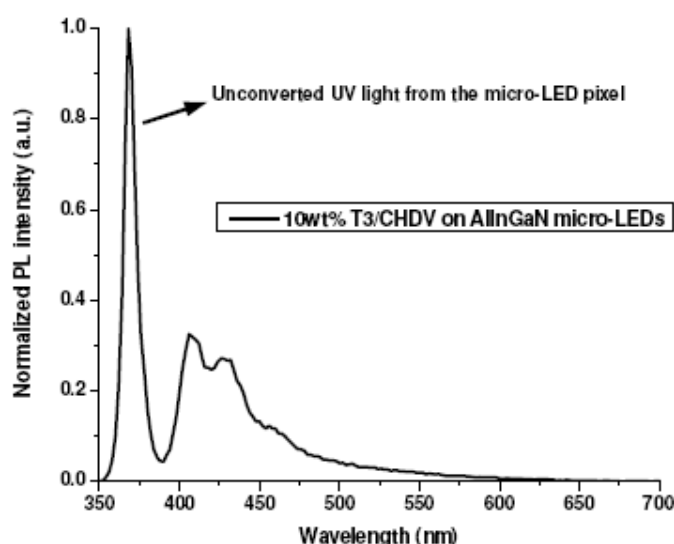

Figure 4.18 Normalized photoluminescence spectrum of a single micro-pixel with integrated T3/CHDV blend driven at 7mA current.

With increased injection current, more photons are generated from the micro-LEDs and, by radiative transfer, the truxene oligofluorene molecules emit higher intensity of (photo)luminescence. To fully understand the emitting performance of the hybrid device, it is necessary to investigate the current dependence of the T3/CHDV blends and the colour conversion saturation of the T3/CHDV microstructure. Figure 4.19, 4.20, and 4.21 show the experimental spectra and images of the 1wt%, 5wt% and 10wt% T3/CHDV blend microstructure pumped by a micro-LED pixel underneath under increasing currents. The spectra show no obvious peak wavelength shift and the peak broadening of both UV and blue emission during the evolution. It can be seen that in all the three concentrations from 1 wt% to 10 wt%, the blue emission from the hybrid pixel increases under increasing current, indicating some saturation of the hybrid device. Moreover, emission at 550nm in the spectra is observed relatively to reduce with increasing concentration of T3, indicating the material photo-oxidation caused by oxygen diffusion is less in higher concentration of T3 in CHDV matrix. This may, however, be due to the thicker polymer layer on the pixel making the oxygen diffuse harder (see discussion referring to Figure 4.15).

Figure 4.22 shows the integrated PL intensity from the blue emission of the hybrid pixel and the UV emission transmitted from the underneath, as a function of the LED driving current, taking the 5wt% T3/CHDV blend as an example. The integrated peak intensity was calculated for the 408nm peak (integrated from 390nm to 418nm). The integrated intensities of the blue peak (S_{T3}) were rising as the current rose suggesting no obvious saturation of the T3 molecules yet at 7mA. Further characterisations of colour conversion saturation and device lifetime are under investigation.
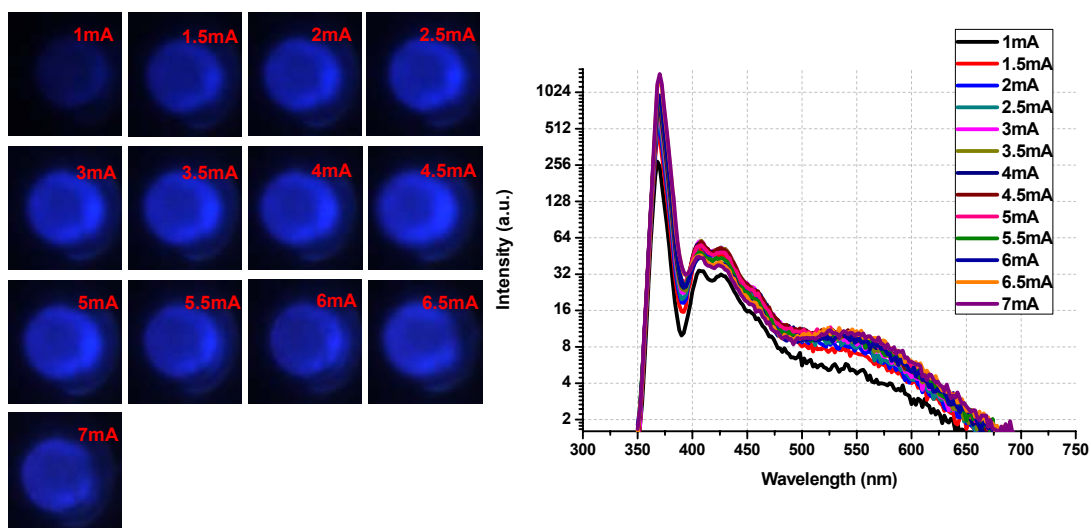
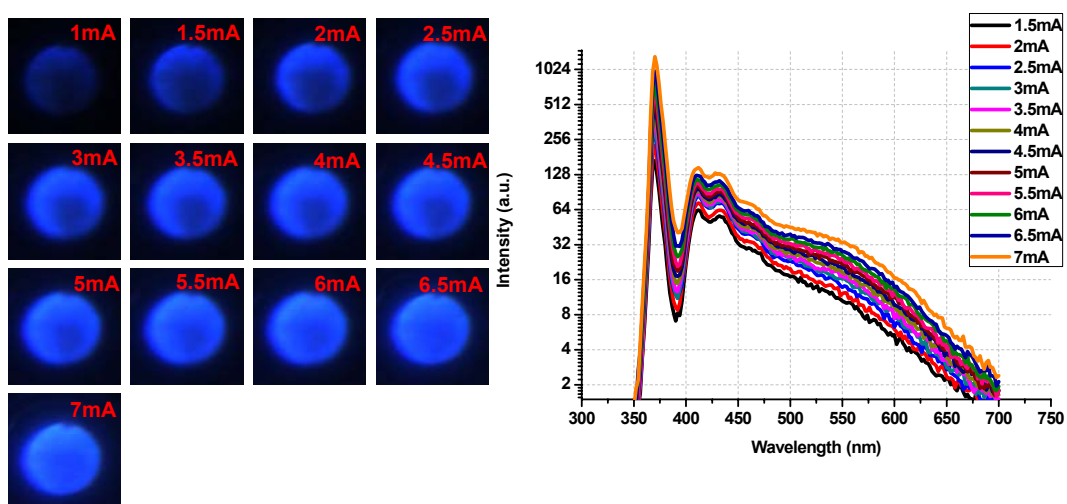Figure 4.19 Images and PL spectra of a 1wt% T3/CHDV hybrid pixel.

Figure 4.20 Images and PL spectra of a 5wt% T3/CHDV hybrid pixel.
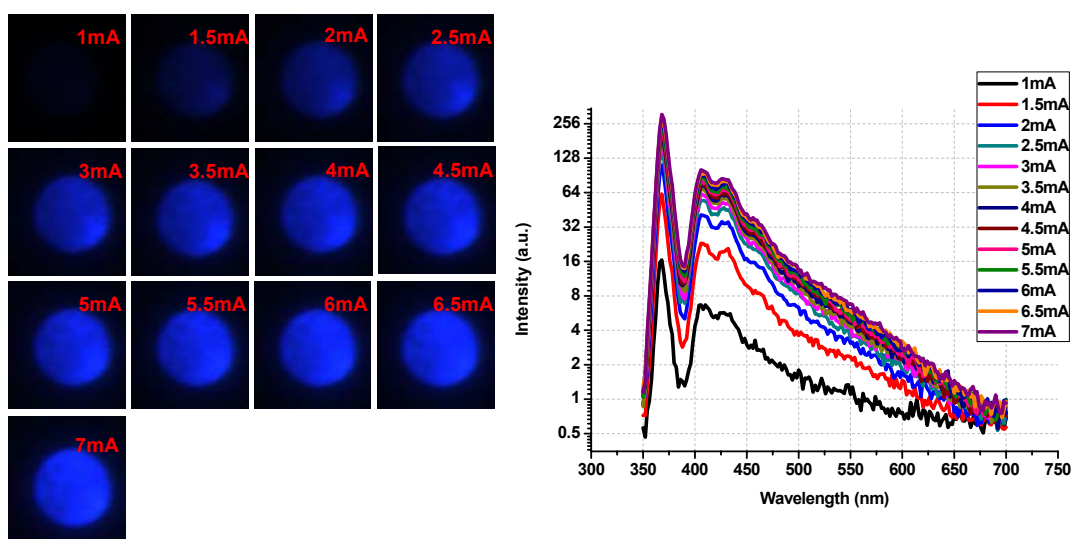

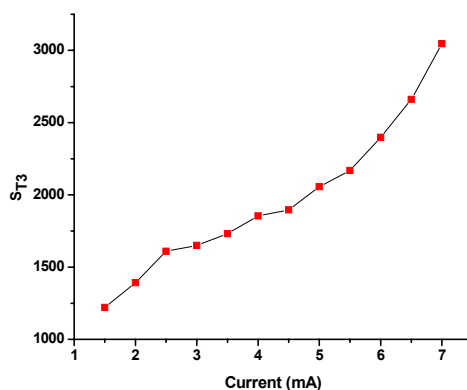Figure 4.21 Images and PL spectra of a 10wt% T3/CHDV hybrid pixel.

Figure 4.22 The plotting of the integrated output intensity of 5 wt% T3/CHDV hybrid pixel as a function of driving current. S_{T3} is the integrated intensity of the peak at 408nm.

To determine the colour conversion efficiency of this hybrid device, the optical output powers of the bare UV LED pixel and T3/CHDV integrated LED pixel were measured. During the measurements, a UV-sensitive Si photo-detector was placed in the close proximity (~2mm) of the LED emitter. The light output powers of 10wt% T3/CHDV hybrid pixel were measured under different injection currents and are plotted in Figure 4.23. It is shown that the bare UV pixel of 16μm in diameter gives a maximum output power of 48nW driven by 7mA current (~5.9mW/cm^2 optical power density at a driving current density of 870.8A/cm^2, current injected through the whole pixel area, 32μm in diameter). It is noted that the bare pixel output power is somewhat low compared to our previous reports [5] as this work was conservatively carried out on a non-optimised device to establish the principle of this pixellated colour conversion scheme. After printing a T3/CHDV blend microstructure on the same pixel, the pixel output power was measured again. As only the emitting power from T3 was required to be characterised, a coloured glass long-pass filter with a cut-off wavelength at 390nm and 70% transmission at 415nm was used to remove the unconverted UV light. The measured output powers of the integrated pixel are also plotted in Figure 4.23. It is shown that the output power of the integrated LED pixel is 17nW at a driving current of 7mA (~2.1mW/cm^2 optical power density at a driving current density of 870.8A/cm^2). Thus, the colour

137

conversion efficiency of the T3/CHDV blend microstructure under 7mA driving current is calculated to be 35.4% (50.5% at 7mA if the compensation of the loss from the filter is taken into account). This colour conversion efficiency is relatively high, demonstrating the T3/CHDV blend is an efficient colour converter and the organic blend microstructure has been successfully integrated with the inorganic LED pixel by inkjet printing. Meanwhile, the conversion efficiency of the 1wt% and 5wt% T3/CHDV hybrid pixels were calculated to be 39% and 59.3%, respectively, with after compensation for filter loss. It may be expected that a still higher concentration of T3 in CHDV matrix would result in higher colour conversion up to the point when the light emitting molecules are saturated. However, the 5 wt% T3/CHDV shows the highest conversion efficiency we found so far and this may due to the broadening of the absorption spectrum of T3 molecules under higher concentration. Figure 4.24 is the absorption spectra of 1wt%, 5wt% and 10wt% T3/CHDV blends and it is observed that the spectrum of 10wt% T3/CHDV is much broader than the others, which would cause extra self-absorption in T3 molecules at the T3 emission wavelength range and might result in decrease of the emission efficiency and conversion efficiency. Therefore the potential conversion improvement of the hybrid device in the future requires careful consideration of the balance between the concentration increase and maintaining conversion efficiency.
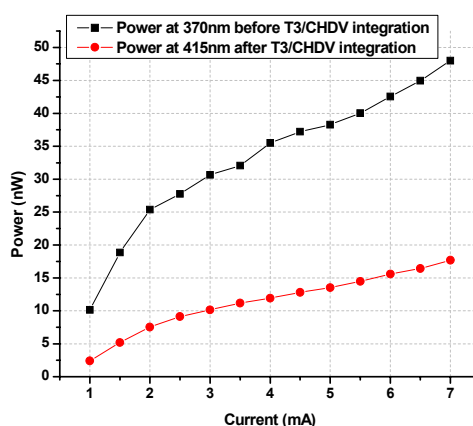

Figure 4.23 Optical output power plotting of the micro-LEDs pixel before and after 10wt% T3/CHDV integration via inkjet printing under increasing injection current
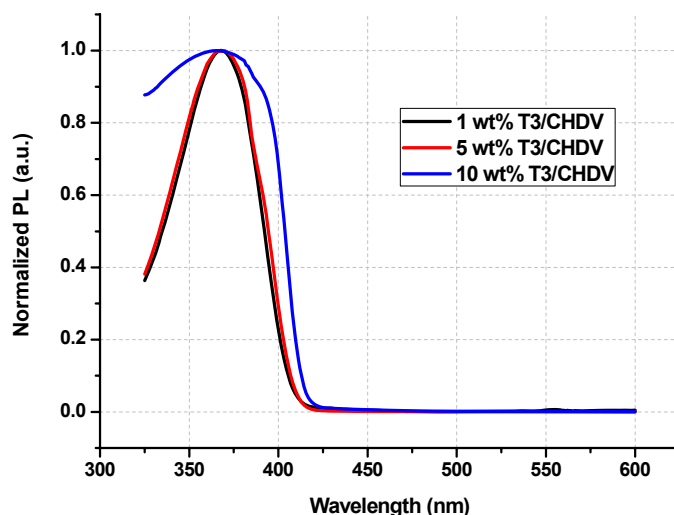
Figure 4.24 Absorption spectra of 1wt%, 5wt% and 10wt% T3/CHDV blends. Note the broadening at the highest concentration.

4.2.2 Polyfluorene as the colour converter

In order to further demonstrate the high versatility of this fabrication technique and the capability of fabricating multi-colour hybrid devices for display applications, we have also integrated photo-crosslinkable F6BT green colour converter onto the micro-LED pixels by inkjet printing. The synthesis and characteristics of the vinyl-functionalized light emitting polymer, the photo-crosslinkable F6BT, have been introduced earlier. Since the miscibility of F6BT with the CHDV transparent polymer matrix was not very good, toluene solvent was used to dissolve the F6BT powder first. Then the toluene solution was mixed with the CHDV polymer and the mixture was put in the heated vacuum oven to remove the toluene afterwards. The preparation methods were studied in Chapter 2. It is observed that the absorption spectrum of the F6BT/CHDV blend overlaps with the emission spectrum of the micro-LED, which shows the blend materials to be suitable as colour converters on the micro-LEDs. The printability of the photo-crosslinkable F6BT/CHDV blends has been proved in Chapter 3. The hybrid device using the F6BT/CHDV blends was

fabricated using the same method as the T3/CHDV hybrid device as we now describe.

A 2wt% F6BT/CHDV was printed on the top of the device pixel and Figure 4.25-a shows the turned-on images of the hybrid pixel (top) and the bare pixel (bottom). Though the converted light is yellow-greenish and similar to the bare pixel, the light from the hybrid pixel is brighter and the green light from the side wall of the pixel indicating the light emitting polymer layer is deposited on the pixel. Figure 4.25-b shows two distant turned-on pixels with the F6BT/CHDV blends on, suggesting excellent controllability of the inkjet printing technique. Moreover, two different colour converters could be deposited on the same device, which further proves high flexibility and controllability of this hybrid device fabrication method and also the future potential applications of full colour display on one single device. The F6BT/CHDV (left) and T3/CHDV (right) blends have been integrated onto the micro-LED pixels at the same time, which is shown comparing with the bare pixel (middle) in Figure 4.25-b.
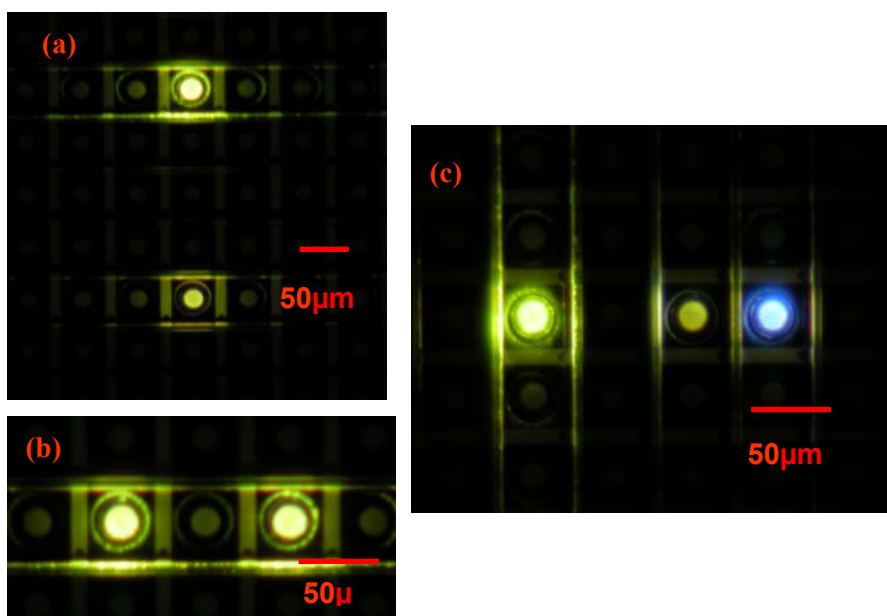

Figure 4.25 Optical microscope images of turned-on (a) two pixels: F6BT/CHDV blend integrated on the pixel (top) and bare micro-LEDs pixel (bottom); (b) two distant pixels with the F6BT/CHDV blends integrated on; (c) three pixels: F6BT/CHDV blend integrated on the pixel (left), bare pixel (middle) and T3/CHDV blend integrated on the pixel (right).

The electrical property is always important to the hybrid device performance. The current-voltage (I-V) curves show whether the device performance has been maintained after the photo-crosslinkable F6BT/CHDV blend was integrated onto the pixel. Figure 4.26 is the I-V curves before and after the F6BT/CHDV blend deposited on the micro-LED pixels, which clearly shows the difference is not severe after the light emitting molecules were printed on the pixel.
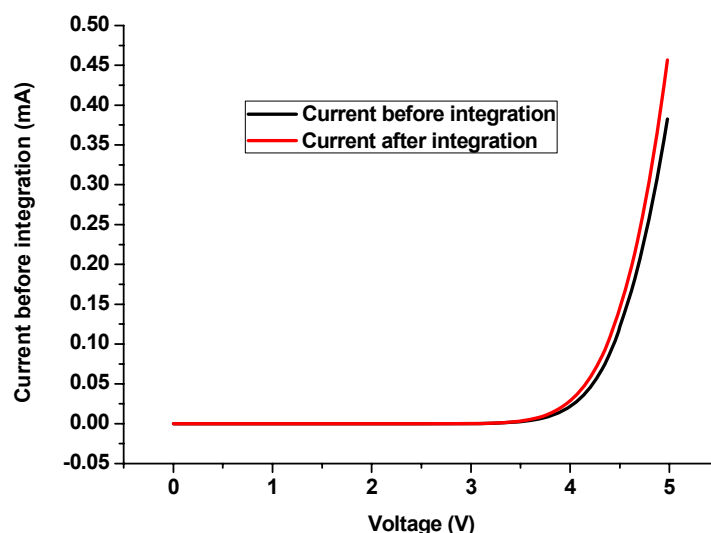
Figure 4.26 I-V curves before and after the F6BT/CHDV blends integrated on the top of the micro-LED pixel.

A photoluminescence spectrum study was carried out for the F6BT/CHDV blend hybrid device. Figure 4.27 shows the normalised photoluminescence (PL) spectrum of the F6BT/CHDV blend hybrid AlInGaN micro-LEDs at an injection current of 0.15mA. From the spectra measured from the home-built micro-PL system, it was observed that there were again two parts of emission in the spectrum as for the blue emission hybrid device, one being the transmitted UV emission at 369nm from the micro-LED pixel and the other one was from the F6BT/CHDV blends at 534nm, similar to the liquid state solution of F6BT. It proves that the photons emitted from the micro-LED pixel were radiatively transferred to the blend materials for longer wavelength emission. The unconverted UV light transmits through the matrix

dominates in the spectrum and the PL spectrum at this low injection current shows obvious green colour conversion from the UV micro-LED pixel.
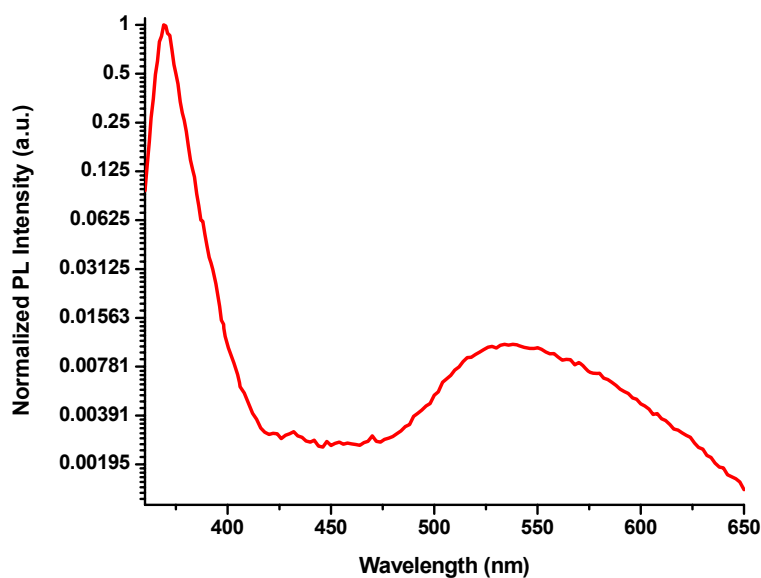
Figure 4.27 Normalized photoluminescence spectrum of a single micro-pixel with integrated F6BT/CHDV blend driven at 0.15mA current.

The colour conversion efficiency was determined by the ratio of optical power after the F6BT/CHDV blends were deposited onto the pixel, compared to the bare pixel before the integration. The method for the measurement was almost same as the one for the T3/CHDV blend hybrid device and the only difference was that the cut-off wavelength of the coloured long-pass filter was 450nm, which transmitted 95% light at 530nm. The light output power is plotted in Figure 4.28. It is observed that before the light emitting colour converter was integrated onto the pixel, the light output power reached 6μW at driving current of 7mA (2985.6mW/cm^2 optical power density at a driving current density of 870.8A/cm^2). After the F6BT/CHDV blend microstructures were fabricated on the micro-LED pixel, the light output power was 1.5μW at driving current of 7mA (746.4mW/cm^2 optical power density at a driving current density of 870.8A/cm^2). It was calculated that around 25% UV light from the

micro-LED pixel has been converted to green light (26.3% at 7mA if the loss from the filter was compensated.). However, the light output power after the light emitting molecules integration was found to gradually decrease when the pixel was continuously turned-on for longer time (e.g. ~10min). It may due to the possible toluene residue in the blends materials destroying the protection of the polymer matrix from the oxidation. Therefore, the conversion efficiency of the F6BT/CHDV hybrid device could be improved not only by increasing the concentration of the light emitting molecules in the polymer matrix, but also by controlling the stability of the F6BT/CHDV blends.
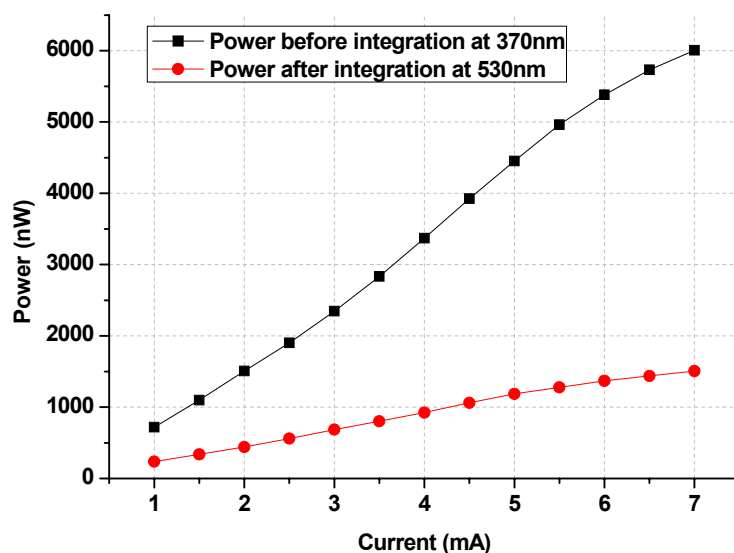

Figure 4.28 Optical output power plot of a micro-LED pixel before and after F6BT/CHDV integration via inkjet printing, versus injection current.

4.3 Summary

In this chapter, we explained that the motivation of fabricating hybrid inorganic/organic devices is to combine the attractive electrical properties of GaN-based materials and high photoluminescence yields of organic molecules to

open a new route of developing low-cost and highly efficient light sources. The fabrication methods of this kind of device have been divided into two categories: radiative and non-radiative.

The radiative route has been reviewed first, in which the organic light emitting materials are used as a colour converter to accomplish the radiative energy transfer from the inorganic semiconductors to organic materials. Red, green and blue light have thus been achieved from both the commercial LEDs and the micro-structured LEDs through film coating. Self-alignment has also been demonstrated to fabricate hybrid devices. Next, the non-radiative method was introduced. The effect of the cap thickness of GaN on the InGaN quantum well has been discussed, and the temperature dependence and dynamics of the non-radiative energy transfer have been studied.

After the background introduction of the hybrid device, the work on fabricating the hybrid inorganic/organic device by inkjet printing via radiative method has been discussed in detail. The blue-emission truxene oligofluorene T3/CHDV blends and green-emission F6BT/CHDV blends were adopted as the colour converters in the hybrid micro-LEDs. Various concentrations (1wt%, 5wt% and 10wt%) of T3/CHDV blends have been used to fabricate hybrid devices. The morphology, electrical performance and conversion efficiency of the hybrid devices were characterised. The integrated polymer blends have a smooth surface on the pixel of the micro-LEDs and the I-V curve was maintained after the converter materials were integrated. The power conversion efficiency of 1wt%, 5wt% and 10wt% T3/CHDV blends converters was calculated to be 39%, 59.3% and 50.5% respectively and that of F6BT/CHDV blends was 26.3%.

References

1. M. Achermann *et al.*, "Energy-transfer pumping of semiconductor nanocrystals using an epitaxial quantum well," *Nature* **429**, 642 (2004).

2. G. Heliotis *et al.*, "Hybrid inorganic/organic semiconductor heterostructures with efficient non-radiative energy transfer," *Adv. Mater.* **18**, 334 (2006).

3. G. Heliotis *et al.*, "Spectral conversion of InGaN ultraviolet microarray light emitting diodes using fluorene-based red-, green-, blue-, and white-light-emitting polymer overlayer films," *Appl. Phys. Lett.* **87**, 103505 (2005).

4. S. Nakamura, "Current status of GaN-based solid state lighting," *MRS Bull.* **34**, 101 (2009).

5. Z. Gong *et al.*, "Matrix-addressable micropixellated InGaN light-emitting diodes with uniform emission and increased light output," *IEEE Trans. Electron Devices* **54**, 2650 (2007).

6. H. Xu *et al.*, "Application of blue-green and ultraviolet micro-LEDs to biological imaging and detection," *J. Phys. D: Appl. Phys.* **41**, 094013 (2008).

7. V. Poher *et al.*, "Optical sectioning microscopes with no moving parts using a micro-stripe array light emitting diodes," *Opt. Express* **15**, 11196 (2007).

8. Y. Yang *et al.*, "Hybrid optoelectronics: a polymer laser pumped by a nitride light-emitting diode," *Appl. Phys. Lett.* **92**, 163306 (2008).

9. S.C. Allen and A.J. Steckl, "A nearly ideal phosphor-converted white light-emitting diode," *Appl. Phys. Lett.* **92**, 143309 (2008).

10. C.R. Belton *et al.*, "New light from hybrid inorganic-organic emitters," *J. Phys. D: Appl. Phys.* **41**, 094006 (2008).

11. P.L. Burn *et al.*, "Chemical tuning of electroluminescent copolymers to improve emission efficiencies and allow patterning," *Nature* **356**, 47 (1992).

12. S. Guha *et al.*, "Hybrid organic-inorganic semiconductor-based light-emitting diodes," *J. Appl. Phys.* **82**, 4126 (1997).

13. O.N. Ermakov *et al.*, "Hybrid organic–inorganic light-emitting diodes,"

Microelectron. Eng. **69**, 208 (2003).

14. F. Hide *et al.*, "White light from InGaN/conjugated polymer hybrid light-emitting diodes," *Appl. Phys. Lett.* **70**, 2664 (1997).

15. E. Gu *et al.*, "Hybrid inorganic/organic micro-structured light-emitting diodes produced using photocurable polymer blends," *Appl. Phys. Lett.* **90** 031116 (2007).

16. T. Förster, "Experimentelle Und Theoretische Untersuchung Des Zwischenmolekularen Ubergangs Von Elektronenregungeneragie," *Z. Natur. A: Phys. Sci.* **4**, 321 (1949)

17. T. Virgili *et al.*, "Efficient Energy Transfer from Blue to Red in Tetraphenylporphyrin-Doped Poly(9,9-dioctylfluorene) Light-Emitting Diodes," *Adv. Mater.*, **12**, 58 (2000).

18. T. Förster, "10th Spiers Memorial Lecture. Transfer mechanisms of electronic excitation," *Discuss. Faraday Soc.*, **27**, 7 (1959).

19. L.T. Tan *et al.*, "Photoluminescence and phonon satellites of single InGaN/GaN quantum wells with varying GaN cap thickness," *Appl. Phys. Lett.* **89**, 101910 (2006).

20. V. Bougrov *et al.*, *Properties of Advanced Semiconductor Materials GaN, AlN, InN, BN, SiC, SiGe* (New York: Wiley, 2001).

21. S. Janietz *et al.*, "Electrochemical determination of the ionization potential and electron affinity of poly(9,9-dioctylfluorene)," *Appl. Phys. Lett.* **73**, 2453 (1998).

22. G. Itskos et al., "Efficient dipole-dipole coupling of Mott-Wannier and Frenkel excitons in (Ga,In)N quantum well/polyfluorene semiconductor heterostructures," *Phys. Rev.* B **76**, 035344 (2007).

23. S. Chi-Kuang *et al.*, "Well-width dependent studies of InGaN–GaN single-quantum wells using time-resolved photoluminescence techniques," *IEEE J. Sel. Top. Quant. Electron.* **3**, 731 (1997).

24. S.M. Olaizola *et al.*, "Phonon satellites and time-resolved studies of carrier

recombination in InGaN qunatum wells," *Superlatt. Microstruct.* **41**, 419 (2007).

25. P. Lefebvre *et al.*, "Effects of GaAlN barriers and of dimensionality on optical recombination processes in InGaN quantum wells and quantum boxes," *Appl. Phys. Lett.* **78**, 1538 (2001).

26. S. Kos *et al.*, "Different regimes of Forster-type energy transfer between an epitaxial quantum well and a proximal monolayer of semiconductor nanocrystals," *Phys. Rev.* B **71**, 205309 (2005).

27. R. Pecharrom´an-Gallego *et al.*, "Investigation of the unusual temperature dependence of InGaN/GaN quantum well photoluminescence over a range of emission energies," *J. Phys. D: Appl. Phys.* **37**, 2954 (2004).

28. A. Hangleiter *et al.*, "Anti-localization suppresses non-radiative recombination in GaInN/GaN quantum wells," *Phil. Mag.* **87**, 2041 (2007).

29. L.M. Herz *et al.*, "Time-dependent energy transfer rates in a conjugated polymer guest–host system," *Phys. Rev.* B **70**, 165207 (2004).

30. J.A. DeFranco *et al.*, "Photolithographic patterning of organic electronic materials," *Org. Electron.* **7**, 22 (2006).

31. A.J.C. Kuehne *et al.*, "Direct laser writing of nanosized oligofluorene truxenes in UV-transparent photoresist microstructures," *Adv. Mater.* **21**, 781 (2009).

32. G. Raabe and J. Michl, *The Chemistry of Organic silicon Compounds* (John Wiley, 1989), Chap. 17.

33. E. Tekin *et al.*, "Inkjet printing of luminescent CdTe nanocrystal-polymer composites," *Adv. Funct. Mater.* **17**, 23 (2007).

Chapter 5 Inkjet printing of silver nanoparticles for electronic applications

In addition to using inkjet printing to deposit light emitting materials for photonic applications, printed electronics provides a pathway towards manufacturing low-cost electronic devices over a range of substrates, as the microfabrication of conductive tracks by photolithography is both time-consuming and expensive. Conductive inks used in printed electronics include several categories such as metallic particle dispersed solution and organometallic inks. Suspensions of metallic nanoparticles have low melting temperature due to the size effect, which makes them suitable for low temperature printed electronics. In this work, we printed conductive tracks using solvent-based silver nanoparticles and studied the electrical resistivity of the track on different substrates. The effect of substrate temperature and annealing temperature is studied. Moreover, these conductive tracks were applied to the matrix-addressable and planar micro-LEDs as the electrical interconnections and bonding pads. The electrical performance of the printed tracks was compared with the Ti/Au tracks deposited by sputtering and we demonstrate that these printed tracks are potential substitutes for electrical connections on the micro-LEDs.

5.1 Background on metallic nanoparticles

Metallic nanoparticles which are extremely small-from 1 to 100nm in diameter-exhibit much lower melting point compared to the bulk materials due to their very small size. When heated up to the appropriate temperature, the nanoparticles weld

themselves together to be highly conductive. The size effect on the melting point of the metallic nanoparticles is the main theoretical basis of nanoparticle inks.

The well-known thermodynamic model of melting small particles has been presented by Pawlow (1909). Pawlow's theory was based on considering the equilibrium of a liquid spherical drop with both a solid spherical particle of the same material and its vapour. The equation was written by Pawlow neglecting temperature dependence of the variables $\gamma_{sv}, \gamma_{lv}, \rho_s, \rho_l$ and L_{sv} and high-order approximation as:

$$\frac{T_\infty - T}{T_\infty} = \frac{2}{\rho_s L_{sv} R_s}\left[\gamma_{sv} - \gamma_{lv}\left(\frac{\rho_s}{\rho_l}\right)^{2/3}\right] \qquad (5.1)$$

where ρ_s is the density of the solid phase; ρ_l is the density of the liquid phase; L_{sv} is the latent heat for the solid-vapour phase transition; R_s is the radius of the sphere solid region; γ_{sv} is the solid vapour interfacial energy; γ_{lv} is the liquid vapour interfacial energy; T_∞ is the bulk melting temperature; T is the small-particle melting temperature. After this approximation, there have been further extended theoretical explanations of the size effect results based on phenomenological thermodynamics, statistical mechanics or computer simulation [1-6]. Choosing either the phenomenological model or a particular fusion criterion depends on the assumptions used.

It is obvious that lower melting temperature causes lower sintering temperature which is a critical temperature when a powder compact is densified and the average grain size increases. However, it is also worth mentioning that during sintering metal particles into dense film, an absolute melting is not required. Powders can be sintered to form dense structures not only in complete liquid-state but also in partial liquid state or even solid state according to the sintering theory [7]. Moreover, the nanoparticles' large surface area and anisotropic surface energy among other factors

leads to different mechanisms and kinetic theories of the densification and grain growth [8]. Therefore, the sintering temperature for metallic nanoparticle suspensions may be even lower than the prediction from theoretical models of melting point.

The major challenge of applying the inkjet printing technique for electrical component fabrication is the ink composition which defines the ejection ability, the adhesion to the substrate and the line resolution and profile. As discussed in Chapter 3, the surface tension and viscosity of the fluid determine the velocity, size and stability of the droplet, which establishes the resolution and thickness of the structure and ultimately affects the functional properties of the structure. Nanoparticles are beneficial in printed electronics processes due to their lower sintering temperature and shorter sintering duration compared to the bulk materials, which reduces energy consumption. Among the conductive metals, silver is the most conductive material under ambient condition and is more abundant and less expensive than gold. Hence, currently the nanoparticle silver ink has been applied widely in printed electronics to create interconnections and solder materials in device packages [9], electrodes on polymeric substrates [10] or solar cells [11], or provide continuous bonding strength in three-dimensional inkjet printing [12].

In addition to the control of physical properties during the synthesis of the silver nanoparticles, a good dispersant should be added to the nanoparticles in order to eliminate the clogging of the nozzles in the piezo inkjet printhead, due to the aggregation of nanoparticles. The dispersant also protects the stability of the nanoparticles from viscosity increase caused by aggregation. The main sintering mechanism of the nanoparticle silver ink during the sintering process is shown in Figure 5.1. The sintering process by heating triggers the degradation of the dispersant and finding the proper temperature removes the dispersant from the nanoparticles surface and allows the nanoparticles contact with each other to weld themselves to achieve electrical conductivity [13].
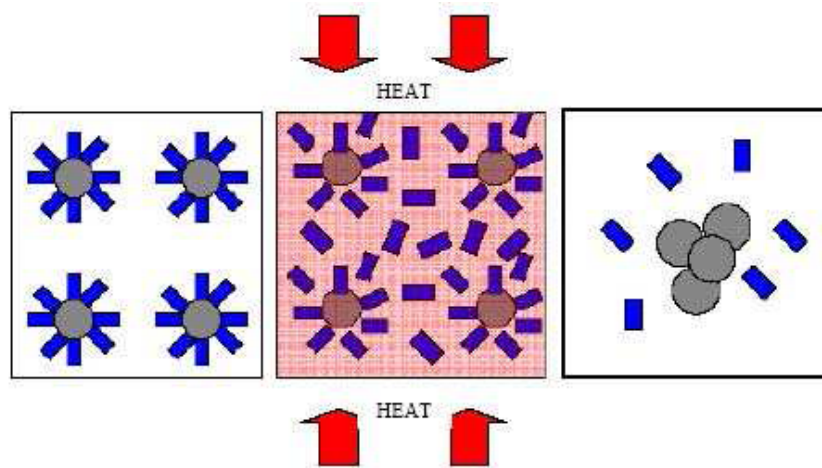
Figure 5.1 Schematic descriptions of the sintering mechanism of nanoparticles with dispersant. The blue bars are the dispersant which prevents the nanoparticles from aggregation. After [13].

The sintering process has been carried out in different ways. Heating by a vacuumed oven or a hotplate under ambient air is the most common method. However, some substrates such as thermoplastic polymers and papers are not suitable for this technique when the sintering temperature is higher than 200℃. Hence, alternative techniques like laser or microwave sintering have been developed to allow the selective heating of the required printed tracks without damaging the substrate [14, 15].

As the main motivation of inkjet printing silver nanoparticles in this work is to fabricate simple interconnections and bonding pads on the micro-LEDs, the printed track needs to be narrow enough to fit the micro-LED design. However, the dimensions of the printed features are normally larger than 100μm as they depend on the nozzle diameter [15, 16]. It would appear that reducing the nozzle size would minimise the line width of the printed structures. However, the requirement on the nanoparticle ink properties becomes stricter with a narrowed nozzle as the size of the nanoparticles should be sufficiently smaller than the nozzle size to prevent clogging. In this work, we adopt the nanoparticle silver ink commercially available from Advanced Nano Products Co., Ltd (ANP), which satisfies the requirements of the DMP inkjet printer and allows comparatively low sintering temperature at ~200℃.

The silver nanoparticles are dispersed in the polar solvent Triethylene Glycol Monoethyl Ether (TGME) and some of the important properties are listed in Table 5.1. The Transmission Electron Microscopy (TEM) images (Figure 5.2) show the silver nanoparticle in the ink are ~7nm in diameter and uniformly distributed in the dispersant matrix (this data obtained from the company product information). The nanoparticle silver ink was printed to form conductive tracks by the DMP-2800 printer on different substrates including glass, silicon and gallium nitride (GaN). These tracks were sintered on the hotplate under ambient air and characterised for their resistivity. Furthermore, the printed silver tracks were also integrated onto the matrix-addressable and planar micro-LEDs surfaces to demonstrate the potential of alternating the metal tracks deposited by the metal evaporator in conventional lithography technique, which simplifies the fabrication process.

Table 5.1 Properties of nanoparticles silver ink from ANP Co. Ltd

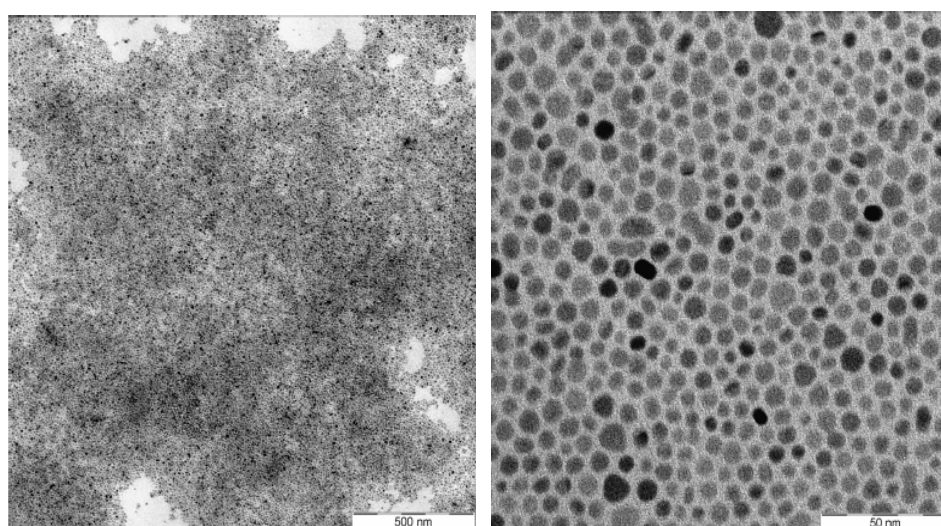| Metal Content (wt%)	35.4
Viscosity (cP)	15.5
Surface tension (mN/m)	37.1

Figure 5.2 TEM images of the nanoparticle silver ink from ANP Co. Ltd.

5.2 Inkjet printing nanoparticle silver ink

Achieving a smooth, narrow printed track from the nanoparticle silver ink depends on the contact angle on the substrate, the drop spacing (distance between the centres of two adjacent droplets) and the substrate temperature during printing. Both the theoretical model and experimental results indicate that the track width is decreased when the contact angle is increased [17-19]. Hence, we adopt the surface treatment described in Chapter 3 to alter the contact angle of the silver ink on various substrates. Table 5.2 shows the contact angle of the silver ink before and after the surface treatment.

Table 5.2 Contact angle of silver ink on various substrates

Effect of PFODCS vapour deposition	Contact angle (°)	
	Before the treatment	After the treatment
Silicon	~9	~35
Glass	~5	~44
GaN	~15	~31

Altering surface-wetting properties of the ink is advantageous to control the printed feature size. In addition, optimising the substrate temperature and the drop spacing is also beneficial in printing solvent-based ink. Increasing the substrate temperature stimulates the evaporation of the solvent in the ink and prevents the printed track from merging and broadening [18, 19]. Figure 5.3 shows typical morphologies of tracks printed at various drop spacing [20]. When two printed drops are far apart, the printed track appears as individual drops (Figure 5.3-a); when the drop spacing decreases, isolated drops overlap but maintain the individual rounded contact line and a scalloped track emerges (Figure 5.3-b); as the drop spacing decreases further, the scalloping is eliminated and a uniform, smooth track is formed (Figure 5.3-c); even closer spacing leads to discrete bulging at the beginning and

along the track (Figure 5.3-d). The bulging is considered to result from the additional drop from printing exceeding the equilibrium contact angle of the bead and outflowing in discrete regions.
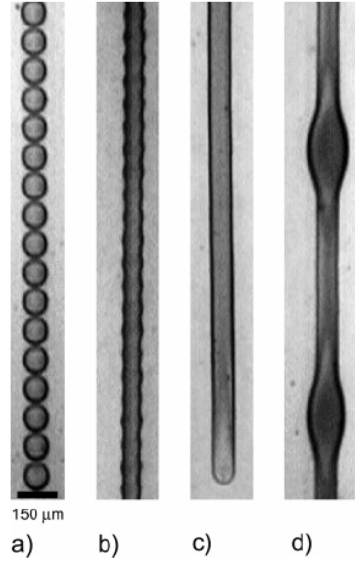

Figure 5.3 Typical morphologies of printed tracks with various drop spacing: a) individual drops; b) scalloped; c) uniform; d) bulging. Drop spacing decreases from left to right. After [20].

Therefore, in this work, the substrate temperature was set at the maximum (60℃) of the DMP printer and the drop spacing of the silver ink on different substrates was optimised as 35μm for glass, 30μm for silicon and 50μm for GaN, respectively. The pulse length and the frequency are 11.520μs and 5kHz when the voltage was adjusted to keep the droplet speed constant at 4m/s for the best performance. The dimensional profile of the printed silver track was measured by stylus profilometry. The electrical resistivity of the printed silver track is calculated from the equation below:

$$\rho = R\frac{S}{l} \tag{5.2}$$

where ρ is the resistivity of the printed silver track; R is the measured resistance; S is the cross-section area of the printed silver track determined by numerical integration of a measured profile; l is the length of the printed silver track.

5.2.1 Printed conductive tracks from silver nanoparticles

The initial stage of fabricating interconnections for micro-LEDs by inkjet printing silver nanoparticles is to test the printability of the silver ink and studying the electrical performance under the preferred sintering conditions.

5.2.1.1 Printability demonstration of the silver ink

The nanoparticle silver ink has been printed on glass to form dots and lines by the DMP printer equipped with the cartridge delivering ~10pl droplets. All the structures were annealed at 200℃ for 60min under ambient air which is the preferred sintering condition from product information. Figure 5.4 shows the dots and lines printed from the ~10pl droplets of nanoparticle silver ink. The dimension of the 1 layer (Figure 5.4-a), 2 layers (Figure 5.4-b), 4 layers (Figure 5.4-c), 6 layers (Figure 5.4-d), 8 layers (Figure 5.4-e) and 10 layers (Figure 5.4-f) dot is 41μm, 49μm, 61μm, 70μm, 77μm and 83μm, respectively, in diameter and 211nm, 434nm, 623mn, 780nm, 1070nm and 1246nm, respectively, in thickness. Meanwhile, the dimension of the line (Figure 5.4-g) is 35μm in width and 209nm thick. All the dots have round shape and the line has as a uniform and smooth edge as Figure 5.3-c, which indicates the drop spacing is appropriate.
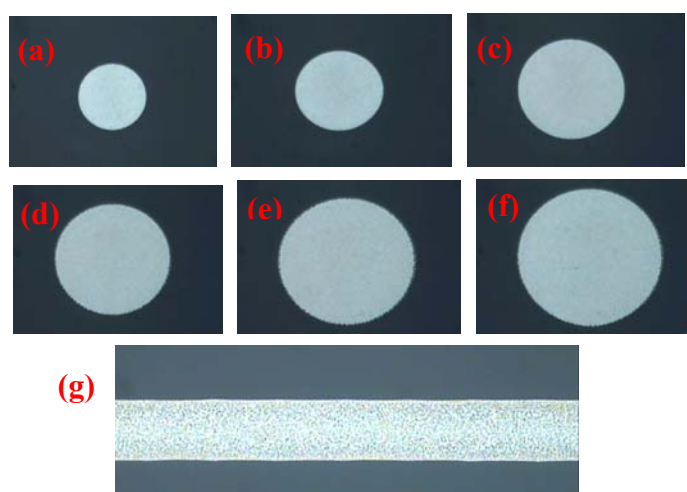

Figure 5.4 Printed dots and line from ~10pl droplets of the nanoparticles silver ink: (a) 1 layer dot; (b) 2 layers dot; (c) 4 layers dot; (d) 6 layers dot; (e) 8 layers dot; (f) 10 layers dot; (g) 1 layer line.

Even smaller dots and narrower lines have been successfully printed onto the glass substrate from the cartridge delivering ~1pl droplets and sintered under same conditions as the structures in Figure 5.4. Figure 5.5 shows (a) a 7×7 array of printed silver dots with a single layer and (b) a straight line. The dimensions of each dot are measured to be ~26μm in diameter and ~260nm in thickness, while the line is ~27μm wide and ~120nm thick. It is obvious that the dots and line have smooth edges and defined shape just as the structures printed from ~10pl droplet, which demonstrates the excellent printability of the nanoparticle silver ink.
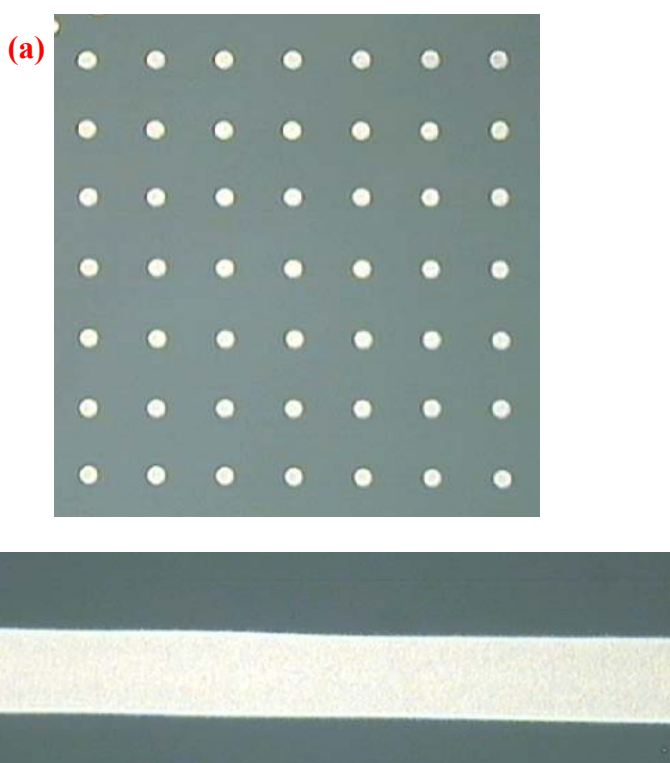

Figure 5.5 Printed dots (a) and line (b) from ~1pl droplets of the nanoparticle silver ink

5.2.1.2 Micro and nano structure of the printed silver track

The microstructure characterisation of the printed silver tracks has been carried out by examining the in surface morphology. Nanoparticle silver ink was printed in a

single layer on the silicon substrate and sintered at 100℃, 150℃ and 200℃ for 30min and 60min, respectively, for microstructure study. The particle size of each track under different sintering conditions was measured by analysing the images taken from the scanning electron microscope (SEM) using image analysis software (Image J).

The printed silver track was also dried at room temperature in atmosphere for comparison of the sintering condition effect (Figure 5.6). The image analysis shows that the particle sizes are distributed monomodally and the average particle size of the dried silver track is 53.9 ± 8.3nm. It is observed from Figure 5.6 that the morphology of the inkjet-printed silver track as dried is approximately described as relatively loose stacks of silver nanoparticles, which could be the initial stage of the coalescence between the nanoparticles. The surface of the dried silver track is not mirror-like as it is for a sputtered silver film suggesting the solvent may not have completely evaporated.
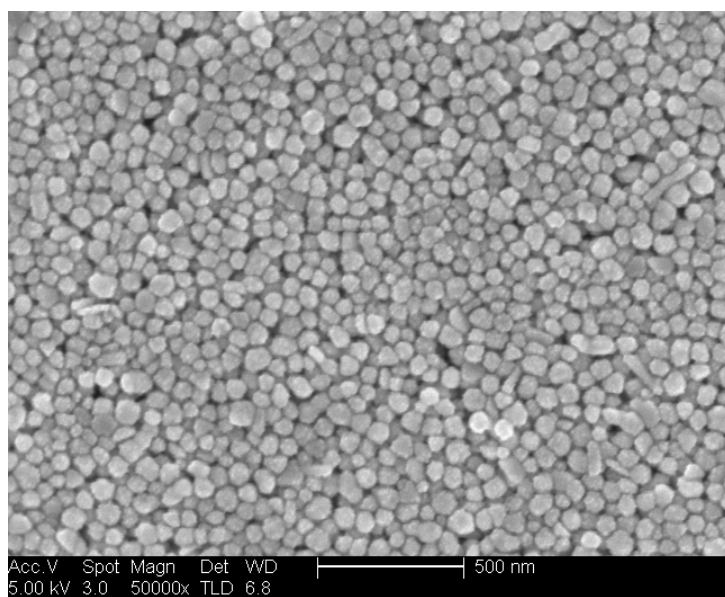
Figure 5.6 SEM image of the dried printed silver track.
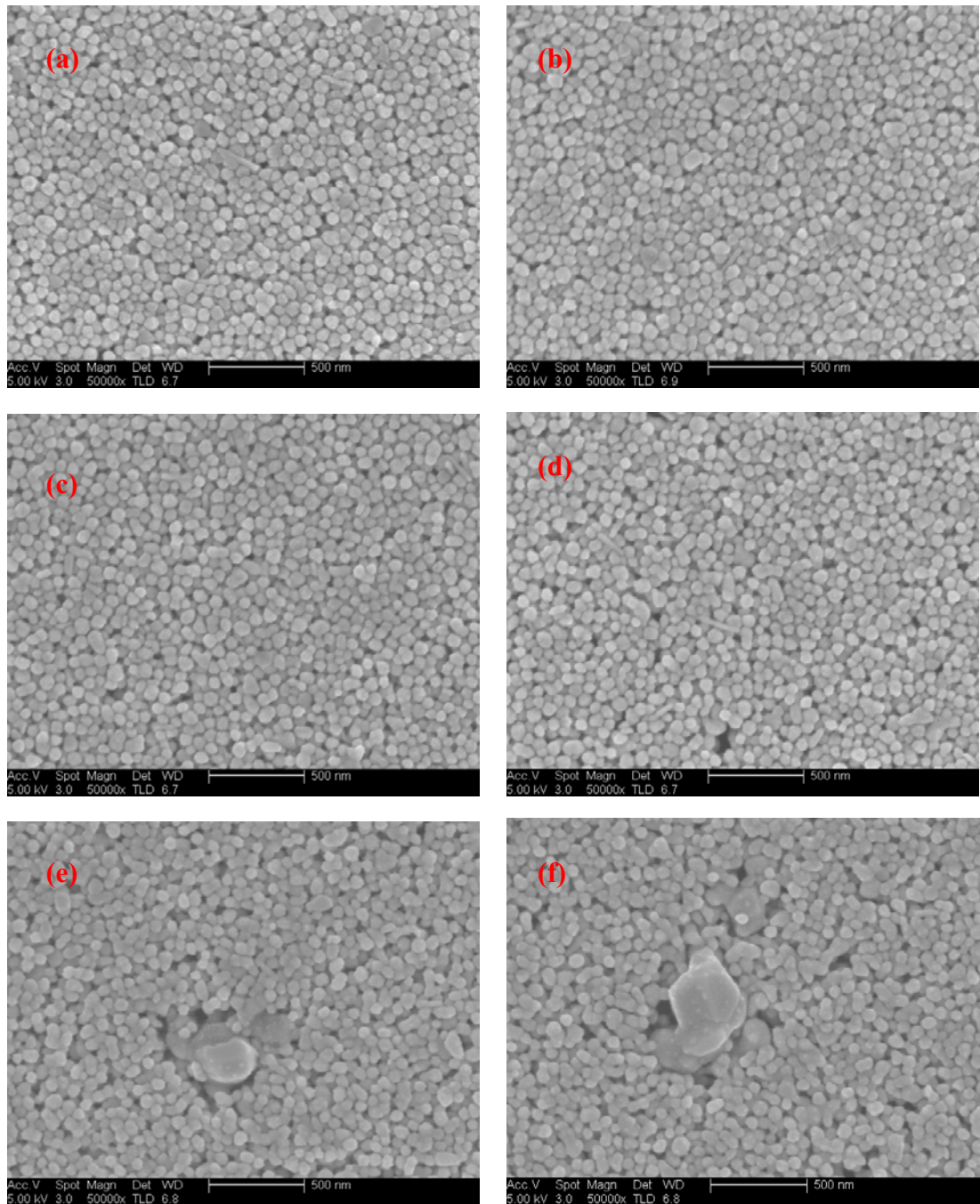
Figure 5.7 SEM images of printed silver track sinter under various temperatures and times: (a) 100℃ for 30min; (b) 100℃ for 60min; (c) 150℃ for 30min; (d) 150℃ for 60min; (e) 200℃ for 30min; (f) 200℃ for 60min.

The inkjet printed silver track as sintered at various temperatures for various times under ambient air is shown in Figure 5.7. When the silver track is sintered at a certain temperature, the dispersant evaporates and then the particles are free from the

prevention of the dispersant and start to contact each other point-to-point for coalescence. Coarsening follows and also grain growth. The silver nanoparticles would form necks with one another and the dimension increases. The average grain sizes in the images (a) to (f) are 65 ± 6.1nm, 68 ± 5.2nm, 77 ± 8.3nm, 79 ± 6.5nm, 93 ± 9.4nm and 105 ± 4.6nm, respectively. It is observed that the grain size does not change much from 100℃ to 150℃, while the grain size at 200℃ is much larger. Also, the grain size is larger for longer sintering time at the same sintering temperature. This may be due to the extent of evaporation of the dispersant during the different sintering conditions. There is also secondary grain growth observed in the samples sintered at 200℃ for 30min and 60min (Figure 5.7-e, f). It was reported previously that silver film deposited in vacuum often shows abnormal grain growth at annealing temperature higher than 240℃ [21, 22]. However, there are also reports on secondary grain growth occurring in silver nanoparticle aggregation at near room temperature [23, 24]. In our work, the observation of this abnormal grain growth at 200℃ in the printed silver track may be due to the specific characteristics of the silver nanoparticles and the dispersant.

5.2.1.3 Resistivity study on the printed conductive tracks

The sintering temperature and time affect the particle size of the printed silver track microstructure and further have an impact on the corresponding electrical resistivity, according to previous reports from other research groups [25, 26]. The electrical resistivity of the printed silver track has been studied and compared with that of bulk silver (1.59μΩ·cm) under different sintering conditions. The effect of various kinds of substrate has also been considered.

The electrical resistivity was calculated from equation (5.2), while the resistance was calculated from the I-V curve obtained by twp-point measurement from two ends of the printed track. The electrical resistivity of printed silver tracks on the

silicon substrates which were used for microstructure analysis was studied first. Table 5.3 summaries the width and resistivity results after sintering at various temperatures and times. The width of the printed track is similar in each case and the typical profile curve of a single layer of printed track is shown in Figure 5.8. The valley at the top of the profile curve of the printed silver track indicates the well-known "ring effect" (described in Chapter 3) which results from dispersant evaporation. The substrate was heated during the printing in order to accelerate the evaporation and suppress the ring effect. However, the maximum setting of the substrate heating in the DMP printer is not high enough to avoid the phenomenon completely. It was also found that the electrical resistivity is dependent on both the sintering temperature and time. The longer sintering time at higher temperature results in lower resistivity. Although the printed silver track shows some conductivity at 100℃, the resistivity can drop to as low as ten times that of the bulk silver when the temperature is 200℃.

Table 5.3 Resistivity and dimension summary of printed silver tracks on silicon

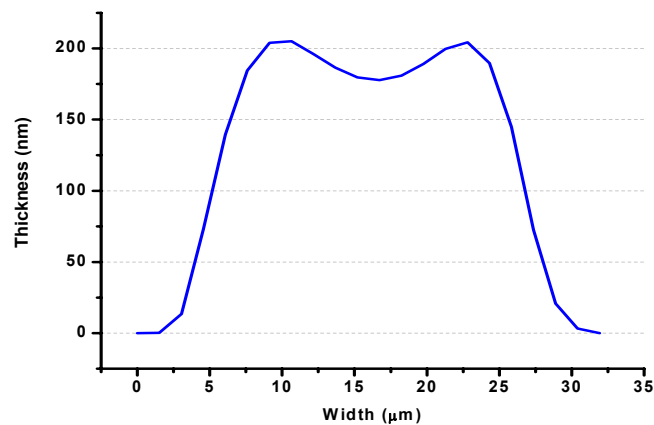|	100℃		150℃		200℃	
	30min	60min	30min	60min	30min	60min
Width (μm)	29	31	32	33	33	33
Resistivity ($\mu\Omega\cdot$cm)	3.42E+07	1.14E+04	36.6	29.8	16.8	15.4

Figure 5.8 Typical profile of the printed silver track as measured by stylus profilometer (Dektak).

The electrical resistivity of the printed silver tracks has also been studied on glass substrates. Figure 5.9 plots the resistivity versus the sintering time for different temperature in this case. It can be seen that there is a significant decrease of the resistivity when the sintering temperature is increased from 100℃ to 200℃, which occurs for the silicon substrate as well. The sintering time usually has a large influence on the resistivity. However, the influence becomes less when the temperature is 150℃ or above and the resistivity tends to reach a plateau after ~30min, which is similar to that reported in [27]. This may imply that the lower temperature sintering could be different from sintering at higher temperature [28, 29].
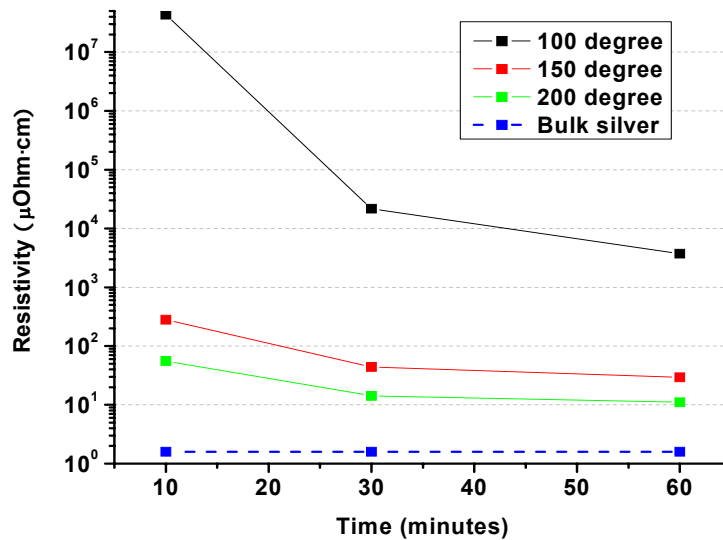
Figure 5.9 Electrical resistivity versus sintering time for different temperatures with tracks printed on glass. The resistivity of bulk silver is also indicated.

As the motivation of this work is to fabricate interconnections and electrodes on the micro-LEDs, the nanoparticle silver ink has also been printed on the usual GaN LED wafer. The sintering condition is 200℃ for 60min and the calculated electrical resistivity is ~37.6μΩ·cm, which is much higher than the one on the silicon or glass substrate under the same sintering temperature and time. This can be explained by

the thermal conductivity difference of silicon, glass and GaN LED wafer. It has been reported that the thermal conductivity of the substrate has an important impact on the droplet evaporation rate [30]. The energy required for the evaporation is gathered not only from the ambient air but also from heat conduction through the substrate if the substrate is thermal conductive. Therefore, when the substrate is less thermally conducting, more energy is maintained in the substrate and the evaporation rate is enhanced. Therefore we compared the thermal conductivities of silicon, glass and GaN LED wafer material. The value for silicon is 149W/mK; glass has a much lower value of 0.8-1.2 W/mK depending on the composition. The GaN LED wafer is grown on sapphire and the thermal conductivity value could vary from 170-180W/mK due to the doping level and defects during the epitaxial growth [31]. As the GaN LED wafer has higher thermal conductivity than the silicon and glass, the heat is dissipated from the substrate and the effective temperature for sintering the silver nanoparticles would be lower leading to the higher resistivity of the ultimate printed track. It is found that the thermal property of a substrate will not significantly affect the resulting resistivity of the printed silver track. Therefore we consider the thermal conductivity of a substrate as a minor effect on electrical resistivity of sintered silver nanoparticles.

5.2.2 Printed conductive tracks applied to device

After the initial study on inkjet printing the nanoparticle silver ink, the printed silver track was applied to the micro-LEDs as interconnections and electrodes. All the silver tracks on the device were printed with ~10pl droplets and sintered at 200℃ for 60min, in ambient air. The printed silver tracks were characterised by measuring the current-voltage (I-V) curves and compared with the standard sputtered Ti/Au metal track.

5.2.2.1 Flip-chip matrix-addressable micro-LEDs

The configuration of the flip-chip matrix-addressable micro-LEDs has been described in the Chapter 1. The silver ink was printed on the SiO_2 insulation layer to connect the pixels on the p-side of the wafer and form electrode pads for p-contact bonding. Figure 5.10 shows that 8 pixels have been interconnected by the printed silver track and the turned-on device image indicates the electrode pads have been successfully wire-bonded. And it is observed that the inkjet printing process and the following sintering did not affect the uniformity of the pixel emission.
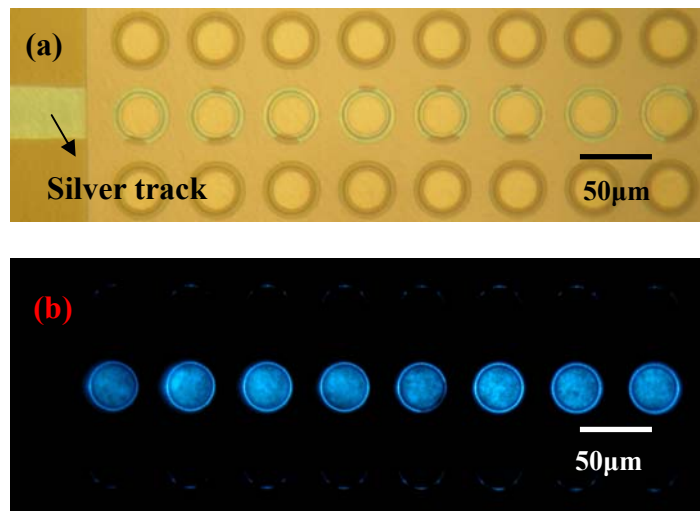

Figure 5.10 Optical microscope images of 8 pixels interconnected by the printed silver track: (a) under normal white light illumination; (b) turned-on.

The printed silver track was characterised by comparing the I-V curve with that of the sputtered Ti/Au track. One pixel was connected by a Ti/Au track and the nanoparticle silver ink was printed and sintered to connect another pixel on the same device. The measured I-V curves are shown in Figure 5.11. It is clear that the I-V curves obtained from the silver track and the Ti/Au track are almost identical indicating that the electrical performance of the printed silver track is comparable to the sputtered Ti/Au track used in the conventional photolithography process. In addition, when the printed silver track connects more than one pixel, the current

under same driving voltage is almost linearly increased as it also is for the normal Ti/Au track (see Figure 5.12).
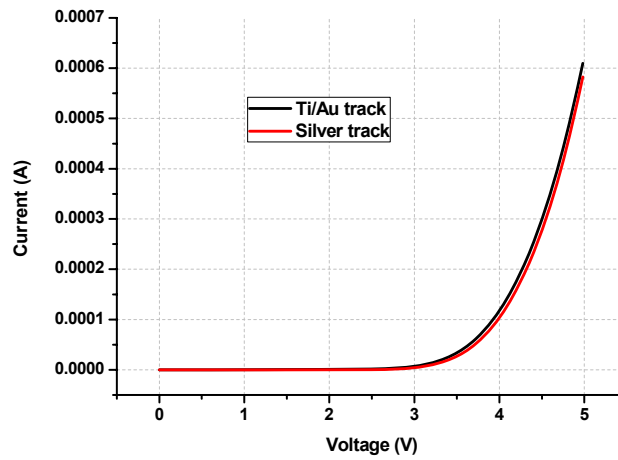
Figure 5.11 I-V curves comparison between the device with a printed silver track and the sputtered Ti/Au track (for one pixel).
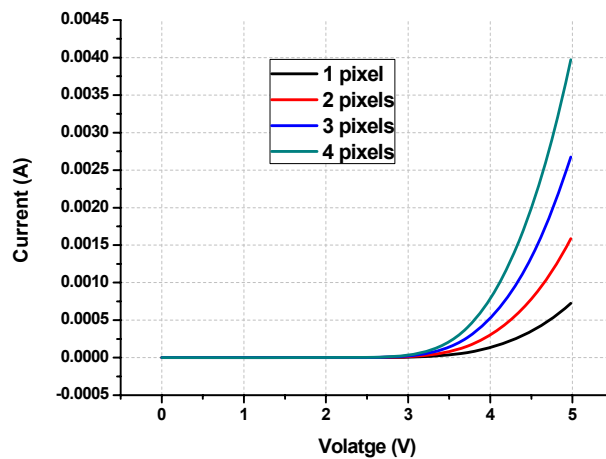
Figure 5.12 I-V curves of the device with printed silver track connecting from one to four pixels.

It is also crucial to study the maximum current the printed silver track could bear as the overloaded current would break down the interconnection on the micro-LEDs. Nine pixels were connected by the printed silver track and the I-V curve shows the silver track could sustain 100mA current without any break-down. The corresponding current density is approximately 2×10^6 A/cm^2 which is much larger than the usual operating current density of the micro-LEDs, (c.f. Chapter 1).

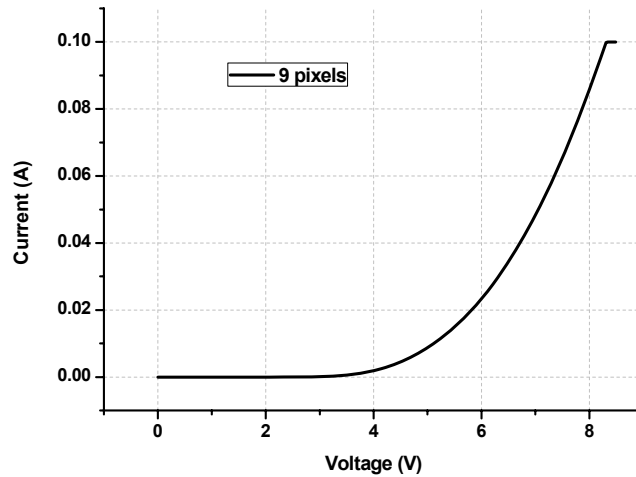Figure 5.13 I-V curve of the device with printed silver track connecting 9 pixels.

5.2.2.2 Planar device

The printed silver track has also been applied to the planar device for the replacement of the Ti/Au track as the p-contact tracks and pads. This process further simplifies the fabrication of the planar device, by avoiding the sputtering deposition. The key process in the fabrication of the planar device is the plasma treatment on the p-GaN surface to increase the resistance and prevent the current leakage from p-GaN-metal interface. In order to demonstrate the printed silver track and the sintering process would not compromise the electrical passivation of the p-GaN surface, silver pads were inkjet printed on both the plasma treated and non-treated p-GaN surfaces and the I-V curves measured. Figure 5.14 shows that the I-V curve of the non-plasma-treated p-GaN surface presents a typical diode characteristic while the current is extremely low on the treated p-GaN surface which could be considered as the passivation layer. The printed silver pads also exhibited excellent electrical conduction during the I-V curve measurements and the capability of wire-bonding.
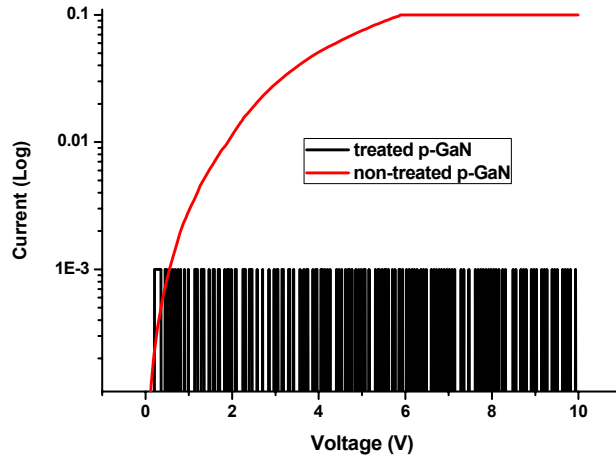
Figure 5.14 Current leakage test of the printed silver track on plasma treated and non-treated p-GaN.

There are different sizes of the round-shape pixel on the planar device varying from 2μm to 100μm in diameter. Due to the mesaless process of the planar device, it was very difficult to see the spreading layer defined by 10nm thick Ni/Au from the fiducial camera on the inkjet printer. Therefore only pixels with diameter larger than 20μm have been connected successfully by the printed silver track. Figure 5.15 shows several examples of different sized pixels connected with the silver track.

Figure 5.15 Optical turned-on images of different sizes of pixel on the planar device: (a) 30μm; (b) 50μm; (c) 70μm; (d) 100μm.

The current-voltage curves are the main factor to characterise whether the printed silver track is comparable to the conventional Ti/Au track. A half of the planar device was deposited with the Ti/Au track and the nanoparticle silver ink was printed and sintered on the other half afterwards. Figure 5.16 shows the I-V curve com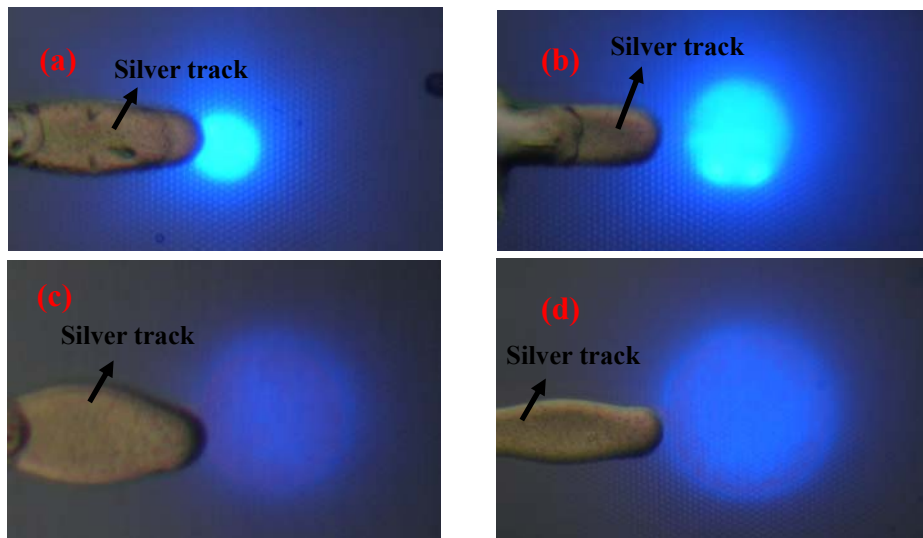parisons between the printed silver track and the sputtered Ti/Au track connecting different sizes of pixel. It can be found that all the I-V curves of the silver track for different diameter pixels are moderately better than those of the Ti/Au track, which may be attributed to slight degradation of the device during the sintering process. The electrical performance of the printed silver track confirms the feasibility of replacing the Ti/Au tracks with silver tracks.
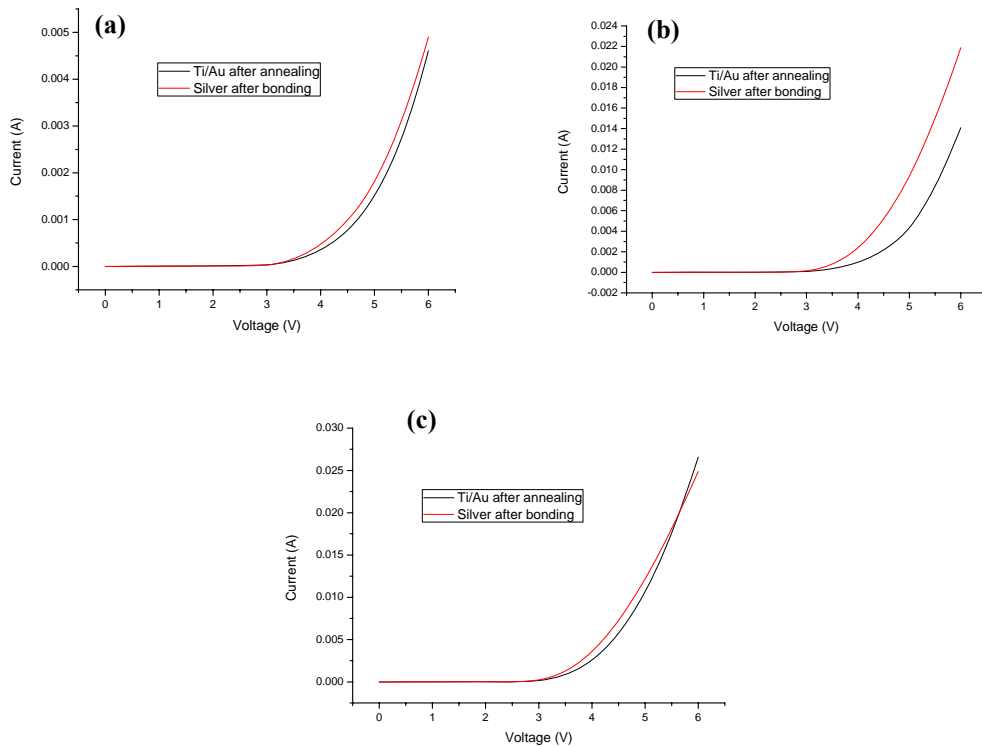
Figure 5.16 I-V curve comparisons for different sizes of pixels connected by the printed silver track and Ti/Au track: (a) 20μm; (b) 70μm; (c) 100μm.

The optical output power of corresponding pixels connected by the printed silver track and the Ti/Au track has also been compared to further prove the

capability of the silver track. Figure 5.17 plots the optical power versus the driving current of pixels 70μm and 100μm in diameter, respectively, as a demonstration. It is obvious that the optical power obtained from the printed silver track is pretty close to that from the Ti/Au track. This suggests the printed silver track is absolutely capable of substituting the conventional sputtered Ti/Au track in the fabrication of the planar device.

Figure 5.17 Power comparison of the pixel size of (a) 70μm and (b) 100μm connected by the printed silver track and Ti/Au track.

5.3 Summary

In this chapter, the motivation of inkjet printing the nanoparticle silver ink is to fabricate a substitute for the conventional Ti/Au track deposited by sputtering. First, the size effect theory on the melting temperature of the metallic nanoparticles, which results in the low temperature sintering, was introduced. Then the basic mechanism of sintering the metallic nanoparticles was described. The nanopartic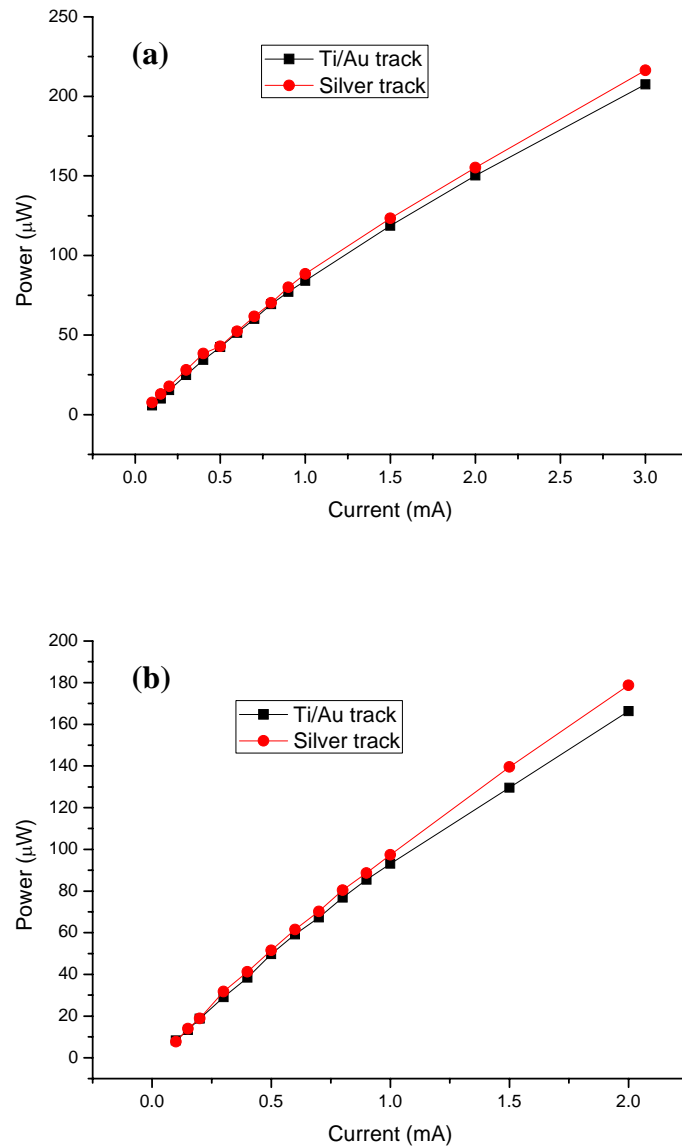le silver ink from ANP was chosen to suit the requirements of the DMP inkjet printer. Silane surface treatment was used to alter the contact angle of the silver ink on different substrates to achieve narrow tracks. Also the drop spacing during the printing was optimised to form uniform tracks with a smooth edge. The printability of the silver ink has been demonstrated on glass substrates by the cartridge delivering both the ~10pl and ~1pl droplets. The microstructure of the silver nanoparticles after sintering has been studied. SEM images under different sintering temperature and time indicate the evolution of the sintering process; the preferred sintering condition was set at 200℃ for 60min. The resistivity, the important electrical property of the printed silver track, has been calculated for the silver tracks on different substrates. It was found that higher sintering temperature and longer sintering time would result in lower resistivity. In addition, the thermal conductivity of the substrate also plays a role in the ultimate resistivity of the printed silver track under same sintering conditions.

After the study on the printability and electrical performance of the nanoparticle silver ink, these printed silver tracks were applied to the flip-chip matrix-addressable and the planar micro-LEDs as the interconnections and bonding pads. In terms of the flip-chip matrix-addressable micro-LEDs, the uniform emission from the turned-on pixels connected by printed silver track suggests the printing and sintering process did not affect the performance of the LED. The current-voltage curve of the printed silver track was measured to be comparable to that of the sputtered Ti/Au track and the silver track could sustain the current density up to 2×10^6 A/cm^2. For the planar

micro-LEDs, the inkjet printing and sintering process have been proved to maintain the passivation properties of the plasma-treated p-GaN surface. Also, the printed silver tracks have been successfully deposited on different sizes of the pixels of the planar device. The current-voltage curves show similar electrical performance between the printed silver track and the Ti/Au track for different pixel sizes. In addition, the optical power measurements provide further evidence for the feasibility of replacing the conventional Ti/Au track with the printed silver track. In summary, we have demonstrated that silver tracks formed by inkjet printing are capable of performing the interconnections in the micro-LEDs.

References

1. J.R. Sambles, "An electron microscope study of evaporating gold particles: the Kelvin equation for liquid gold and the lowering of the melting point of solid gold particles," *Proc. R. Soc. Lond. A.* **324**, 339 (1971).

2. M. Hasegawa *et al.*, "A theory of melting in metallic small particles," *J. Phys. F: Metal Phys.* **10**, 619 (1980).

3. P. Buffand *et al.*, "Size effect on the melting point of gold particles", *Physic. Rev. A* **13**, 2287 (1976).

4. Q. Jiang *et al.*, "Thermal stability of crystalline thin film," *Thin Solid Films* **312**, 357 (1998).

5. Z. Zhang *et al.*, "Modelling for size-dependent and dimension-dependent melting of nanocrystals," *J. Phys. D: Appl. Phys.* **33**, 2653 (2000).

6. K. Dick *et al.*, "Size-dependent melting of silica-encapsulated gold nanoparticles," *J. Am. Chem. Soc.* **124**, 2312 (2002).

7. Suk-Joong L. Kang, *Sintering: densification, grain growth, and microstructure* (Elsevier Butterworth-Heinemann, Oxford, 2005).

8. C.C. Koch, *Nanostructured Materials: Processing Properties, and Potential Applications* (William Andrew Publishing/Noyes, Norwich, 2002).

9. J.G. Bai *et al.*, "Low-temperature sintered nanoscale silver as a novel semiconductor device-metallized substrate interconnect material," *IEEE Trans. Compon. Packag. Technol.* **29**, 589 (2006).

10. T.H.J. van Osch *et al.*, "Inkjet printing of narrow conductive tracks on untreated polymeric substrates," *Adv. Mater.* **20**, 343 (2008).

11. B.Y. Ahn *et al.*, "Omnidirectional printing of flexible, stretchable, and spanning silver microelectrodes," *Scienceexpress Reports* 1168375, 12 Feb (2009).

12. J.G. Bai *et al.*, "Inkjet printable nanosilver suspensions for enhanced sintering quality in rapid manufacturing," *Nanotechnology* **18**, 185701 (2007).

13. U. Caglar *et al.*, "Analysis of mechanical performance of silver inkjet printed

structures," *IEEE Internationcal Nanoelectronics Conference* 851 (2008).

14. K.C. Yung *et al.*, "Synthesis of submicron sized silver powder for metal deposition via laser sintered inkjet printing," *J. Mater. Sci.* **44**, 154 (2009).

15. J. Perelaer *et al.*, "In-jet printing and microwave sintering of conductive silver tracks," *Adv. Mater.* **18**, 2101 (2006).

16. H.H. Lee *et al.*, "Inkjet printing of nanosized silver colloid," *Nanotechnology* **16**, 2436 (2005).

17. M. Ikegawa *et al.*, "Droplet behaviours on substrates in thin-film formation using ink-jet printing," *JSME Int J. Ser. B* **47**, 3 (2004).

18. S.H. Lee *et al.*, "Silver inkjet printing with control of surface energy and substrate temperature," *J. Micromech. Microeng.* **18**, 075014 (2008).

19. R. Bonadiman *et al.*, "Evaluation of printing parameters and substrate treatment over the quality of printed silver traces," *2nd IEEE Electronics System Integration Technology Conference* 1343 (2008).

20. D. Soltman *et al.*, "Inkjet printed line morphologies and temperature control of the coffee ring effect," *Langmuir* **24**, 2224 (2008).

21. F. Ma *et al.*, "Surface-energy-driven abnormal grain growth in Cu and Ag films," *Appl. Surf. Sci.* **242**, 55 (2005).

22. J. Greiser *et al.*, "Abnormal growth of 'giant' grains in silver thin films," *Acta Mater.* **49**, 1041 (2001).

23. V.Y. Gertsman *et al.*, "On the room temperature grain growth in nanocrystalline copper," *Scripta Metall. Mater.* **30**, 577 (1994).

24. B. Günther *et al.*, "Secondary recrystallization effects in nanostructured elemental metals," *Scripta Metall. Mater.* **27**, 833 (1992).

25. S.P. Wu et al., "Fabrication of polymer silver conductor using inkjet printing and low temperature sintering process," *IEEE Trans. Electron. Packag. Manuf.* 31, 291 (2009).

26. J.K. Jung *et al.*, "Characteristics of microstructure and electrical resistivity of

inkjet-printed nanoparticles silver films annealed under ambient air," *Philos. Mag.* **88**, 339 (2008).

27. J. Perelaer *et al*., "One-step inkjet printing of conductive silver tracks on polymer substrates," *Nanotechnology* **20**, 165303 (2009).

28. D.C. Huang *et al*., "Plastic-compatible low resistance printable gold Nanoparticle conductors for flexible electronics," *J. Electrochem. Soc.* **150**, G412 (2003).

29. K.S. Moon *et al*., "Thermal behaviour of silver nanoparticles for low-temperature interconnect applications," *J. Electron. Mater.* **34**, 168 (2005).

30. S. David *et al*., "Experimental investigation of the effect of thermal properties of the substrate in the wetting and evaporation of sessile drops," *Colloids Surf. A* **298**, 108 (2007).

31. V.M. Asnin *et al*., "High spatial resolution thermal conductivity of lateral epitaxial overgrown GaN/sapphire (0001) using a scanning thermal microscope," *Appl. Phys. Lett.* **75**, 1240 (1999).

Chapter 6 Conclusions

This thesis work has focused on combining organic materials with inorganic semiconductor devices, primarily using the inkjet printing technique. The particular inorganic semiconductor devices used are the novel AlInGaN micro-structured light emitting diodes (micro-LEDs) which offer an efficient and versatile light source for display and instrumentation applications. The organic materials are new light emitting polymer guest-host blend systems consisting of an organic light emitting guest and a novel deep-UV transparent polymers host. The integration of the organic light emitting blend polymers by inkjet printing onto the micro-LEDs creates a wavelength-converted hybrid device with different colours on a single device chip.

A general introduction was given in Chapter 1 concerning the light emitting diodes (LEDs), the organic electronic materials and various patterning techniques for polymeric materials. The basic principles of the LEDs were presented such as the p-n homojunction and heterojunction. The primary materials for the LEDs used here are GaN-based inorganic semiconductors which can cover the emission wavelength range from UV to green and in principle even further to red. The special focus of the LEDs in Chapter 1 was the AlInGaN micro-LEDs with two light extraction configurations used in this thesis work, namely the top-emitting and the flip-chip formats. Light is extracted from the p-doped GaN in the first format, while in the latter format light is extracted from the n-GaN side of the epilayer through the thinned sapphire substrate. The matrix-addressable top-emitting micro-LEDs for this work have 64×64 microdisk emitters each 16μm in diameter on a 50μm pitch. The "turn on" voltage of the device emitting at UV (370nm) wavelength is ~4.4V and the

corresponding optical light output power density is 2.98W/cm^2 under 870.8A/cm^2 injection current density. For the flip-chip device, the "turn on" voltage varies from the 3.2V to 4.8V depending on the emission wavelength and the size of the active area. The optical power density per pixel can reach as high as 55W/cm^2 for the blue emitting 32×32 microdisk array. The third type of device used in this work is the planar micro-LEDs. Plasma treatment of the p-type GaN results in selective electrical passivation above the LED active region. The "turn on" voltage of the planar device with an emission area ~70μm in diameter is ~4.8V and the optical power density is 5394.5W/cm^2 under injected current density of 77.9A/cm^2.

Optoelectronic organics are explored in this thesis for fabricating the hybrid inorganic/organic devices, hence, some basic concepts of the organic materials and their various processing techniques were also reviewed. Two representative categories of polymeric materials are introduced, which are transparent polymers and the light emitting polymers. The transparent polymers are usually applied in encapsulation of the LED while the light emitting polymers are adopted for displays. The typical fluorescence process of the light emitting polymers was also presented. As the polymer materials have been widely applied, fabricating the functional polymeric structures attracts much interest. Two categories of patterning techniques were presented as examples: conventional photolithography and mask-free printing such as nanoimprinting, microcontact printing and dip-pen nanolithography. The mask-free printing techniques are attractive alternatives to the conventional photolithography as they can maintain the polymer properties with low cost and high resolution. In this thesis, we use the inkjet printing technique as the main method to fabricate functional polymeric microstructures.

After the general introduction, in Chapter 2 the novel organic guest-host materials system used in this thesis was described and some novel patterning methods were also explored for fabricating functional microstructures from these materials. The novel deep UV transparent polymers are formed from CHDG and

CHDV monomers and have over ~80% transparency in the wavelength range above 300nm. These materials are photocurable which makes them suitable for the standard photolithography technique. In addition, the low viscosity of the CHDV monomer allows the printability required in the inkjet printing process used in this work. Furthermore, novel patterning methods without lithography such as the electrohydrodynamic technique and the "bottom up" curing have been used to form structures from these UV transparent polymers. The electrohydrodynamic technique originates from the strong force experienced by dielectric media in the electric field created by two electrodes. The force can overcome the surface tension and form pillars from the polymer film. The minimum dimension of the pillars from the prepolymerised CHDG film is 10μm in diameter and 1μm in thickness. An array of the prepolymerised CHDG polymers has been fabricated by the "bottom up" curing for bio-analysis applications as well. The polymers are cured through an aperture from the bottom of the film and an array of polymeric dots is left after washing away the uncured materials. The labelled oligonucleotides attached to the polymeric dot are used for disease diagnosis.

These photocurable polymers also act as the host materials in the blend system due to their good miscibility with the light emitting polymers. The light emitting polymers used in this work are novel truxene oligofluorenes and crosslinkable polyfluorenes. The truxene oligofluorenes are a series of three-arm star-shaped molecules with a truxene central core and from mono- to quarter- fluorenes in each arm (T1-T4). The truxene oligofluorene family emits from ~377nm to ~472nm and the PL spectrum shows the fluorescence property has been maintained after being blended with the CHDV polymers. The fluorescence lifetime in liquid and solid state of neat T3 material and the T3/CHDV blend has also been studied. The similarity of the time-resolved measurement results further prove the optical properties are not strongly altered. Another light emitting polymer is the crosslinkable vinyl ether functionalized polymer emitting from blue to red and these polymers have common

absorption maximum at ~368nm. These crosslinkable polyfluorenes have good miscibility with the CHDV polymers and create a crosslinked network after the polymerization with the CHDV matrix.

The inkjet printing technique is the primary method for fabricating the hybrid inorganic/organic devices which form the main interest of this work. In Chapter 3, the instrumentation and applications of the inkjet printing technique used were described. A general introduction of the inkjet printing technique has been given regarding its broad application in light emitting displays, organic electronics, tissue engineering and nanotechnology. This "add on" direct write technique avoids the usage of masks and leads to low-cost, maximum use of materials and elimination of the contamination. The inkjet printing technique was divided into two categories: continuous inkjet and drop-on-demand inkjet. In this thesis, we used the DMP-2800 drop-on-demand piezoelectric-driven inkjet printer which is capable of delivering ~10pl and ~1pl drops and suitable for fabricating microstructures down to ~12μm in diameter, taking the T3/CHDV materials as an example. The drop is generated from the compression of the ink chamber and the formation of the drop is influenced by the frequency, the pulse length and the driving voltage. The fluid properties such as the viscosity, surface tension, density and volatility also affect the drop formation during the printing. In order to fabricate defined structures from the organic light emitting blend materials, the printing parameters are optimised to obtain best printing performance. The optimized parameters for the CHDV polymers are ~17.8V for the applied voltage, 5 kHz for the frequency and 14.080μs for the pulse length. PFODCS is also used to treat the substrates for altering the contact angle of the fluid.

Functional patterns are fabricated by the DMP inkjet printer from various materials such as the truxene oligofluorene T3/CHDV blends, crosslinkable polyfluorene F6BT/CHDV blends, and silver nanoparticle-dispersed water solution. The dimensions of the T3/CHDV printed microstructures are 24μm wide and 2.6μm high for an ~10pl droplet, and 12μm wide and 1μm high for an ~1pl droplet. Their

profiles are well-fitted to a spherical shape. The diameter of the printed F6BT/CHDV blend is ~23μm. Micro-PL measurements prove that the fluorescence properties of the blends are similar the neat materials. Besides the organic light emitting materials, the inorganic silver nanoparticle dispersion was printed and assembled with azo dyes for detecting DNA sequences by SERRS.

After the micro-dot array of T3/CHDV and F6BT/CHDV materials was successfully fabricated by inkjet printing, these features were integrated onto the micro-LEDs as colour conversion elements, as described in Chapter 4. There are two main routes to fabricate the hybrid inorganic/organic device, being radiative and non-radiative (FRET). The mechanism of both routes has been explained. The organic materials act as the colour-converters in the hybrid device by radiatively transferring energy from the shorter emitting wavelength of the LEDs to longer emitting wavelength of the organic light emitting polymer film. The non-radiative method was also introduced. As the requirements for the resonant energy coupling between the inorganic and organic materials are very strict and the organic materials have high photoluminescence yields, we fabricated the hybrid device via the common radiative route. Functional micro-dots were integrated on the pixels of top-emitting matrix-addressable micro-LEDs by inkjet printing. The morphology, electrical performance and the conversion efficiency of the hybrid devices were characterised. The printed dots are well-aligned to the micro-pixels and the surface of the integrated dots is smooth. The I-V curve of the pixel after integration is almost identical to that before, demonstrating no compromise for the electrical performance of the LED after integration. The "in house" micro-PL measurements show similar emission properties from the printed colour-converters and the spectral evolution under increasing injection current. For 1wt%, 5wt% and 10wt% T3/CHDV blend converters, the conversion efficiency calculated by output power is 39%, 59.3% and 50.5%, respectively, and for F6BT/CHDV blends it was 26.3%. The hybrid device formed by inkjet printing in this work shows potential for full colour emission on a

single LED chip which can be applied to displays and instrumentation.

Organics are not the only materials that can be applied on the AlInGaN micro-LEDs by inkjet printing. Inorganic nanoparticle silver ink has been printed to form electrodes on the micro-LEDs as well. The melting temperature of the metallic nanoparticles is reduced due to the size effect resulting in low sintering temperature. During the sintering, heating removes the dispersant and leads to the aggregation of the nanoparticles. After the nanoparticles make contact with each other, the grain grows and the printed structure presents conductivity. The silver nanoparticles ink from ANP was chosen due to its suitable physical properties for the inkjet printing process. The drop spacing and substrate temperature in the printing process are critical for achieving uniform features and the contact angle affects the printed feature size. The sintering temperature and time can also influence the electrical resistivity, which is important for applications as electrodes. Therefore, the drop spacing and substrate surface property are well optimised for different substrates. Before applying the printed silver features to the micro-LEDs, the dimensions, microstructure and the electrical performance were studied. The minimum dimension of the printed dot was measured to be ~26μm in diameter and ~260nm in thickness while the printed line is ~27μm wide and ~120nm thick which are formed from an ~1pl droplet. From the SEM study, the grain size is increased under higher sintering temperature and longer sintering time. The preferred sintering conditions are chosen as 200℃ for 60min. Lower electrical resistivity is obtained under the preferred sintering conditions. The calculated electrical resistivity of printed silver track on silicon, glass and GaN is ~15.4μΩ·cm, ~11μΩ·cm and ~37.6μΩ·cm respectively. The substrate with higher thermal conductivity (GaN) results in higher electrical resistivity of the printed silver track. These printed silver tracks are applied onto the flip-chip matrix-addressable and the planar micro-LEDs as the interconnections and bonding pads. The I-V curves indicate the printed silver track is comparable to the standard sputtered Ti/Au track without serious damage from the sintering process.

The printed silver track on the flip-chip micro-LEDs could sustain current density up to 2×10^6 A/cm^2 without break down. Moreover, the optical output power measured from the printed silver track is similar as the one from the Ti/Au track suggesting the feasibility to replace the sputtered Ti/Au track by printed silver track.

To conclude this thesis work, we presented the potential of using inkjet printing technique to combine the novel inorganic AlInGaN micro-LEDs and the novel organic light emitting blend materials to create full-colour emitting hybrid device.

Future work plans:

First, organic light emitting materials with RGB emission will be integrated on top of the micro-LEDs via inkjet printing to form full-colour hybrid device for micro-displays. The devices used will be further explored in the flip-chip format as the sapphire offers an inert and chemically resistant platform for fabricating organic microstructures. The flip-chip format is also beneficial in higher performance of current handling and output power. White emission hybrid GaN/organic devices can be fabricated by printing a certain mixture of the RGB emitting materials, which will be potentially applied in white light wireless communications.

The micro-LEDs can also act as pumping sources for organic lasers. The flip-chip format will be used for this purpose. The sapphire will be firstly coated with a layer of high reflectivity dielectric mirror. Organic semiconductor materials will be inkjet printed in a lens shape on the mirror and afterwards another layer of dielectric mirror will be deposited on the surface of these organic microstructures. All these organic microlenses will be aligned to the underlying micro-LED pixels during the printing process. In the final format, the flip-chip devices will be associated with CMOS drivers for pulsed operation. An array of surface-emitting organic lasers will thus be created, which are indirectly electrically pumped rather than optically pumped by a laser. The array of polymer lasers can be made with different emission

wavelengths if possible. The schematics of this objective are shown in Figure 6.1. Three optical microscope images displayed on the right side of Figure 6.1 show representatives of an organic micro-array (top), an array of pixels in flip-chip micro-LEDs (middle) and Si-CMOS backplane (bottom) in this objective.
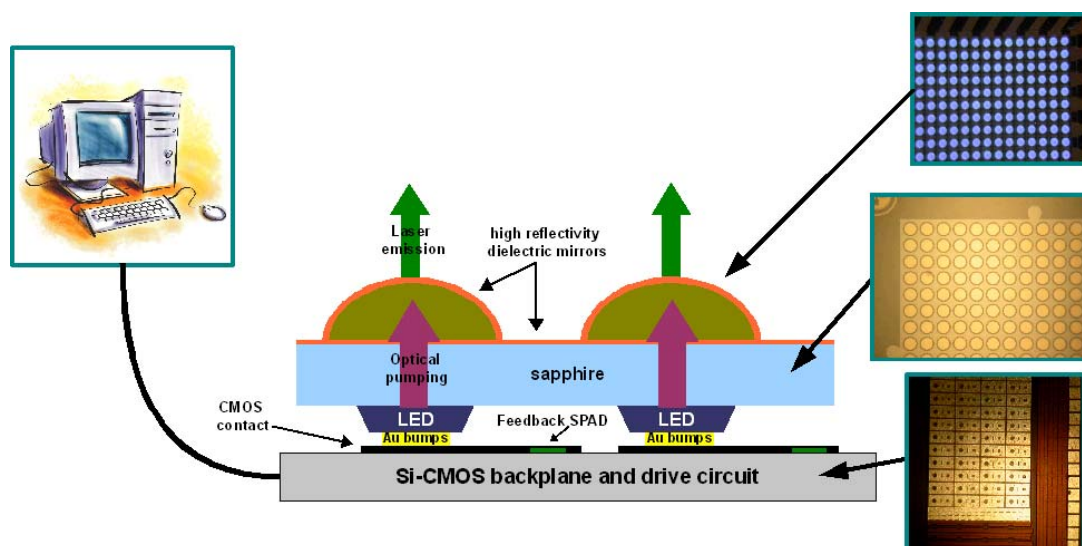

Figure 6.1 Schematic of micro-LED pixels integrated with an array of surface-emitting organic lasers.

To pump the organic semiconductor materials, we need optical pumping frequency between few Hz to up to 10kHz which is possible with the micro-LED array (to avoid accumulation of triplet exciton which would compete with the stimulated emission by losses). An energy density per pixel above 100nJ/cm^2 is also necessary, which is achievable with the micro-LED. The important parameter in pumping conditions is the pulse width, which must be below 10ns (giving time to the gain medium to recover prior to the next excitation pulse arriving). The pulse width of our micro-LED is limited by the driver at 18ns for now, but the use of a CMOS driver directly integrated with the flip-chip micro-LEDs is expected to provide shorter pulse width in the order of the nanosecond or even less. This work is involved in the ongoing research project "HYPIX" supported by EPSRC.

Publications and presentations

1. M. Wu, Z. Gong, A.J.C. Kuehne, A.L. Kanibolotsky, Y.J. Chen, I.F. Perepichka, A.R. Mackintosh, E. Gu, P.J. Skabara, R.A. Pethrick and M.D. Dawson, "Hybrid GaN/organic microstructured light emitting devices via ink-jet printing," *Opt. Express* **17**, 16436 (2009).

2. M. Wu, E. Gu, A. Zarowna, A.L. Kanibolotsky, A.J.C. Kuehne, A.R. Mackintosh, P.R. Edwards, O.J. Rolinski, I.F. Perepichka, P.J. Skabara, R.W. Martin, R.A. Pethrick, D.J.S. Birch and M.D. Dawson, "Star-shaped oligofluorene nanostructured blend materials: controlled micro-patterning and physical characteristics," *Appl. Phys. A* **97**, 119 (2009).

3. M. Wu, D. Elfstrom, Z. Gong, B. Guilhabert, A. Zarowna, E. Gu, M.D. Dawson, A.L. Kanibolotsky, P.J. Skabara, A.J.C. Kuehne, A.R. Mackintosh, R.A. Pethrick P.R. Edwards, R.W. Martin, O.J. Rolinski, D.J.S. Birch and I.F. Perepichka, "Controlled micro-patterning of highly-fluorescent truxene-oligofluorene nanostructured blends," *Proc. IEEE LEOS 2008* **WAA2** (2008).

4. M. Wu, A. Zarowna, D. Elfstrom, B. Guilhabert, C.L. Lee, E. Gu, M.D. Dawson, A.L. Kanibolotsky, P.J. Skabara, A.J.C. Kuehne, A.R. Mackintosh, R.A. Pethrick, P.R. Edwards, O.J. Rolinski, R.W. Martin, D.J.S. Birch and I.F. Perepichka, "Drop-on-demand inkjet printing of organic and inorganic fluorescent nano-particles," *3rd International colloquium on integrated manufacture by printing* (2007).

5. M. Wu, D. Elfstrom, B. Guilhabert, E. Gu, M.D. Dawson, P.J. Skabara, A.L. Kanibolotsky, A.R. Mackintosh and R.A. Pethrick, "Photoluminescence and micro-patterning of the star-shaped truxene-core oligofluorenes," *SID organic electronics for displays UK 2007* (2007).

Hybrid GaN/organic microstructured light-emitting devices via ink-jet printing

M.Wu[1], Z. Gong[1], A.J.C. Kuehne[2], A.L. Kanibolotsky[3], Y.J. Chen[1], I.F. Perepichka[4], A.R. Mackintosh[3], E. Gu[1*], P.J. Skabara[3], R.A. Pethrick[3] and M.D. Dawson[1]

[1]*Institute of Photonics, University of Strathclyde, Glasgow G4 0NW, UK*
[2]*Institut für Physikalische Chemie, University of Cologne, D-50939 Köln, Germany*
[3]*WestCHEM, Department of Pure and Applied Chemistry, University of Strathclyde, Glasgow G1 1XL, UK*
[4]*School of Forensic and Investigative Sciences, University of Central Lancashire, Preston PR1 2HE, UK*
[*]*Corresponding author: erdan.gu@strath.ac.uk*

Abstract: We report what we believe to be the first use of *organic* nanostructures for efficient colour conversion of gallium nitride light emitting diodes (LEDs). The particular nanomaterials, based on star-shaped truxene oligofluorenes, offer an attractive alternative to inorganic colloidal quantum dots in the search for novel and functional 'nanophosphors'. The truxenes have been formed into a composite with photoresist and ink-jet printed onto microstructured gallium nitride LEDs, resulting in a demonstrator hybrid microdisplay technology with pixel size ~32μm. The output power density of the hybrid device was measured to be ~8.4mW/cm^2 per pixel at driving current density of 870.8A/cm^2 and the efficiency of colour conversion at drive current of 7mA was estimated to be approximately 50%.

OCIS codes: (230.3670) Light-emitting diodes, (230.3990) Micro-optical devices, (220.4000) Microstructure fabrication, (160.5470) Polymers, (130.7405) Wavelength conversion devices.

References and links

1. M. Achermann, M.A. Petruska, S. Kos, D.L. Smith, D.D. Koleske and V.I. Klimov, "Energy-transfer pumping of semiconductor nanocrystals using an epitaxial quantum well," Nature **429**, 642-646 (2004).
2. G. Heliotis, G. Itskos, R. Murray, M.D. Dawson, I.M. Watson and D.D.C. Bradley, "Hybrid inorganic/organic semiconductor heterostructures with efficient non-radiative energy transfer," Adv. Mater. **18**, 334-338 (2006).
3. G. Heliotis, P.N. Stavrinou, D.D.C. Bradley, E. Gu, C. Griffin, C.W. Jeon and M.D. Dawson, "Spectral conversion of InGaN ultraviolet microarray light emitting diodes using fluorene-based red-, green-, blue-, and white-light-emitting polymer overlayer films," Appl. Phys. Lett. **87**, 103505 (2005).
4. S. Nakamura, "Current status of GaN-based solid state lighting," MRS Bull. **34**, 101-107 (2009).
5. Z. Gong, H.X. Zhang, E. Gu, C. Griffin, M.D. Dawson, V. Poher, G. Kennedy, P.M.W. French, and M.A.A. Neil, "Matrix-addressable micropixellated InGaN light-emitting diodes with uniform emission and increased light output," IEEE Trans. Electron Devices **54**, 2650-2658 (2007).
6. H. Xu, J. Zhang, K.M. Davitt, Y.K. Song and A.V. Nurmikko, "Application of blue-green and ultraviolet micro-LEDs to biological imaging and detection," J. Phys. D: Appl. Phys. **41**, 094013 (2008).
7. V. Poher, H.X. Zhang, G.T. Kennedy, C. Griffin, S. Oddos, E. Gu, D.S. Elson, J.M. Girkin, P.M.W. French, M.D. Dawson and M.A.A. Neil, "Optical sectioning microscopes with no moving parts using a micro-stripe array light emitting diodes," Opt. Express **15**, 11196-11206 (2007).
8. Y. Yang, G.A. Turnbull and I.D.W. Samuel, "Hybrid optoelectronics: a polymer laser pumped by a nitride light-emitting diode," Appl. Phys. Lett. **92**, 163306 (2008).
9. S.C. Allen and A.J. Steckl, "A nearly ideal phosphor-converted white light-emitting diode," Appl. Phys. Lett. **92**, 143309 (2008).
10. L.A. Kim, P.O. Anikeeva, S.A. Coe-Sullivan, J.S. Steckel, M.G. Bawendi and V. Bulovic, "Contact printing of quantum dot light emitting devices," Nano Lett. **8**, 4513-4517 (2008).
11. A.L. Kanibolotsky, R. Berridge, P.J. Skabara, I.F. Perepichka, D.D.C. Bradley and M. Koeberg, "Synthesis and properties of monodisperse oligofluorene-functionalized truxenes: highly fluorescent star-shaped architectures," J. Am. Chem. Soc. **126**, 13695-13702 (2004).

12. W.Y. Lai, R.D. Xia, Q.Y. He, P.A. Levermore, W. Huang and D.D.C. Bradley, "Enhanced solid-state luminescence and low-threshold lasing from starburst macromolecular materials," Adv. Mater. **21**, 355-360 (2009).
13. G. Heliotis, S.A. Choulis, G. Itskos, R. Xia, R. Murray, P.N. Stavrinou and D.D.C. Bradley, "Low-threshold lasers based on a high-mobility semiconducting polymer," Appl. Phys. Lett. **88**, 081104 (2006).
14. A.J.C. Kuehne, D. Elfstrom, A.R. Mackintosh, A.L. Kanibolotsky, B. Guilhabert, E. Gu, I.F. Perepichka, P.J. Skabara, M.D. Dawson and R.A. Pethrick, "Direct laser writing of nanosized oligofluorene truxenes in UV-transparent photoresist microstructures," Adv. Mater. **21**, 781-785 (2009).
15. G. Tsiminis, Y. Wang, P.E. Shaw, A.L. Kanibolotsky, I.F. Perepichka, M.D. Dawson, P.J. Skabara, G.A. Turnbull and I.D.W. Samuel, "Low-threshold organic laser based on an oligofluorene truxene with low optical losses," Appl. Phys. Lett. **94**, 243304 (2009).
16. Cluster issue on 'Micro-pixellated LED's for science and instrumentation' (Guest Editors, M.D. Dawson and M.A.A. Neil) J. Phys. D: Appl. Phys. **41**, 090301 (2008).
17. J.A. DeFranco, B.S. Schmidt, M. Lipson, and G.G. Malliaras, "Photolithographic patterning of organic electronic materials," Org. Electron. **7**, 22-28 (2006).
18. G. Raabe and J. Michl, *The Chemistry of Organic Silicon Compounds* (John Wiley, 1989), Chap. 17.
19. E. Tekin, P.J. Smith, S. Hoeppener, A.M.J. van den Berg, A.S. Susha, A.L. Rogach, J. Feldmann and U.S. Schubert, "Inkjet printing of luminescent CdTe nanocrystal-polymer composites," Adv. Funct. Mater. **17**, 23-28 (2007).

1. Introduction

Recently, there has been considerable interest in developing 'hybrid' light-emitting technologies based upon gallium nitride optoelectronics. Electrically injected gallium nitride hetero-structures offer customised direct band-gaps in the ultraviolet to visible spectral range and can selectively and efficiently transfer excitation either non-radiatively (Förster Resonance Energy Transfer or FRET) [1,2] or radiatively [3] to an overlayer based on alternative light-emitting materials. This approach has important implications for areas including; colour conversion and white-light generation for solid-state lighting [4], microdisplays [5], bioscience [6], instrumentation [7] and photo-pumped organic semiconductor lasers [8]. It has to date been embodied primarily using conventional inorganic phosphors [9], inorganic semiconductor nanocrystals (mainly CdSe/ZnS colloidal quantum dots) [1] and, to a lesser degree, organic polymers [3]. The case of colloidal quantum dots is particularly interesting, because it offers a means of 'indirect' electrical injection into nanostructured light emitters, and is a competitive approach to e.g. microdisplays and nanolasers being developed based on direct electrical injection into quantum dot containing conductive composite thin films [10]. Here, we report development of such devices based on *organic* nanostructures as a technologically and scientifically interesting alternative.

The particular materials we used are star-shaped nanostructures of the truxene oligofluorene type, consisting of oligofluorene arms attached to a central truxene core. These materials [11, 12], related to the polyfluorene polymers used very widely in organic optoelectronics [13], have engendered considerable interest recently, in terms of their attractive physical properties, processability [14] and demonstration of laser action [15]. They share the attractions common to their polymeric counterparts of efficient and wavelength-versatile colour conversion, blendability, ready conformability to microstructured surfaces and amenability to a variety of 'soft' micro- and nano-patterning techniques. In addition, they also offer advantages of chemical purity, structural uniformity and resistance to degradation [11]. When blended into a photo-resist host, these materials form a composite that we demonstrate can be readily micro-patterned via inkjet printing onto gallium nitride devices, as the basis of a new hybrid device technology.

Our demonstrations of this capability here utilise the specific truxene oligofluorene 'T3' [11], wherein three terfluorenyl arms are attached to the central truxene core, giving a 3.1nm molecular radius. These molecules were blended into a photo-resist based on 1,4-cyclohexyldimethanol divinyl ether (CHDV), and the T3/CHDV composite printed onto 370nm-emitting micro-pixellated AlInGaN light emitting devices. The resulting hybrid

devices show per pixel output power density of ~8.4mW/cm^2 at driving current density of 870.8A/cm^2 and reach colour conversion efficiencies of ~50% at drive current of 7mA.

2. Integration experiments

The structure, fabrication and performance of the gallium nitride devices used here has been described in detail elsewhere, together with their use for micro-display and instrumentation purposes [5,16]. Briefly, these devices were micro-structured quantum well light emitting diodes (LEDs) made from AlInGaN epi-structures grown on sapphire and designed to emit at ~370nm. They were patterned using inductively-coupled plasma dry etching techniques into matrix-addressable arrays of 64×64 micro-pixels, where each pixel had a 16µm emission aperture and the pixel-to-pixel pitch was 50µm. The structure of these pixels is indicated schematically in Fig. 1, wherein it is seen that a Ti/Au annular contact (thickness 250nm, outer diameter 32 µm, inner diameter 16µm) defined the emission aperture, which consisted of a 200nm thick silicon oxide isolation layer above a Ni (3nm)/Au (9nm) current spreading layer. The individual pixels in this work had turn-on voltages of 3.6V, and emitted continuous wave output powers of 48nW at a current of 7mA (see later).
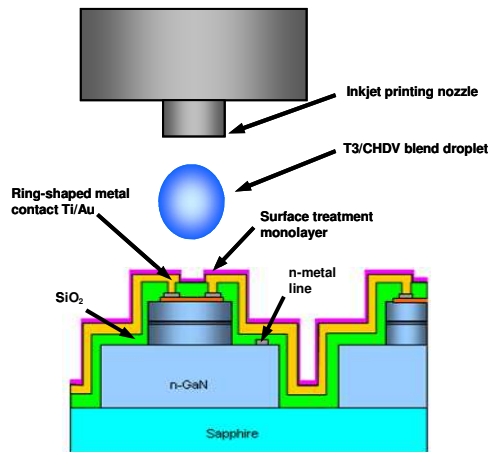

Fig. 1 Schematic picture of inkjet printing one T3/CHDV blend droplet on one pixel of the matrix addressable micro-pixellated LEDs

There are two related challenges for integrating the organic materials onto such gallium nitride devices; one is how to process the organics and another is how to deposit the materials precisely, uniformly and reproducibly onto such small (32µm diameter) device elements:

The main technical challenge of processing organic light-emitting materials is the incompatibility with conventional photolithography methods [17]. Recently, we have shown that incorporation of the oligofluorene truxene T4 with novel UV-transparent organic photoresist materials has opened up alternative approaches to processing and micro-patterning organic fluorescent nanocomposites [14]. The polymerisation of oligofluorene truxene blends is in this case photo-induced and leads to a cross-linked network allowing the creation of optical structures. The UV-transparent negative photoresist matrix used, and exploited further in the current work, is 1,4-cyclohexanedimethanol divinyl ether (CHDV)(Sigma-Aldrich) with the photo-acid generator (PAG): p-(octyloxyphenyl) phenyliodonium hexafluoroantimonate (ABCR, Karlsruhe, Germany). Our study suggested a reduction of oxygen diffusion and photo-oxidation after encapsulating the fluorescent molecules with this polymer matrix [14], which is one of the attractions of this approach. The photo-polymerization mechanism has also been studied in the previous report [14]. The T3 molecules used here (see Fig. 2(a)) exhibit high blue photoluminescence quantum yields both in solution and solid state (83% and

60% respectively) [11]. We prepared various T3/CHDV blends, with T3 concentrations ranging from 0.5wt% to 10wt%. For reference spectroscopic measurements, blends with 0.5wt% PAG were drop-cast onto a quartz substrate and cured under ~370nm wavelength irradiation at 15mW/cm^2. The absorption maximum for the blend was at ~368nm (matching the emission wavelength ~368nm of the gallium nitride LEDs) whilst the emission maximum was at ~408nm, ~430nm and ~460nm. These spectral characteristics are similar to those shown by T3 in solution and spin-coated films [11]. Figure 2(b) shows that the LED emission matches very well with the T3/CHDV blend absorption, which allows sufficient colour down-conversion.
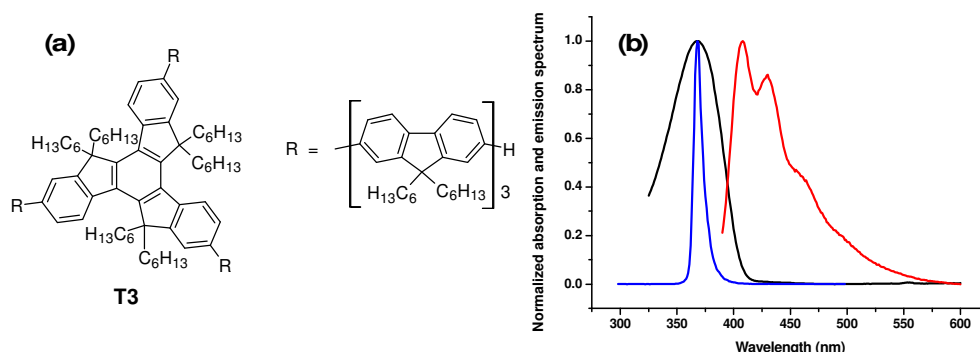

Fig. 2 (a) chemical structure of T3 molecule; (b) normalized absorption (black) and emission (red) spectra of T3/CHDV blends and normalized emission (blue) spectrum of micro-LEDs

In order to address another challenge of integration, we explored the inkjet printing technique using the T3/CHDV blends to create oligofluorene truxene microstructures on the top of GaN-LED micro pixels to achieve colour down-conversion. The Dimatix DMP-2800 inkjet printing system used consists of a heated vacuum platen with XYZ control, built-in drop jetting observation, fiducial camera for pattern monitoring and alignment. The piezo-driven cartridges with silicon micro-electro-mechanical-systems (MEMS) fabricated print-heads could deliver ~1pL or ~10pL droplets with which we have found it possible to create microstructures down to ~12μm in diameter. The jettable fluid viscosity in this piezoelectric drop-on-demand print head is ~2-30 cP, and the viscosity of oligofluorene truxene blends (0.5wt% T3 concentration) was measured to be ~15 cP, which is in the viscosity range required. It was observed that varying the concentration of T3 had little effect on the viscosity. Precise alignment and controllable flow are required for this experiment. Thanks to the intelligent functioning of the instrument (computer interfacing, active position monitoring and repeatable stepper control accuracy of ±1μm), we could successfully achieve accurate alignment during the deposition. In addition, we required the printed organic droplet to remain stable on the top of the pixel prior to photopolymerisation without any excess flowing into the channels between pixels. As the printing was carried out onto the exposed SiO$_2$ insulation layer within the ring-shaped GaN device p-contact (see Fig. 1), we applied a treatment with 1H,1H,2H,2H-perfluorooctyldimethylchlorosilane (ABCR, Karlsruhe, Germany) via vapour deposition at room temperature and atmospheric pressure. This formed a monolayer to change the surface energy and thus the contact angle of the organic droplet generated from the nozzle of the inkjet printing system (see Fig. 1) [18]. By using this treatment, the measured contact angle of truxene blends on the SiO$_2$ surface was altered from ~2° to ~39°, which effectively prevents the oligofluorene truxene drop from overflowing.

A T3/CHDV blend with 10 wt% T3 concentration and 0.5 wt% PAG to initiate the photopolymerisation was prepared for the fabrication of hybrid inorganic/organic LED

devices. It is estimated that, at this concentration, there are around 10^{13} T3 molecules in 1 pL of blend. Due to the high miscibility of T3 molecules in the CHDV matrix, it is not necessary to add any solvent into the blend to obtain a phase-uniform solution. This solventless blend facilitated the fabrication of uniform microstructures by preventing the 'coffee ring' stain formation due to solvent evaporation [19]. After printing the blend droplets onto the top of micro-LED pixels, the whole packaged device was exposed under an ultraviolet (370 nm in wavelength) lamp at an energy density of ~15mW/cm^2 for 15min in order to fully polymerize the CHDV monomers.

3. Results

Figure 3(a) is a plan-view optical micrograph under white light illumination, which shows that microstructures of 10wt% T3 in CHDV matrix have been successfully inkjet printed onto the treated LED micropixels. For illustration purposes, we chose here to print alternate pixels to form a simple 3×3 hybrid array. It can be seen that the diameter of the organic structures is ~40µm and that each has not flowed, before photocuring, beyond the boundary of the respective underlying GaN pixel. The close-up image of the microstructure taken by scanning electron microscopy (SEM) (Fig. 3(b)) shows the printed polymer microstructure has a smooth surface and well defined edges, demonstrating the effect of the surface treatment and the accurate printing alignment. The shape of the microstructure is dome-like and the thickness is approximately 2.9µm.
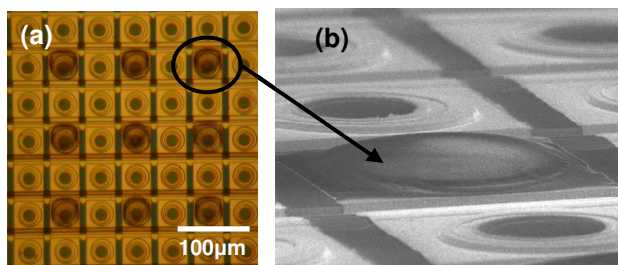

Fig. 3 (a) Plan view optical micrograph of 3x3 array of 10wt% T3 in CHDV matrix integrated on the GaN LED micropixels; (b) oblique SEM image of the inkjet printed T3/CHDV blend microstructure on one single LED micropixel

Figure 4(a) is an optical micrograph comparing a turned on bare GaN pixel (upper) with a turned on T3/CHDV integrated pixel (lower). The bare pixel emits UV light at ~368nm wavelength (see the unconverted light in Fig. 5 later). The integrated pixel emitted blue light from the oligofluorene truxene molecules photo-pumped by the underlying UV LED, showing colour conversion to the visible in an integrated device format. Figure 4(b) shows a demonstration combination of multiple illuminated hybrid pixels.
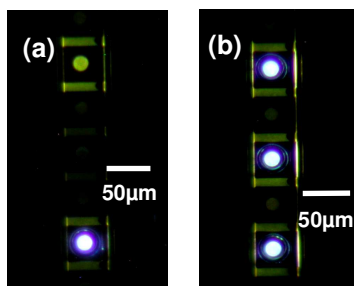

Fig. 4 Optical micrographs of (a) two pixels: bare micro-LEDs pixel (top) and T3/CHDV blend integrated on the pixel (bottom); (b) three alternating pixels with T3/CHDV blend

Ideally, the electrical properties of the inorganic light emitter should not be influenced by the integration of the organic fluorescent microstructures. We therefore first characterized the current-voltage (I-V) performance of the LED pixels before and after the integration of T3/CHDV blend microstructures. Our measurements show that the turn-on voltage (3.6V) and I-V characteristics of the representative micro-LED pixels did not change after T3/CHDV integration. As the aim of the integration is to down convert the UV light emitted from the inorganic LED to the visible wavelength via optically pumping the organic light emitting molecules, we have carried out spectral and optical power measurements to investigate the colour conversion of the integrated device. Figure 5 is the normalized photoluminescence (PL) spectrum of a representative T3/CHDV blend microstructure pumped by the AlInGaN LED pixel underneath operated at an injection current of 7mA. This spectrum was measured by using a home-built micro-PL system, which allowed the emission from a single target pixel to be imaged and analysed. It is observed that the emission spectrum is composed of unconverted and/or leakage/scattered LED pump light peaked at 368nm together with the characteristic emission of the T3 organic material showing vibronic peaks at 408nm, 428nm and 458nm respectively. As the CHDV matrix is UV-transparent after photocuring [14], the unconverted UV light transmits through the matrix, forming the predominant peak in the spectrum. This observation clearly demonstrates the optical pumping of the organic light emitting molecules by the UV micro-LED pixel to achieve UV to blue colour conversion.
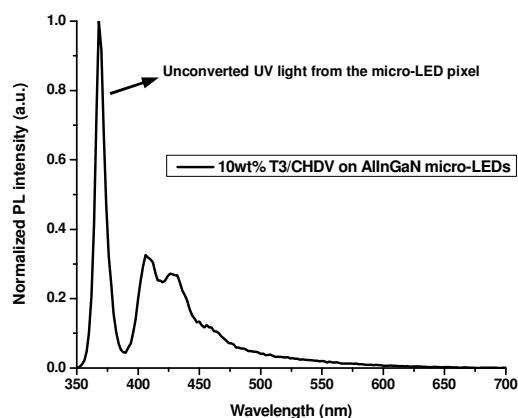

Fig. 5 Spectral output of a single hybrid pixel showing integrated photopumping by the underlying electroluminescent gallium nitride ultraviolet LED. The peak at 368nm is unconverted and/or scattered pump light and the broad vibronic-structured emission between 400nm and 600nm is from the T3 organic nanostructures

To further study the emitting performance of the hybrid device, it is necessary to investigate the colour conversion of the T3/CHDV microstructures under various driving currents. Figure 6 shows the experimental spectra of the T3/CHDV blend microstructure pumped by the underlying GaN micropixel under increasing currents. Over this range of currents (1-7mA) the spectra show no obvious peak wavelength shift or broadening at either UV or blue wavelengths. Moreover, the integrated intensity of the 408nm (integrated from 390nm to 418nm) blue peak (S_{T3}) is plotted versus the driving current in the inset of Fig. 6, showing no strong saturation effects over the range though there is some modest saturation observed higher than 2.5mA.
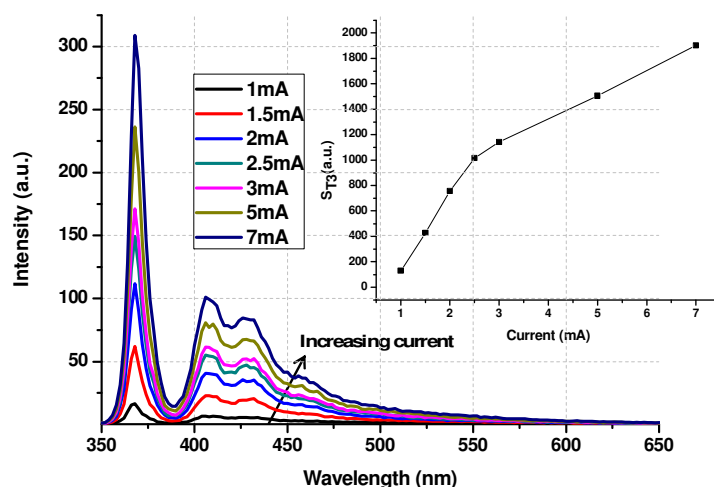
Fig. 6 Photoluminescence spectra of T3/CHDV blend microstructure pumped by the micro-LEDs underneath under increasing current; Inset, the integrated peak intensity of emission at 408nm

To determine the colour conversion efficiency of this hybrid device, the optical output powers of the bare UV LED pixel and T3/CHDV integrated LED pixel were measured. During the measurements, a calibrated UV-sensitive Si photo-detector (of active area 78.5 mm^2) was placed ~2mm from the LED emitter. The light output powers were measured under different injection currents and are plotted in Fig. 7. It is shown that the bare UV pixel emission area of 16μm in diameter gives a maximum measured output power of 48nW when driven by 7mA current (~23.8mW/cm^2 optical power density at a driving current density of 870.8A/cm^2, current injected through the whole pixel area, 32μm in diameter). It is noted that the output power is somewhat low compared to our previous report [5] as this work was conservatively carried out on a non-optimized device to establish the principle of this pixellated colour conversion scheme. After printing a T3/CHDV blend microstructure on the same pixel, the pixel output power was measured again. As only the emitting power from T3 was desired to be characterised, a coloured glass long-pass filter with a cut-off wavelength at 390nm and 70% transmission at 415nm was used to remove the unconverted UV light, and the measured powers adjusted accordingly. The measured output powers of the integrated pixel are also plotted in Fig. 7. It is shown that the output power of the integrated LED pixel is 17nW at a driving current of 7mA (~8.4mW/cm^2 optical power density at a driving current density of 870.8A/cm^2). Thus, the colour conversion efficiency of the T3/CHDV blend microstructure under 7mA driving current is calculated to be 35.4% (50.5% at 7mA if the compensation of the loss from the filter is taken into account). This promising, but non-optimised demonstration shows the promise of these organic nanostructure colour converters. The conversion efficiency may be increased by further increasing the concentration of T3 in the CHDV matrix.
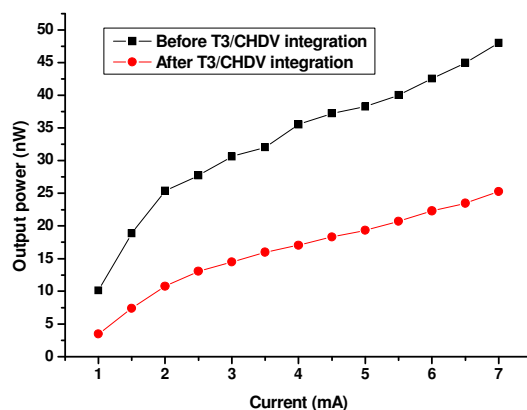
Fig. 7 Optical output power plotting of the micro-LEDs pixel before and after T3/CHDV integration via inkjet printing under increasing injection current. The latter have here been corrected for the effects of the filter

4. Conclusions

We have demonstrated that organic nanostructures, here represented by the 'T3' type of truxene oligofluorenes, can be successfully used as efficient colour converters for gallium nitride optoelectronics. When incorporated into a novel form of photocurable polymer matrix, these materials are suitable for solventless ink-jet printing to form controlled microstructured nanocomposites on device surfaces. By utilising a micro-pixellated and matrix-addressable format of underlying ultraviolet gallium nitride light-emitting diode, we provide an ideal photopumping device underlayer for the printed organics, allowing a simple hybrid micro-display technology to be demonstrated. This type of approach is anticipated to be of both fundamental interest, in delivering 'indirect' electrical excitation to organic nanostructures, and technological interest as a form of micro-display competitive with other approaches [10]. As a further interest, the recent demonstration of photo-pumped laser action in the truxene oligofluorenes [15] offers the prospect, using the advances demonstrated here, of integrated photo-pumped organic lasers.

Star-shaped oligofluorene nanostructured blend materials: controlled micro-patterning and physical characteristics

M. Wu · E. Gu · A. Zarowna · A.L. Kanibolotsky · A.J.C. Kuehne · A.R. Mackintosh ·
P.R. Edwards · O.J. Rolinski · I.F. Perepichka · P.J. Skabara · R.W. Martin ·
R.A. Pethrick · D.J.S. Birch · M.D. Dawson

Abstract Star-shaped oligofluorene consists of highly-fluorescent macromolecules of considerable interest for organic electronics. Here, we demonstrate controlled micro-patterning of these organic nanostructured molecules by blending them with custom-synthesized photo-curable aliphatic polymer matrices to facilitate solventless inkjet printing. The printed microstructures are spherical with minimum dimensions of 12 μm diameter and 1 μm height when using a cartridge delivering ∼1 pL droplets. We evaluate the physical characteristics of the printed structures. Photoluminescence studies indicate that the blend materials possess similar fluorescence properties to neat materials in solid films or toluene solution. The fluorescence lifetime consists of two components, respectively 0.68 ± 0.01 ns (τ_1) and 1.23 ± 0.12 ns (τ_2). This work demonstrates that inkjet printing of such blends provides an attractive method of handling fluorescent nano-scaled molecules for photonic and opto-electronic applications.

1 Introduction

Currently, inorganic semiconductor quantum dots (or nanocrystals) are widely applied in selective biological labelling [1], and optoelectronics [2]. In parallel to the development of these inorganic luminescent nanocrystals, π-conjugated organic materials have also attracted much attention as promising candidates for various optoelectronic applications, including organic light-emitting diodes [3], and lasers [4, 5]. They possess bright optical emission, high hole mobility and ease of functionalization [3]. Among those functional conjugated organic materials, monodisperse star-shaped oligomers have been shown to offer advantages in chemical purity, structural uniformity and resistance to degradation, and they are also non-toxic, unlike heavy metal-based inorganic semiconductor nanocrystals. The star-shaped architecture combines the conjugated character and arms bringing new optical, electrical and morphological properties to the system [6]. Recently, we have developed a series of novel star-shaped truxene core oligofluorenes with mono-fluorene to quater-fluorene arms (T1 ∼ T4) [7], resulting in fluorescent macromolecules up to 4 nm in radius. It is true that the star-shaped oligofluorene dendrimers are still relatively unexplored. In particular, the physics and devices community is quite unfamiliar with these materials, which have only recently been reported by the chemists who have synthesised the materials. Their potential relevance as fluorescent labels, optoelectronic colour conversion and laser gain materials is, we believe, important to

M. Wu · E. Gu (✉) · A. Zarowna · M.D. Dawson
Institute of Photonics, University of Strathclyde, SUPA,
Glasgow G4 0NW, UK
e-mail: erdan.gu@strath.ac.uk
Fax: +44-(0)141-5521575

A.L. Kanibolotsky · A.J.C. Kuehne · A.R. Mackintosh (✉) ·
P.J. Skabara · R.A. Pethrick
Department of Pure and Applied Chemistry, University
of Strathclyde, Glasgow G1 1XL, UK
e-mail: allan.mackintosh@strath.ac.uk

P.R. Edwards · O.J. Rolinski · R.W. Martin · D.J.S. Birch
Department of Physics, University of Strathclyde, SUPA,
Glasgow G4 0NG, UK

I.F. Perepichka
Centre for Materials Science, University of Central Lancashire,
Preston PR1 2HE, UK

communicate to the physics-based materials and devices community. The truxene oligofluorenes are related to the polyfluorene polymers used very widely in organic opto-electronics. These truxene materials show highly efficient blue-violet light emission (photoluminescence (PL) maxima 380–460 nm) in both solution and solid state, and high thermal and electrochemical stability [7]. However, micro-patterning of such luminescent organic materials using traditional optical lithographic techniques is time-consuming and requires major supporting infrastructure. Moreover, due to the recognized incompatibilities between the organic light-emitting materials and the chemicals used in photolithographic processes, fabricating microstructures in such chemically sensitive organic materials presents a considerable technical challenge [8]. Recently, the inkjet printing technique has presented excellent performance in micro-patterning organic molecules due to its mask-free approach, tiny drop deposition, low materials waste and low cost [9]. In this work, a representative truxene oligofluorene compound, dodecakis(dihexyl)tris(terfluorenyl)truxene (T3) was mixed with a custom-synthesized photocurable aliphatic polymer matrix [10]. When blended into the photo-resist host, these materials form a composite that we demonstrate can be readily micro-patterned via drop-on-demand inkjet printing [11, 12] and photo-curing as shown in this work. The structural and optical properties of the printed microstructures have been investigated. Our results demonstrate that well-defined micro-patterns of the truxene blend have been successfully fabricated and the highly fluorescent properties of the truxene oligomers are fully retained during the process.

2 Inkjet printing the oligofluorene truxenes blends

The inkjet printing system used in these experiments (Dimatix DMP-2800) consisted of a heated vacuum plate with XYZ control, built-in drop jetting observation, fiducial camera for pattern monitoring and alignment and piezo-driven cartridges with silicon micro-electro-mechanical-systems (MEMS) fabricated printheads. The jettable fluid viscosity in this piezoelectric drop-on-demand printhead is ∼2–30 cP and the effective diameter of the nozzle is 21.5 μm, which can deliver a drop with a volume of 10 pL. The light-emitting component, T3, is a member of a family of compounds with excellent electrochemical and thermal stability (up to 410°C), good solubility in common organic solvents and efficient blue photoluminescence [7]. The material is easily purified by column chromatography and can be obtained in gram quantities. T3 is a monodisperse compound, consisting of a truxene core and three pendant terfluorenyl arms; each fluorene unit in the structure is derivatised with hexyl groups attached to the 9 positions (see Fig. 1), providing sufficient solubility for facile solution-based processability. The polymer matrix for blending the oligofluorenes was prepared by mixing the monomer 1,4-cyclohexanedimethanol divinyl ether (CHDV) (Sigma-Aldrich) with the photoacid generator (PAG): p-(octyloxyphenyl) phenyliodonium hexafluoroantimonate (ABCR, Karlsruhe, Germany). This matrix is photo-curable by using UV light (370 nm). After curing, the polymer is almost 100% transparent over the deep UV and the visible wavelength range [13]. The concentration of T3 blended into this matrix was 0.5 wt% with 0.5 wt% PAG to polymerize the monomer, which gave a jettable viscosity of 15 cP. It is estimated that, at this concentration, there are around 10^9 T3 molecules in 1 pL of blend. This solventless blending process facilitated good uniformity of the microstructures by preventing ring-like stain formation due to the evaporation of the solvents [14]. Furthermore, recently reported star-shaped macromolecular materials with six oligofluorene arms possess similar absorption and emission characteristics [5]. In that work, the direct analogue (Tr3) to our T3 has greater values for PL quantum efficiency in solution and solid state, indicating a higher tendency for

Fig. 1 Chemical (*left*) and three-dimensional (*right*) structure of dodecakis(dihexyl)tris(terfluorenyl)truxene (T3) compound
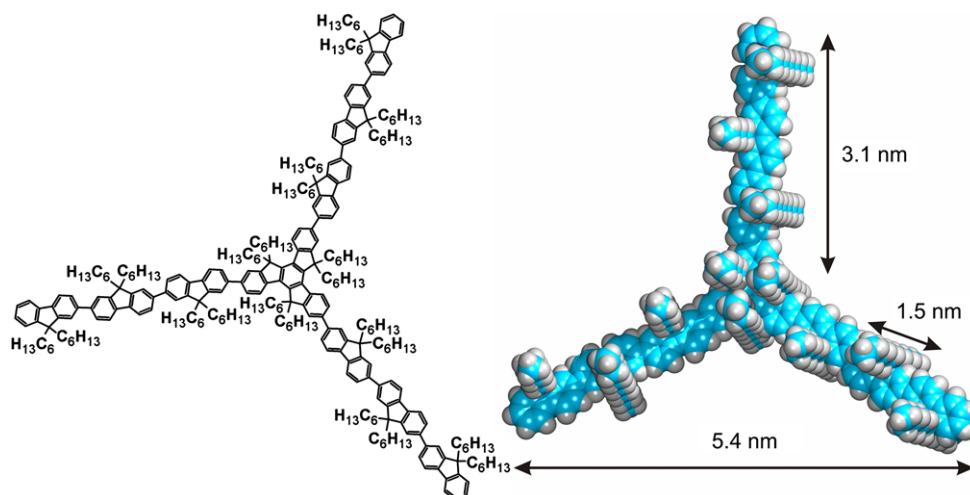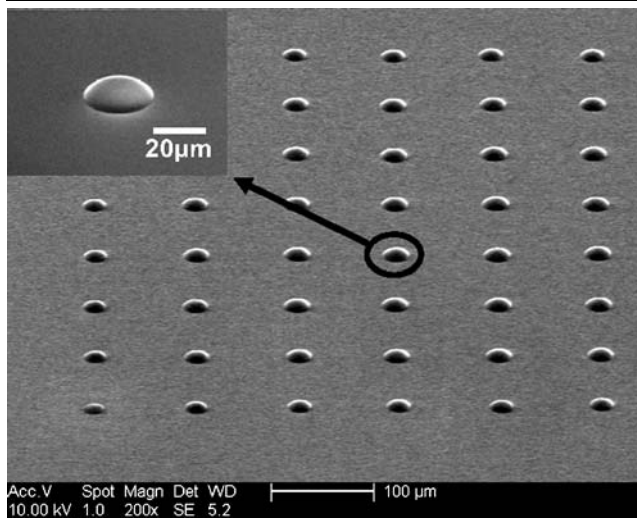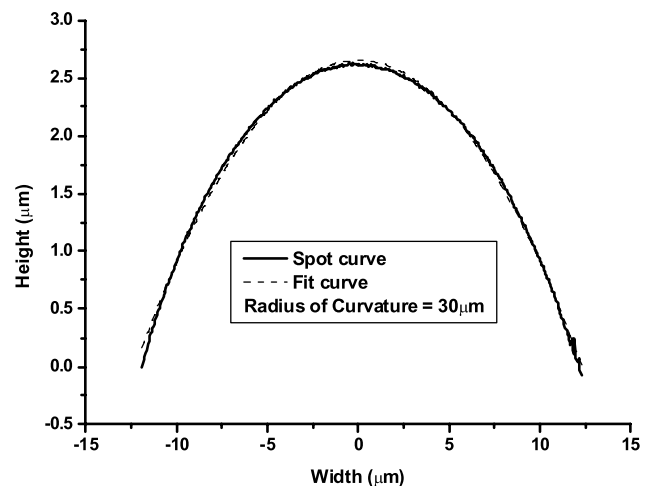
Fig. 2 Oblique SEM images of the dot array and of a representative single micro-dot

Fig. 3 AFM profile curve (*bold*) of a representative micro-dot, together with fitting (*dashed*)

T3 to aggregate. This underlines the advantage of blending T3 with the polydivinyl ether to suppress aggregation effects.

Highly n-doped Si (100) substrates were used for printing. They were first washed by Piranha solution (H_2SO_4: $H_2O_2 = 1:4$), and then ultrasonicated for 3 minutes each in both acetone and methanol. After drying with a N_2 flow, the substrates were treated with 1H,1H,2H,2H-perfluorooctyldimethylchlorosilane (ABCR, Karlsruhe, Germany) through vapour deposition to change the surface energy and thus the contact angle of the drops [15]. We observed that the truxene blend materials are almost wetting the substrate without such treatment. However, after treatment the contact angle was altered to give a measured value of 51°. When the voltage in the silicon MEMS inkjet printhead is increased, the zirconate titanate piezoelectric (PZT)/Si bimorph in the printhead deforms, compressing the chamber of the printhead to generate the pressure to eject a drop [16]. Uniform ∼10 pL truxene blend droplets were formed from the nozzles at 14.5 V, allowing for printing of a 'test' 8 × 8 array pattern with 100 μm centre-to-centre pitch on the pre-treated Si substrate. After the array was printed, the sample was put under an ultraviolet (370 nm in wavelength) lamp at an energy density of 15 mW cm^{-2} for 15 min in order to polymerize the monomer. A well-defined 'micro-dot' array was thus fabricated.

## 3 Microstructures characterization and discussion

Scanning Electron Microscopy (SEM) characterized the shape of the micro-patterned arrays and the image is shown in Fig. 2. The image was taken using an accelerating voltage of 10 kV with 200× and 1500× (inset) magnification,

respectively. From these images, it is evident that the micro-dot structures in the array are quite uniform and that the base diameter and height of each dot are around 24 μm and 2.6 μm, respectively. The surface topography of the micro-dot formed by a 10 pL droplet was studied by Atomic Force Microscopy (AFM). Figure 3 shows that the profile curve of the dot fits the calculated curve very well with a radius of curvature of 30 μm, which means that the micro-dot has a spherical shape. We also fabricated, following the same procedure, truxene blend micro-arrays under 16.5 V nozzle voltage using a newly developed cartridge delivering ∼1 pL drops. The shape of these micro-dots was measured by AFM to be 12 μm in diameter and 1 μm in height. These lens-shape structures are transparent to the ultraviolet light due to the polymer matrix and offer potential as surface-emitting organic laser structures, for example, if printed on laser mirrors [17]. A volume reduction up to ∼20% of the uncured material was observed during the process, but it was confirmed that there is no mass reduction due to volatilisation of the printed blend. It is possible that this volume reduction is caused by the wetting and absorption of the blend material into the treated substrate or the density increase by cationic polymerization of the CHDV molecule, which leads to volume shrinkage [18]. Nevertheless, this in no way detracts from the reproducibility of the printed arrays. Further investigation into this phenomenon is on going. Since the fluorescent nano-materials are embedded in the UV transparent polymer matrix, we took a wide field optical microscope image of the whole micro-dot array under UV lamp illumination. Inset (a) in Fig. 4 shows this micrograph with an image capture time of 8 s. All the dots emitted bright and uniform photoluminescence, indicating that blending the truxene oligofluorenes into the polymer matrix had not significantly affected their fluorescence properties. This assumption was further tested by measuring the PL of a single

Fig. 4 Photoluminescence spectrum of a single photoexcited micro-dot, together with (*inset*) optical micrographs of the full photoexcited array (**a**) and a single-photoexcited micro-dot (**b**)
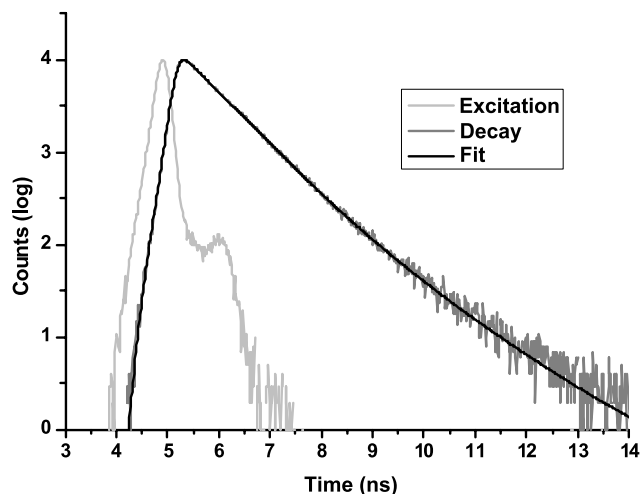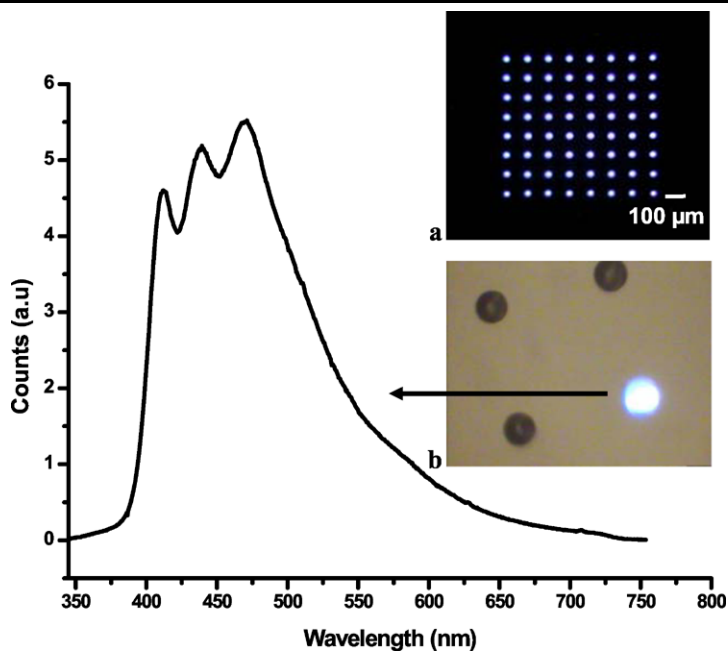
Fig. 5 Luminescence decay curve of the polymerized truxene blend and the fitting result described in the text

micro-dot in the array. A laser beam at 325 nm wavelength was used as the excitation source for the measurement and focused to a spot 10 μm in diameter by an objective lens. The power density of the focused laser beam was estimated to be 3 W cm^{-2}. Inset (b) in Fig. 4 shows the image taken under such excitation conditions and the main part of the figure shows the single micro-dot PL spectrum. Luminescence peaks were found for blue emission at 412, 438 and 470 nm, which is very close to those obtained from the neat truxene material [7]. These results indicate that both the blending and ink-jet printing processes have not had noticeable detrimental effects on the truxene oligofluorenes.

For optoelectronic applications such as organic lasers, the fluorescence lifetime of the materials is an important parameter to be considered, and this has yet to be explored for these truxene oligofluorenes. We therefore measured these characteristics using time-correlated single photon counting (TCSPC). The sample was excited by a laser diode emitting at 374 nm with 200 ps pulse width and 1.0 MHz maximum repetition rate [19]. The fluorescence was collected by an objective lens. A time-to-amplitude converter (TAC) generated voltage pulses proportional to time delays between START and STOP signals [20]. These pulses were then collected and accumulated in a multi-channel analyzer (MCA) to create the intensity vs. time decay curve. The time decay of fluorescence intensity can be represented by a model of the form:

$$I(t) = \sum_i \alpha_i e^{-t/\tau_i} \tag{1}$$

where α_i and τ_i are the amplitude and decay time of the ith component respectively [19]. In this work, the fluorescence signal was collected at 450 nm, being close to the main wavelength peak of the truxene blend. The values of α_i and τ_i were determined from the experimental data by a non-linear least-squared fitting procedure. This fitting process was repeated until the value of the reduced chi-squared (χ^2) passed through the minimum. The corresponding fluorescence lifetime parameters were then found [21]. In Fig. 5, the light grey curve is the reference (prompt) function characterizing the impulse response of the excitation source and detection system, the dark grey curve is the fluorescence decay of the cured truxene blend material, while the black curve is the fitted function. The TCSPC

data revealed that the fluorescence decay of the polymerized truxene blend was best fitted by a bi-exponential decay ($\chi^2 = 1.001$) with the lifetime errors shown 3 deviations. These data yielded a strong short lifetime component of 0.68 ± 0.01 ns (τ_1) (82.5%) and a weaker long lifetime component of 1.23 ± 0.12 ns (τ_2) (17.5%). We also studied the fluorescence lifetime of the truxene blend solution and the fitted data showed that it was a single exponential decay with a lifetime of 0.67 ± 0.01 ns, which was consistent with the strong short lifetime component of the polymerized truxene blend materials. The weak long lifetime component appearing in the cured materials is postulated to result from some aggregate formation of truxene oligomers in the polymer matrix. In the solution state, the oligomer molecules are presumably isolated, while after curing, the molecules may aggregate and be trapped in the matrix creating a new absorption band, which has a longer radiative lifetime than normal intrachain excitation [22]. Further detailed study is required to understand the full effects of the blending process, but the time-resolved measurements provide further evidence that the optical properties are not much altered.

4 Conclusion

In summary, we have demonstrated an attractive means to controllably micro-pattern highly-fluorescent truxene oligomer nanostructures for a wide range of applications including optoelectronics. By blending the truxene oligomers into a photocurable polymer matrix suitable for ink-jet printing, demonstrator arrays of spherically-shaped micro-dots have been produced, of diameters in the range 12–25 µm. Single micro-dot PL measurements and time-resolved luminescence measurements indicate that the blend materials retain their advantageous optical properties during this processing.

References

1. W.J. Parak, T. Pellegrino, C. Plank, Nanotechnology **16**, R9 (2005)
2. L. Yan, J.Y. Zhang, Y. Cui, Y. Qiao, Appl. Phys. Lett. **91**, 243114 (2007)
3. A.W. Grice, D.D.C. Bradley, M.T. Bernius, M. Inbasekaran, W.W. Wu, E.P. Woo, Appl. Phys. Lett. **73**, 629 (1998)
4. G. Heliotis, S.A. Choulis, G. Itskos, R. Xia, R. Murray, P.N. Stavrinou, D.D.C. Bradley, Appl. Phys. Lett. **88**, 081104 (2006)
5. W.Y. Lai, R.D. Xia, Q.Y. He, P.A. Levermore, W. Huang, D.D.C. Bradley, Adv. Mater. **21**, 355 (2009)
6. Y. Geng, S.W. Culligan, A. Trajkowska, J.U. Wallace, S.H. Chen, Chem. Mater. **15**, 542 (2003)
7. A.L. Kanibolotsky, R. Berridge, P.J. Skabara, I. Perepichka, D.D.C. Bradley, M. Koeberg, J. Am. Chem. Soc. **126**, 13695 (2004)
8. J.A. DeFranco, B.S. Schmidt, M. Lipson, G.G. Malliaras, Org. Electron. **7**, 22 (2006)
9. Z.H. Nie, E. Kumacheva, Nat. Mater. **7**, 277 (2008)
10. E. Gu, A. Mackintosh, A.J.C. Kuhne, R.A. Pethrick, C. Belton, D.D.C. Bradley, M.D. Dawson, Appl. Phys. Lett. **90**, 031116 (2007)
11. Y. Wang, J. Bokor, A. Lee, Proc. SPIE **5374**, 628 (2004)
12. P. Calvert, Chem. Mater. **13**, 3299 (2001)
13. A.J.C. Kuehne, D. Elfstrom, A.R. Mackintosh, A.L. Kanibolotsky, B. Guilhabert, E. Gu, I.F. Perepichka, P.J. Skabara, M.D. Dawson, R.A. Pethrick, Adv. Mater. **21**, 781 (2009)
14. E. Tekin, P.J. Smith, S. Hoeppener, A.M.J. van den Berg, A.S. Susha, A.L. Rogach, J. Feldmann, U.S. Schubert, Adv. Funct. Mater. **17**, 23 (2007)
15. G. Raabe, J. Michl, *The Chemistry of Organic Silicon Compounds* (Wiley, New York, 1989), Chap. 17
16. J. Sumerel, J. Lewis, A. Doraiswamy, L.F. Deravi, S.L. Sewell, A.E. Gerdon, D.W. Wright, R.J. Narayan, Biotechnol. J. **1**, 976 (2006)
17. N. Laurand, B. Guilhabert, E. Gu, S. Calvez, M.D. Dawson, Opt. Lett. **32**, 2831 (2007)
18. T.H. Chiang, T.E. Hsieh, Int. J. Adhes. Adhes. **26**, 520 (2006)
19. C.D. McGuinness, K. Sagoo, D. McLoskey, D.J.S. Birch, Appl. Phys. Lett. **86**, 261911 (2005)
20. D.J.S. Birch, R.E. Imhof, *Topics in Fluorescence Spectroscopy, vol. 1: Techniques* (Plenum, New York, 1991), Chap. 1
21. R.F. Steiner, *Topics in Fluorescence Spectroscopy, vol. 2: Principles* (Plenum, New York, 1992), Chap. 1
22. T. Nguyen, V. Doan, B.J. Schwartz, J. Chem. Phys. **110**, 4068 (1999)